SLAC-357
UC-414
(E)

DEEP INELASTIC STRUCTURE FUNCTIONS FROM ELECTRON SCATTERING ON HYDROGEN, DEUTERIUM, AND IRON AT 0.6 GeV$^2 \leq Q^2 \leq$30.0 GeV^2*

L. W. Whitlow

Stanford Linear Accelerator Center
Stanford University
Stanford, California 94309

March 1990

Prepared for the Department of Energy
under contract number DE-AC03-76SF00515

Printed in the United States of America. Available from the National Technical Information Service, U.S. Department of Commerce, 5285 Port Royal Road, Springfield, Virginia 22161. Price: Printed Copy A10, Microfiche A01.

* Ph.D. thesis

Abstract

We report the final results from experiment E140, a recent deep inelastic electron–deuterium and electron-iron scattering experiment at SLAC. In addition, we present the results of a combined global analysis of all SLAC deep inelastic electron–hydrogen and electron–deuterium cross section measurements between 1970 and 1983. Data from seven earlier experiments are re-radiatively corrected and normalized to experiment E140. We report extractions of $R(x,Q^2)$ and $F_2(x,Q^2)$ for hydrogen and deuterium over the entire SLAC kinematic range: $.06 \leq x \leq .90$ and $0.6 \leq Q^2 \leq 30.0$ (GeV^2).

We find that $R^p = R^d$, as expected by QCD. Extracted values of $R(x,Q^2)$ are significantly larger than predictions based on QCD and on QCD with the inclusion of kinematic target mass terms. This difference indicates that dynamical higher twist effects may be important in the SLAC kinematic range.

A best fit empirical model of $R(x,Q^2)$ is used to extract F_2 from each cross section measurement. These F_2 extractions are compared with F_2 data from EMC and BCDMS. Agreement is observed with EMC when the EMC data are multiplied by $\times 1.07$. Agreement is observed with BCDMS over a limited range in x. The ratios of F_2^d/F_2^p are examined for Q^2 dependence. We observe a significant negative slope for $x \leq .6$, and a significant positive slope above $x > .7$, in excellent agreement with predictions based on QCD with the inclusion of kinematic target mass terms.

Acknowledgments

I would like to thank several individuals without whom this thesis would not have happened. In chronology, I first thank Jim Skinner for providing the tools and the foundation for my work as a physicist. Next I thank Ted Hayden for his confidence in my abilities and the lasting impact of his friendship. I thank Gail Nishioka and Dave Spooner for their friendship and support during the long span of my graduate career. I am indebted to Karl Van Bibber and Mason Yearian for their support and encouragement during the experiment and the analysis. I thank Lisa Clogher, my wife and best friend, for her love and understanding throughout this arduous portion of our lives. I am greatly indebted to Arie Bodek and Sridhara Dasu for their many technical contributions to this work. I thank Mike Riordan for his wise council both as a physicist and as a friend. I greatly thank Steve Rock for his excellent guidance throughout the entirety of this work, and equally for his friendship and understanding. And finally, I thank Elliott Bloom for his inspiration and generous support during the later stages of this thesis.

Table of Contents

List of Tables

List of Figures

Chapter 1

Introduction

The objective of this experimental and analytical thesis is to clarify and expand our knowledge of hydrogen and deuterium structure functions in the intermediate Q^2 range between the nucleon resonance region and the high Q^2 domain of perturbative QCD. Our goal is to create a rigorous statistical framework for the extraction of SLAC structure functions, and to use this framework in the reanalysis of all deep inelastic cross section measurements at SLAC, including those of our recent experiment E140.

In this chapter we discuss our motivation and provide a brief overview of E140 and the global reanalysis effort. In Chapters 2 and 3, we discuss the experimental and analytical details of E140, with emphasis on the origin and propagation of experimental and theoretical uncertainty in the cross section measurements. In Chapter 4 we present the final structure function results for E140, superceding the results of our two previous reports.[1,2] Chapter 5 is devoted to the rigorous extraction of the structure functions $R(x, Q^2)$ and $F_2(x, Q^2)$ from the combined set of all deep inelastic cross section measurements at SLAC, improving on two previous similar efforts.[3,4]

Section 1.3 explains the notation conventions used throughout this report. Appendix A provides a brief reference for deep inelastic electron scattering – both a concise definition of the scattering kinematics and an elementary introduction to the subject. Appendix B provides a review of several important statistical ideas used frequently in this report. Appendix E and the enclosed IBM and Macintosh diskettes present the final SLAC structure function tables for hydrogen and deuterium.

1.1 Motivation

Currently there exist large disparities within and among the structure function results of various collaborations. This situation is worsened by the fact that the experimental datasets are often kinematically disjoint, making comparisons difficult and subjecting global analyses to large systematic error. These discrepancies propagate into large uncertainties in the parton distribution functions, impairing the calculational ability of QCD. A precise knowledge of the parton distributions is critical in any attempt to compare the fundamental interactions of the theory with measured cross sections.

Any rigorous test of QCD, however, must additionally contend with target mass and higher twist power corrections. These corrections obscure the logarithmic scaling of the structure functions, adding ambiguity to measurements of $\Lambda_{\rm QCD}$ and clouding the extraction of the parton distributions. The importance of the deep inelastic scattering data in understanding nucleon structure and power corrections to QCD cannot be overstated.

1.1.1 The Structure Function $R = \sigma_L/\sigma_T$

Experimental determinations of the structure functions $F_2(x,Q^2)$ and $R(x,Q^2)$ require cross section measurements at the same (x,Q^2) over a range of ϵ. The relationship between these quantities is

$$\frac{\sigma(x,Q^2,\epsilon)}{\sigma^{mott}}\,\nu = F_2(x,Q^2)\left[1+\frac{1-\epsilon}{\epsilon}\frac{1}{1+R(x,Q^2)}\right]\,, \tag{1.1}$$

though, in practice we exploit the linear relationship between σ/Γ and ϵ,

$$\sigma(x,Q^2,\epsilon)\,\frac{1}{\Gamma} = \sigma_T(x,Q^2)\left[1+\epsilon\,R(x,Q^2)\right]\,, \tag{1.2}$$

to extract R and F_2 from the parameters of the best fit line. The impact of this technique is directly tied to the span in ϵ, or $\Delta\epsilon$, over which the cross sections are accurately measured.

With the End Station A apparatus[5] at SLAC it is difficult to measure cross sections over a large $\Delta\epsilon$ with a single spectrometer. By combining data from three experiments taken with two spectrometers, Bodek *et al.*[3] were able to extract $R(x,Q^2)$ and $F_2(x,Q^2)$ for hydrogen and deuterium over a wide kinematic range. Their results for $R(x,Q^2)$ are consistent with no kinematic dependence,

$$R^p = .138 \pm .011 \pm .056 \ , \qquad R^d = .175 \pm .009 \pm .060 \ . \tag{1.3}$$

and are shown in Figure 1.1 averaged over x and averaged over Q^2. In a similar analysis, Mestayer *et al.*[4] combined data from seven experiments and three spectrometers, to extract $R(x,Q^2)$ over a smaller kinematic range. Their values are likewise consistent with simple constants,

$$R^p = .21 \pm .10 \ , \qquad R^d = .22 \pm .10 \ , \tag{1.4}$$

and are similarly shown in Figure 1.1. As the data analyzed by Bodek *et al.*[3] is a subset of that used by Mestayer *et al.*,[4] these results are not entirely independent.

Also presented in Figure 1.1 are calculations[6] of R based on QCD[7] and on QCD with the inclusion of target mass effects[8] (QCD+TM). These calculations are presented at the mean x and mean Q^2 of each datum of Bodek *et al.*[3] These early SLAC measurements of R are consistently higher than R^{QCD} and $R^{\mathrm{QCD+TM}}$. At low x the data seems to rise in good agreement with theory, though, the data is equally consistent with the constant values of Equations 1.3 and 1.4.

At very high Q^2, R goes to zero according to the Callan-Gross relation. Observations of R from deep inelastic muon scattering from hydrogen[9] and iron[10] by EMC are in good agreement with this. These EMC values are consistent with both $R = R^{\mathrm{QCD}}$ and $R = 0$ for a mean Q^2 of 25 GeV^2, and display overall averages of

$$R^p = -.019 \pm .034 \pm .118 \ , \qquad R^d = .036 \pm .040 \pm .087 \ . \tag{1.5}$$

A smooth transition between the large R seen at intermediate Q^2 and the small R

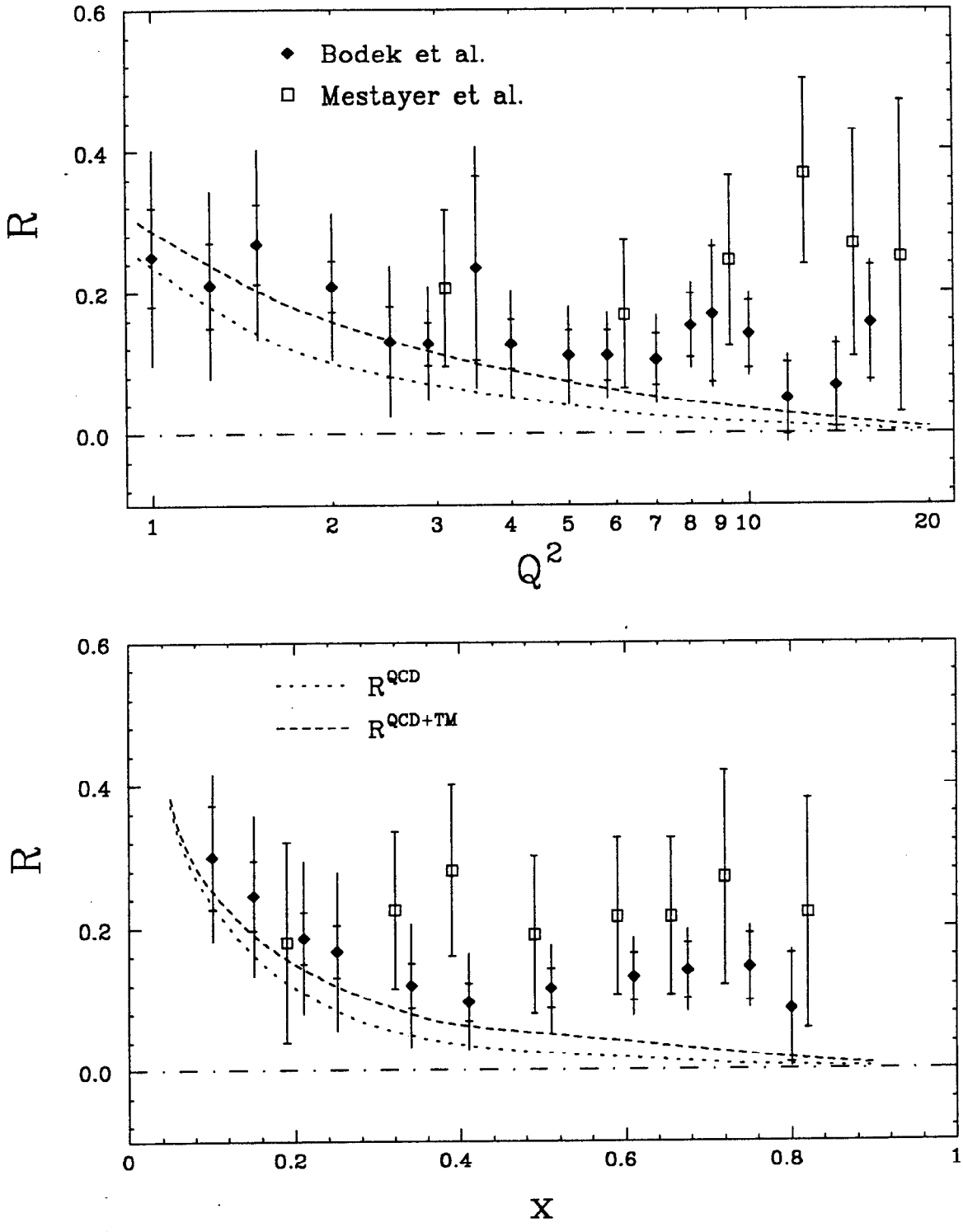

Figure 1.1. Shown are the SLAC measurements of R^p from two previous analyses. Data are systematically higher than R^{QCD} and $R^{\mathrm{QCD+TM}}$, and everywhere consistent with $R(x,Q^2)=.17$. Results for R^d from these analyses are similar. Errors bars on the Mestayer *et al.*[4] results include both statistical and systematic uncertainties.

observed at high Q^2 is consistent with both SLAC and EMC, but is nowhere evidenced. Other measurements of R^{Fe} from muon[11,12] and neutrino[13–15] scattering display no kinematic dependence and are consistent with any constant value of R between zero and .2.†

A precise experimental determination of $R(x, Q^2)$ would permit a critical test of QCD, QCD+TM, and higher twist effects. In the SLAC kinematic range, the contributions to R arising from target mass and higher twist effects are expected to be large compared to leading order QCD. A significant difference between measured R and $R^{\mathrm{QCD+TM}}$ would be a primary observation of higher twist effects in nuclear structure. A precise measurement of R would test the predictions of other proposed nonperturbative contributions to nuclear structure, most notably, diquark formation.[19]

1.1.2 The Structure Function F_2

To extract F_2 from the measured cross sections one must either simultaneously extract R or claim *a prior* knowledge of R. In muon scattering, for example, F_2 follows directly from Equation 1.1 under the assumption that $R = R^{\mathrm{QCD}}$ or $R = 0$. This is a reasonable assumption, except at small x where R may not be so small and where ϵ becomes a strong function of Q^2 at fixed beam energy. On the other hand, in electron scattering at SLAC, F_2 and R are simultaneously determined from linear regression analyses to Equation 1.2. This technique yields relatively large statistical uncertainties in F_2, but is necessary in light of the absence an adequate model of R in the SLAC kinematic range.

It is highly desirable to combine the F_2 results from muon and electron scattering to form a single dataset spanning two orders of magnitude in Q^2. This combined F_2 dataset would permit tests of QCD over a wide span in Q^2, while simultaneously exposing target mass and higher twist contributions to theoretical or phenomeno-

† Recent high precision results from the BCDMS[16,17] and CDHSW[18] collaborations are compared with our results in Sections 4 and 5.

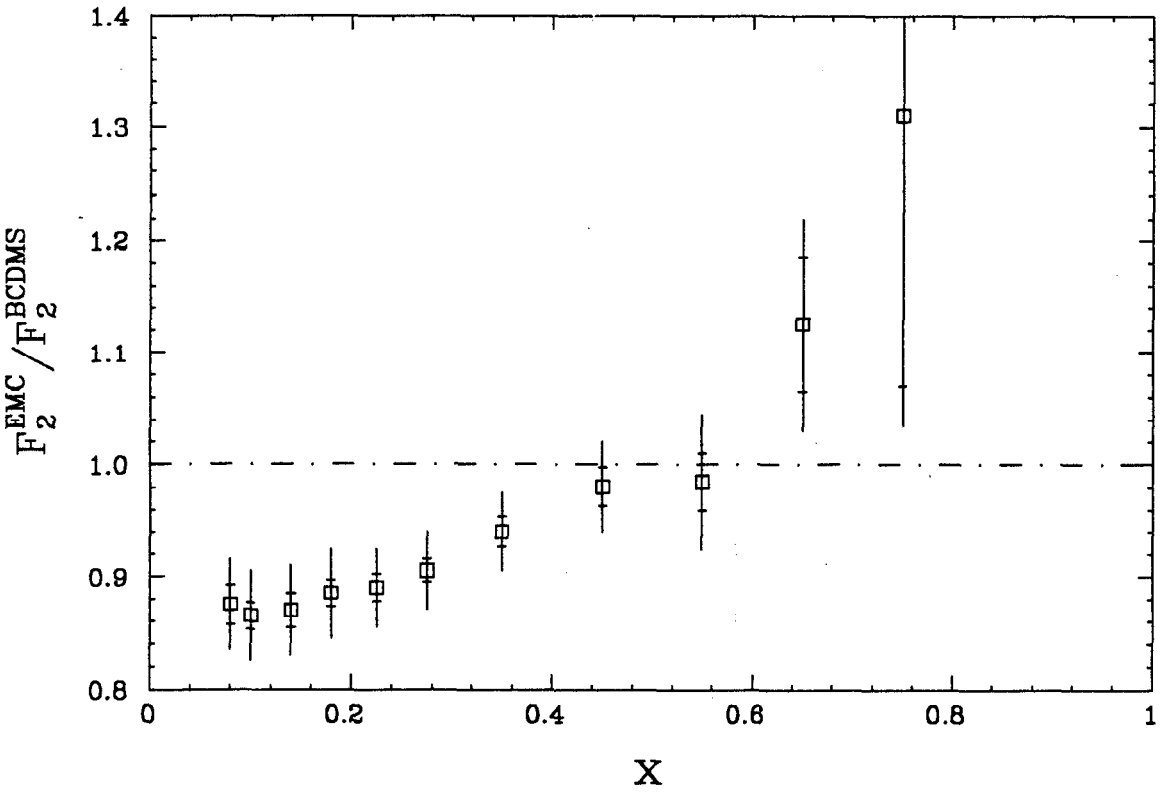

Figure 1.2. Shown are the EMC/BCDMS hydrogen F_2 ratios,[16] averaged over Q^2. Results[17] for F_2^d ratios are similar.

logical analysis. Most important, perhaps, in light of the current discrepancy[16,17,20] between EMC[9,21] and BCDMS[16,17] hydrogen and deuterium structure functions, would be the simple unification of the SLAC F_2 results with one or the other of these high precision F_2 datasets. This discrepancy, shown in Figure 1.2, is not resolvable by comparison[16,17,20] with the early SLAC results of Bodek *et al.*,[3] which are at lower Q^2 (compare Figure 5.13 with Figures 5.14 through 5.17).

A precise experimental determination of $R(x, Q^2)$ could be used to derive an accurate model of R in the SLAC kinematic range. This model could then be used to precisely extract F_2, via Equation 1.1, from each cross section measurement. This technique would yield F_2 extractions at twice the Q^2 previously reported by Bodek *et al.*,[3] extending well into the high Q^2-domain of the EMC and BCDMS datasets.

1.1.3 Neutron/Proton Studies

In practice, the difference between R^d and R^p is obtained with minimal systematic uncertainty via

$$\frac{\sigma^d}{\sigma^p} = \frac{\sigma_T^d}{\sigma_T^p}\left[1 + \epsilon'\left(R^d - R^p\right)\right] , \tag{1.6}$$

where

$$\epsilon' = \frac{\epsilon}{1 + \epsilon R^d} , \tag{1.7}$$

which follows directly from Equation 1.2. Assuming the smearing corrections for F_1 and F_2 are the same, this difference is related to R^n by[3]

$$R^n = R^d + \left[R^d - R^p\right]\frac{(F_1^p)_S}{(F_1^n)_S} , \tag{1.8}$$

where $(F_1)_S$ denotes the smeared structure function. While QCD does not predict a significant difference between R^d and R^p, nonperturbative diquark formation[19] predicts $R^d - R^p \approx .07$ for $x > .6$. Measured values of $R^d - R^p$ by Bodek *et al.*[3] are shown in Figure 1.3, averaged over Q^2. While consistent with zero, the large uncertainties do not rule out a significant kinematic dependence, including that predicted by diquark formation. The overall average of the Bodek *et al.*[3] data is

$$R^d - R^p = .031 \pm .015 \pm .036 , \tag{1.9}$$

where the systematic error is dominated by uncertainties in the relative normalizations of the three experimental datasets included in the analysis.

Recent attempts[22,23] to determine an upper limit on the mass of the top quark from the ratio

$$\mathbf{R} = \frac{\#\left(W \rightarrow e\nu\right)}{\#\left(Z \rightarrow ee\right)} \tag{1.10}$$

from UA1[24] and UA2[25] measurements, have become muddled by differences between the quark distributions obtained from the EMC and the BCDMS data. In particular,

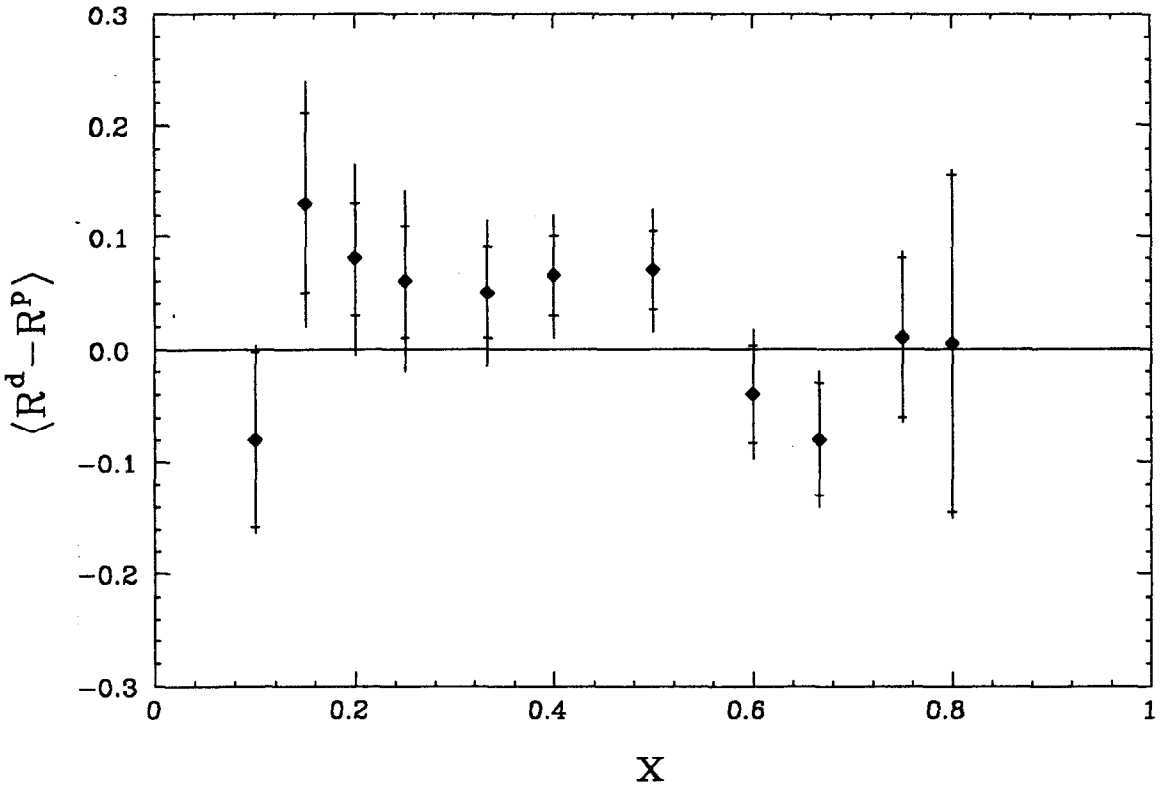

Figure 1.3. Shown are measurements of $R^d - R^p$ by Bodek *et al.*,[3] averaged over Q^2.

R is sensitive to the ratio of up to down quark distributions,[28] as is the ratio F_2^n/F_2^p. The current disparity[26] in F_2^n/F_2^p between EMC, BCDMS and the SLAC results of Bodek *et al.*,[3] shown in Figure 1.4, propagates into large uncertainties in the upper limit for the top quark mass.

While the extraction of neutron structure functions is beyond the scope of this thesis, a precise determination of the ratio $F_2^d(x,Q^2)/F_2^p(x,Q^2)$ would permit comparisons with similar ratios from EMC and BCDMS. The most important region for this comparison is at low x where smearing effects are quite small. Alternatively, precise measurements of F_2^d/F_2^p might reveal a significant negative slope with respect to $[\ln Q^2]$, which would be consistent with the data shown in Figure 1.4.

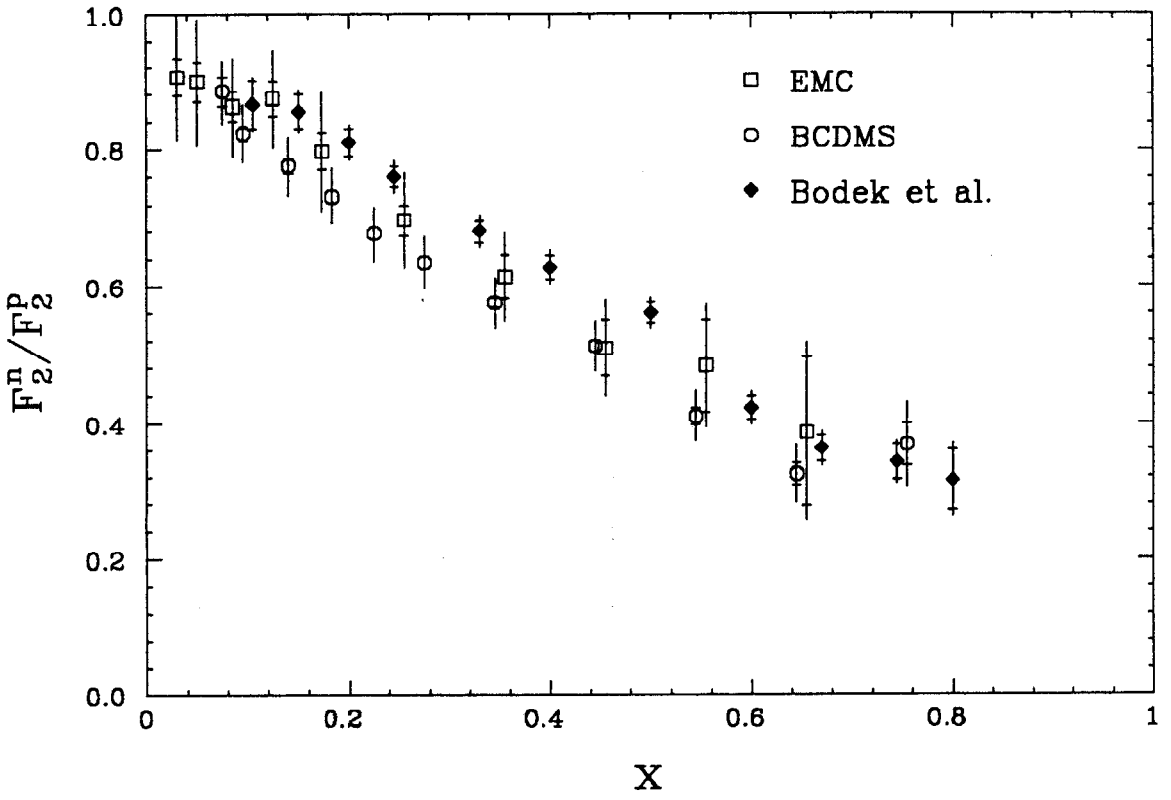

Figure 1.4. Shown are the ratios of F_2^n/F_2^p for the EMC,[21] BCDMS,[26] and SLAC[3] datasets. The SLAC data shown here have been re-corrected[26] for smearing effects a la Frankfurt and Strikman.[27]

1.2 Overview

Our response to the need for more accurate knowledge of structure functions in the SLAC kinematic range is twofold. First, experiment E140 addresses the kinematic variation of R using a single spectrometer in a dedicated effort to reduce systematic uncertainties in R to the $\pm.03$ level. And second, a global reanalysis of the earlier cross section measurements results in more extractions of R and F_2 over a much wider span in (x, Q^2), and occasionally rivaling the statistical and systematic accuracy of the E140 results. Neither of these efforts would be possible without the recent improvements to our radiative corrections procedure. Our new Bardin/Tsai radiative corrections procedure is described in Section 3.2.2 and in more detail in Reference 29.

1.2.1 Experiment E140

Experiment E140 is designed to measure $R(x,Q^2)$ to $\pm.04\pm.03$ statistical and systematic accuracy. By using a single spectrometer, we explicitly remove the largest source of uncertainty faced by Bodek *et al.*[3] and Mestayer *et al.*[4], though in doing so, we impose tight limits on the range of accessible (x,Q^2,ϵ). Our choice of the 8 GeV Spectrometer facility[5] of End Station A is made to maximize, for a wide range of (x,Q^2), the span in ϵ over which we can accurately measure cross sections.

Figure 1.5 shows the (x,Q^2) point selection for E140. Limitations in x and Q^2 are dictated primarily by the resonance region and the maximum electron beam energy and intensity. The upper limit in ϵ is determined by the minimum scattering angle (11.5°) and by the maximum scattering momentum (8.0 GeV). The lower limit in ϵ is a product of several concerns: minimum scattering momentum (1.0 GeV), maximum radiative correction (−40%), and maximum acceptable background rates (13% charge symmetric; 125 π^-/e^- ratio). The available span in ϵ under these constraints is $\Delta\epsilon\approx.35$ for all (x,Q^2), demanding $\pm1\%$ cross section measurements to meet the statistical goal of E140.

An additional goal of E140 was to measure the differences $R^{Fe}-R^d$ and R^d-R^p. Discrepancies at low x between the original report[21] of the EMC effect and subsequent low Q^2 observations[30,31] from SLAC gave cause to suspect[32] that $R^{Fe}\gg R^d$ in the SLAC Q^2 range, contrary to QCD predictions.[33] Our results for R^{Fe} and $R^{Fe}-R^d$ are included in this report. However, as our hydrogen target was irreparably damaged very early in E140, no results are reported for R^p or R^d-R^p.

As each (x,Q^2,ϵ) point corresponds to a unique set of laboratory scattering parameters, (E_o,E',θ), cross sections were measured in the virtually random order dictated by the need to minimize the number of beam energy changes. Careful attention to all known systematic effects was critical to ensure the integrity of our extractions of R from cross sections measured days, or weeks, apart. At each (E_o,E',θ), cross section measurements on all scheduled targets were interleaved to eliminate many relative systematic errors.

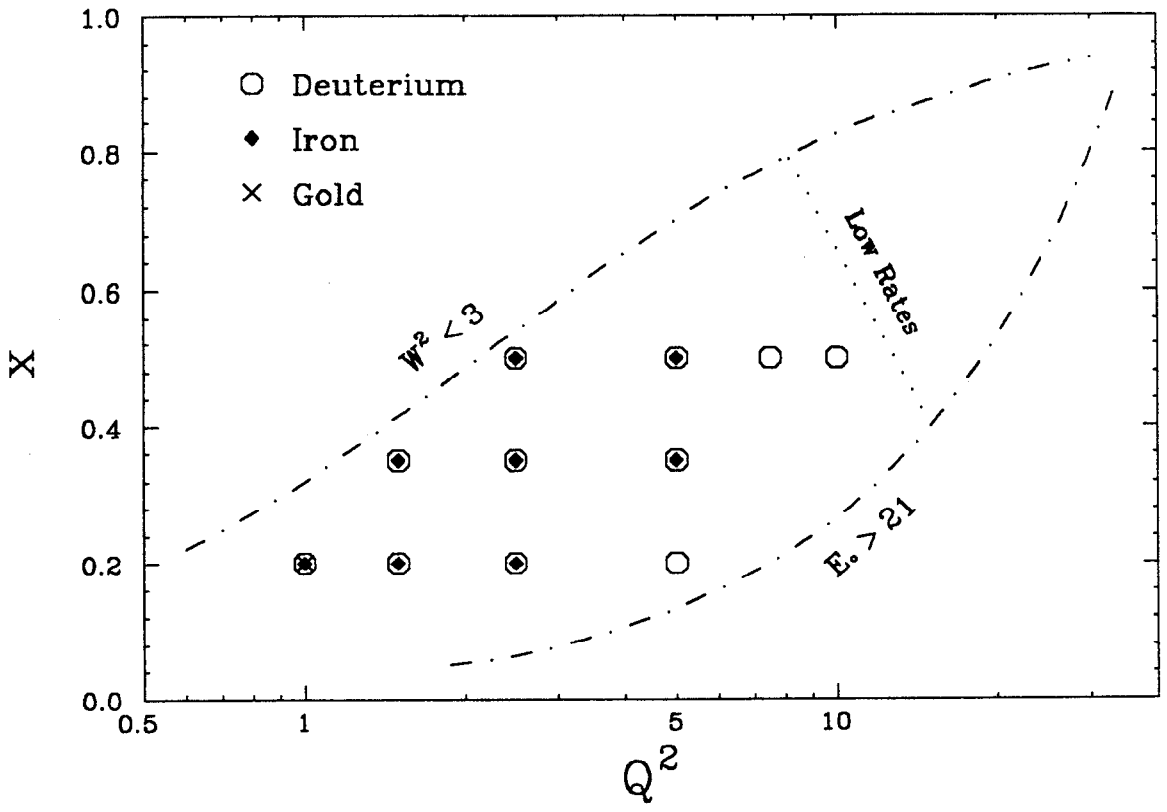

Figure 1.5. Shown is the E140 kinematic point selection for each target, with curves indicating kinematic restrictions.

1.2.2 Global Reanalysis

This global reanalysis is the third attempt to assimilate all prior deep inelastic cross sections measurements at SLAC into a single coherent, consistent dataset for the extraction of the structure functions R and F_2. Both previous attempts met with only limited success:

- The 1979 study by Bodek *et al.*,[3] while rigorous in the treatment of systematic uncertainties, suffered largely from the limited statistics and kinematic range spanned by only three experiments. Uncertainties of $\pm 1\%$ in the relative normalizations of the datasets and of $\pm 5\%$ in the MIT radiative corrections procedure[3,34] greatly limited the resolution of their analysis.

- The 1983 study by Mestayer *et al.*,[4] while abounding in statistics and kinematic range, suffered largely from the nonrigorous treatment of systematic errors. The dominant uncertainties in this study were the large uncertainties in the relative normalizations of the datasets.† Of lesser importance, though still significant, was the ±5% uncertainty of the Tsai radiative corrections procedure.[36]

Our reanalysis is founded on three major analytical advancements: First, the new Bardin/Tsai radiative corrections procedure reduces the systematic uncertainties due to radiative corrections to below the ±1% level. Second, a new technique is used to precisely determine the relative normalizations of the datasets, yielding typical uncertainties of ±.7%. And third, a highly detailed propagation of systematic errors exploits all known correlations, resulting in smaller, more accurate estimates of the structure function uncertainties.

We include in our global reanalysis all deep inelastic experiments at SLAC dating back to 1970. These experiments were performed at the End Station A experimental facility using one of three spectrometers: the 1.6 GeV,[37] the 8 GeV,[5] or the 20 GeV.[38] Given the excellent documentation that exists for these experiments, we are confident of our grasp of most or all of the experimental details. The eight experiments included in our reanalysis are listed in Table 1.1.‡ Noteworthy among these is E139, a high precision study of the EMC effect which rivals E140 in the measurement of deuterium cross sections.

The kinematic ranges of these eight experiments are shown in Figure 1.6. Each point represents either an individual cross section measurement or the centroid of a

† It should be noted that despite observing[35] normalization differences among the datasets as large as 5.5%, no correction was made for these disparities. Rather, these differences were taken to be normalization *uncertainties* and were propagated through the R extractions, resulting in the inflated statistical errors shown in Figure 1.1.

‡ Earlier deep inelastic data which are not included in this study are summarized in Reference 39. We do not include in our study the portion of experiment E4b due to Miller *et al.*,[40] though this data is included in the analysis of Mestayer *et al.*[4]

Table 1.1. Presented is a summary of the datasets included in our global reanalysis. The year is that in which the experiment was performed. The two SLAC collaborations are Group A and the Spectrometer Facilities Group, denoted SGA and SFG, respectively.

Experiment	Spec-trometer	Targets	Thesis	Primary Reference	Collab-oration	Year
E49a † ‡	20.	H D	41	3,42	MIT/SGA	1970
E49b † ‡	8.	H D	34,43	3	MIT/SFG	1970
E61 ‡	20.	H D	none	44	SGA	1971
E87 † ‡	8.	H D	none	3	MIT/SFG	1972
E89a ‡	1.6	H D	45	46	SGA	1974
E89b ‡	20.	H D	35	4	SGA	1974
E139	8.	D	30	31	E139	1983
E140	8.	D	29,47	47	E140	1985

† Included in 1979 study by Bodek *et al.*[3]
‡ Included in 1983 study by Mestayer *et al.*[4]

set of adjacent measurements. All experiments prior to E139 were constrained by radiative corrections considerations[34,36] to measure cross sections in E'-spectra for each (E_o^j, θ), for several beam energies $E_o^j \leq E_o$. Thus, each upward-sweeping spectra in Figure 1.6 represents measurements over a span in E' for a specific (E_o, θ). Cross sections were measured on hydrogen and deuterium in an interleaving fashion to eliminate or reduce many relative systematic errors.

A composite of Figure 1.6 is presented in Figure 1.7 with E139 and E140 data highlighted. Visible are our imposed cuts at $W^2 \geq 3$ GeV^2, and our cuts at

$$x \geq .062\,, \quad \text{and} \quad Q^2 \geq .566 \text{ GeV}^2\,, \tag{1.11}$$

made to guarantee convergence of the radiative corrections. Also indicated in Figure 1.7 is the overlap of the SLAC data with those of EMC and BCDMS. Though not extensive, this overlap is critical if the SLAC data is to resolve the EMC/BCDMS discrepancy shown in Figure 1.2.

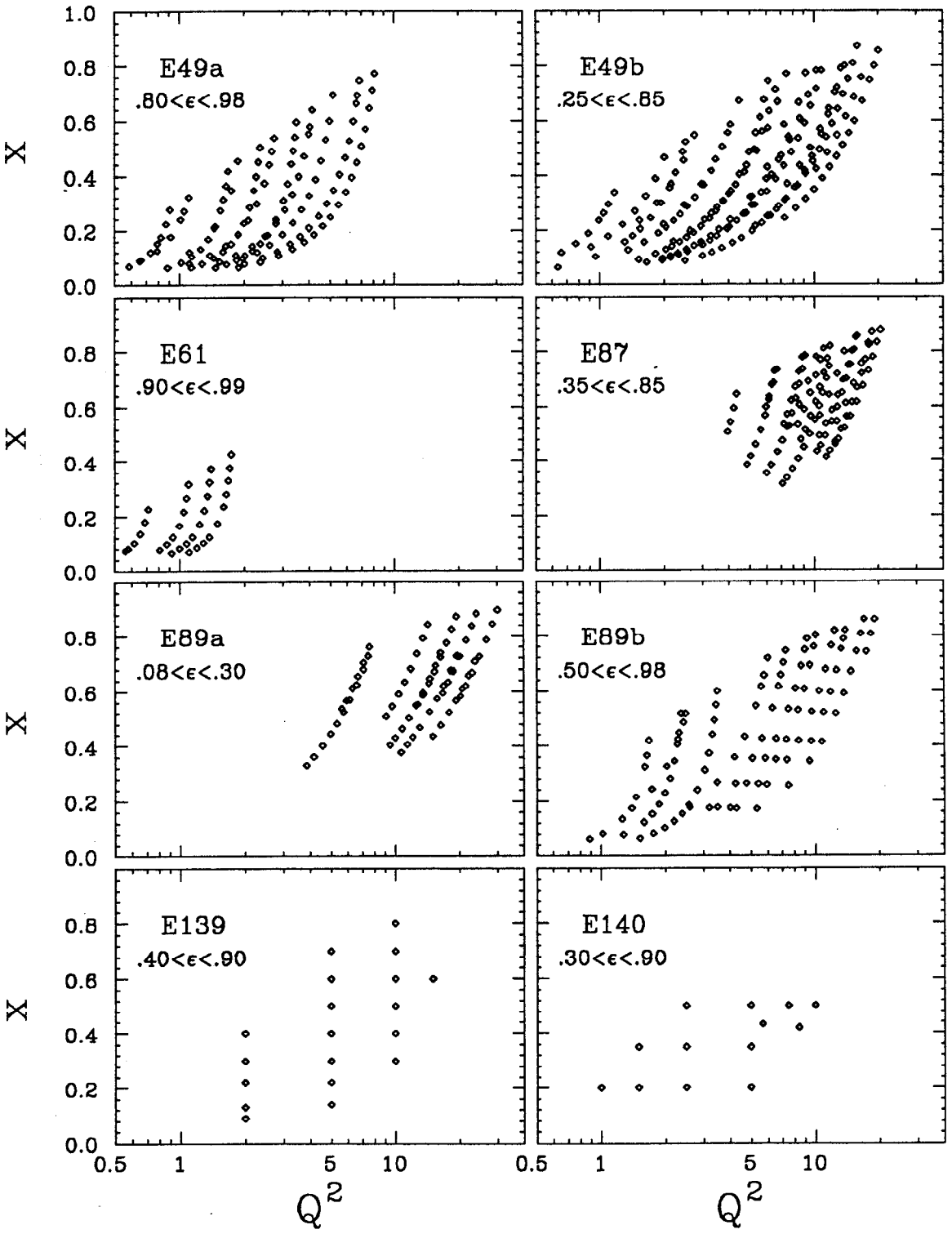

Figure 1.6. Shown are scatterplots in (x, Q^2) of the scattering kinematics of each of early SLAC experiments. The ϵ range of each experiment is also indicated. See text for more details.

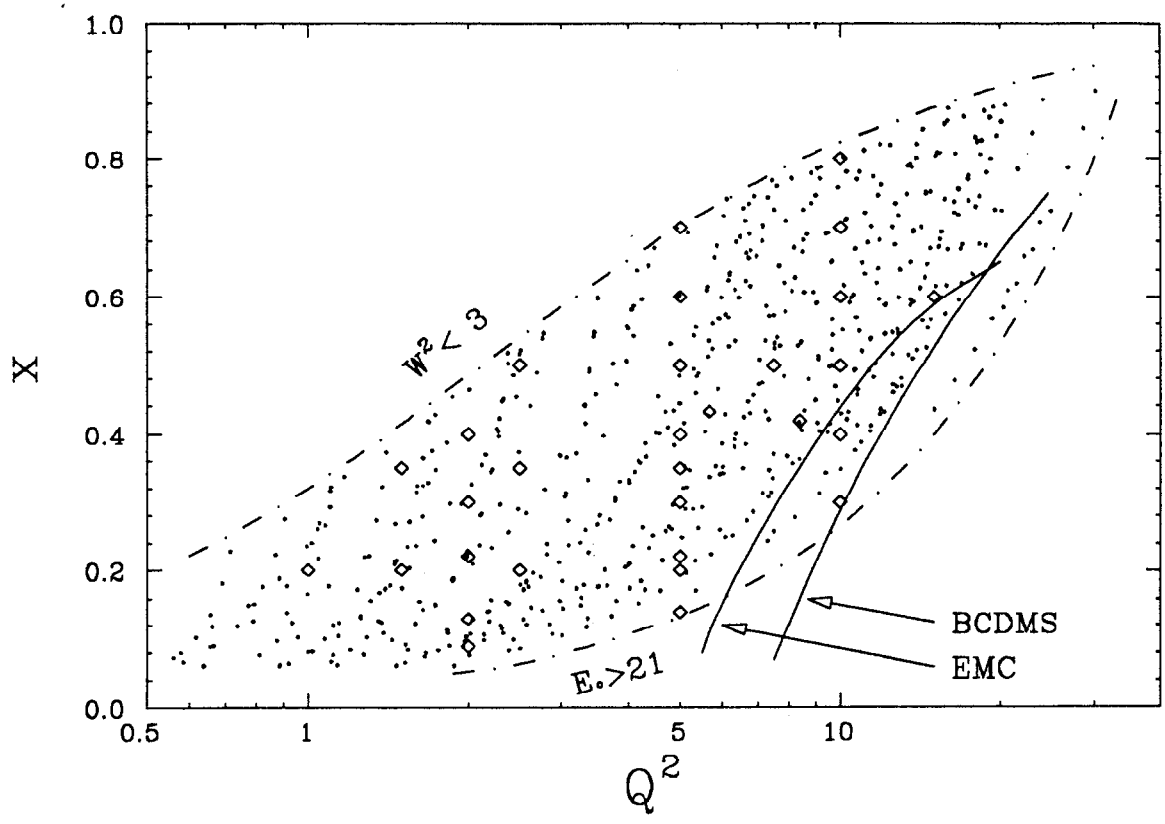

Figure 1.7. Shown is a composite scatterplot of all SLAC cross section measurements. High statistics measurements (±.8%) by E139 and E140 are shown as large diamonds. The low Q^2 extents of the EMC and BCDMS hydrogen measurements are also indicated.

1.3 Notation Conventions

Throughout this report we employ the usual $\hbar = c = 1$ notation, we use only *natural* logarithms, and in paired coordinates such as $(x, Q^2) = (.2, 5)$, we suppress the obvious units.

Cross sections are expressed in units of $[\text{pb}/(\text{sr}\,\text{GeV})]$ and defined per target nucleon. Structure functions are similarly defined per target nucleon. Iron and gold cross sections and structure functions, as reported, include a symmetrizing correction for neutron excess (Equations 3.8 and 5.49).

Uncertainties in the cross sections and extracted values of F_2 are always expressed relatively. Uncertainties in R are always expressed absolutely.

In all plots, the data are presented with the total error given by the full error bar, and with the statistical (or random) component of the total error designated by the hashmark on the error bar. Exceptions to this rule are at all times clearly noted.

Correction factors are quantities by which one *multipies* the data. Normalization factors are likewise the number by which one multiplies. For example, the normalization factor of dataset A to dataset B is the number by which dataset A must be multiplied to make it compatible with dataset B.

Calculations[6] of R and F_2 based on QCD plus target mass effects (QCD+TM) are made according to the prescription of Georgi and Politzer.[8]

Lastly, our need to work both in the laboratory frame and in the spectrometer, or TRANSPORT,[48] frame introduces notational ambiguities. To avoid double uses of the symbols theta and phi, we let (θ,ϕ) represent quantities in the laboratory frame, and (ϑ,φ) represent quantities in the spectrometer frame. Double uses of the symbol "δ" cannot be avoided, however. We use this symbol both as a TRANSPORT variable and as a differential, to represent uncertainties.

Chapter 2

E140 Experimental Apparatus

A schematic representation of the 8 GeV spectrometer facility at SLAC is shown in Figure 2.1. The detector package performs the dual role of electron/background discrimination and particle trajectory analysis. For particle identification we rely on a threshold hydrogen gas Čerenkov counter plus calorimetric information from a lead glass shower array. Scattering trajectories are determined with ten planes of multiwire proportional chambers (the MWPC).

Our primary trigger components are a high signal from the Čerenkov counter and an early shower development in the lead glass array. Event signals are recorded by a PDP-11/04 and VAX-11/780 computers. Other experimental parameters are monitored by an LSI-11 computer and passed to the VAX-11/780 at ten minute intervals.

2.1 The Electron Beam

The E140 electron beam originates at the Main Injector for beam energies greater than 4.25 GeV and otherwise at the more luminous Nuclear Physics Injector.[49] The electrons are accelerated by the Stanford Linear Accelerator[50] and momentum analyzed in the A-bend[3,30,50] of the beam switchyard before being sent to the target. The central energy of the beam is determined to an absolute accuracy of $\pm.1\%$.[50] The maximum permitted total energy spread of the beam during E140 is $\pm.1\%$, though, for some low rate kinematics this condition is relaxed to $\pm.3\%$.

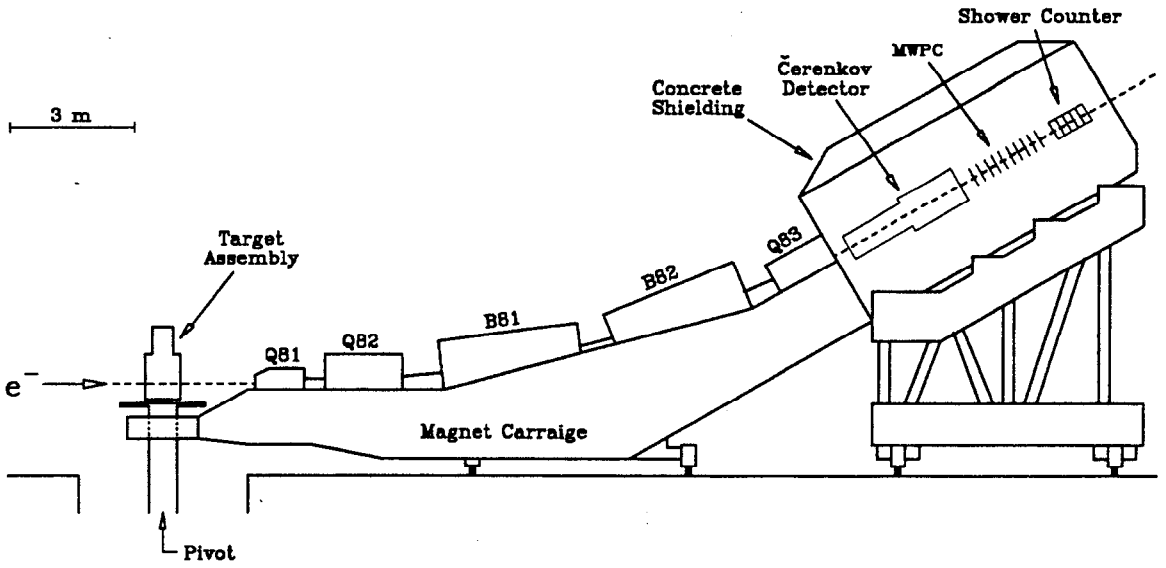

Figure 2.1. Shown is the 8 GeV Spectrometer apparatus of End Station A at SLAC. The two dipole magnets achieve momentum analysis through a 30° bend in the vertical. The three quadrupole magnets yield line-to-point focusing in the horizontal (along beamline) and point-to-point focusing in the vertical. Also indicated are the main E140 detector components inside the concrete shielding. During E140, additional concrete shielding was placed atop magnets Q82, B81 and B82.

The incident beam is continuously monitored[30] and steered by the LSI-11 computer, which maintains an incident angle within $\pm.003°$ of nominal beamline. Frequent visual confirmation of the steering alignment (at the $\pm.008°$ level) is made by inserting two ZnS screens into the beam. Beam profile is also monitored by the LSI-11. Typical spot sizes are .3 to .5 mm in diameter.

Beam intensities vary from 1 to 40×10^{10} electrons per 1.6 μs pulse, with typically 60 to 90 pulses per second. Two slightly different toroidal beam charge monitors[30,51,52] are used to estimate the charge in each beam pulse. These two systems typically agree to better than $\pm.2\%$. The toroids are calibrated against a charged capacitor every

few hours to correct the effects of fluctuations in temperature, amplifier gains, and timing signals. A detailed study[53] of our calibration system evaluates the uncertainty in our knowledge of the beam charge to be ±.3% (relative to a charged capacitor). This uncertainty is believed to be uncorrelated between measurements separated in time by an hour or so. Over much briefer periods, this uncertainty is more accurately estimated to be ±.2% and strongly self-correlated.

The absolute calibration of our beam charge monitoring system is known from three previous comparisons against a high precision Faraday cup.[54] Results from a detailed 1967-1968 study,[52] and two subsequent measurements[34,55] are summarized in Table 1.1. Agreement is observed at the ±.5% level for various beam energies, intensities, and pulse shapes.

Table 2.1. Shown are the results of three tests of the toroidal beam charge calibration system against a Faraday cup known to be accurate to ±.3%.

Study	Toroid/Faraday Cup
1968	1.0076 ± .0003
	1.0073 ± .0026
	.9978 ± .0006
	.9978 ± .0003
1970	.9980 ± .0050
1979	.9965 ± .0015

2.2 The Targets

To minimize systematic errors in the study of $R^{Fe}-R^{d}$ and $R^{Au}-R^{d}$ our target assembly is designed to rotate frequently between all targets. By interleaving partial cross section measurements on the scheduled targets, relative systematic errors due to beam charge fluctuations are reduced below the ±.1% level. Our target assembly[29,51] is modified from an earlier design[56] to include a set of thin solid targets, and is virtually identical to that used in the previous experiment E139.[30]

Table 2.2. Shown are the thin solid target thicknesses, measurements are ±.0005 cm.

Target	Thickness (cm)	Thickness (RL)	Uncertainty (%)
Fe#1	.1067	.0606	± .5
Fe#2	.0470	.0267	± 1.1
Au	.0198	.0592	± 2.5

Table 2.2 shows the thicknesses of our thin solid targets. We use two iron targets of different thicknesses to check the "external" portion of our radiative corrections procedure (see Section 3.2.2).

Additionally, we use two liquid deuterium targets of different lengths. Virtually all our deuterium measurements are with the long target which matches in radiation lengths (RL) the thin iron target. A description of the long deuterium target is given in Appendix D. The background contribution due to scattering from the aluminum entrance and exit windows of the target is measured at each kinematic point with an empty target replica.[57] This correction to the measured deuterium cross section is typically −1.1% and contributes ±.1% Poisson counting uncertainty to the measured cross section.

The deuterium density is measured at the entrance and exit of the target cell by platinum resistors and by hydrogen vapor pressure bulbs. Temperatures are measured and recorded every 10 sec. Random fluctuations in temperature are observed at the ±1° level.

Density changes due to heating by the beam[56] are minimized[58] by forced convection through a heat exchanger in thermal contact with a 21° liquid hydrogen reservoir. Temperature variations across the target length are typically .2°, indicating a density variation of .3%. Uncertainties in the calibrations of the two temperature measurement techniques are estimated to be less than ±.1°, though, our measurements indi-

cate a systematic disparity of .2° between the two techniques. The dominant source of uncertainty in the target density, however, is the cryogenic data for deuterium density at this temperature,[59] which is quoted to only ±.6%.

The deuterium target length is measured optically to ±.2%. The uncertainty in interaction length due to target cell misalignment is estimated to be ±.2%. And lastly, an uncertainty in the 2% hydrogen contamination of our deuterium supply propagates into ±.2% in the deuterium cross sections. A summary of the uncertainties due to the liquid deuterium target is presented in Table 2.3.

Table 2.3. Shown are the uncertainties to the cross section which originate at the liquid deuterium target. Most contributions are perfectly correlated across all kinematics, contributing only to the overall normalization uncertainty of E140.

Source	Cross Section Uncertainty (±%)
Counting Errors (δ^{ST})	
Endcap subtraction	±.1%
Random Errors (δ^{SR})	
Temperature fluctuations	±.3%
Normalization Errors (δ^{NM})	
Temperature calibration	.3
Temperature variation across target cell	.3
Cryogenic data	.6
Target length	.2
Target misalignment	.2
Target impurities	.2
Total Normalization Error	±.8%

2.3 The 8 GeV Spectrometer

Scattered particles from the target were momentum analyzed using the 8 GeV spectrometer.[3,5,60] Several recent reports[29,30,51,61] provide excellent descriptions of the optical properties of the 8 GeV spectrometer. We discuss here only new results relevant to the analysis of E140, and in particular, the results of our recent floating-wire[62] calibration study[63] of the 8 GeV spectrometer.

2.3.1 Scattering Kinematics

The central scattering angle of the spectrometer is calibrated[64,65] relative to the nominal incident beamline to an accuracy of $\pm.003°$. This uncertainty includes contributions due to survey errors ($\pm.001°$), uncertainties in the nominal beamline ($\pm.001°$), effects originating in the noncentral rotation of the spectrometer ($\pm.002°$), and uncertainties in the wirefloat determination[63] of the optical axis of spectrometer relative to its own physical axis [a $-.009°$ effect] ($\pm.002°$). As the 8 GeV spectrometer is not a perfectly elastic rigid rotor, there is an additional uncertainty which is not correlated with the absolute calibration. A statistical study[64] of the repeatability of the spectrometer axis versus large and small angular displacements measures a $\pm.002°$ random uncertainty in the scattering angle.

The central momentum of the spectrometer is calibrated to $\pm.04\%$ by the wire-float study,[63] and confirmed by subsequent extensive NMR studies.[66] Statistical fluctuations in the computer controlled magnet currents contributed[67] an additional $\pm.03\%$ random uncertainty to the energy of the scattered particle. A cross calibration of the incident and scattered energies, E_o and E', based on elastic hydrogen cross sections measured during E140 reports:[51]

- Assuming perfect knowledge of E', the observed E_o is less than the calibrated value by .15% and displays random fluctuations of $\pm.05\%$.
- Assuming perfect knowledge of E_o, the observed E' is greater than the calibrated value by .11% and displays random fluctuations of $\pm.04\%$.

We conclude that a combination of these scenarios is likely and that these observations are consistent with the individual calibrations and the known fluctuations of E_o and E'.

2.3.2 Acceptance

To determine the total acceptance of our spectrometer we rely on a high statistics technique used successfully in the previous deep inelastic experiment E139.[30] The scattering trajectory of all observed electrons (see Section 3.1) are reconstructed using the TRANSPORT[48]-like model of the spectrometer given in Table 2.4. We then compare the number of observed electrons in a particular $(\vartheta, \delta, \varphi)$ bin to the number of electrons observed in the fiducial region of the spectrometer acceptance, given by

$$\begin{aligned} -3.0 \text{ mr} \leq \vartheta \leq \ 3.0 \text{ mr} , \\ -1.5 \ \% \ \leq \delta \leq \ 1.5 \ \% \ , \\ -10.0 \text{ mr} \leq \varphi \leq 10.0 \text{ mr} . \end{aligned} \tag{2.1}$$

Electrons within this region encounter are detected with perfect efficiency. Using the cross section model to the deep inelastic region of Bodek *et al.*,[3] we determine the expected number of counts in each $(\vartheta, \delta, \varphi)$ bin from the number of counts in the fiducial. The acceptance function, $\text{Acc}(\vartheta, \delta, \varphi)$ is defined as the ratio of observed counts to expected counts in the $(\vartheta, \delta, \varphi)$ bin, and is determined using the sum of the data from the thin solid targets. The acceptance criteria and total acceptance for E140 are given by

$$\begin{aligned} -6.0 \text{ mr} \leq \vartheta \leq \ 6.0 \text{ mr} , \\ -3.5 \ \% \ \leq \delta \leq \ 3.5 \ \% \ , \\ -28.0 \text{ mr} \leq \varphi \leq 28.0 \text{ mr} , \end{aligned} \tag{2.2}$$

and

$$\text{Total Acceptance} = 3.659 \pm .014 \text{ msr\%} , \tag{2.3}$$

where the total acceptance is the average of $\text{Acc}(\vartheta, \delta, \varphi)$ over this region times the volume of this region. Studies of other possible acceptance criteria indicate effects of

Table 2.4. Presented is the TRANSPORT matrix used to reconstruct the exact scattering (tgt) kinematics from the wire chamber trajectory. The implicit units are powers of [cm], [mr], and [%].

	x_{tgt}	ϑ_{tgt}	φ_{tgt}	δ_{tgt}
x	4.55362	.19387	−.03694	−.00205
ϑ	−4.29185	.02408	.03954	.00245
y	−.06007	.00050	−.02689	−.34275
φ	−.00142	−.00419	−.92820	.00074
x^2	.01756	.00051	.01063	−.00013
$x\vartheta$	−.03237	−.00103	−.01993	.00012
xy	−.00492	.01458	.00034	.00059
$x\varphi$	.00133	−.00098	.00056	.00005
ϑ^2	.01543	.00051	.00930	.00000
ϑy	.00850	−.01421	−.00037	−.00059
$\vartheta\varphi$	−.00106	.00082	−.00052	−.00003
y^2	−.00411	−.00012	−.00525	.00020
$y\varphi$	−.00019	.00003	−.00083	.00136
φ^2	−.00005	.00001	−.00009	.00004

size ±.3% in the measured cross sections and no effect in the extraction of R. Plots of $\mathrm{Acc}(\vartheta, \delta, \varphi)$ and additional discussion are given in Reference 29.

Our single largest concern regarding systematic errors in R comes from possible E' dependence of the spectrometer acceptance. This concern prompted the extensive floating wire calibration study[63] of the 8 GeV spectrometer, which measured all primary first order optics coefficients as a function of E'. These wirefloat coefficients are used to calculate a correction factor to the nominal acceptance, Equation 2.3, obtained from the coefficients of Table 2.4, for each value of E'. These correction factors[63] are plotted in Figure 2.2 and are given by the best fit line

$$\mathrm{Acc}^{\mathrm{True}}/\mathrm{Acc}^{\mathrm{Nominal}} = .9815 - .00049\,(\mathrm{E}' - 3.99\ \mathrm{GeV})\ , \tag{2.4}$$

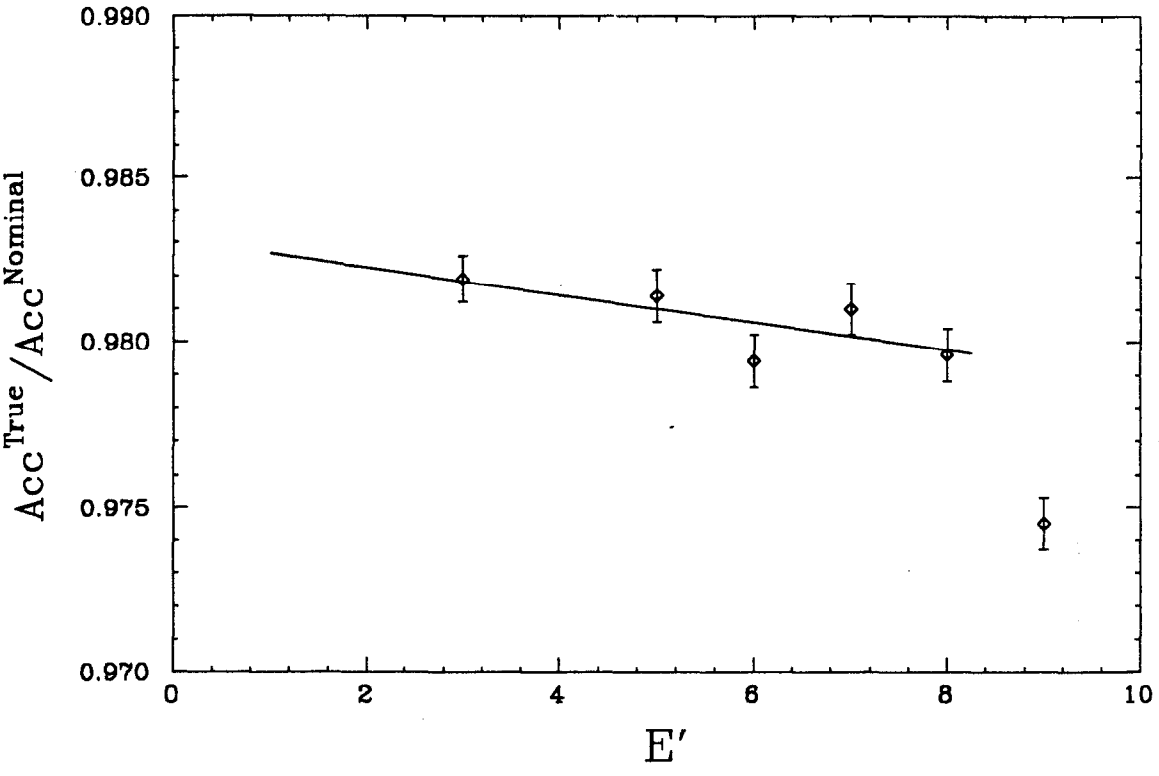

Figure 2.2. Shown is the wirefloat measurement of the E' dependence of our acceptance. The 9 GeV value evidences magnet saturation. Shown is the best fit line to the data at and below 8 GeV, the maximum value of E' used in E140.

where 3.99 GeV is the weighted mean E' of the E140 data. The uncertainty in this slope is $\pm.00036$ GeV^{-1}. The uncertainty in the intercept, $\pm.010$, is the systematic uncertainty in our knowledge of the acceptance and is dominated by systematic survey uncertainties. .

A similar concern regards the possible θ dependence of the spectrometer acceptance for the 20 cm long deuterium target, despite line-to-point horizontal focusing of the 8 GeV spectrometer. Monte carlo studies[29,51] for the acceptance criteria of Equation 2.2 indicate a slight negative effect, modeled well by

$$\mathrm{Acc}(\theta)/\mathrm{Acc}(0) = 1 - .008 \sin^2\theta \; . \tag{2.5}$$

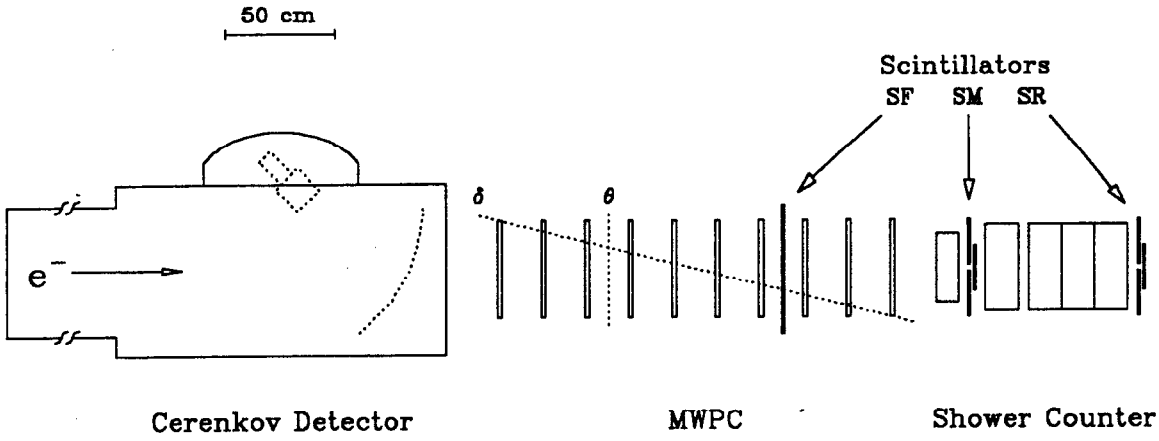

Figure 2.3. Shown is a schematic of the E140 detector package as viewed from the side. Also indicated are the focal planes of the spectrometer, which pass through the MWPC. Gravity, in this picture, points at 7 o'clock.

For Acc(0) we use the Equation 2.3 determined with the thin solid targets. This very small effect is seen[51] to increase sharply for larger φ acceptance ranges than Equation 2.2 (c).

2.4 The Detectors

Our detector package is shown schematically in Figure 2.3. Improvements over recent previous experiments[30,61] include the use of hydrogen as a Čerenkov gas and a new highly-segmented shower counter. We present here only a concise description of each portion of the detector. More extensive discussions of the E140 detector package are provided by References 29 and 51.

A brief summary of the properties of our Čerenkov detector is given by Table 2.5. Our selection of hydrogen gas greatly decreases the knock-on background, those events in which a pion triggers the Čerenkov detector through an intermediary atomic electron knocked above the electron threshold. Similarly, hydrogen gas results in fewer multiple-scattering events, increasing our tracking efficiency.

Table 2.5. Shown is a summary of our hydrogen gas Čerenkov detector properties. The last category is addressed in Chapter 3.

Hydrogen pressure	1 atm
Scattering chamber	3.15 m
Index of Refraction	1.000140
Threshold energy for e^-	.031 GeV
Threshold energy for π^-	8.40 GeV
	RCA
Photomultiplier tube	Quanticon 8854
Quantum efficiency	15–20%
Number photoelectrons	6–8
Knock-on probability	.2%
Electron efficiency	99.7%

Our MWPC[68] is composed of ten planes which are spread out to cover the focal planes of the spectrometer. These chambers are the same as those used in two previous high energy experiments.[30,61] The primary features of our MWPC are summarized in Table 2.6.

Our lead glass shower counter is divided, as indicated in Figures 2.3 and 2.4, into five layers of thicknesses 3.2 RL and 4×6.8 RL. We use longitudinal segmentation[69] to reject those pions which undergo charge-exchange interactions by looking for early shower development within the PR. Electron showers, except at very high energies, are contained entirely within the PR, TA, and TB layers. To improve our energy measurement in the TA layer, where the electron shower is a maximum, we attach a phototubes to each end of each counter. Using a detailed calibration procedure[29] we achieve an energy resolution of $18\%/\sqrt{E'}$ full width at half maximum. Additional discussion regarding the use of shower counters in the 8 GeV spectrometer is provided by Reference 70.

Table 2.6. Shown is a summary of the primary features of our MWPC. The last category is addressed in Chapter 3 and in more detail in Reference 51.

Number of δ planes	5
Number of ϑ planes	5
Plane size	35 cm × 93 cm
Plane separation	20 cm
Wire composition	Au-plated W
Wire diameter	20 μm
Wire separation	2 mm
δ resolution	$\pm$.05 %
ϑ resolution	$\pm$.07 mrd
Single plane efficiency	90–95%
Total tracking efficiency	99.8%

Our three planes of plastic scintillator arrays, shown in Figure 2.3, provide additional timing and hodoscope information about charged tracks. The SF counter is composed of six vertical slats, while the SM counter is composed of three horizontal slats with a phototube at each end. Additionally, the SM counter is sensitive to shower development in the PR.

2.5 Electronics and Data Acquisition

Our event logic is similar to that of two recent previous high energy experiments,[30,61] and is described in detail in References 29 and 51. A simplified schematic of our electronics is presented in Figure 2.5. Signals from the individual PR and TA counters are summed in analog. Signals from the SF and SM scintillators are summed logically. Our electron trigger accepts two sets of event criteria,

$$\mathrm{ELEC} = \mathrm{EL}^1 \vee \mathrm{EL}^2 \ , \tag{2.6}$$

where

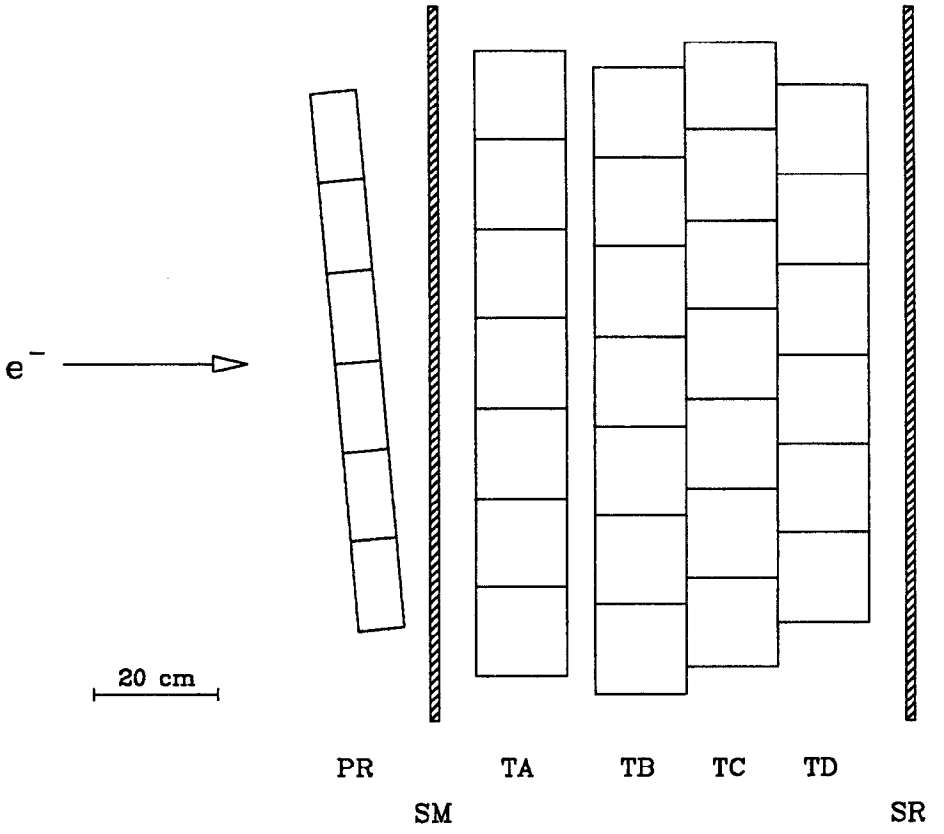

Figure 2.4. Shown is a schematic representation of the lead glass shower counter as viewed from above. Efficiencies are improved by rotating and staggering the layers as shown. Also shown are the second and third layers of plastic scintillator, SM and SR.

$$\begin{aligned} \mathrm{EL}^1 &= [\check{\mathrm{C}} \wedge \mathrm{PR} \wedge \mathrm{TA}] \vee [\check{\mathrm{C}} \wedge \mathrm{PR} \wedge \mathrm{SM}] \\ &\qquad \vee [\check{\mathrm{C}} \wedge \mathrm{TA} \wedge \mathrm{SM}] \vee [\mathrm{PR} \wedge \mathrm{TA} \wedge \mathrm{SM}] \ , \\ \mathrm{EL}^2 &= \check{\mathrm{C}} \wedge \Big\{ [\mathrm{PR} \wedge \mathrm{SF}] \vee [\mathrm{PR} \wedge \mathrm{SM}] \vee [\mathrm{SF} \wedge \mathrm{SM}] \Big\} \ . \end{aligned} \tag{2.7}$$

The second of these greatly increases our detection efficiency for electrons of $E' < 4$, which shower almost entirely within the PR. Discriminator thresholds are set low, yielding an electron trigger efficiency greater than 99.99% and a pion rejection factor of roughly 6.

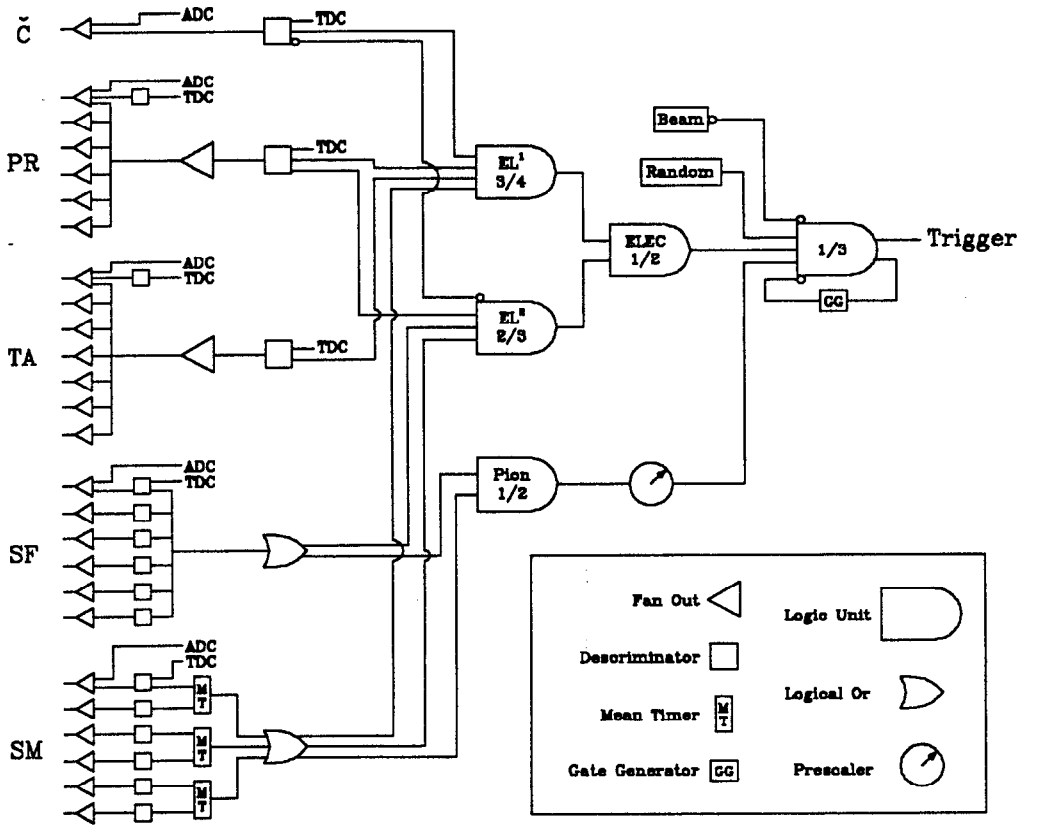

Figure 2.5. Shown is a simplified schematic of the fast electronics and trigger.

We sample the background with two additional trigger elements: a pion trigger which requires only SF and SM (and is prescaled by 2^8) and a random trigger which fires at infrequent intervals.

Triggers generate 100 ns gates for ADCs, scalers and latches and a common start for all TDCs. Coincidences (not shown in Figure 2.5) between various logical elements are used to calculate computer deadtime corrections. Identical trigger logics (also not shown) with varying signal widths are used to calculate electronics deadtime corrections. To minimize deadtime corrections, we lower the beam intensity to maintain a trigger rate below .2 per beam pulse and the pion flux below 2 per beam pulse.†

† In retrospect, higher discriminator thresholds would have given Equation 2.7 a

All detector information is read by a PDP-11/04 computer through a CAMAC interface and loaded into rotating memory buffers shared with a VAX-11/780 computer. Additionally, the VAX-11/780 monitors and assimilates scalers, target temperatures, detector high voltages, and spectrometer magnetic fields. The VAX-11/780 receives data from the LSI-11 computer regarding beam steering, profile, and charge measurements, and from the Main Control Center computer regarding the incident beam energy. The online analysis program, also running on the VAX-11/780, provides histograms of all ADCs and TDCs to help monitor the stabilities of the electronics, the detectors, and the spectrometer.

---

much greater pion rejection factor, allowing us to use a more intense beam and to reduce significantly the running time at those kinematics with large π^-/e^- ratios.

Chapter 3

E140 Data Analysis

The data analysis proceeds in three primary stages. The first stage is the event-by-event analysis which performs the task of particle identification and produces the final electron count for each run. Also at this stage, detector efficiencies, beam charge, target temperatures, etc., are averaged or summed over each run. The second stage is the run-by-run analysis which combines together runs with the same target at the same kinematics, applies corrections for all known systematic effects, resulting in the final cross sections.

3.1 Event-By-Event Analysis

Our three types of experimental runs are analyzed identically. These include: 1) the primary data runs using deuterium, iron, and gold targets; 2) empty liquid target replica runs, needed to correct the measured deuterium cross sections;[57] and 3) runs made with reversed spectrometer polarity to measure the charge-symmetric background.[71] Only ELEC events are analyzed in full detail, though pion and random triggers provide additional informative detector spectra.

3.1.1 Tracking

The goal of our trajectory analysis is to correctly identify the electron track even in the presence of other (presumably) pion tracks and spurious background hits. We achieve this through a series of searches and cuts:

① Our searching algorithm finds all tracks which record hits in at least seven chambers, of which at least three are ϑ chambers and three are δ chambers. If no tracks are found, this requirement is softened to six chambers, with at least two of each type.

② We discard all tracks which do not point to an energy deposition in the shower counter.

③ We discard all tracks which pass within 3.5 cm of any edge of the PR.

④ We discard all tracks which do not originate at the target, as determined with the optics matrix, Table 2.4.

If at least one track survives to this point the event is identified by the pnemonic "GOODTRACK." If multiple tracks survive (~10% of all events), we apply an additional set of criteria to choose the most probable electron track, discarding the others.

Events for which no track survives these cuts are due to pions, and are discarded. For roughly 2% of these events, however, no tracks are found at stage ①. Studies[51] indicate that the vast majority of these trajectories pass through the very edges of MWPC, where detection efficiency falls off rapidly. Such rays do not contribute to the acceptance function calculation of Section 2.3.2, and so, are discarded. The inefficiency of the non-edge regions of the MWPC is very small, and is addressed in Section 3.2.1.

For each GOODTRACK event we calculate[29] the total energy deposited in the shower counter, E_{sh}, by summing the energies deposited in all PR, TA, TB, and TC counters which lie on or adjacent to the identified track.

For each GOODTRACK event we compare the reconstructed scattering trajectory with the acceptance criteria of Equation 2.2, denoting those events which lie inside acceptance region by the mnemonic "$\in$ACC."

3.1.2 Particle Identification

Electron identification and pion rejection is at the heart of any deep inelastic electron scattering experiment. Our ELEC trigger is very highly efficient for electrons

at the expense of also triggering on a significant fraction of the pion background. We remove these pions by placing cuts on the Čerenkov and shower energy spectra.

In Figure 3.1 we present the Čerenkov and shower energy spectra for our deuterium run with the worst case π^-/e^- flux ratio of 125:1, namely

$$\begin{aligned}(x, Q^2, \epsilon) &= (.2,\ 5.,\ .31)\ , \\ (E_o, E', \theta\,) &= (16.,\ 2.68,\ 19.6^\circ)\ .\end{aligned} \tag{3.1}$$

Included are all [GOODTRACK $\wedge$ ELEC] events. Aided by pion rejection factors of 6 from [ELEC] and 2 from [GOODTRACK], the spectra presented in Figure 3.1 display a π^-/e^- ratio of only 11:1.

In Figure 3.1, curves (a) and (b) show the observed Čerenkov spectrum for this run with and without, respectively, a cut on E_{sh}. The first 25 channels of these curves are dominated by pion events passed by the EL^1 trigger. The large peak in (a) centered at channel 200 contains both electron events and pion events with a knock-on electron. These masquerading pions are eliminated in (b) by the E_{sh} cut. We observe a knock-on probability of less than .2%, much smaller than observed previously[30] with the same chamber filled with nitrogen.

Our cut on Čerenkov signal strength, $\check{C}^{min}$, is indicated Figure 3.1. We estimate the electron inefficiency of this cut with a Poisson fit (consistent with six to eight photoelectrons) to the electron peak of (b). Using only runs with π^-/e^- flux ratios $\ll 1$, we measure the electron inefficiency to be .25%. The probability for pion events to pass this $\check{C}^{min}$ cut is discussed below.

In Figure 3.1, curves (c) and (d) show the observed E_{sh} spectrum for this run with and without, respectively, the cut at $\check{C}^{min}$. Pion events with hadronic showers give rise to the low energy peaks in both (c) and (d), entering primarily through the EL^1 trigger. The peak in (c) centered at $E_{sh} = E'$ represents the electromagnetic showers of both electron events and those pion events which undergo charge exchange interactions early in the PR. These latter are removed in (d) by the cut at $\check{C}^{min}$.

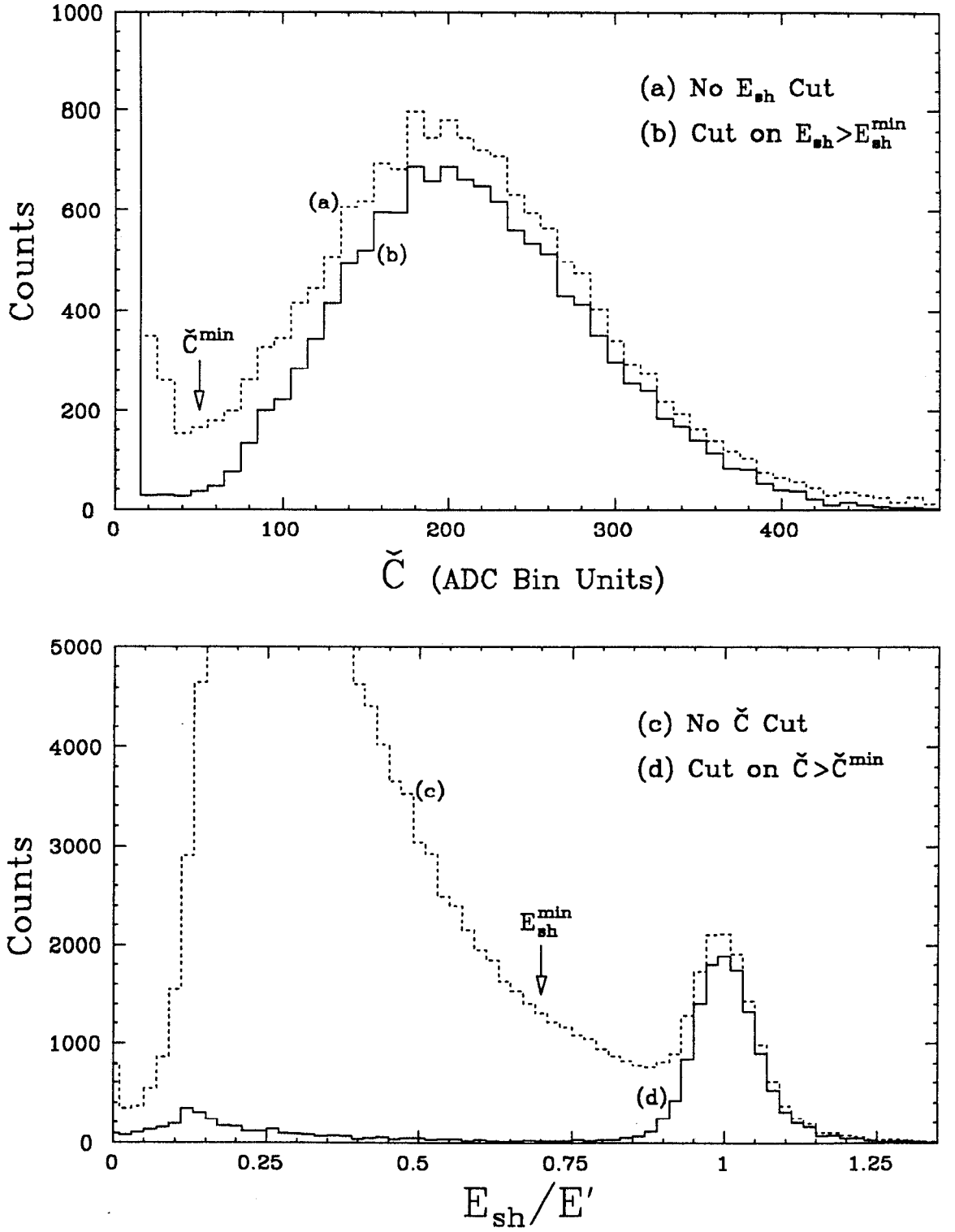

Figure 3.1. Plotted are the observed Čerenkov and shower spectra with and without cuts on the other. Spectra shown are from the run with the worst π^-/e^- flux ratio of 125. In the spectra shown, pions outnumber electrons by 11 to 1. See text for details.

The observed width of the electron peak in Figure 3.1 (d) is $18\%/\sqrt{E'}$ full width at half maximum. The cut on shower energy at $E_{sh}^{min} = .7E'$ approximately corresponds to a three standard deviation cut on a Gaussian distribution. Further studies[51] using only runs with π^-/e^- flux ratios $\ll 1$ reveal that at most .25% of all electrons fail to pass this cut. The number of pions which succeed in passing both shower and Čerenkov cuts is evaluated by extrapolating the pion peak in Figure 3.1 (d) into the electron peak. This contamination is less than .2% of the electron peak in (d), and correspondingly less for runs with lower π^-/e^- ratios.

3.2 Run-By-Run Analysis

For each run, the measured electron count, N_{e^-}, is the sum of all events which satisfy

$$\text{GOODTRACK} \wedge \in\text{ACC} \wedge [\check{C} > \check{C}^{min}] \wedge [E_{sh} > E_{sh}^{min}] \ . \tag{3.2}$$

Different runs at the same kinematic point with the same target are combined together and the cross section is calculated. The naive cross section formula is given by

$$\sigma^{naive} \equiv \frac{\partial^2\sigma}{\partial\Omega\partial E'} = \frac{N_{e^-}}{\Delta\Omega\Delta E' \, \mathcal{Q} \, N_t} \ , \tag{3.3}$$

where $\Delta\Omega\Delta E'$ is given by Equation 2.3, $\mathcal{Q}$ is the number of incident electrons, and N_t is the target thickness expressed in nucleons per unit area. We apply a series of corrections to the naive cross section to account for every known systematic effect of size .1% or greater. These corrections are given in Table 3.1 and briefly described below.

3.2.1 Corrections to the Cross Section

We remove from the electron count, N_{e^-}, all sources of background particles. First, from the deuterium cross sections we subtract the measured background due to the aluminum target cell walls (Section 2.2). Second, we subtract the calculated pion contamination from each run (Section 3.1.2). Third, we correct for the background of

Table 3.1. Shown is a summary of the applied corrections to the naive cross section of Equation 3.3. The right-hand column specifies the propagational properties of the uncertainty given (see Chapter 4, for example). Uncertainties of type δ^{ST} are due to counting statistics and are included in the quoted statistical uncertainties in the cross sections; other uncertainties are systematic in origin and are propagated explicitly throughout this study.

Source	Correction Sign	Correction Size (%)	Uncertainty (±%)	Type
Background Corrections				
Target end caps	−	1.1	.1	δ^{ST}
Pion contamination	−	$\leq$ .2	.0	
Charge symmetric	−	$\leq$ 12.5	$\leq$ 1.0	δ^{ST}
sources			$\leq$ .4	δ^{SY}
Deadtime Corrections				
Electronics	+	$\leq$ .5	.1	δ^{ST}
Computer	+	$\leq$ 18.0	.2	δ^{ST}
Efficiency Corrections				
Čerenkov	+	.3	.1	δ^{SR}
Shower counter	+	.2	.1	δ^{SR}
MWPC	+	$\leq$ .4	.0	
Optics Corrections				
Acceptance	±	$\leq$ 1.7	.1	δ^{SE}
Average vs central kinematic	−	$\leq$ .8	.0	
Miscellaneous				
Neutron excess	+	$\approx$ 1.5	.1	δ^{NM}
Kinematic mismatch	±	$\leq$ 1.0	.0	
Radiative Corrections				
Internal	±	$\leq$ 28.0		
External	±	$\leq$ 14.0		
Total	±	$\leq$ 29.0	$\leq$ 1.0	δ^{RC}
			1.0	δ^{NM}

high energy electrons originating from intermediate sources, predominantly from π° production and decay to $\gamma\gamma$ followed by pair production. Assuming charge symmetry of such sources,[71] we measure this correction by reversing the spectrometer polarity to the flux of e^+. Asymmetry in $K^\pm$ production, however, has not been ruled out at the 10% level.[71] Subsequent studies[29] of the E140 data indicate that no more than 10% of the observed e^+ are due to K^+ decays, and thus limit the systematic error due asymmetric intermediate sources at $\pm 1\%$ of the observed effect.

These background subtractions are made by replacing N_{e^-} in the cross section calculation by $\mathcal{N}_{e^-}$, where

$$\mathcal{N}_{e^-} = N_{e^-} - N_{cap}^{end} - N_{e^+} - N_{\pi^-} \ . \tag{3.4}$$

The statistical uncertainty of $\mathcal{N}_{e^-}$ is the sum in quadrature of the counting statistics of N_{e^-}, N_{cap}^{end} and N_{e^+}. Systematic uncertainties in $\mathcal{N}_{e^-}$ due to possible charge-asymmetries in the N_{e^+} term are estimated to be

$$\delta N_{e^+} = \pm \max(.06,\ .8 - 1.3\,\epsilon)\,\% \ . \tag{3.5}$$

The electronics deadtime correction accounts for electron coincidences within the 20 ns logic signal width. The computer deadtime correction accounts for trigger coincidences within the 1.6 μs beam pulse. These corrections are measured[29,51] for each run. We find excellent agreement between the measured computer deadtime and the theoretical deadtime based on simple Poisson statistics. Uncertainties in these corrections are due to counting statistics are added in quadrature to the statistical uncertainties of the cross sections.

The Čerenkov and shower counter efficiencies are calculated for the entire experiment using runs with a low π^-/e^- flux ratio (Section 3.1.2). Possible systematic fluctations in these efficiencies are estimated to be $\pm .1\%$ or less. The SF and SM efficiencies are greater than 99.9%. And, the trigger efficiency is calculated from the efficiencies of the individual trigger elements to be 99.99%.

The efficiency of the MWPC is calculated by comparing the number of tracking successes (at ① in Section 3.1.1) to the number of good-candidate events. An event is considered a good-candidate if it meets the criteria

$$\in\text{SFSM} \wedge \text{PR} \wedge \text{TA} \wedge \left[\check{\text{C}} > \check{\text{C}}^{\text{min}}\right] \wedge \left[\text{E}_{\text{sh}} > \text{E}_{\text{sh}}^{\text{min}}\right] \ , \tag{3.6}$$

where $\in$SFSM is a cut based on the SF and SM detectors which places the event in the central region of the detector package. The MWPC efficiency correction is calculated for each run with negligible uncertainty.

The optics corrections of Equations 2.4 and 2.5 are applied to nominal total acceptance of Equation 2.3. The uncertainty in the slope of Equation 2.4 generates an E' dependent systematic uncertainty in the cross section, which is calculated for each cross section and treated specially in later stages of the analysis. The uncertainty in the intercept of Equation 2.4, which contributes only to the overall normalization of E140, is discussed in Section 3.3.

The finite acceptance of the spectrometer necessitates a correction for the fact that central kinematic of the spectrometer is not equal to the average measured kinematic. The correction for this effect is

$$C^{center} = \sigma^{center} \Big/ \left[\frac{\sum_j \sigma(j)\text{Acc}(j)}{\sum_j \text{Acc}(j)}\right] \ , \tag{3.7}$$

where the sum is taken over the $(\vartheta, \delta, \varphi)$ bins of Section 2.3.2. For $\sigma(j)$ we use the cross section model of Bodek *et al.*,[3] after removing the effects of the radiative corrections.

Experimentally, it is difficult to perfectly realize a specific set of scattering kinematics. We apply a "kinematic mismatch" correction to account for small differences between the realized and the targeted (x, Q^2) point. Typically, this correction is .5% or less.

We apply a neutron excess correction to the iron and gold cross sections, which effectively converts some neutrons into protons, resulting in a symmetrized nucleus. This correction is

$$C^{Z,A} = \frac{1 + \sigma^n/\sigma^p}{1 + (\frac{A}{Z} - 1)\ \sigma^n/\sigma^p} \left[\frac{A}{2Z}\right] , \tag{3.8}$$

where, since $x \leq .5$, we use our new model for σ^n/σ^p given by Equation 5.49. Use of this more exact model gives cross sections larger by .3% for iron and .7% for gold than our previously reported[2,29] values.

3.2.2 Bardin/Tsai Radiative Corrections to the Cross Section

We apply a radiative correction to the measured cross sections to account for higher order contributions both "internal" and "external" to the first order born diagram. We calculate the internal radiative corrections according to the formulation of Bardin *et al.*,[72] to which we apply an ad hoc correction based on the formulation of Tsai[36] to account for external effects. Our Bardin/Tsai radiative correction is given by

$$C^{RC} = \left[(1 + \delta_{\text{int}}^{\text{Bardin}})\ \frac{(1 + \delta_{\text{int+ext}}^{\text{Tsai}})}{(1 + \delta_{\text{int}}^{\text{Tsai}})}\right]^{-1} , \tag{3.9}$$

where δ, as defined by Bardin *et al.*,[72] is the fractional difference between the radiative and nonradiative cross sections.

To calculate $\delta_{\text{int}}^{\text{Bardin}}$ we use the program TERAD authored by Bardin *et al.*[72] with models of $F_2(x, Q^2)$ and $R(x, Q^2)$ in the SLAC kinematic range. We have produced a version of this program, known as INTERNAL, expressly for deep inelastic electron scattering and coded it in Fortran 77. Hadronic contributions, γ-Z_o interference, and a parameterization of α^4 contributions in the SLAC energy range are included in our calculations, though, each contributes typically less than 1% to the total radiative correction. We do not exponentiate the soft photon term as such effects are more

correctly approximated by the α^4 parameterization.[73] We do exponentiate the vacuum polarization term via

$$\delta_{\rm vac} \rightarrow \frac{\delta_{\rm vac}}{1 - .5\delta_{\rm vac}} \ . \tag{3.10}$$

And lastly, we apply a smearing correction to the quasi-elastic tail contributions, based on calculations from program EXTERNAL, described below.

Our coding of the Tsai formulation, program EXTERNAL, follows closely the prescription of Tsai's 1971 publication with two important modifications. First, we correct the expression for $\delta_{\rm vac}$ to include muon and tau loops, and to include hadronic polarization effects as parameterized in program TERAD. Second, and more importantly, we do not make the energy peaking approximation, instead integrating the double integral over $dE_o dE'$. We calculate $\delta_{\rm int}^{\rm Tsai}$ by assuming a target of zero thickness, and for deuterium, we average $\delta_{\rm int+ext}^{\rm Tsai}$ over the length of the target.

As the calculation of radiative corrections is inherently iterative, the final radiative correction factors were calculated using the R^{1990} and $F_2^{\Omega_9}$ models of Chapter 5. The dependence of our procedure on the structure function models is very slight, typically .2% or less. The range of contributions from internal and external processes is given in Table 3.1, and the final radiative correction factors, Equation 3.9, are given in Tables 3.3 through 3.6.

We have made a comparison[29] between $\delta_{\rm int}^{\rm Bardin}$ and $\delta_{\rm int}^{\rm Tsai}$ in an attempt to understand the possible theoretical uncertainties of our internal radiative corrections. For this comparison we have produced a more exact version of program EXTERNAL, known as MT-EXACT. This program[29] makes neither the equivalent radiator approximation nor the angle peaking approximation, instead integrating Equation C.24 of Tsai's 1971 report while sidestepping the infrared divergences with a familiar (nonphysical) Δ cutoff parameter separating soft and hard photon effects. Our treatment improves upon a previous similar effort by EMC.[9]

Comparisons between INTERNAL (not including the γ-Z_o and hadronic terms) and MT-EXACT display excellent agreement over the entire E140 kinematic range. Plots of these comparisons are given in Reference 29. The disagreement between these two formalisms is parameterized by:

$$\delta_{\rm int}^{\rm Bardin} - \delta_{\rm int}^{\rm MTexact} = -.014 + .017\,\epsilon\ , \tag{3.11}$$

with no apparent dependence on x or Q^2.

To test the external portion of our radiative corrections, we compare cross sections measured on targets of different thicknesses. In our experiment, we have data from .026 and .06 RL iron targets and in E139 there are data from .02, .06, and .12 RL iron, aluminum, and gold targets. Differences between the radiatively corrected cross sections are, for each comparison, consistent with the relative target thickness uncertainties.

We take Equation 3.11 as an estimate of the ϵ-correlated component of the systematic uncertainty in our Bardin/Tsai radiative corrections,

$$\delta^{RC} = \pm\,{\rm abs}[-1.4 + 1.7\,\epsilon]\ \%\ . \tag{3.12}$$

This uncertainty propagates directly through Equation 1.2 to become a systematic uncertainty in R,

$$\delta R^{RC} \approx .025\ , \tag{3.13}$$

which is very strongly correlated across all R measurements reported in this thesis.

Note that Equation 3.11 is, in general, also consistent with a non-ϵ-dependent difference between INTERNAL and MT-EXACT on the order of $\pm 1\%$. In other words, there is no *a prior* reason to suspect that both programs are perfectly accurate at $\epsilon = .824$ as implied by Equation 3.12. The correct treatment of this phenomenon is to include an additional $\pm 1.0\%$ uncertainty in the overall experimental normalization, as indicated in Table 3.2.

Table 3.2. Shown are the total normalization uncertainties, δ^{NM}, for the E140 data. Also presented is a breakdown of the contributions to δ^{NM} for each target.

Source	Normalization Uncertainty (±%)			
	Deuterium	Iron #1	Iron #2	Gold
Beam Charge	.5	.5	.5	.5
Target	.8	.5	1.1	2.5
Acceptance				
Statistical	.4	.4	.4	.4
Systematic	1.0	1.0	1.0	1.0
Neutron Excess Correction	.0	.1	.1	.2
Radiative Correction	1.0	1.0	1.0	1.0
Total Uncertainty (δ^{NM})	±1.7%	±1.6%	±1.9%	±2.9%

3.3 E140 Cross Section Results

In Tables 3.3 through 3.6 we present the final E140 cross sections. The total uncertainty of each cross section reported in these tables is broken down into four component uncertainties. These components are defined as follows:

- δ^{ST} is the statistical uncertainty, and includes only Poisson counting errors;
- δ^{SS} is the experimental systematic uncertainty, defined as the quadrature sum of all systematic errors *except* the following;
- δ^{RC} is the systematic radiative corrections uncertainty given by Equation 3.12;
- δ^{NM} is the overall normalization uncertainty, and includes those contributions summarized in Table 3.2.

Only the δ^{ST} and δ^{SS} uncertainties are presented in the tables. The δ^{RC} uncertainty is given by Equation 3.12 and is perfectly correlated across all cross sections. The δ^{NM} uncertainties are presented in Table 3.2, and, as indicated by the breakdown,

are strongly correlated across the four targets.[†]

The cross sections in Tables 3.3 through 3.6 are presented *per nucleon* and, for iron and gold, are corrected for neutron excess (using Equations 3.8 and 5.49). These cross sections supercede those reported previously,[29] benefiting from iterated radiative corrections (see Section 5.1), final optics calibrations, and more precise neutron excess corrections.

The uncertainties δ^{ST} and δ^{SS} shown in Tables 3.3 through 3.6 are defined *fractionally.* Also presented are the Bardin/Tsai radiative correction factors, defined by Equation 3.9.

Finally, we note that the iron #2 data is systematically lower than the iron #1 data by $1.8\% \pm .5\%$. This overall normalization shift is at the 1.5 standard deviation level of the combined target length uncertainties. Tables 3.4 and 3.5 do not incorporate a correction for this difference, though, for most purposes (see for example Section 4.2), we suggest normalizing the iron #2 data to the iron #1 data.

[†] Note that a more complex breakdown of δ^{SS}, as indicated within Tables 2.3 and 3.1, is utilized in the next chapter. See Appendix C for more information and Appendix E for the values of each component of the error vector of each cross section.

Table 3.3. Shown are the final E140 deuterium cross sections. See text for details. Table continues on next page.

E_o (GeV)	E' (GeV)	θ (deg)	ϵ	C^{RC}	σ^{meas} (pb/sr GeV)	$\pm\delta^{ST}$	$\pm\delta^{SS}$
$x = .20, \quad Q^2 = 1.0$							
3.748	1.084	28.728	.485	.773	.1820 E05	.009	.005
4.006	1.342	24.906	.559	.803	.2472 E05	.009	.006
4.251	1.586	22.205	.616	.825	.3248 E05	.008	.006
5.507	2.843	14.520	.792	.889	.8708 E05	.008	.006
6.251	3.586	12.124	.845	.915	.1334 E06	.007	.007
$x = .20, \quad Q^2 = 1.5$							
5.507	1.510	24.519	.476	.779	.1133 E05	.009	.005
6.250	2.253	18.783	.611	.835	.2018 E05	.006	.006
7.002	3.005	15.343	.703	.869	.3243 E05	.006	.006
7.498	3.502	13.727	.748	.885	.4235 E05	.006	.006
8.251	4.254	11.866	.799	.905	.5950 E05	.006	.006
$x = .20, \quad Q^2 = 2.5$							
8.251	1.589	25.220	.348	.721	.3761 E04	.014	.006
10.243	3.582	14.999	.606	.850	.1158 E05	.004	.006
11.744	5.083	11.746	.716	.889	.2013 E05	.007	.006
$x = .20, \quad Q^2 = 5.0$							
16.005	2.683	19.647	.314	.713	.1466 E04	.011	.006
17.255	3.933	15.600	.422	.790	.2423 E04	.008	.006
18.491	5.169	13.134	.508	.832	.3538 E04	.007	.006
19.493	6.171	11.702	.566	.854	.4624 E04	.006	.006
$x = .35, \quad Q^2 = 1.5$							
3.748	1.464	30.304	.604	.933	.1133 E05	.007	.006
4.007	1.723	26.950	.660	.953	.1472 E05	.007	.006
4.250	1.966	24.459	.704	.967	.1823 E05	.007	.006
5.507	3.223	16.715	.838	1.025	.4398 E05	.007	.006
7.002	4.718	12.232	.907	1.072	.8930 E05	.013	.007
$x = .35, \quad Q^2 = 2.5$							
5.501	1.695	30.008	.506	.914	.3794 E04	.008	.005
6.250	2.443	23.345	.633	.959	.6539 E04	.007	.006
7.081	3.274	18.900	.726	.994	.1053 E05	.007	.006
7.498	3.692	17.283	.761	1.008	.1306 E05	.006	.006
9.710	5.904	11.986	.870	1.062	.2977 E05	.007	.006

Table 3.3/continued: E140 deuterium cross sections.

E_o (GeV)	E' (GeV)	θ (deg)	ϵ	C^{RC}	σ^{meas} (pb/sr GeV)	$\pm\delta^{ST}$	$\pm\delta^{SS}$
$x = .35,\quad Q^2 = 5.0$							
10.243	2.630	24.878	.449	.919	.1250 E04	.010	.005
11.753	4.140	18.447	.601	.975	.2396 E04	.006	.006
13.320	5.707	14.735	.704	1.011	.4009 E04	.006	.006
15.004	7.391	12.189	.777	1.040	.6126 E04	.006	.006
$x = .50,\quad Q^2 = 2.5$							
3.749	1.084	46.177	.417	.962	.1505 E04	.009	.006
4.251	1.587	35.447	.561	1.015	.2655 E04	.010	.006
5.502	2.838	23.082	.758	1.088	.6874 E04	.009	.006
7.082	4.418	16.250	.865	1.148	.1531 E05	.006	.006
9.248	6.584	11.630	.926	1.206	.3182 E05	.007	.006
$x = .50,\quad Q^2 = 5.0$							
7.084	1.755	36.976	.401	.985	.4727 E03	.013	.006
8.250	2.921	26.331	.578	1.050	.9818 E03	.007	.005
9.710	4.381	19.742	.712	1.099	.1874 E04	.007	.006
13.316	7.987	12.448	.863	1.179	.5241 E04	.005	.006
$x = .50,\quad Q^2 = 7.5$							
10.243	2.249	33.152	.372	.990	.2339 E03	.016	.007
14.991	6.997	15.367	.743	1.128	.1278 E04	.010	.006
$x = .50,\quad Q^2 = 10.$							
13.319	2.661	30.802	.348	.991	.1458 E03	.012	.007
15.005	4.348	22.578	.504	1.050	.2790 E03	.012	.006
18.490	7.832	15.100	.697	1.119	.6756 E03	.006	.006
Miscellaneous							
13.320	5.500	18.062	.676	1.094	.9985 E03	.015	.006
13.320	6.318	14.927	.752	1.084	.2846 E04	.014	.006
16.006	5.331	18.042	.576	1.023	.7865 E03	.019	.006

Table 3.4. Shown are the final E140 iron #1 cross sections. See text for details. Table continues on next page.

E_o (GeV)	E' (GeV)	θ (deg)	ϵ	C^{RC}	σ^{meas} (pb/sr GeV)	$\pm\delta^{ST}$	$\pm\delta^{SS}$
$x = .20, \quad Q^2 = 1.0$							
3.748	1.084	28.728	.485	.741	.1867 E05	.013	.005
4.006	1.342	24.906	.559	.777	.2615 E05	.009	.005
4.251	1.586	22.205	.616	.804	.3276 E05	.012	.005
5.507	2.843	14.520	.792	.886	.8891 E05	.008	.006
6.251	3.586	12.124	.845	.918	.1356 E06	.007	.006
$x = .20, \quad Q^2 = 1.5$							
5.507	1.510	24.519	.476	.746	.1185 E05	.010	.005
6.250	2.253	18.783	.611	.815	.2112 E05	.006	.005
7.002	3.005	15.343	.703	.859	.3363 E05	.006	.005
7.498	3.502	13.727	.748	.880	.4318 E05	.007	.006
8.251	4.254	11.866	.799	.908	.6061 E05	.006	.006
$x = .20, \quad Q^2 = 2.5$							
8.251	1.589	25.220	.348	.680	.3695 E04	.016	.006
10.243	3.582	14.999	.606	.834	.1196 E05	.006	.005
11.744	5.083	11.746	.716	.885	.2077 E05	.007	.006
$x = .35, \quad Q^2 = 1.5$							
3.748	1.464	30.304	.604	.955	.1129 E05	.010	.005
4.007	1.723	26.950	.660	.980	.1489 E05	.008	.005
4.250	1.966	24.459	.704	1.000	.1823 E05	.008	.005
5.507	3.223	16.715	.838	1.073	.4494 E05	.008	.006
7.002	4.718	12.232	.907	1.132	.9119 E05	.012	.006
$x = .35, \quad Q^2 = 2.5$							
5.501	1.695	30.008	.506	.929	.3668 E04	.011	.005
6.250	2.443	23.345	.633	.988	.6558 E04	.009	.005
7.081	3.274	18.900	.726	1.030	.1059 E05	.007	.005
7.498	3.692	17.283	.761	1.049	.1309 E05	.007	.005
9.710	5.904	11.986	.870	1.117	.2983 E05	.007	.006

Table 3.4/continued: E140 iron #1 cross sections.

E_o (GeV)	E' (GeV)	θ (deg)	ϵ	C^{RC}	σ^{meas} (pb/sr GeV)	$\pm\delta^{ST}$	$\pm\delta^{SS}$
$x = .35, \quad Q^2 = 5.0$							
10.243	2.630	24.878	.449	.933	.1220 E04	.012	.005
11.753	4.140	18.447	.601	1.003	.2371 E04	.008	.005
13.320	5.707	14.735	.704	1.050	.3931 E04	.007	.005
15.004	7.391	12.189	.777	1.083	.6053 E04	.006	.005
$x = .50, \quad Q^2 = 2.5$							
3.749	1.084	46.177	.417	1.011	.1412 E04	.011	.006
4.251	1.587	35.447	.561	1.073	.2444 E04	.010	.005
5.502	2.838	23.082	.758	1.163	.6504 E04	.011	.005
7.082	4.418	16.250	.865	1.235	.1423 E05	.007	.005
9.248	6.584	11.630	.926	1.307	.3001 E05	.007	.005
$x = .50, \quad Q^2 = 5.0$							
7.084	1.755	36.976	.401	1.033	.4481 E03	.022	.006
8.250	2.921	26.331	.578	1.115	.9297 E03	.011	.005
9.710	4.381	19.742	.712	1.175	.1752 E04	.009	.005
13.316	7.987	12.448	.863	1.271	.4939 E04	.008	.005

Table 3.5. Shown are the final E140 iron #2 cross sections. See text for details.

E_o (GeV)	E' (GeV)	θ (deg)	ϵ	C^{RC}	σ^{meas} (pb/sr GeV)	$\pm\delta^{ST}$	$\pm\delta^{SS}$
$x = .20,\ Q^2 = 1.0$							
3.748	1.084	28.728	.485	.793	.1840 E05	.014	.005
4.006	1.342	24.906	.559	.820	.2515 E05	.008	.005
4.251	1.586	22.205	.616	.841	.3285 E05	.008	.005
5.507	2.843	14.520	.792	.901	.8775 E05	.008	.006
6.251	3.586	12.124	.845	.924	.1340 E06	.007	.006
$x = .50,\ Q^2 = 2.5$							
3.749	1.084	46.177	.417	.991	.1381 E04	.007	.006
9.248	6.584	11.630	.926	1.196	.2954 E05	.018	.005

Table 3.6. Shown are the final E140 gold cross sections. See text for details.

E_o (GeV)	E' (GeV)	θ (deg)	ϵ	C^{RC}	σ^{meas} (pb/sr GeV)	$\pm\delta^{ST}$	$\pm\delta^{SS}$
$x = .20,\ Q^2 = 1.0$							
3.748	1.084	28.728	.485	.753	.1875 E05	.014	.005
4.006	1.342	24.906	.559	.787	.2566 E05	.009	.005
4.251	1.586	22.205	.616	.814	.3341 E05	.007	.005
5.507	2.843	14.520	.792	.893	.8905 E05	.008	.006
6.251	3.586	12.124	.845	.925	.1367 E06	.006	.006

Chapter 4

E140 Structure Function Results

The fourth and final stage of our analysis is the extraction of R and F_2 from the experimental cross sections via the linear relationship of Equation 1.2. The primary focus of this final stage is the accurate propagation of the systematic errors, δ^{SS}, through the regression analysis. The results we obtain in this analysis have smaller, more accurate, uncertainties than our previously reported results.[1,2,29]

Figure 4.1 shows a sample linear regression analysis for the deuterium data at $(x, Q^2) = (.2, 1)$. R is given by the ratio of slope to intercept and F_2 is related to the value at $\epsilon = 1$. The other E140 regression analyses follow similarly from Tables 3.3 through 3.6, and are plotted in Reference 29.

4.1 Error Propagation

We explicitly propagate all uncertainties through the regression analyses. We respect correlations among the data of each regression analysis by first resolving δ^{SS} into its three component uncertainties,

$$\delta^{SS} \equiv \pm \delta^{SR} \pm \delta^{SY} \pm \delta^{SE} , \tag{4.1}$$

each of which propagates differently through the regression. Table 4.1 summarizes the six components of the *error vector* of each cross section measurement and their assumed correlational properties with respect to the regression analyses. For more information and numerical values of the E140 error vectors see Appendices C and E.

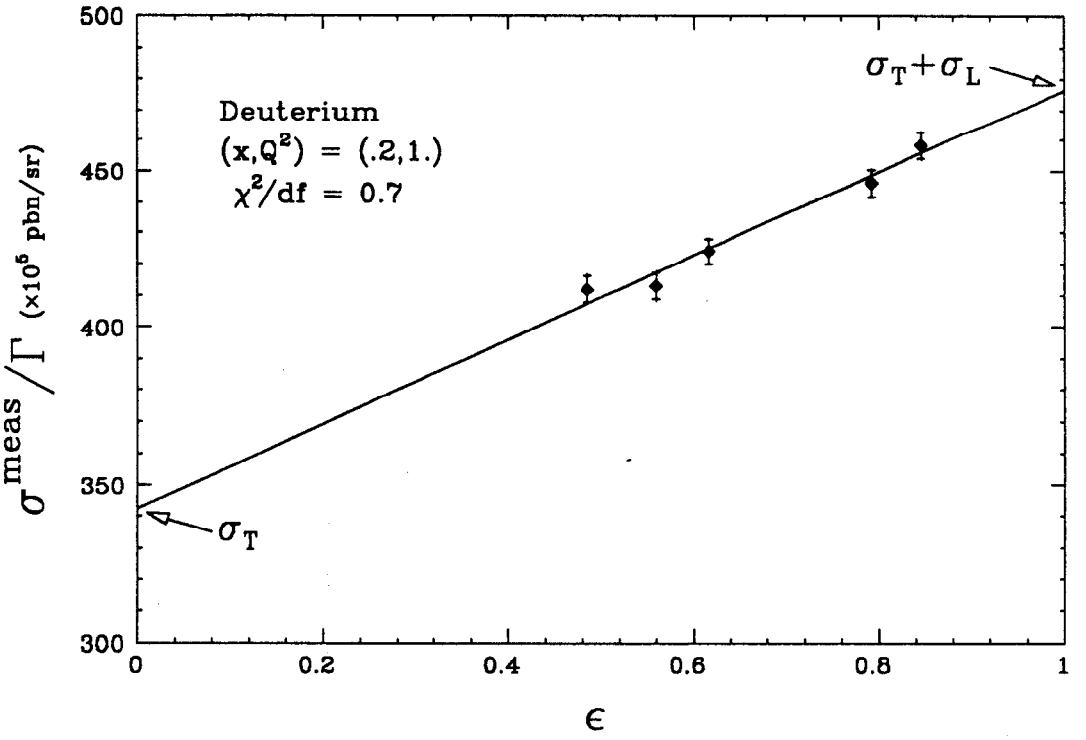

Figure 4.1. Shown is a sample E140 regression analysis. The full error bar represents the total error, given by the quadrature sum of δ^{ST} and δ^{SS}. The hashmark represents the random component of the total error, given by the quadrature sum of δ^{ST} and the random elements of δ^{SS}. Because the random component dominates the E140 errors, the extension of the error bar beyond the hashmark is barely visible (see text).

The weights for the regression analyses are determined by the total random error,

$$wt_j = 1 \Big/ \left[\left(\delta^{ST}\right)^2 + \left(\delta^{SR}\right)^2 \right] , \tag{4.2}$$

and the resulting statistical errors in R and F_2 are denoted by δR^{ST} and δF_2^{ST}. We propagate the other types of uncertainties through each regression analysis by directly measuring the perturbation in R due to each. We define an operator "LR" which takes as input a set of cross sections $\{\sigma^j\}$ and linearly regresses them to yield as output R, specifically

$$R = \mathrm{LR}\{\sigma^j\} . \tag{4.3}$$

Table 4.1. Presented is a brief summary of the E140 six-component error vector. Also given is the correlation of each error across the datapoints of our regression analyses.

	Source	Correlation
δ^{ST}	counting statistics;	random, no correlation.
δ^{SR}	fluctuations in: beam charge, target density, detector efficiences, and scattering kinematics;	random, no correlation.
δ^{SY}	non-charge symmetric background, kinematic calibrations;	strongly correlated.
δ^{SE}	E' dependence of acceptance;	strongly correlated with ϵ.
δ^{RC}	radiative corrections;	strongly correlated with ϵ.
δ^{NM}	various sources, see Table 3.2;	perfectly correlated, no effect on R extractions.

Then the uncertainty in R due to the errors δ_j^k is given by

$$\delta R^k = R - \mathrm{LR}\left\{\left(\sigma_j\left(1+\delta_j^k\right)\right)\right\} \ , \qquad k = SY,\ SE \ . \tag{4.4}$$

Uncertainties of type δ^{RC} are calculated in this way using Equation 3.12 and yield

$$\delta R^{RC} = .023\,(1 + \Delta\epsilon R) \approx .025 \ , \tag{4.5}$$

for E140 values of $\Delta\epsilon R$.

In Figure 4.1 the error bars are dominated by the statistical portion of the uncertainty vector. In general, for E140, the δ^{SY} and δ^{SE} uncertainties are small relative to the δ^{ST} and δ^{SR} uncertainties. Typically,

$$(\delta^{ST})^2 \geq (\delta^{SR})^2 \gg (\delta^{SY})^2 \gg (\delta^{SE})^2 \ , \tag{4.6}$$

resulting in

$$(\delta R^{ST})^2 \gg (\delta R^{SY})^2 \approx (\delta R^{SE})^2 \ . \tag{4.7}$$

In the combined analysis of Chapter 5 the δ^{SY} and δ^{SE} errors are much larger, necessitating the rigorous propagation of Equations 4.3 and 4.4. For the specific E140 regression analysis presented in Figure 4.1, we obtain

$$\begin{aligned} R &= .370 \ , \\ \left.\begin{aligned} \delta R^{ST} &= .049 \ , \\ \delta R^{SY} &= .003 \ , \\ \delta R^{SE} &= .004 \ , \\ \delta R^{RC} &= .025 \ , \end{aligned}\right\} \quad & \delta R^{SS} = .005 \ , \end{aligned} \tag{4.8}$$

where δR^{SS} is the total experimental systematic error.

The 20 linear regression analyses form a set of linearity measurements versus ϵ. In general, an uncorrected systematic effect in the cross sections would contribute curvature to the regression analyses. Figure 4.2 presents the distribution of observed χ^2/df of the regressions. The curve shown is the expected χ^2 distribution for an average number of 2.45 uncorrelated measurements gaussian-distributed about a parent distribution. The agreement is excellent. The three regressions which yield $\chi^2/df > 1.3$ are statistically expected and require no further treatment.†

† Some sources[74–76] claim that the uncertainty on any parameter determined via a fitting procedure should be multiplied by a factor of $\sqrt{\chi^2/df}$. We address this wayward assertion in Appendix B.3 with a monte carlo analysis of the R extractions.

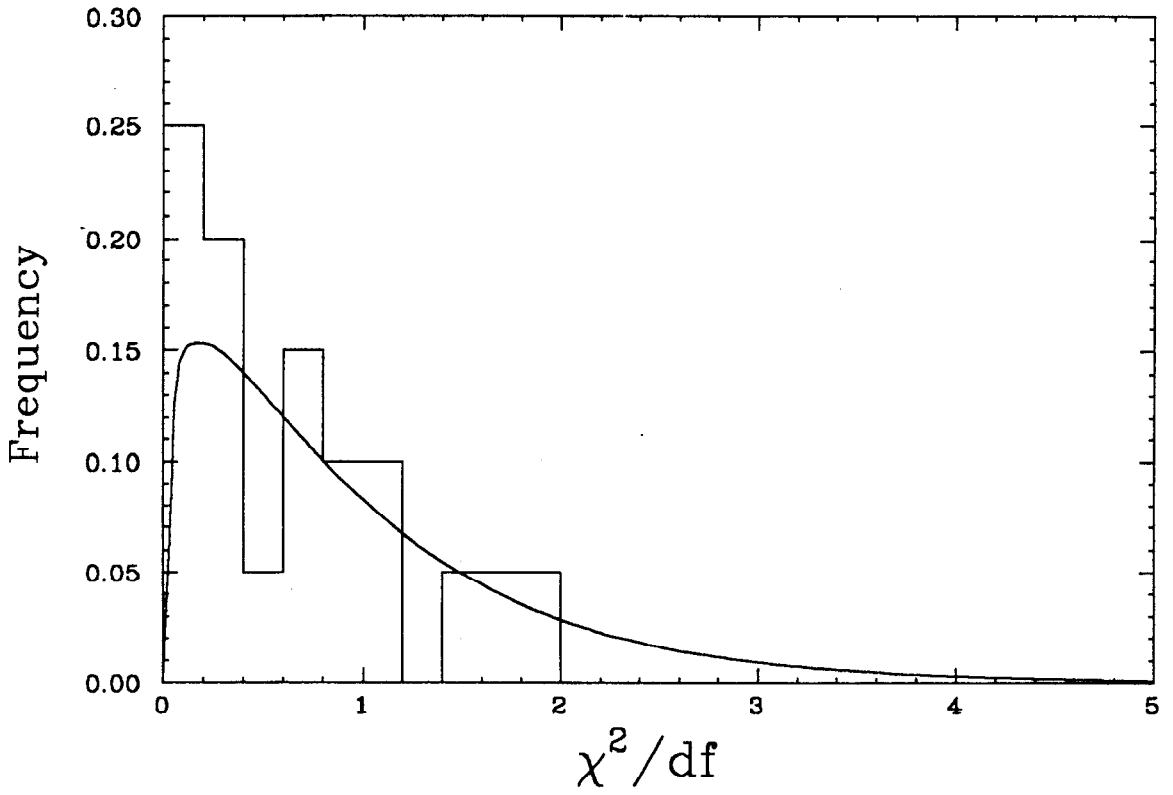

Figure 4.2. Shown is the observed distribution of χ^2/df for the 20 E140 regression analyses. The curve is the expected χ^2 distribution for 2.45 degrees of freedom, assuming that all errors are gaussian and uncorrelated.

Overall, the observed χ^2/df distribution is somewhat shifted toward zero relative to the theoretical distribution. This is due the inclusion of some systematic errors (the random component δ^{SR}) in the regression analyses. To quantify the "goodness-of-fit" between observed and expected, we utilize the additive property of χ^2 distributions.[77] Summing the observed χ^2's and the degrees of freedom over all 20 linear regressions, we have

$$\langle \chi^2/df \rangle = 34.7/49 \ . \tag{4.9}$$

The probability of observing a $\chi^2 \leq 34.7$ based on 49 degrees of freedom is 12.4%. The value of $\langle \chi^2/df \rangle$ we would get if no systematic errors had been included in the

regression analysis is larger by a factor of

$$\frac{\left(\delta^{ST}\right)^2+\left(\delta^{SR}\right)^2}{\left(\delta^{ST}\right)^2} \approx 1.45 \ , \tag{4.10}$$

or roughly 50.3/49, soundly in the center of the expected distribution.

The observed linearity of the regression analyses greatly credits our experimental effort. The somewhat small $\langle \chi^2/df \rangle$ reflects a conservative estimate of the systematic errors δ^{SR}, and is inconsistent with the hypothesis that large systematic effects remain uncorrected in the cross section measurements.

4.2 E140 Iron/Deuterium Comparison

We first present the results of our iron/deuterium comparison study. We extract $R^{Fe}-R^d$ directly by linearly regressing the cross section ratios σ^{Fe}/σ^d against the parameter ϵ' via

$$\frac{\sigma^{Fe}}{\sigma^d} = \frac{\sigma_T^{Fe}}{\sigma_T^d}\left[1+\epsilon'\left(R^{Fe}-R^d\right)\right] \ , \tag{4.11}$$

where

$$\epsilon' = \frac{\epsilon}{1+\epsilon R^d} \ , \tag{4.12}$$

which follows from Equation 1.2. This approach exploits the fact that most components of the error vector cancel, or approximately cancel, in the ratio σ^{Fe}/σ^d. However, because the ratio of two cross sections does not have a symmetric error distribution (see Appendix B.2), we perform the regression analyses once for σ^{Fe}/σ^d and once for σ^d/σ^{Fe}, and average the results $R^{Fe}-R^d$ and $-\left(R^d-R^{Fe}\right)$. Systematic errors introduced by this approximate statistical treatment are negligible.

Systematic errors of type δ^{SR}, δ^{SY}, and δ^{RC} approximately cancel in the cross section ratio, and become negligible with the exception of fluctuations in deuterium target density. Errors of type δ^{SE} cancel by definition. Similarly, all δ^{NM} uncertainties also cancel, with the exception of target thicknesses and neutron excess corrections. We avoid correlations by combining the two sets of iron data before, rather than

Table 4.2. Shown are the E140 iron/deuterium structure function comparisons. Uncertainties are fractional in F_2 and absolute in R. Systematic uncertainties are negligible, with the exception of normalization uncertainties in F_2^{Fe}/F_2^d and F_2^{Au}/F_2^d of $\pm 1.0\%$ and $\pm 2.6\%$, respectively. More accurate estimates of F_2^{Fe}/F_2^d and F_2^{Au}/F_2^d are presented in Table 4.3. Also presented is the χ^2/df of the regression analyses.

x	Q^2	F_2^{Fe}/F_2^d	$\pm\delta F_2^{ST}$	$R^{Fe}-R^d$	$\pm\delta R^{ST}$	χ^2/df
Iron/Deuterium						
.20	1.0	1.013	.012	−.064	.051	.9
.20	1.5	1.000	.013	−.143	.056	.7
.20	2.5	1.070	.022	.148	.077	1.2
.35	1.5	1.011	.016	.032	.078	.6
.35	2.5	1.018	.013	.095	.056	1.0
.35	5.0	.992	.016	.024	.058	.4
.50	2.5	.939	.008	.018	.033	.8
.50	5.0	.939	.013	−.016	.052	.2
Gold/Deuterium						
.20	1.0	1.018	.012	−.045	.058	.4

after, the comparison to deuterium. From Tables 3.4 and 3.5 we determine a relative normalization of

$$\begin{aligned} \langle \sigma^{Fe\#1}/\sigma^{Fe\#2} \rangle &= 1.018 \pm .005 \ , \\ \chi^2/df &= 5.9/6 \ , \end{aligned} \tag{4.13}$$

which we use to combine the iron cross sections into a single dataset.

Presented in Table 4.2 are the iron/deuterium comparisons. The values for $R^{Fe}-R^d$ are plotted in Figure 4.3 versus x and Q^2. As no significant kinematic dependence is observed, we calculate the overall average of the $R^{Fe}-R^d$ measurements,

$$\begin{aligned} \langle R^{Fe}-R^d \rangle &= .003 \pm .018 \ , \\ \langle \chi^2/df \rangle &= 15.4/7 \ . \end{aligned} \tag{4.14}$$

Table 4.3. Shown are the E140 EMC effect ratios extracted by assuming $R^{Fe} = R^{Au} = R^d$. Uncertainties are fractional. Systematic uncertainties are negligible, with the exception of normalization uncertainties of $\pm 1.0\%$ and $\pm 2.6\%$ for F_2^{Fe}/F_2^d and F_2^{Au}/F_2^d, respectively. Also shown are the χ^2/df for the averagings over ϵ.

x	Q^2	$\langle F_2^{Fe}/F_2^d \rangle \pm \delta F_2^{ST}$		χ^2/df
Iron/Deuterium				
.20	1.0	1.028	.005	1.3
.20	1.5	1.031	.004	2.3
.20	2.5	1.027	.006	1.0
.35	1.5	1.005	.006	.4
.35	2.5	.998	.005	1.4
.35	5.0	.985	.005	.3
.50	2.5	.935	.005	.7
.50	5.0	.942	.006	.2
Gold/Deuterium				
.20	1.0	1.027	.005	.4

The probability of observing a $\chi^2/df \geq 15.4$ based on 7 degrees of freedom is 3.5%. This large χ^2/df reflects the large scatter at $x = .2$, which is in turn traceable (see below) to an iron measurement at $(x, Q^2) = (.2, 1.5)$ and a deuterium measurement at $(x, Q^2) = (.2, 2.5)$ which are much lower than adjacent measurements on the same targets. Because these two measurements of R^{Fe}–R^d are also adjacent in Q^2, we believe the global average expressed in Equation 4.14 is a valid representation of the data. However, in light of the large observed scatter, we believe that the standard deviation of the eight differences about their mean is a better estimate of the uncertainty in the mean. We thus conclude that

$$R^{Fe} = R^{Au} = R^d \ , \tag{4.15}$$

within $\pm .027$ total estimated experimental uncertainty.

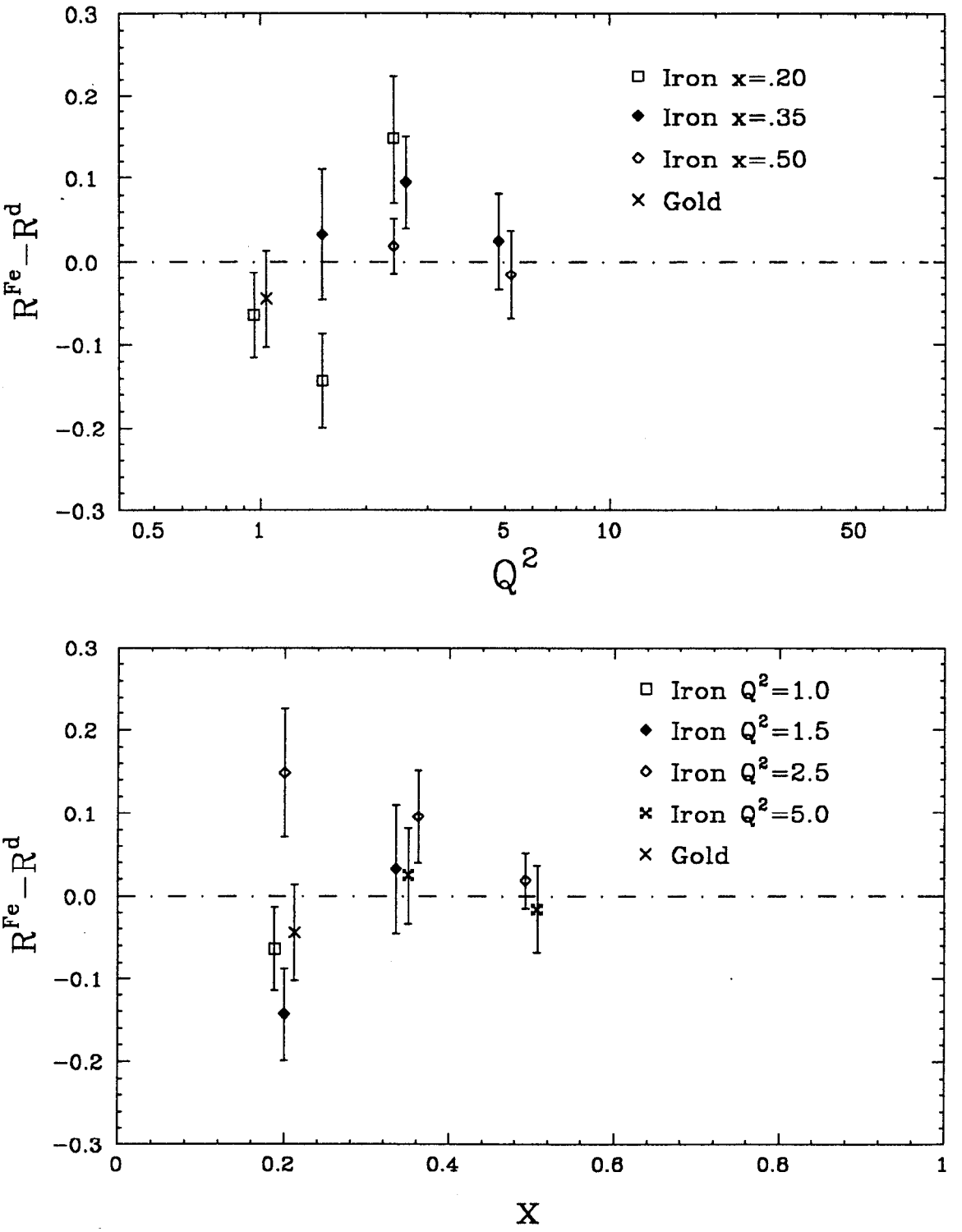

Figure 4.3. Shown are the E140 measurements of $R^{Fe}-R^d$ and $R^{Au}-R^d$ from Table 4.2. Systematic errors are negligible. The global average of $R^{Fe}-R^d$ is $.003 \pm .018$ (see text).

Under the assumption that $R^{Fe} = R^d$, we obtain a better estimate of F_2^{Fe}/F_2^d by averaging the σ^{Fe}/σ^d ratios over ϵ for each (x, Q^2). These EMC effect ratios are given in Table 4.3. The lack of ϵ dependence of the cross section ratios is evidenced in the χ^2/df observed in the averaging processes. The total $\langle \chi^2/df \rangle$ over Table 4.3 is 32.0/32. These EMC ratios are systematically higher than our previously reported[1,29] values primarily due to the improved neutron excess correction used here.

4.3 E140 Deuterium and Iron Results

Presented in Table 4.4 are the E140 extracted values of F_2 and R, with their statistical and systematic uncertainties. The uncertainty due to radiative corrections, $\delta R^{RC} = .025$, is very strongly correlated across all E140 measurements of R. In Chapter 5, more precise values of F_2 are extracted directly from the cross sections using a model for $R(x, Q^2)$. The values of F_2 in Table 4.4 are presented for completeness only, and are not discussed further.

The extracted R values from Table 4.4 are plotted in Figure 4.4 along with measurements of R from the EMC,[9,21] BCDMS,[16,17] and CDHSW[18] collaborations. Those measurements from EMC have been condensed in x and Q^2 and averaged over targets in order to reduce scatter. Also shown in Figure 4.4 are calculations[6] of R based QCD[7] and on QCD with the inclusion of target mass effects[8] (QCD+TM).

The E140 R measurements are systematically greater than R^{QCD}, and, with two notable exceptions, everywhere greater than $R^{\mathrm{QCD+TM}}$. These two points, the iron #1 measurement at $(x, Q^2) = (.2, 1.5)$ and the deuterium measurement at $(x, Q^2) = (.2, 2.5)$, are much lower than adjacent measurements with the same targets (as noted in the previous section). An examination of the individual cross section measurements leading to these extracted R values does not indicate the presence of any systematic problems. Thus, we treat these two measurements as statistical fluctuations. See also Section 5.3.3.

Table 4.4. Shown are the E140 deuterium and iron structure functions. Uncertainties are fractional in F_2 and absolute in R. Not shown are uncertainties due to radiative corrections, which are less than $\pm.5\%$ for F_2 (see Equation 5.39) and $\pm.025$ for R. Normalization uncertainties in F_2 are given in Table 3.2. In Chapter 5, more precise values of F_2 are extracted directly from the cross sections using a model for $R(x, Q^2)$.

x	Q^2	$F_2 \pm \delta F_2^{ST} \pm \delta F_2^{SS}$			$R \pm \delta R^{ST} \pm \delta R^{SS}$			χ^2/df
Deuterium								
.20	1.0	.2964	.010	.010	.370	.049	.005	.7
.20	1.5	.2996	.011	.010	.280	.050	.005	1.8
.20	2.5	.2907	.017	.010	.105	.051	.005	.0
.20	5.0	.3034	.025	.010	.233	.065	.011	.2
.35	1.5	.2331	.012	.010	.308	.062	.005	.3
.35	2.5	.2198	.010	.010	.159	.040	.005	.6
.35	5.0	.2081	.013	.010	.126	.045	.005	.4
.50	2.5	.1412	.007	.010	.202	.029	.005	.8
.50	5.0	.1174	.009	.010	.100	.033	.006	.8
.50	7.5	.1109	.022	.010	.152	.065	.005	–
.50	10.0	.1019	.019	.010	.045	.044	.008	.0
Iron #1								
.20	1.0	.2990	.010	.009	.284	.045	.005	1.8
.20	1.5	.3002	.011	.009	.159	.042	.005	.5
.20	2.5	.3112	.017	.010	.254	.062	.005	1.5
.35	1.5	.2360	.012	.009	.356	.069	.005	1.2
.35	2.5	.2239	.010	.009	.260	.051	.005	1.1
.35	5.0	.2063	.014	.009	.151	.050	.005	.1
.50	2.5	.1325	.008	.009	.220	.033	.005	.6
.50	5.0	.1100	.014	.009	.078	.048	.006	.1
Iron #2								
.20	1.0	.2968	.010	.010	.340	.048	.005	.2
.50	2.5	.1310	.022	.009	.218	.056	.006	–
Gold								
.20	1.0	.3024	.010	.010	.339	.046	.005	.4

We quantify the disparity between our data at R^{QCD} and $R^{\mathrm{QCD+TM}}$ with χ^2 goodness-of-fit tests. Table 4.5 shows a comparison of our data with several simple functional forms. The large χ^2's indicate these are not successful models for $R(x, Q^2)$.

Using our earlier conclusion that $R^{Fe} = R^{Au} = R^d$, we average the R extractions of Table 4.4 over targets, using the logarithmic variable of Appendix B.2 to account for the askew probability distribution of R. These results are presented in Table 4.6. The total χ^2/df of these averaging processes is

$$\langle \chi^2/df \rangle = 12.8/11 \ . \tag{4.16}$$

While this is consistent with the expected χ^2 distribution, the measurement at $(x, Q^2) = (.2, 1.5)$ again contributes a disproportionate share of the χ^2. For comparison with Figure 4.4, we plot the average $R(x, Q^2)$ in Figure 4.5.

In summary, the measured R values from E140 are consistently higher than theoretical predictions based on QCD even with the inclusion of target mass contributions. This discrepancy may be explained in terms of additional higher twist contributions to F_L. Further discussion of the E140 data is reserved until Section 5.3.3 where comparisons are made with the results of the global reanalysis of the early SLAC data.

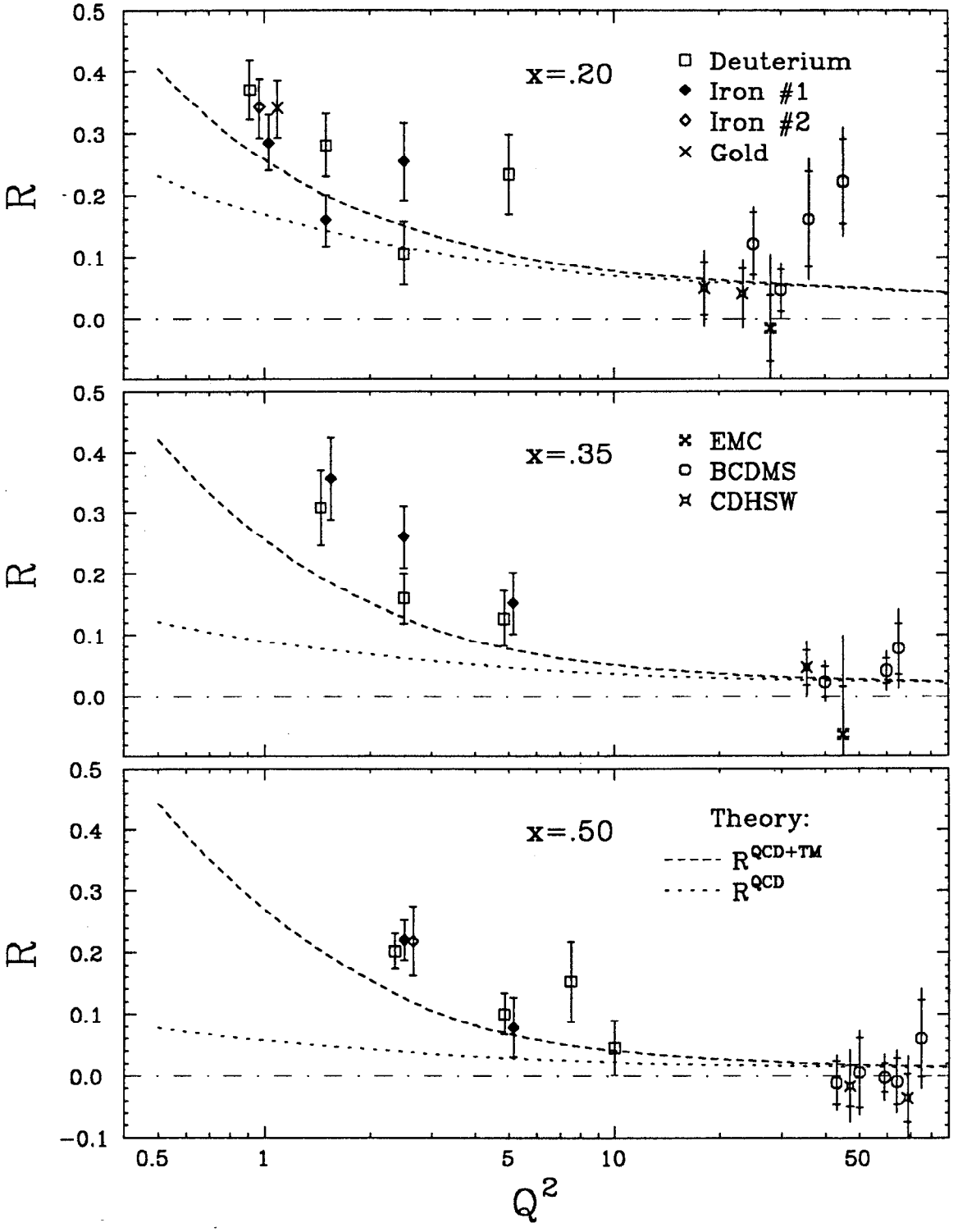

Figure 4.4. Shown are the E140 measurements of $R(x, Q^2)$ from Table 4.4. The errors δR^{SS} are much smaller than δR^{ST} and are plotted, but not visible. Errors do not include the strongly correlated $\delta R^{RC} = .025$. See text for further discussion.

Table 4.5. Shown are goodness-of-fit tests of the E140 data to various models and calculations, including the naive parton model prediction, $R^{\rm npm} = 4M_p^2x^2/Q^2$, and the global mean value, $.207 \pm .010$.

Model	χ^2/df
$R = 0$	579 / 22
$R = R^{\rm QCD}$	225 / 22
$R = R^{\rm npm}$	175 / 22
$R = .207 \pm .010$	83 / 21
$R = R^{\rm QCD+TM}$	67 / 22

Table 4.6. Shown are the E140 $R(x, Q^2)$ combined over all targets. Uncertainties are absolute. Not shown are the uncertainties due to radiative corrections, which are $\pm.025$. The total χ^2/df of all averagings over targets is 12.8/11.

x	Q^2	$\langle R \rangle \pm \delta R^{ST} \pm \delta R^{SS}$		
.20	1.0	.330	.023	.005
.20	1.5	.211	.032	.003
.20	2.5	.168	.039	.003
.20	5.0	.231	.065	.010
.35	1.5	.330	.046	.005
.35	2.5	.197	.031	.000
.35	5.0	.136	.033	.004
.50	2.5	.210	.020	.004
.50	5.0	.094	.027	.003
.50	7.5	.151	.065	.004
.50	10.0	.044	.044	.006

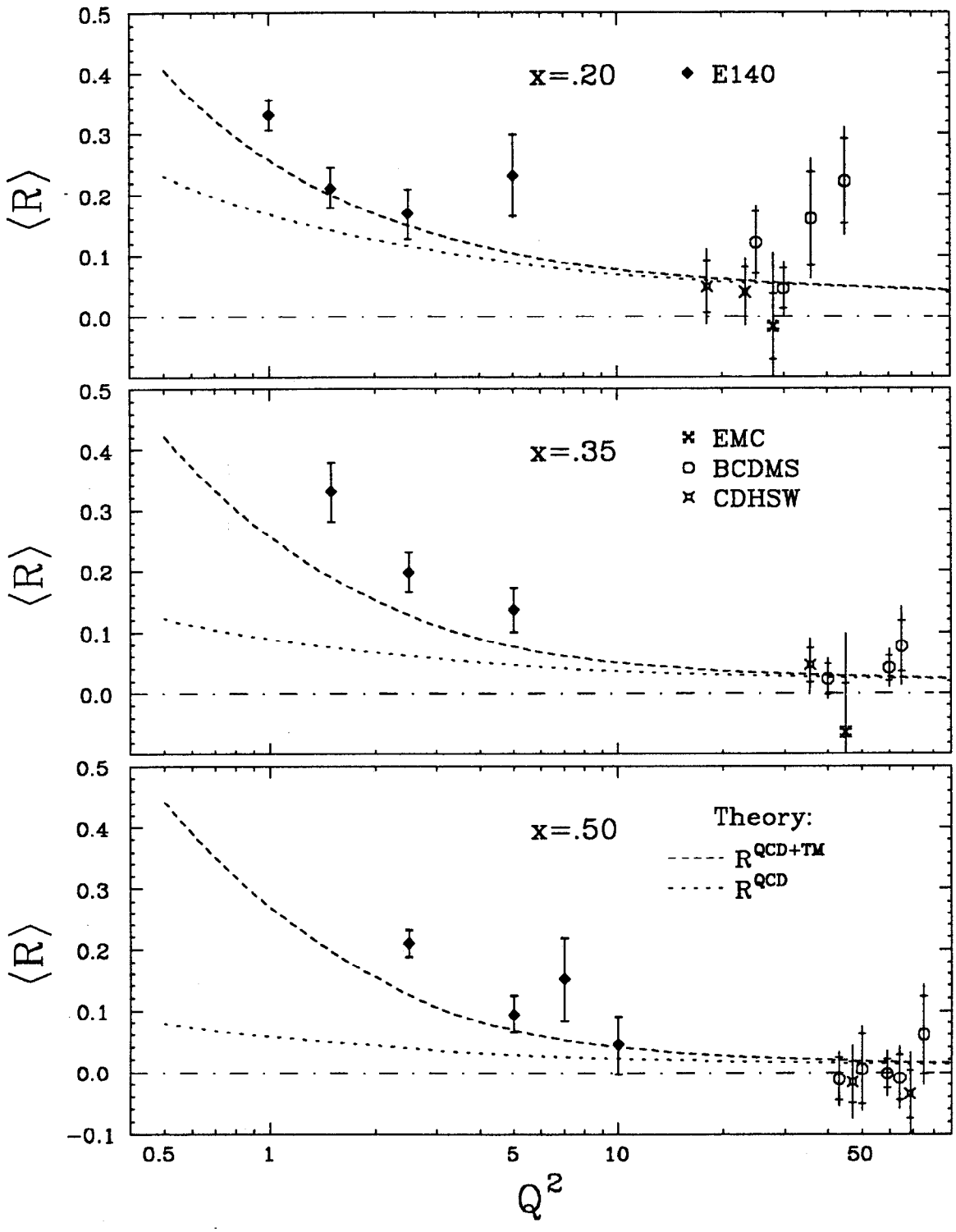

Figure 4.5. Shown are the E140 measurements of R averaged over all targets. See Figure 4.4 and text for details.

Chapter 5

Global Reanalysis of the SLAC Data

The cross sections from experiments E49a, E49b, E61, E89a, and E89b are archived at SLAC in the TASI Databank,[78] both in their final form and in their pre-radiatively corrected form. Information about the target thicknesses and additional radiators is similarly archived, making it feasible to re-radiatively correct the data. Pre-radiatively corrected cross sections from E87 are obtained from the MIT Pass II analysis dumps, while target and radiator information for E87 is taken from the E87 hardware logbooks. Final cross sections from E139 are on hand, and as yet, unpublished. Our primary references for the details of these experiments are listed in Table 1.1.

At the start of the analysis, we attach an eight-component error vector to each cross section measurement. The components of this error vector are described in Table 4.1, with the exception of two new components, δ^{NM_1} and δ^{NM_2}, which represent uncertainties in the relative normalizations of the eight experiments and are discussed in Section 5.2. Where possible, we assign values to the error vector components based on the publications and theses; otherwise, we estimate values. A complete summary of the contributions to the error vectors is presented in Appendix C.

For the deuterium/hydrogen comparisons, we note that systematic errors of type δ^{SR}, δ^{SY}, and δ^{RC} approximately cancel in the ratio of σ^d/σ^p, and become negligible with the exception of the independent target density fluctuations. Similarly, errors of type δ^{SE} cancel perfectly in the cross section ratio.

It is crucial to our analysis that we rigorously propagate all systematic errors. As this subject is not treated in most statistics texts, we present in Appendix B.1 our formula for the propagation of the error vector through a general operator, assuming the correlations among the data are known or can be estimated.

Figure 5.1 presents a basic flowchart of the reanalysis procedure. Its primary feature is the inherently recursive structure imposed by the radiative corrections procedure. Within each loop, there are additional frequent calls for structure function models, which are also updated at each iteration of the main procedure. In practice, two full loops were required to reduce structure function variations below $\pm 1\%$ at all kinematics.

5.1 Radiative Corrections

Combining information from the TASI Databank with detailed information from the theses (when available), we are able to reconstruct the dimensions of the targets and upstream and downstream radiators for each of the experiments. These target reconstructions, described at length in Appendix D, are used to calculate the radiative corrections using our Bardin/Tsai procedure.

The complete hydrogen and deuterium datasets contain together 7,810 individual cross section measurements. However, as noted in Section 1.2.2, almost all of these cross sections were measured in densely packed E'-spectra. We radiatively correct only a sample of each E'-spectrum and interpolate the radiative corrections to the other points. Using the previous calculations of the Tsai radiative corrections as a guide, we permit interpolation spans as large as 8% (full width) in the calculated correction, though smaller spans of 5% are typical. This strategy introduces $\pm .2\%$ additional systematic uncertainty in the cross sections while reducing computation time to 60 hours of cpu on an IBM 3081/K processor.[†]

[†] The hydrogen resonance region was scanned to see if this approach would work there. Interpolation spans of 5% yielded unreliable results, indicating that a large cpu investment would be needed for a similar reanalysis of the resonance region.

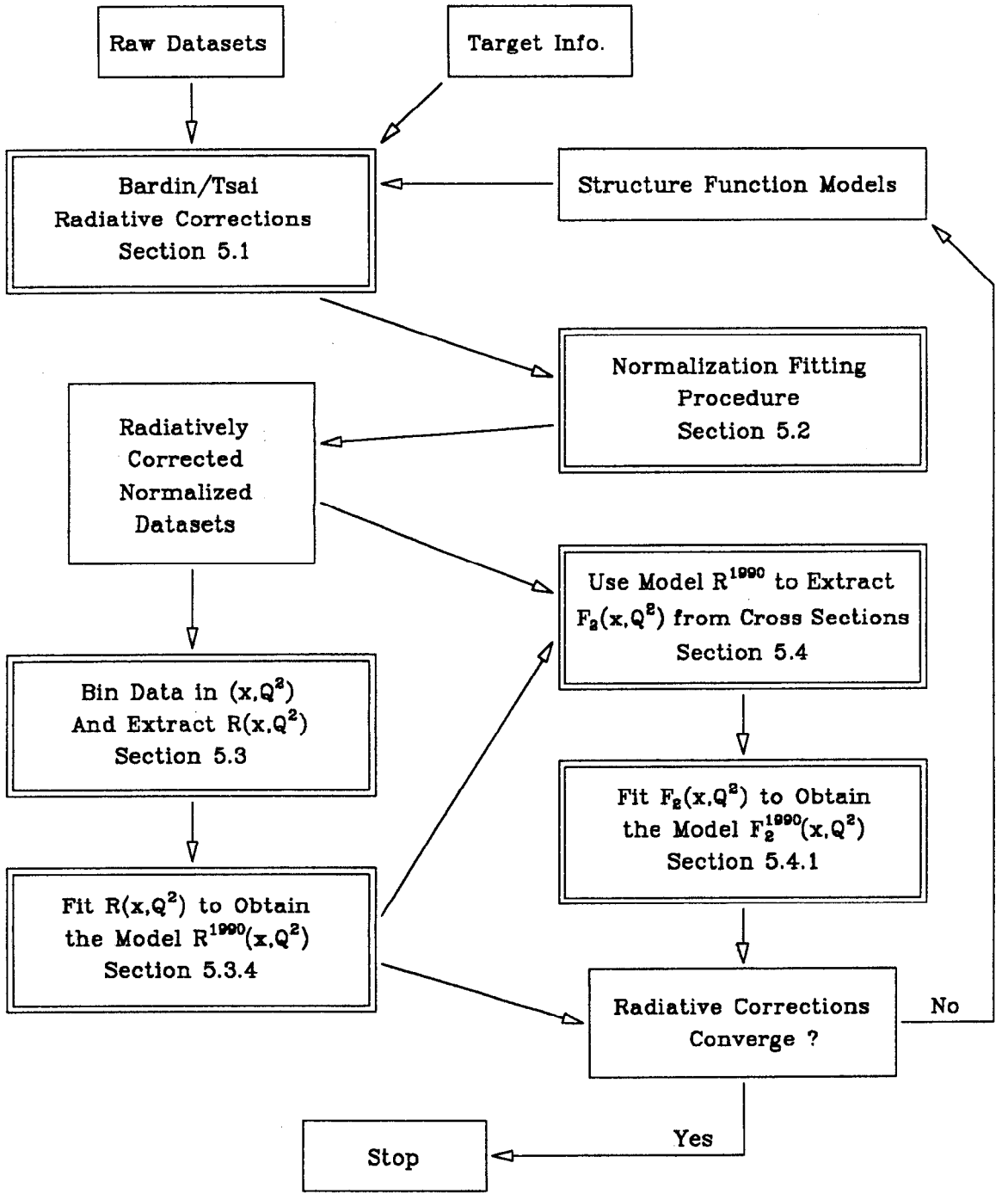

Figure 5.1. Shown is a flowchart of the global reanalysis procedure. F_2^{1990} is an abbreviation for either of the two F_2 models introduced in later sections.

Figure 5.2 shows a comparison between of our Bardin/Tsai radiative correction calculations and the Tsai calculations[36] used previously. The wiggles and extreme points observed represent variations and spikes within the Tsai calculations only. These early Tsai radiative corrections were "unfolded"[36] in an iterative fashion, and thus susceptible to long range correlations and systematic shifts. The discrepancies observed in Figure 5.2 are well within the ±5% uncertainty of the Tsai radiative correction procedure.

The model dependence of the radiative corrections is very slight. Convergence of the main loop in Figure 5.1 is typically ±.2% for all kinematics $x > .1$ and $Q^2 > 1$. We expand the kinematic range of our analysis, however, to include all data satisfying Equation 1.11. For these additional low-x and low-Q^2 data, the radiative corrections convergence is everywhere better than ±1%.

Uncertainties due to radiative corrections are the same as for E140, defined by Equation 3.12 and in Table 3.2. For the low-x and low-Q^2 cross sections, we increase these uncertainties by a factor of 1.5.

5.2 Normalization Fits

Accurate knowledge of the relative normalizations of the eight experiments is critical: a normalization uncertainty of 5% between two cross sections separated by $\Delta\epsilon = .5$ propagates into $\delta R = .11$. In fact, normalization discrepancies of this size were noted by Mestayer *et al.*,[4] though no correction was applied for these effects resulting in the large uncertainties shown in Figure 1.1.

The obvious normalization technique is to compare cross sections measured at identical (E_o, E', θ). This procedure requires high statistics, even when two experiments overlap significantly, as E49b and E87 do. In the analysis of Bodek *et al.*,[3] the uncertainty in the relative normalizations was determined to only ±1.0%. When more than two experiments are to be mutually normalized, correlations develop and the obvious procedure is unsatisfactory.

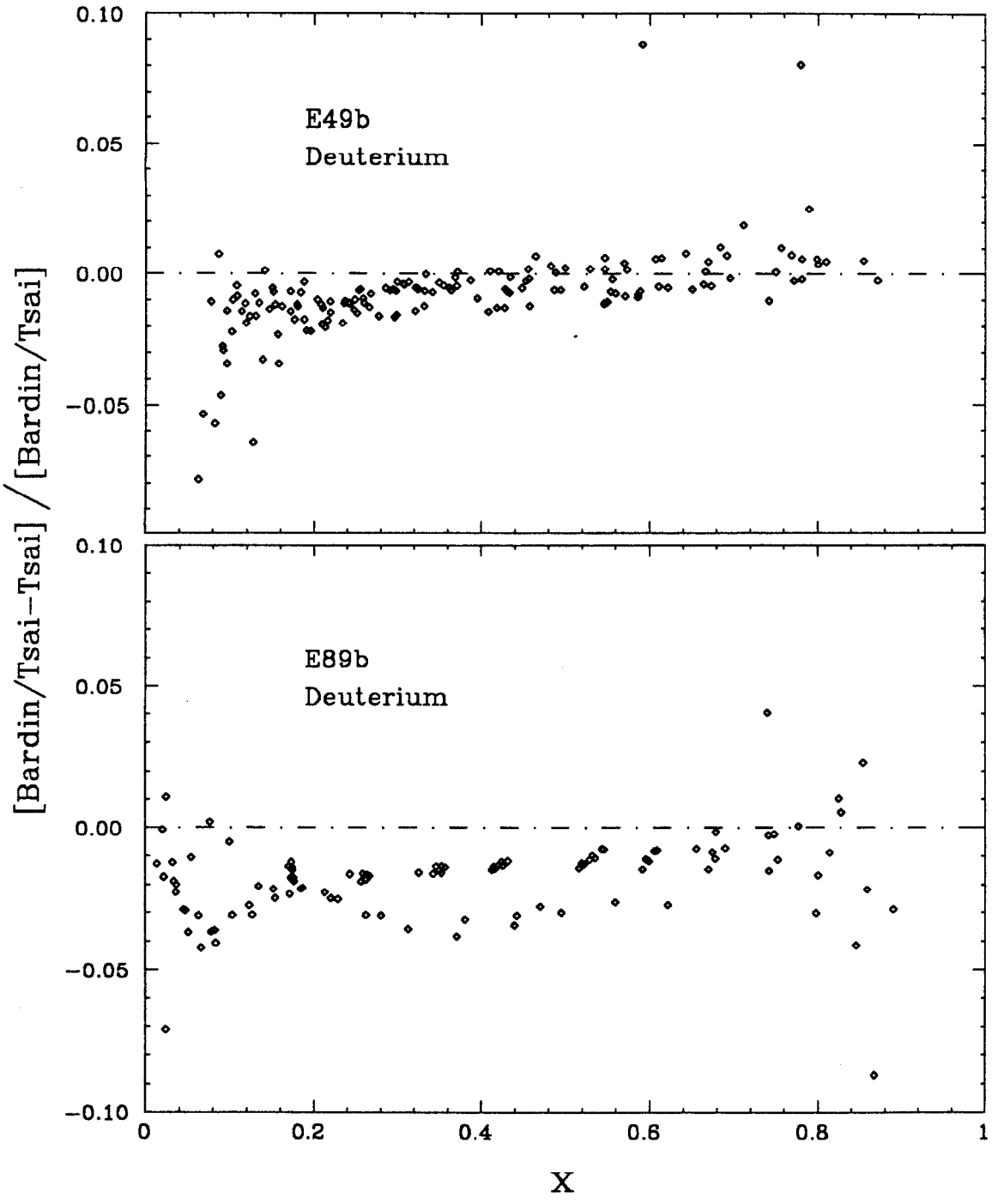

Figure 5.2. Shown is a comparison of our Bardin/Tsai radiative correction calculations with those of SGA and SFG using the Tsai[36] procedure. The wiggles and spikes in the difference originate in the Tsai calculations only.

Our solution to this problem is to apply a fitting technique which simultaneously determines the mutual normalizations of the eight experiments and their correlations. Cross sections from all experiments are fit to a 15 parameter cross section model, allowing the normalizations of each experiment to vary as additional parameters. We fix the normalization of E140, which defines the overall normalization of our global reanalysis.

5.2.1 Condensing the Data

Before fitting, each dataset is *condensed* by combining together nearby cross sections from the same experiment. Condensing the data improves the way in which systematic errors are propagated through a fitting procedure. In particular, it provides the correct propagation of the largest systematic error, δ^{SR}, which is strongly correlated *locally* but not globally.† The procedure for condensing a set of cross sections, $\{\sigma_j\}$, is

$$\sigma_{j_\circ} = \left[\sum_j \frac{\sigma_j}{\sigma_j^{model}} wt_j \Big/ \sum_j wt_j\right] \sigma_{j_\circ}^{model} , \tag{5.1}$$

where $j_\circ$ is the average kinematic, σ^{model} is a cross section model, and the weights are determined by the δ^{ST} uncertainty only. The systematic errors are essentially averaged over range, propagating according to Equation B.8. The maximum span in kinematics over which we condense is given by

$$\Delta x < .03 , \qquad \frac{\Delta Q^2}{Q^2} < 6\% , \qquad \Delta\epsilon < .05 , \tag{5.2}$$

which seemed adequate, without introducing a graininess to the distribution of kinematics. A study of other condensing parameters showed negligible differences.

† Sources contributing to δ^{SR} are auto-correlated over short periods of time, which, for the early SLAC experiments, is over adjacent kinematics on a single E'-spectrum. Thus, it is correct to use the word "local" both in a kinematic and in a temporal sense.

5.2.2 Model and Algorithm

The relative normalizations of the eight experiments are determined by simultaneously fitting the condensed cross sections to a cross section model of the form

$$\frac{\sigma^{meas}}{\sigma^{mott}}\nu = F_2^{\Omega_9}(x,Q^2)\left[1+\frac{1-\epsilon}{\epsilon}\frac{1}{1+R^{model}(x,Q^2)}\right]\Big/ N^{Expt}\,, \tag{5.3}$$

where

$$F_2^{\Omega_9}(x,Q^2) = \frac{x}{x''}\sum_{n=3}^{7} C_{n+2}(1-x')^n\,,$$

$$x' = \frac{Q^2+C_3}{2M_p\nu+C_4}\,, \tag{5.4}$$

$$x'' = \frac{Q^2+C_1}{2M_p\nu+C_2}\,,$$

$$R^{model}(x,Q^2) = \left[\sum_{n=0}^{3} C_{n+10}x^n\right]\Big/ Q^{C_{14}+C_{15}x}\,, \tag{5.5}$$

and

$$\begin{aligned} N^{Expt} = 1 &+ C_{16}\xi^{E49a} + C_{17}\xi^{E49b} + C_{18}\xi^{E61} \\ &+ C_{19}\xi^{E87} + C_{20}\xi^{E89b} + C_{21}\xi^{E139}\,. \end{aligned} \tag{5.6}$$

Our model $F_2^{\Omega_9}(x,Q^2)$ improves on the form of Bodek *et al.*,[3] who use instead $x''=x'$. The original motivation for Equation 5.4 comes from Bloom and Gilman,[79] who observe approximate scaling in

$$\tilde{x} = \frac{Q^2}{2M_p\nu+M_p^2} \tag{5.7}$$

in the very early SLAC data.[39] The data presented here, in particular the E140 and E139 contributions, now require two scaling variables, x' at large x, and x'' at small x.

The functional form of R^{model} is chosen to be particularly free from any assumptions about the kinematic dependence of $R(x,Q^2)$. Both theory and experiment indicate that $R(x,Q^2)$ is smooth and featureless in this kinematic range.

The ξ terms in N^{Expt} are Kronecker-like delta functions defined on the set of experiments,

$$\xi^k = \begin{cases} 1, & \text{for experiment "k";} \\ 0, & \text{otherwise.} \end{cases} \tag{5.8}$$

As defined, the normalization correction factor for experiment "k" relative to E140 is given by $[1 + C_k]$ which is the number by which dataset "k" must be multiplied to bring it into agreement with E140. The normalization factor for E89a is determined separately in the following section.

And lastly, for deuterium, $F_2^{\Omega_9}$ is defined with an additional multiplicative factor,[3]

$$\beta = 1 - \mathrm{e}^{-7.7\left(x^{-1}+M_p^2/Q^2-1\right)} , \tag{5.9}$$

to account for nuclear binding effects at large x.

The weights in the fitting procedure are determined by the total uncertainties,

$$wt_j = 1 \Big/ \left[\left(\delta^{ST}\right)^2 + \left(\delta^{SR}\right)^2 + \left(\delta^{SY}\right)^2 + \left(\delta^{SE}\right)^2 \right] . \tag{5.10}$$

While a more correct procedure for the propagation of the δ^{SE} errors is available (after Equation 4.4), and a similar though more complicated procedure exists for the δ^{SY} errors, the approximate propagation offered by Equation 5.10 simple and estimated to be accurate to $\pm.1\%$ in the N^k.

Given the normalization factors for hydrogen and deuterium, the relative normalizations of the cross section ratios, σ^d/σ^p, are calculable. A better approach to the study of deuterium/hydrogen differences is to perform a similar normalization fit to σ^d/σ^p. We account for the asymmetric error distribution of the σ^d/σ^p by fitting instead the logarithms of the data (see Appendix B.2),

$$\ln\left(\frac{\sigma^d}{\sigma^p}\nu\right) = \ln\left(F_2^{dp}(x,Q^2) \times R^{factor}(x,Q^2) \times \frac{1}{N^{Expt}}\right) , \tag{5.11}$$

where

$$F_2^{dp}(x,Q^2) = \beta \frac{x}{x''} \sum_{n=0}^{3} C_{n+3} x^n \ ,$$

$$R^{factor}(x,Q^2) = \frac{1 + R^{1990}(x,Q^2) + \frac{1-\epsilon}{\epsilon}\left[1 + R^{dp}(x,Q^2)\right]^{-1}}{1 + R^{1990}(x,Q^2) + \frac{1-\epsilon}{\epsilon}} \ , \tag{5.12}$$

where R^{1990} is a fit to the previously extracted R^p values, and where $R^{dp}(x,Q^2)$ is a model of $R^d - R^p$ with a functional form given by Equation 5.5.

Our fitting routine, FITPAR,[44] is a χ^2 minimization program based on the gradient expansion algorithm.[80] Typically, five iterations of the main routine are required to find a local χ^2 minima. In practice, these numerical solutions are found somewhat chaotically:† two nearly identical initial parameter sets can lead to entirely different χ^2 minima. As it is not feasible to exhaustively explore the 21-dimensional parameter space, an alternative technique is used. We perform initial fits with fewer parameters, reducing the dimensionality of the problem and thus the "ruggedness" of the χ^2 surface being searched. Solutions to the lower dimensional fits are then used as initial parameter sets for higher dimensional fits. This technique leads to "physical values" of the sensitive parameters C_1 through C_4. The best fit solution to Equation 5.3 displays parameters C_1 through C_9 closely related to those presented in Table 5.11.

5.2.3 E89a Normalization

The normalization coefficient of E89a could not be determined with the above normalization fit, as the E89a data are at very low ϵ, kinematically disjoint from the other experiments. The fitting technique fails because the best fit value of N^{E89a} is dictated by R^{model} rather than the other data. Numerically, such attempts yield large correlations between N^{E89a} and the parameters of R^{model}. Conversely, the E89a data

† (in double precision Fortran real variables)

potentially carry significant weight in the extraction of R. In practice, however, the large 5–10% statistical uncertainties in the E89a data yield only small contributions to the R extractions.

To normalize E89a with the other experiments we instead compare elastic hydrogen cross sections from E89a[45] with those from E89b[35] and E140.[51] The standard treatment is to compare measurements of $\left[G_m^p(Q^2)\right]^2$, assuming form factor scaling and the empirical dipole formula. However, over the wide range in scattering angles spanned by these three experiments, such a comparison is sensitive to possible deviations of G_e^p from G^{dip}. Results[81] from the E140 elastic measurements suggest a simple parameterization of G_e^p/G^{dip} in our kinematic range,

$$\frac{G_e^p}{G^{dip}} = \begin{cases} 1.0\,, & Q^2 \leq 1.0\,; \\ .9+.1Q^2\,, & 1.0 < Q^2 \leq 3.0\,; \\ 1.2\,, & 3.0 < Q^2\,. \end{cases} \tag{5.13}$$

Using this parameterization of G_e^p we extract and compare $\left(G_m^p/G^{dip}\right)^2$ from the three experiments, taking into account recent advances in the Bardin/Tsai radiative corrections to the elastic peak.[51,82] Comparisons are made at comparable Q^2, then averaged.

Table 5.1. Presented are the relative normalizations of E89a, E89b, and E140 based on comparisons of elastic hydrogen cross sections. Corrections have been made for $G_e^p \neq G^{dip}$ and for differences in radiative corrections. The errors shown are statistical only.

Experiments		Hydrogen Normalization
E89a > E140	by	$1.1\% \pm 2.8\%$
E89b > E140	by	$4.5\% \pm 2.2\%$
E89b > E89a	by	$3.6\% \pm 2.7\%$

Table 5.1 presents the results of this study, which are in basic agreement with the findings of the E89b thesis.† We take the first value from this table to define N^{E89a} for hydrogen. For deuterium we assume

$$\frac{N_p^{E89a}}{N_p^{E89b}} = \frac{N_d^{E89a}}{N_d^{E89b}} , \tag{5.14}$$

as experiments E89a and E89b were run simultaneously with the same target, and where the E89b normalizations are determined by the fit. We estimate a ±2% systematic uncertainty to account for expected differences between elastic and inelastic normalizations, and an additional ±.5% uncertainty for the extension to deuterium.

5.2.4 Normalization Results

The best fit normalization factors are presented in Table 5.2. Two uncertainties are quoted for each N^k, δ^{NM_1} which is correlated between experiments (for the same target) and δ^{NM_2} which is uncorrelated between experiments.

The uncertainty δ^{NM_1} includes the statistical uncertainties due to the uncertainties in the data, plus estimates of the model dependence of N^k. The normalization fits were repeated with several alternate models for both R and F_2, including, for example, the $F_2^{\Lambda_{12}}$ mode of Section 5.4.1. Model sensitivities in the N^k, typically ±.3%, are assumed to display the same correlations between experiments as the statistical uncertainties. The correlation matrices for δ^{NM_1}, are discussed below.

The uncertainty δ^{NM_2} includes estimates of the dependence of the N^k on the specific kinematic cuts applied to the data before fitting. For example, we cut the hydrogen data at $W^2 \geq 4$ for these normalization studies to avoid any possible problems due to resonances. Additionally, two other sources of uncorrelated error are included in this error term: the uncertainty in N^{E89a} as discussed in Section 5.2.3, and a presumed systematic uncertainty in N^{E87} as discussed below.

† Note that Figure IV-6 of the E89b thesis contains a mislabeled data point, giving the visual impression of a larger normalization difference.

Table 5.2. Shown are the normalization factors of early SLAC experiments to E140. Errors are explained in the text. The overall normalization uncertainty is ±2.1% for hydrogen, ±1.7% for deuterium, and ±1.0% for σ^d/σ^p.

	N	$\pm\delta^{NM_1}$	$\pm\delta^{NM_2}$
Hydrogen			
E49a	1.012	.005	.003
E49b	.981		
E61	1.011	.008	.004
E87	.982	.005	.011
E89a †	.989		.028
E89b	.953	.004	.004
Deuterium			
E49a	1.001	.006	.002
E49b	.981	.005	.002
E61	1.033	.007	.003
E87	.986	.004	.010
E89a †	.985	.005	.029
E89b	.949	.004	.001
E139	1.008	.004	.002
E140	1.000		
σ^d/σ^p			
E49a	.992	.005	.003
E49b	1.000		
E61	1.020	.005	.003
E87	1.013	.005	.010
E89a †	.995	.004	.005
E89b	.995	.004	.002

† See Section 5.4.4.

Since E140 measures only deuterium cross sections, we choose E49b as the anchor for normalization of the hydrogen data. By demanding that $N_p^{E49b} = N_d^{E49b}$, we use E49b to define a normalization *bridge* between E140 and the hydrogen data. While any other experiment might equally serve as the bridge, the −1.9% hydrogen offset

indicated by E49b deuterium data comes very close to minimizing the χ^2-like quantity

$$\sum_k \frac{\left(N_p^k - N_d^k\right)^2}{\left(\delta_p^{NM_1}\right)^2 + \left(\delta_d^{NM_1}\right)^2} \quad , \tag{5.15}$$

and is thus the best choice. We estimate the uncertainty due to this bridging technique to be $\pm 1.0\%$. Thus, the overall normalization uncertainty of the deuterium data is $\pm 1.7\%$ (see Table 3.2), that of the hydrogen data is $\pm 2.1\%$, and that of the deuterium/hydrogen cross section ratios is $\pm 1.0\%$.

We check the internal consistency of the normalization fitting procedure by comparing the ratio of N_d^k/N_p^k with the N_{dp}^k. Discrepancies of size $\pm .2\%$ are expected, and observed, with the single exception of E87. For this experiment, we obtain an difference of .9%, which is not explainable in terms of any known systematic effect. While such a difference could be caused by the presence of very large *anti*-correlated fluctuations in the E87 hydrogen and deuterium data, this possibility is ruled out on the basis of the excellent χ^2/df observed for the E87 data (see below). While not understanding the origin of the observed difference, we account for it by assigning an additional $\pm 1\%$ systematic uncertainty to the N_p, N_d, and N_{dp} of the E87 data.

The observed χ^2/df of the normalization fits are presented in Table 5.3. All experiments contribute a χ^2/df of roughly one, with the exceptions of E49a, E61, and E139. Experiments E49a and E61, as listed in TASI Dataset, display "overstated" statistical uncertainties. Published plots of these data,[44,42] with only statistical uncertainties, display too much regularity and not enough scatter. A concerted effort to identify the exact origin of this phenomenon was unsuccessful, and the effect is attributed to experimental conservatism. The small χ^2/df contribution of E139, on the other hand, reflects our conservative estimates of the systematic errors. For E139, $\delta^{SR} \approx \delta^{ST}$, and so the inclusion of δ^{SR} in Equation 5.10 reduces the χ^2 contribution by a factor of two.

Table 5.3. Shown is the χ^2 summary of the normalization fits. Anomalously small χ^2/df are observed for E49a and E61.

Experiment	χ^2/df Hydrogen	χ^2/df Deuterium	χ^2/df $[\sigma^d/\sigma^p]$
E49a	42 / 98	45 / 117	81 / 98
E49b	193 / 187	222 / 193	160 / 174
E61	4 / 25	4 / 31	21 / 24
E87	74 / 93	106 / 109	87 / 93
E89a	71 / 70	56 / 71	74 / 66
E89b	88 / 98	73 / 100	77 / 82
E139		15 / 32	
E140		41 / 48	
Total	476 / 552	564 / 680	500 / 524

The correlation matrices of the normalization fits offer additional insight into the quality of the information extracted. We observe no large off-diagonal elements of $\mathcal{M}$ indicative of a correlation between any normalization coefficient and a coefficient of $F_2^{\Omega_s}$ or R^{model}. This supports the earlier assertion that the normalization factors of display no model dependence beyond the $\pm.3\%$ level.

The correlations between the N^k are given by Table 5.4. Presented is the lower half of $\mathcal{M}_{ij}$, the lower right submatrix of the correlation matrix for each normalization fit. The matrix $\mathcal{M}_{ij}$ is related to the more familiar covariance matrix by Equation B.6. The degree of correlation between two experiments is proportional to the statistical impact of the data in the regions of overlap. The fact that all elements of $\mathcal{M}_{ij}$ are positive (as they must be) greatly reduces the propagation of the δ^{NM_1} through the regression analyses into R.

Table 5.5 presents a comparison of our normalization results with all previous studies of the relative normalizations. Included are normalization results based on the

Table 5.4. Shown are the normalization submatrices of the correlation matrices of the fits to Equations 5.3 and 5.11.

	$\mathcal{M}_{ij}$					
Hydrogen						
E49a	1.00					
E49b	.00	1.00				
E61	.43	.00	1.00			
E87	.36	.00	.23	1.00		
E89b	.52	.00	.36	.56	1.00	
Deuterium						
E49a	1.00					
E49b	.23	1.00				
E61	.35	.13	1.00			
E87	.25	.32	.13	1.00		
E89b	.37	.37	.25	.43	1.00	
E139	.30	.31	.16	.34	.37	1.00
σ^d/σ^p						
E49a	1.00					
E49b	.00	1.00				
E61	.56	.00	1.00			
E87	.32	.00	.24	1.00		
E89b	.51	.00	.46	.55	1.00	

first and third "miscellaneous" E140 cross sections in Table 3.3, which repeat earlier measurements by E49b and E87, respectively. Note the excellent agreement across the entire table. Note also that the extreme value we obtain for the normalization of E89b is firmly supported by each previous comparison, and is due in part from the normalization-like change in radiative corrections for E89b (see Figure 5.2).

We conclude that the relative normalizations reported in Table 5.2 are reasonable and internally consistent at the level of the quoted uncertainties. All subsequent usage of the measured cross sections presumes the application of these normalization correction factors.

Table 5.5. Presented is a comparison of our normalizaion results of Table 5.3 with other normalization studies. "I" denotes comparisons based on inelastic data, "E" denotes comparisons based on elastic data.

	Region	Ref.	Other Comparison	Table 5.2
Hydrogen				
E49b > E87	I	3	$1.0\% \pm 1.0\%$	$0.1\% \pm 1.2\%$
E49b > E87	E	3	$.6\% \pm .8\%$	
E49b > E49a	E	3	$1.9\% \pm 1.7\%$	$3.1\% \pm .6\%$
E89b > E87	I	35	5.5%	$2.9\% \pm 1.3\%$
E89b > E49b	I	35	3.0%	$2.8\% \pm .6\%$
E89b > E89a	E	35	5.0%	$3.6\% \pm 2.9\%$
E89b > E89a	E	†	$3.6\% \pm 2.7\%$	
E89b > E140	E	†	$4.5\% \pm 2.2\%$	$4.7\% \pm 1.1\%$
Deuterium				
E49b > E87	I	3	$1.0\% \pm .7\%$	$0.5\% \pm 1.2\%$
E49b > E140	I	‡	$2.4\% \pm 2.0\%$	$1.9\% \pm .5\%$
E89b > E140	I	‡	$6.2\% \pm 2.7\%$	$5.1\% \pm .4\%$

‡ Table 3.3, miscellaneous E140 measurement.
† Table 5.1.

5.2.5 *The "E89b Effect"*

Hindsight in a recursive analysis is as useful as foresight. At the end of the first cycle of Figure 5.1 we carefully examined all three sets of global data, looking for remnant uncorrected systematic effects. We examined residuals of the data to the final F_2 fit plotted versus E_o, E', θ, x, Q^2, ϵ, and W^2. A large systematic effect was identified for E89b hydrogen and deuterium, linearly proportional to E', as shown in Figure 5.3. The likely origin[83] of this effect is an applied correction[35] for the E' dependence of the 20 GeV Spectrometer acceptance, given by

$$\sigma^{final} = \sigma^{meas} \left[1 - .0089 \left(E' - \langle E' \rangle \right)\right] \tag{5.16}$$

(compare with Equation 2.4). The E' dependence of the $\langle\vartheta|x\rangle$ dispersion is directly measured[35] with a "jailbar" optics study to be $-.0028$ GeV^{-1}. The measurement[35] of the E' dependence of the $\langle\delta|y\rangle$ dispersion, however, is much less direct, relying on calculated elastic peak positions and simultaneously determined higher order optics matrix elements. Furthermore, these measurements display large scatter, and are consistent[83] with a much smaller E' dependence than the quoted $-.0061$ GeV^{-1}.

To treat this problem statistically, we performed a χ^2 minimization fit to Equation 5.3 with each N^{Expt} defined with an additional parameter linear in E'. Fits were made for hydrogen and deuterium simultaneously, forcing this E' dependence to be identical. The E' "slope" terms we obtained were largely uncorrelated between experiments.† We thus determine a best-fit counter-correction to Equation 5.16,

$$\sigma^{E89a} = \sigma^{final}\left[1 + \left(.0042 \pm .0006 \pm .0010\right)\left(E' - \langle E'\rangle\right)\right] , \qquad (5.17)$$

where the second error reflects an exhaustive study of possible systematic errors arising from kinematic cuts, F_2 model forms, and correlations across experiments.

Additionally, we became aware of significant effects in E49a and E49b, of size $-.0034$ GeV^{-1} and $-.0086$ GeV^{-1}, respectively. A careful review of the documentation of these experiments failed to clearly identify the source of these effects. Thus, for E49a and E49b we take a conservative stance and correct one half of the measured effect and assign an uncertainty to δ^{SE} equal to the size of our applied correction (see Table C.1). It is important to note that searches for similar "slopes" in the other kinematic variables were, in each case, statistically consistent with no effect.

After making these corrections, we began the entire analysis again from the beginning. The results presented in this chapter were yielded two full iterations (of Figure 5.1) later.

† In fact, we note that a fit to data from a single experiment alone is sufficient to quantify the presence of an E' slope. This is because we have *a prior* knowledge that F_2 is not linear in E' over a significant kinematic range, as reflected in our choices of functional forms for F_2 (see also Section 5.4.1).

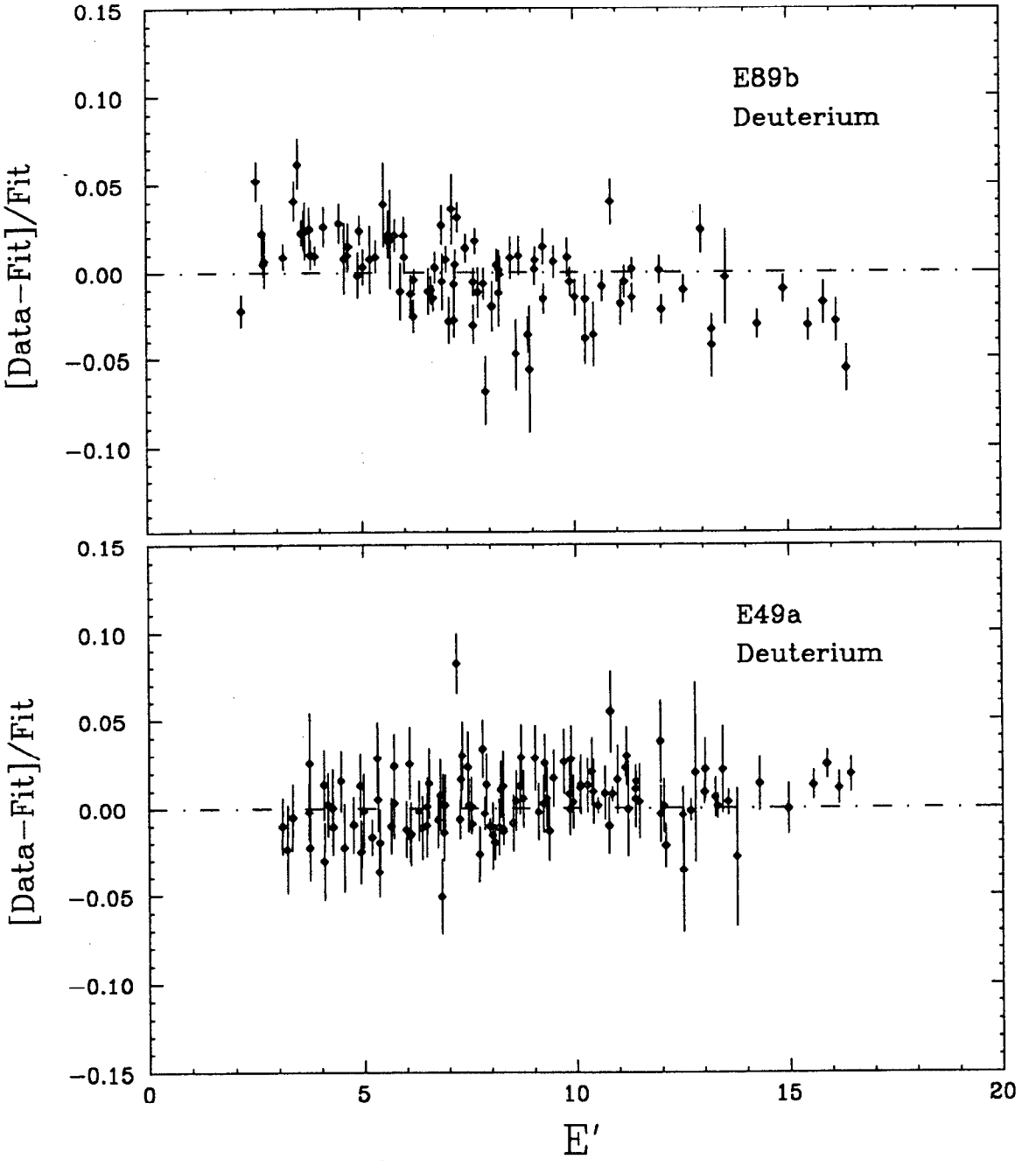

Figure 5.3. Shown are the residuals studies comparing the original E89b, E49a, and E49b data to the best fit cross section model to all eight experiments. E140 is presented as a basis for comparison and shows no statistically significant slope. The observed effects for hydrogen are identical. The error bars represent the total uncertainties, as denoted in Equation 5.10. Figure continues on next page.

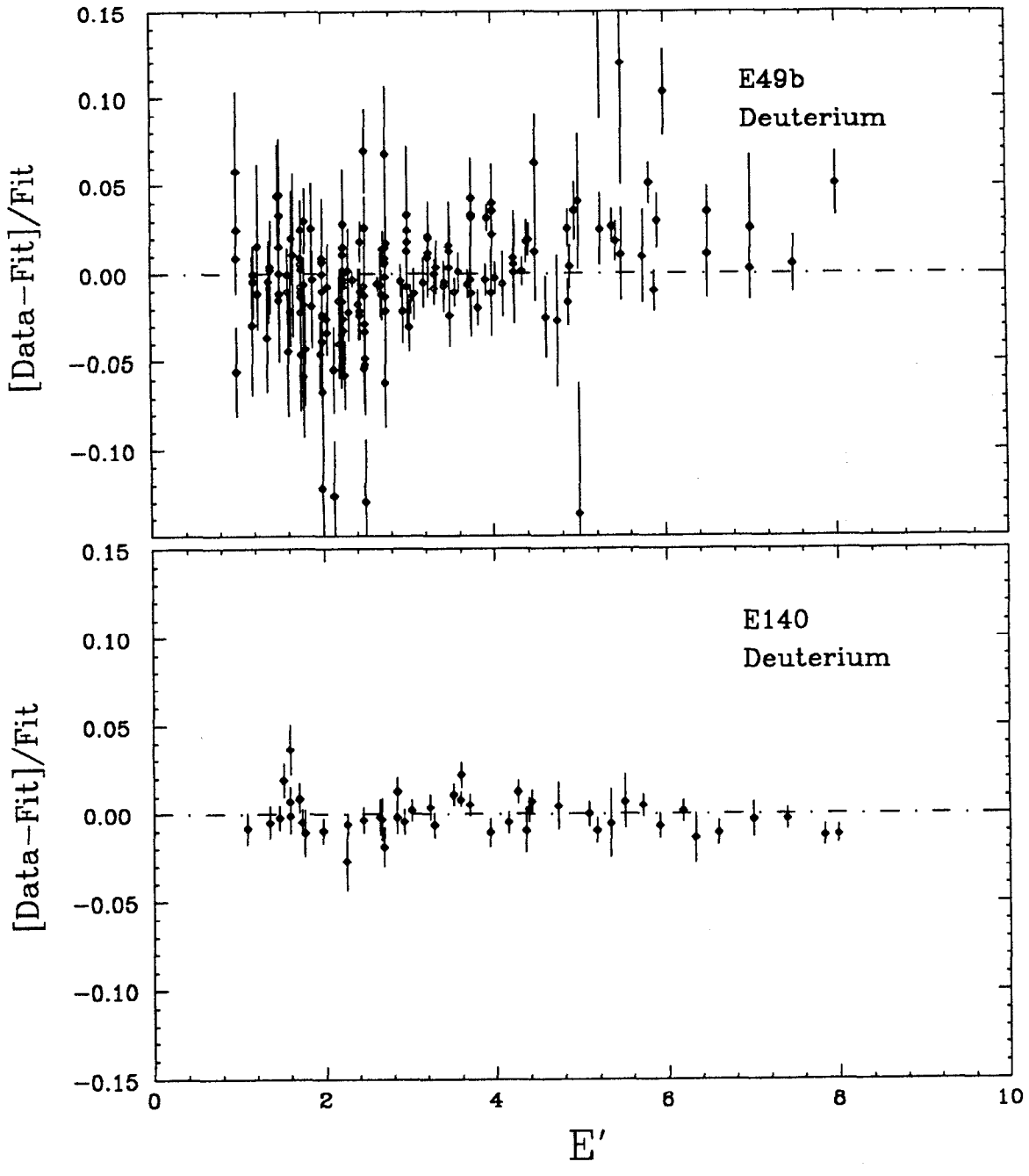

Figure 5.3/continued: Residuals studies of the "E89b effect."

5.3 R Extraction and Modeling

The set of normalized cross sections are binned in (x, Q^2). Rather than using the condensed cross sections of Section 5.2.1, we begin with the larger set of original measurements, and later condense with respect to ϵ inside each bin. A correction must be applied to each cross sections to effectively shift the measured (x, Q^2) to the center of the bin, $(x_\circ, Q^2_\circ)$. In simplest form, this is just the kinematic mismatch correction of Section 3.2.1, which implicitly assumes

$$\frac{\sigma^{meas}(x, Q^2, \epsilon)}{\sigma^{model}(x, Q^2, \epsilon)} = \frac{\sigma^{meas}(x_\circ, Q^2_\circ, \epsilon)}{\sigma^{model}(x_\circ, Q^2_\circ, \epsilon)} \tag{5.18}$$

Given the same assumption, it is easier in practice to use

$$\frac{\sigma^{meas}(x, Q^2, \epsilon)}{\sigma^{model}(x, Q^2, \epsilon)} = \frac{\sigma_T^{meas}(x_\circ, Q^2_\circ)}{\sigma_T^{model}(x_\circ, Q^2_\circ)} \left[1 + \epsilon' \widetilde{R}(x_\circ, Q^2_\circ)\right] , \tag{5.19}$$

where

$$\begin{aligned} \widetilde{R} &= R^{meas}(x_\circ, Q^2_\circ) - R^{model}(x_\circ, Q^2_\circ) , \\ \epsilon' &= \epsilon \Big/ \left[1 + \epsilon R^{model}(x_\circ, Q^2_\circ)\right] , \end{aligned} \tag{5.20}$$

which follows from Equations 4.11 and 4.12. Thus, for each (x, Q^2) bin, we apply a regression analysis to the set of ratios $\sigma^{meas}/\sigma^{model}$ versus ϵ to determine the $R^{meas}(x_\circ, Q^2_\circ)$.

A similar utility simplifies the extraction of $R^d - R^p$, namely

$$\frac{\sigma_d^{meas}(x, Q^2, \epsilon)/\sigma_d^{model}(x, Q^2, \epsilon)}{\sigma_p^{meas}(x, Q^2, \epsilon)/\sigma_p^{model}(x, Q^2, \epsilon)} =$$

$$\frac{\sigma_{dT}^{meas}(x_\circ, Q^2_\circ)/\sigma_{dT}^{model}(x_\circ, Q^2_\circ)}{\sigma_{pT}^{meas}(x_\circ, Q^2_\circ)/\sigma_{pT}^{model}(x_\circ, Q^2_\circ)} \left[1 + \epsilon'' \left[R^d(x_\circ, Q^2_\circ) - R^d(x_\circ, Q^2_\circ, \epsilon)\right]\right] , \tag{5.21}$$

where

$$\epsilon'' = \epsilon \Big/ \left[1 + \epsilon R^{1990}(x_\circ, Q^2_\circ)\right] , \tag{5.22}$$

and R^{1990} is a fit to the previously extracted R^p values. This reduction presumes that the deuterium and hydrogen cross section models are defined with identical models of R. See also the important procedural note in reference to Equations 4.11 and 4.12.

We condense the data with respect to ϵ before applying the regression analyses (see Section 5.2.1). The maximum span in ϵ over which we condense is $\Delta\epsilon = .05$. Following condensing, each (x, Q^2) bin typically contains four to eight values, representing three or four experiments, and spanning a width in ϵ of $\Delta\epsilon = .50$.

An advantage of the approach of Equations 5.19 and 5.21 is that we no longer work in tiny dimensional quantities, as in Figure 4.1, but rather, unit free quantities on the scale of 1. Figure 5.4 shows two such sample linear regression analyses for the deuterium data. Two additional regression analyses, ones which do not yield such good χ^2/df, are presented in Appendix B.3.

Because E140 measures R to high accuracy by itself, we do not include the E140 cross sections in the combined global extraction of R. Rather, the E140 R extractions are reserved as an independent set of ideal (single experiment) measurements for comparison with the results of the global study.

5.3.1 Error Propagation

The δ^{ST} and δ^{SR} uncertainties in the cross section measurements are propagated through the weights of the regression analysis (given by Equation 4.2) into the δR^{ST} uncertianty in R. The other components of the error vector are propagated by directly measuring the perturbation in R due to each type of error in each experiment. We extend the formalism of Equations 4.3 and 4.4 to account for multiple experiments:

- Let $\{\sigma_j\}$ represent a set of data in a single (x, Q^2) bin.
- Let the experiment from which the datum σ_j originates be represented by E_j.
- Let $\xi^{E_i E_j}$ be a Kronecker-like delta function defined on the set of experiments by

$$\xi^{E_i E_j} = \begin{cases} 1, & \text{for } E_i = E_j \ ; \\ 0, & \text{otherwise} \ . \end{cases} \tag{5.23}$$

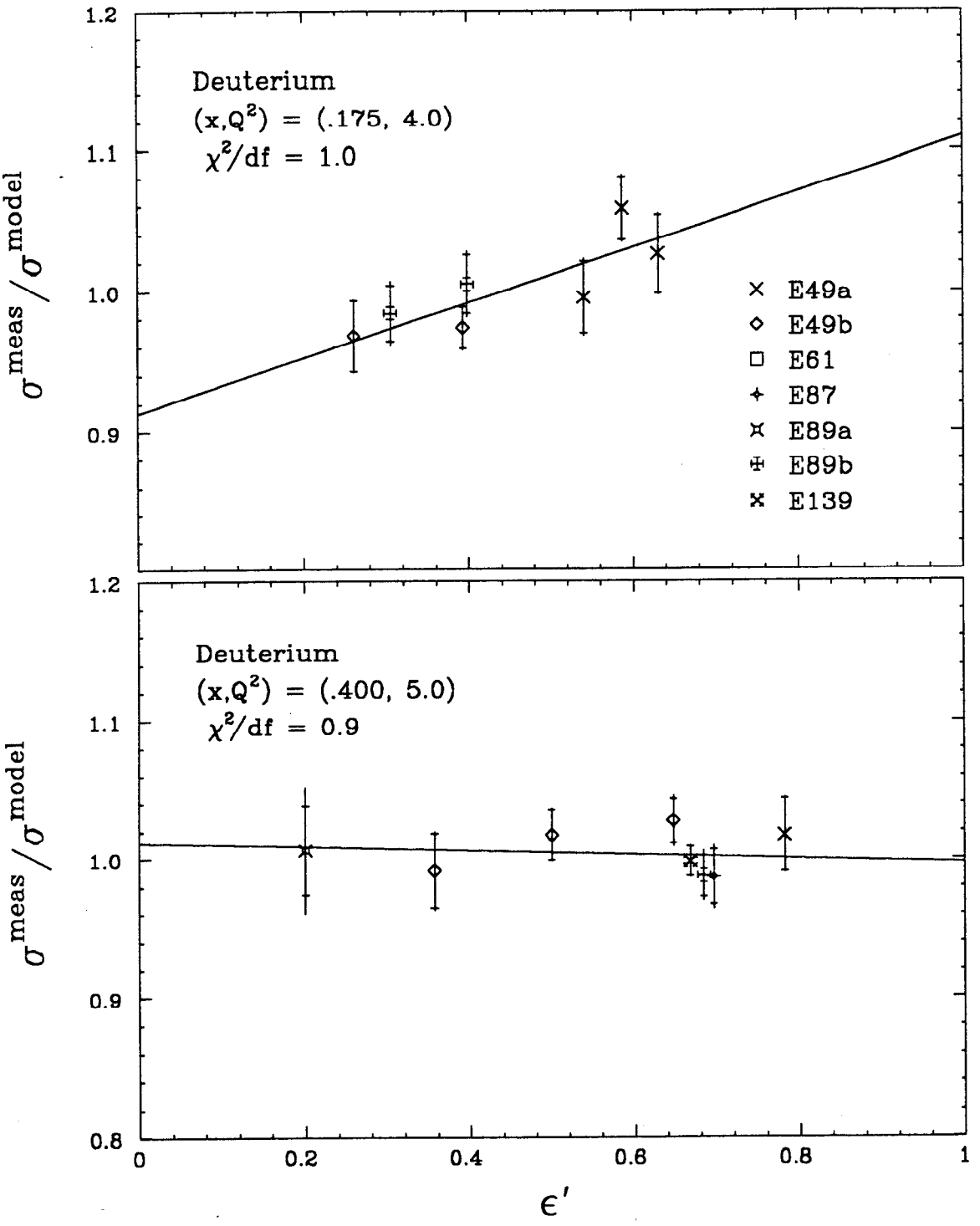

Figure 5.4. Shown are two sample regression analyses. The full error bar represents the total error, given by the quadrature sum of δ^{ST}, δ^{SR},δ^{SY}, δ^{SE}, δ^{NM_1}, and δ^{NM_2}. The hashmark represents the random component of the total error, given by the quadrature sum of δ^{ST} and δ^{SR}.

- Define an operator "LR" as in Equation 4.3.

Then, the uncertainty in R due to experiment E_i is given by

$$\delta R^k_{E_i} = R - \mathrm{LR}\{\sigma_j(1+\xi^{E_i E_j}\delta^k_i)\} \ , \qquad k = SY,\ SE,\ NM_1,\ NM_2 \ . \tag{5.24}$$

These uncertainties are correlated over the E_i for $k = NM_1$, but otherwise uncorrelated. Thus,

$$\delta R^k = \left[\sum_i \left(\delta R^k_{E_i}\right)^2\right]^{1/2} , \qquad k = SY,\ SE,\ NM_2 \ , \tag{5.25}$$

and

$$\delta R^k = \left[\sum_{i,j} \delta R^k_{E_i} \times \mathcal{M}_{ij} \times \delta R^k_{E_j}\right]^{1/2} , \qquad k = NM_1 \ , \tag{5.26}$$

where $\mathcal{M}$ is given in Table 5.4. Note that for uncorrelated errors, $\mathcal{M} = \mathbf{1}$, and Equation 5.26 reduces to Equation 5.25. Uncertainties of type δR^{RC} are calculated in this way, yielding Equation 4.5.

For the first regression analysis of Figure 5.4 we obtain

$$\begin{aligned} R &= .381 \ , \\ \left.\begin{aligned} \delta R^{ST} &= .082 \ , \\ \delta R^{SY} &= .026 \ , \\ \delta R^{SE} &= .024 \ , \\ \delta R^{NM_1} &= .024 \ , \\ \delta R^{NM_2} &= .008 \ , \\ \delta R^{RC} &= .025 \ , \end{aligned}\right\} \quad \delta R^{SS} &= .044 \ , \end{aligned} \tag{5.27}$$

where δR^{SS} is the total experimental systematic error.

The 260 linear regression analyses form a set of linearity measurements versus ϵ. As discussed in Section 4.1, uncorrected systematic effects in the data would contribute, in general, curvature to the regression analyses. Figure 5.5 presents the distribution of observed χ^2/df of the regressions. The curves shown are the expected χ^2/df distributions for the average number of 3.63 uncorrelated measurements gaussian-distributed about a parent distribution.

There is generally good agreement in Figure 5.5 between the observed and expected χ^2/df. The observed distributions are shifted towards zero relative of the theoretical distributions due to the inclusion of δ^{SR} in the regression weights. Using the additive property of χ^2 distributions, we calculate the total χ^2/df for each set of analyses,

$$\begin{aligned} \langle \chi^2/df \rangle_p &= 299.6 \,/\, 332 \ , \\ \langle \chi^2/df \rangle_d &= 300.2 \,/\, 325 \ , \\ \langle \chi^2/df \rangle_{dp} &= 298.0 \,/\, 300 \ , \end{aligned} \tag{5.28}$$

each soundly in the center of the expected distribution. That the fits to σ^d/σ^p display slightly more scatter is to be expected from Table 5.3, and is because the δ^{SR} errors for σ^d/σ^p are much smaller than those for hydrogen and deuterium.

Both the shape and area of the observed χ^2/df distributions are in excellent agreement with the theoretical distributions. This confirms our claim that the δ^{ST} and δ^{SR} uncertainties in the data are gaussian with correctly estimated magnitudes. Regression analyses with χ^2/df as large as 3.1 are statistically expected and require no further treatment.† Six of the regression studies, however, yield anomalously large χ^2/df values, well outside the expected distribution. For these six analyses, we adopt the conservative approach[74–76] and multiply δR^{ST} by the factor $\sqrt{\chi^2/df}$ (see Appendix B.3).

† Some sources[74–76] claim that the uncertainty on any parameter determined via a fitting procedure should be multiplied by a factor of $\sqrt{\chi^2/df}$. We address this wayward assertion in Appendix B.3 with a monte carlo analysis of the R extractions.

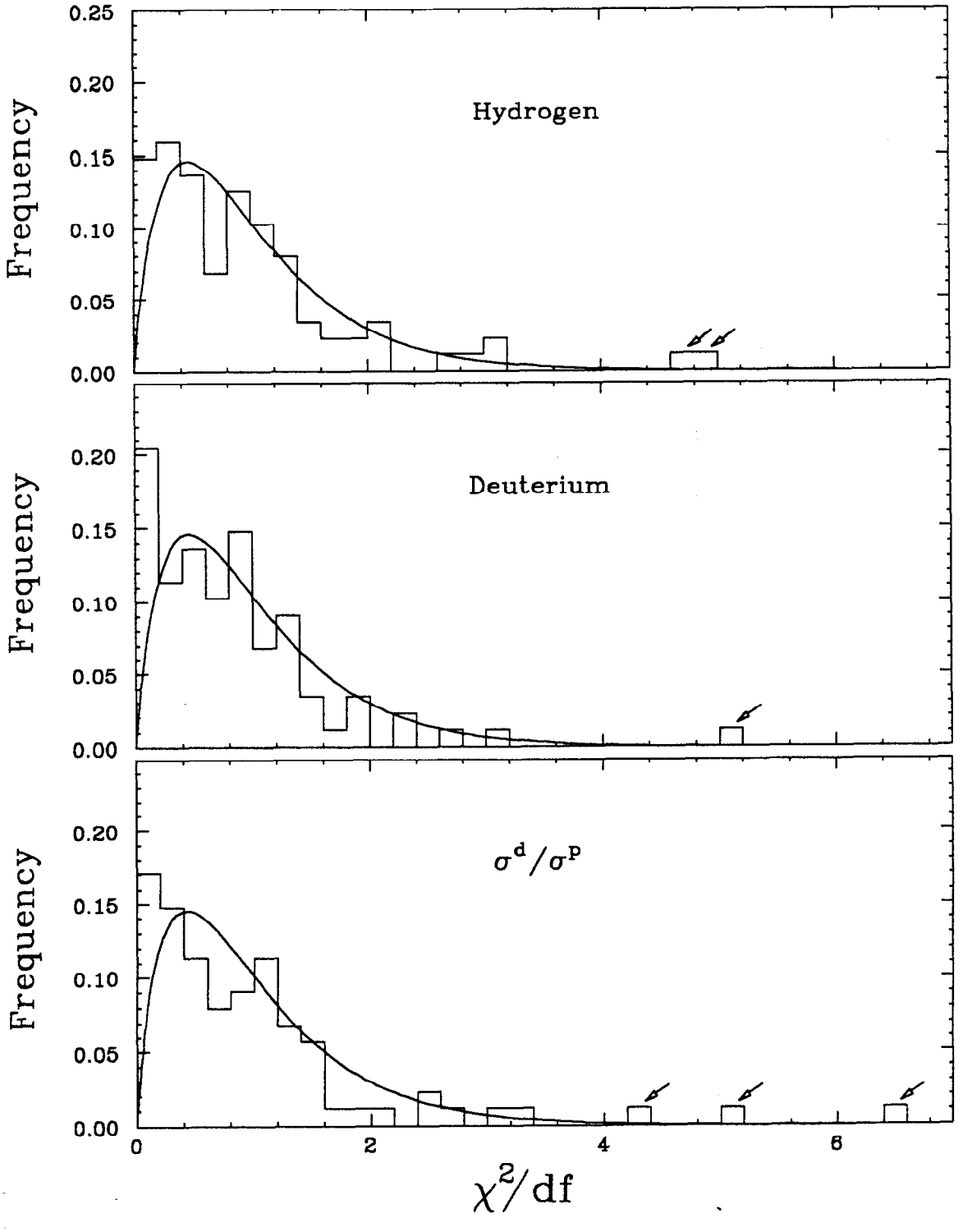

Figure 5.5. Shown is the distribution of observed χ^2/df for each of the three sets of regression analyses. The curves are the expected χ^2/df distributions for 3.63 degrees of freedom, assuming that all errors are gaussian and uncorrelated. The arrows indicate outlying points which receive special treatment, as described in the text.

The observed linearity of these regression analyses greatly credits the experimental efforts of the SGA, MIT, and E139 collaborations. The somewhat small $\langle \chi^2/df \rangle$ reflects both the conservative estimate of the systematic errors δ^{SR}, and the "conservative" published statistical uncertainties of E49a and E61. Statistically, the data are not consistent with the hypothesis that large systematic effects remain uncorrected in the cross sections including large errors in the relative normalizations of these seven experiments.

5.3.2 Deuterium/Hydrogen Difference

Table 5.6 presents the results of the σ^d/σ^p linear regression analyses. The results are consistent with the hypothesis that there is no Q^2 dependence to $R^d - R^p$. Thus, we average the results over Q^2 to look for x dependence. These results are shown in Table 5.7. The careful propagation of the δ^{NM_1} and δ^{NM_2} through the averaging process is critical. By returning to the fundamental uncertainty contributions of Equation 5.24, we obtain smaller, more accurate estimates of the normalization uncertainties in $\langle R^d - R^p \rangle$. At fixed x, a normalization shift to a particular experiment would contribute positively to R^d–R^p at some Q^2, and negatively at others. Thus, the careful propagation of these correlated opposite uncertainties yields the much smaller systematic uncertainties shown in Table 5.7.

The χ^2/df for the averages shown in Table 5.7 are consistent with our assumption of Q^2 independence. These values of $\langle R^d - R^p \rangle$ are plotted versus x in Figure 5.6. No x dependence is observed, and $R^d - R^p$ is consistent with zero. The average over (x, Q^2) is similarly calculated,

$$\begin{aligned} \langle R^d - R^p \rangle &= -.001 \pm .009 \pm .008 \pm .005 \ , \\ \chi^2/df &= 83.4/85 \ , \end{aligned} \tag{5.29}$$

where the uncertainties are of type δR^{ST}, δR^{NM_1}, and δR^{NM_2}, respectively. While very little scatter is evidenced in Figure 5.6, the overall average, calculated directly from Table 5.6, is in agreement with statistical expectations.

Table 5.6. Shown are the global extractions of $R^d - R^p$. Uncertainties are absolute. Uncertainties of type δR^{SY} δR^{SE}, and δR^{RC} are negligible. Table continues on next two pages.

x	Q^2	$R^d - R^p$	$\pm\delta R^{ST}$	$\pm\delta R^{NM_1}$	$\pm\delta R^{NM_2}$	χ^2/df
.100	0.63	.119	.075	.021	.012	.5
.100	0.80	.039	.170	.038	.025	.3
.100	1.00	−.078	.070	.016	.010	.2
.100	1.25	−.169	.086	.021	.015	.8
.100	1.60	.046	.072	.006	.004	.3
.100	2.00	.005	.055	.008	.004	.1
.100	2.50	−.026	.149	.021	.013	1.4
.100	3.20	−.043	.168	.017	.011	2.7
.175	0.80	−.143	.079	.024	.016	.2
.175	1.00	.076	.057	.014	.007	.5
.175	1.25	−.048	.050	.017	.009	.1
.175	1.60	−.045	.062	.019	.009	.1
.175	2.00	.020	.063	.008	.004	.5
.175	2.50	−.025	.045	.008	.004	.3
.175	3.20	−.103	.108	.015	.011	.9
.175	4.00	.160	.083	.015	.012	.9
.250	1.00	.038	.082	.037	.016	1.3
.250	1.25	−.139	.076	.016	.008	–
.250	1.60	.015	.047	.015	.008	.8
.250	2.00	−.050	.076	.010	.005	1.6
.250	2.50	−.044	.076	.010	.005	1.1
.250	3.20	−.012	.045	.008	.004	.8
.250	4.00	.189	.106	.016	.010	1.0
.250	5.00	.045	.080	.012	.007	.3
.250	6.40	−.381	.250	.019	.010	.3
.250	8.00	−.225	.399	.024	.013	–
.325	1.00	.036	.122	.044	.019	.2
.325	1.25	−.171	.106	.048	.022	.9
.325	1.60	.099	.105	.018	.008	1.4
.325	2.00	.074	.178	.014	.009	6.9
.325	2.50	.040	.079	.011	.007	1.0

Table 5.6/continued: Global extractions of $R^d - R^p$.

x	Q^2	$R^d - R^p$	$\pm\delta R^{ST}$	$\pm\delta R^{NM_1}$	$\pm\delta R^{NM_2}$	χ^2/df
.325	3.20	−.013	.113	.011	.005	.5
.325	4.00	.100	.068	.009	.006	1.5
.325	5.00	.095	.069	.014	.007	1.3
.325	6.40	−.096	.097	.012	.008	1.3
.325	8.00	.000	.120	.019	.040	.6
.325	10.00	.162	.226	.020	.011	–
.400	2.00	−.151	.258	.001	.001	5.3
.400	2.50	.020	.128	.027	.022	.2
.400	3.20	−.006	.057	.010	.005	1.9
.400	4.00	.129	.078	.010	.008	2.2
.400	5.00	.053	.065	.009	.008	1.6
.400	6.40	.120	.088	.011	.016	1.1
.400	8.00	−.078	.074	.011	.011	.6
.400	10.00	.000	.089	.009	.007	1.2
.400	12.50	−.358	.470	.013	.032	5.6
.475	2.00	−.326	.204	.021	.013	–
.475	2.50	.025	.092	.020	.015	2.2
.475	3.20	−.108	.082	.009	.004	.2
.475	4.00	.233	.164	.017	.012	.0
.475	5.00	−.016	.071	.007	.012	.5
.475	6.40	.006	.100	.014	.011	2.3
.475	8.00	.163	.138	.013	.029	1.0
.475	10.00	−.036	.079	.008	.017	1.6
.475	12.50	.006	.113	.012	.027	.4
.550	2.50	−.175	.110	.020	.015	2.6
.550	4.00	−.095	.113	.016	.031	.4
.550	5.00	−.184	.189	.018	.015	1.3
.550	6.40	.055	.055	.008	.010	.1
.550	8.00	.013	.068	.007	.009	1.1
.550	10.00	−.041	.067	.004	.006	.7
.550	12.50	.035	.090	.005	.006	.7
.550	16.00	−.062	.150	.010	.025	.2

Table 5.6/continued: Global extractions of $R^d - R^p$.

x	Q^2	$R^d - R^p$	$\pm\delta R^{ST}$	$\pm\delta R^{NM_1}$	$\pm\delta R^{NM_2}$	χ^2/df
.625	5.00	−.097	.425	.033	.027	.0
.625	6.40	.014	.034	.006	.010	.6
.625	8.00	.140	.086	.007	.016	.4
.625	10.00	−.066	.063	.008	.018	1.0
.625	12.50	−.102	.059	.007	.015	.9
.625	16.00	−.096	.088	.010	.024	1.3
.700	4.00	−.057	.233	.018	.040	−
.700	6.40	.030	.042	.006	.010	1.2
.700	8.00	.063	.063	.006	.010	1.5
.700	10.00	−.055	.097	.011	.026	.4
.700	12.50	.081	.056	.005	.008	.6
.700	16.00	−.106	.070	.005	.009	.7
.700	20.00	−.290	.209	.012	.031	.3
.775	6.40	−.189	.264	.012	.029	3.3
.775	8.00	.047	.052	.007	.013	.4
.775	10.00	−.033	.105	.009	.021	.7
.775	12.50	−.036	.073	.006	.010	1.2
.775	16.00	−.071	.077	.005	.008	1.1
.775	20.00	.034	.101	.008	.015	.3
.860	10.00	−.007	.484	.023	.061	−
.860	12.50	−.065	.180	.007	.011	3.5
.860	16.00	−.232	.145	.005	.009	.9
.860	20.00	−.126	.094	.008	.016	.8

The 1979 results of Bodek *et al.*,[??] shown in Figure ?.? and summarized by Equation ?.? are inconclusive because of their large errors. Our improved statistical uncertainty is due to the inclusion of more data, while our improved systematic uncertainty originates in our advanced methodology, primarily the determination of the relative normalizations and the correct propagation of their uncertainties. We conclude, then, that $R^d = R^p$ within our total experimental error of $\pm.013$.

Table 5.7. Shown are the global extractions of $R^d - R^p$ averaged over Q^2. Uncertainties are absolute. Uncertainties of type δR^{SY}, δR^{SE}, and δR^{RC} are negligible. Values of χ^2/df are for the averages.

x	$\langle Q^2 \rangle$	$\langle R^d - R^p \rangle$	$\pm\delta R^{ST}$	$\pm\delta R^{NM_1}$	$\pm\delta R^{NM_2}$	χ^2/df
.100	1.47	−.005	.029	.011	.005	1.1
.175	1.90	−.010	.022	.012	.005	1.6
.250	2.53	−.008	.023	.012	.005	1.1
.325	3.87	.036	.030	.015	.006	.8
.400	5.34	.026	.029	.009	.006	.8
.475	6.16	−.009	.033	.010	.011	1.0
.550	8.04	−.011	.030	.007	.006	.8
.625	8.70	−.016	.024	.005	.007	1.6
.700	9.59	.017	.026	.005	.008	1.2
.775	11.72	−.005	.033	.005	.008	.5
.860	17.60	−.139	.072	.006	.011	.2

5.3.3 Hydrogen and Deuterium Results

The individual results of the hydrogen and deuterium regression analyses are tabled in Appendix E. In this section, we exploit the result from the previous section and report the average of R^p and R^d. Because the error vectors of R^p and R^d are partially correlated, in most applications it is required to use the average of R^p and R^d and the correctly propagated error vector. Further, we denote the values of R reported here as "SLAC" values to distinguish them from the independent "E140" values presented in Chapter 4.

We average the R^p and R^d values using the logarithmic variable of Appendix B.2 to account for the askew probability distribution of R. We conservatively assume that the δR^{SY}, δR^{SE} and δR^{RC} errors are perfectly correlated between targets, while the δR^{NM_1} and δR^{NM_2} errors are uncorrelated (with the exception of $\delta^{NM_2}_{E89a}$ which is perfectly correlated). We make the simplifying assumption that the δR^{ST} are uncorrelated, though, some correlated elements enter through the δ^{SR} in the definition

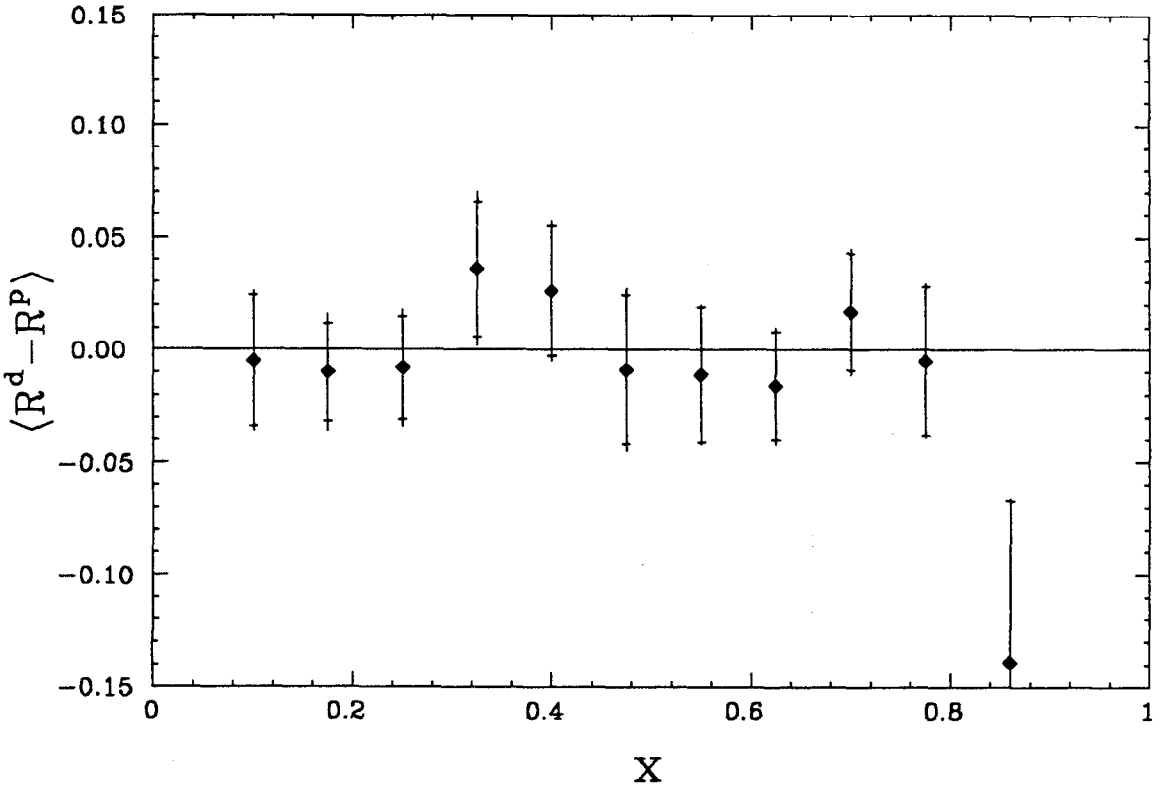

Figure 5.6. Shown are the extractions of $R^d - R^p$ averaged over Q^2, from Table 5.7. Compare with Figure 1.3 and note change of scale.

of the weights (for example, beam charge fluctuations). To correctly account for these correlations we average Equation 5.24 over targets before proceeding to Equations 5.25 and 5.26.

The total χ^2/df for all the averagings is

$$\langle \chi^2/df \rangle = 67.2/89 \ , \tag{5.30}$$

and a comparison of the individual R^p and R^d values reveal no large contradictions. Of the three outliers in Figure 5.5, the deuterium and one of the hydrogen outliers occur at the same kinematic, $(x, Q^2) = (.5, 2.5)$. The hydrogen and deuterium regression analyses at this kinematic, however, do not show similar features, indicating that the large observed χ^2's do not originate in a correlated spurious effect.

These extracted values of R are presented in Table 5.8 and plotted versus x and Q^2 in Figures 5.7 and 5.8. The E140 results from Table 4.6 are also included in these plots, as are the high-Q^2 values from the EMC,[9,21] BCDMS,[16,17] and CDHSW[18] collaborations.† Those measurements from EMC have been condensed in x and Q^2 and averaged over targets to reduce scatter. Also shown in Figures 5.7 and 5.8 are calculations[29] of R based on QCD[7] and QCD+TM.[8] The bold curve is the best fit model, R^{1990}, discussed in the next section.

Good agreement is observed between the SLAC and E140 measurements of R. In particular, we observe some disagreement associated with the E140 values at $(x, Q^2) = (.2, 1.5)$ and $(.2, 2.5)$, which are noted in connection with the large χ^2's of Equations 4.14 and 4.16 (see also Figure 4.3). Given the large scatter of the SLAC data in this region, we cannot make a conclusive comparison, though, we note that despite the relatively small uncertainties in the E140 data, the large number of SLAC measurements in this low-x region statistically dominates the local average as represented (presumably) by the best fit curve, R^{1990}.

We observe that the measured R values are systematically higher than $R^{\mathrm{QCD+TM}}$. Of the 89 SLAC and 11 E140 measurements, only 17 are smaller than $R^{\mathrm{QCD+TM}}$, and none by more than a standard deviation. This is a strong indication that QCD+TM is an inadequate theory in the SLAC kinematic range. In particular, we interpret this discrepancy as evidence of higher twist contributions to F_L, which are expected to be positive at the next order. A phenomenological analysis[84] of this twist four contribution to R finds excellent agreement with our preliminary SLAC deuterium results.[85] The R calculations of this study ($R^{\tau-4}$) though limited to $Q^2 > 4\mathrm{GeV}^2$, are in good agreement with our best fit model, within the theoretical limitations imposed by the parton distribution uncertainties. In Table 5.9 we present a goodness-of-fit comparison of these calculations to the data presented in Figures 5.7 and 5.8.

† For convenience and completeness, a table of these "world" values, as plotted in Figures 5.7 and 5.8, is presented in Appendix E.

Table 5.8. Shown are the global extractions of $R(x, Q^2)$ averaged over hydrogen and deuterium. The uncertainty δR^{SS} is the total experimental systematic uncertainty, and is the quadrature sum of the four uncertainties at the right. The uncertainty due to radiative corrections is $\delta R^{RC} = \pm.025$ and is correlated across all data (for $Q^2 < 1$ GeV^2, δR^{RC} is increased by a factor of 1.5, see Section 5.1). Table continues on next two pages.

x	Q^2	R	$\pm\delta R^{ST}$	$\pm\delta R^{SS}$	δR^{SY}	δR^{SE}	δR^{NM_1}	δR^{NM_2}
.100	.63	.256	.059	.044	.022	.034	.016	.007
.100	.80	.210	.123	.081	.071	.022	.028	.017
.100	1.00	.326	.047	.030	.015	.022	.012	.005
.100	1.25	.313	.058	.022	.011	.017	.009	.004
.100	1.60	.351	.041	.022	.013	.017	.006	.003
.100	2.00	.285	.034	.018	.008	.014	.006	.003
.100	2.50	.447	.101	.072	.041	.056	.018	.008
.100	3.20	.434	.108	.058	.033	.045	.016	.006
.175	.80	.291	.094	.045	.018	.036	.019	.008
.175	1.00	.240	.041	.031	.012	.026	.011	.004
.175	1.25	.463	.064	.031	.018	.017	.017	.007
.175	1.60	.364	.054	.028	.016	.019	.013	.005
.175	2.00	.275	.038	.023	.012	.018	.008	.004
.175	2.50	.235	.034	.019	.008	.015	.007	.003
.175	3.20	.374	.077	.043	.029	.027	.014	.006
.175	4.00	.297	.055	.029	.018	.019	.011	.004
.175	5.00	.432	.157	.057	.040	.029	.027	.012
.250	1.00	.196	.091	.054	.030	.032	.030	.011
.250	1.25	.308	.062	.036	.016	.027	.017	.007
.250	1.60	.246	.039	.026	.010	.022	.010	.004
.250	2.00	.281	.049	.025	.011	.020	.008	.004
.250	2.50	.213	.046	.024	.013	.017	.009	.004
.250	3.20	.215	.035	.020	.009	.015	.008	.003
.250	4.00	.085	.063	.023	.013	.010	.014	.006
.250	5.00	.115	.041	.036	.033	.009	.008	.005
.250	6.40	.441	.177	.058	.030	.047	.016	.010
.250	8.00	.337	.235	.057	.035	.038	.022	.011

Table 5.8/continued: Global extracted R.

x	Q^2	R	$\pm\delta R^{ST}$	$\pm\delta R^{SS}$	δR^{SY}	δR^{SE}	δR^{NM_1}	δR^{NM_2}
.325	1.00	.285	.133	.067	.040	.035	.038	.015
.325	1.25	.569	.218	.108	.071	.045	.063	.025
.325	1.60	.300	.072	.036	.017	.028	.014	.006
.325	2.00	.205	.049	.028	.011	.024	.009	.004
.325	2.50	.214	.048	.024	.013	.018	.010	.004
.325	3.20	.193	.058	.029	.015	.021	.010	.006
.325	4.00	.148	.042	.037	.024	.017	.005	.022
.325	5.00	.121	.040	.020	.017	.007	.007	.003
.325	6.40	.026	.043	.016	.012	.005	.008	.006
.325	8.00	.162	.073	.035	.017	.010	.014	.026
.325	10.00	.348	.128	.031	.020	.013	.017	.009
.400	2.00	.276	.080	.041	.011	.036	.014	.007
.400	2.50	.383	.141	.081	.020	.075	.021	.009
.400	3.20	.212	.041	.029	.012	.025	.009	.004
.400	4.00	.093	.047	.038	.024	.008	.007	.028
.400	5.00	.036	.032	.041	.024	.008	.005	.031
.400	6.40	.024	.038	.013	.007	.006	.008	.006
.400	8.00	.098	.043	.028	.023	.007	.010	.010
.400	10.00	.109	.048	.031	.024	.004	.008	.017
.400	12.50	−.119	.096	.140	.123	.004	.010	.066
.475	2.00	.239	.168	.069	.043	.046	.027	.010
.475	2.50	.149	.059	.028	.011	.023	.009	.004
.475	3.20	.147	.046	.028	.010	.024	.008	.003
.475	4.00	.114	.102	.028	.017	.004	.017	.013
.475	5.00	.096	.033	.041	.018	.008	.005	.035
.475	6.40	.120	.060	.018	.009	.009	.010	.006
.475	8.00	.005	.067	.027	.015	.004	.010	.020
.475	10.00	.050	.041	.029	.015	.007	.006	.023
.475	12.50	.132	.066	.067	.049	.001	.009	.045
.550	2.50	.192	.170	.031	.012	.025	.011	.004
.550	4.00	.094	.061	.032	.014	.014	.013	.021

Table 5.8/continued: Global extracted R.

x	Q^2	R	$\pm\delta R^{ST}$	$\pm\delta R^{SS}$	δR^{SY}	δR^{SE}	δR^{NM_1}	δR^{NM_2}
.550	5.00	.039	.090	.044	.024	.009	.010	.035
.550	6.40	.036	.030	.042	.018	.004	.004	.037
.550	8.00	.096	.037	.015	.011	.007	.005	.007
.550	10.00	.053	.037	.038	.025	.004	.002	.029
.550	12.50	.004	.044	.058	.041	.002	.004	.041
.550	16.00	.205	.091	.086	.060	.003	.008	.060
.625	4.00	.643	.646	.256	.087	.208	.098	.070
.625	5.00	.161	.254	.102	.064	.069	.035	.015
.625	6.40	.093	.027	.049	.019	.003	.004	.045
.625	8.00	.058	.046	.017	.009	.008	.005	.011
.625	10.00	.068	.039	.044	.019	.004	.005	.039
.625	12.50	.008	.034	.029	.020	.010	.004	.018
.625	16.00	−.044	.042	.065	.040	.003	.007	.051
.700	4.00	.161	.147	.047	.016	.021	.017	.035
.700	5.00	.178	.171	.009	.003	.004	.007	.003
.700	6.40	.078	.031	.045	.015	.004	.004	.042
.700	8.00	.123	.041	.048	.016	.004	.004	.045
.700	10.00	.087	.061	.027	.020	.004	.007	.016
.700	12.50	.072	.038	.033	.012	.008	.002	.030
.700	16.00	.054	.043	.046	.022	.002	.003	.040
.700	20.00	.175	.118	.133	.105	.001	.011	.081
.775	6.40	.018	.140	.034	.012	.020	.010	.022
.775	8.00	.077	.036	.047	.015	.003	.005	.045
.775	10.00	.109	.072	.018	.010	.004	.006	.013
.775	12.50	.037	.044	.040	.012	.009	.003	.037
.775	16.00	.153	.055	.047	.021	.002	.003	.042
.775	20.00	.047	.061	.080	.055	.004	.005	.058
.860	10.00	.476	.406	.074	.049	.017	.021	.049
.860	12.50	.262	.117	.052	.019	.004	.003	.049
.860	16.00	.041	.090	.051	.017	.003	.005	.048
.860	20.00	.082	.064	.057	.019	.004	.005	.053

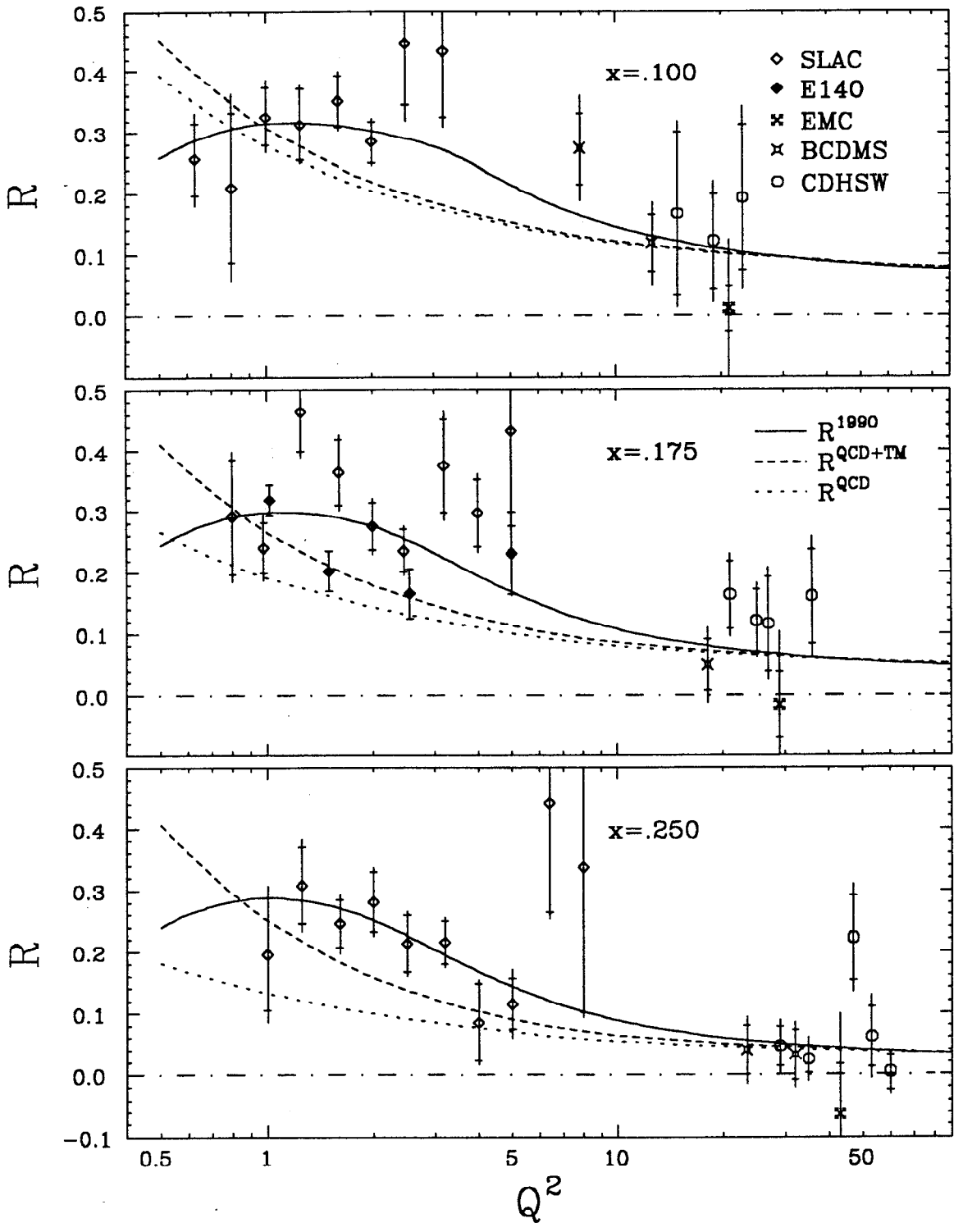

Figure 5.7. Shown are the global extractions of R from Table 5.8. Errors do not include the strongly correlated $\delta R^{RC} \approx .025$. See text for further details. Figure continues on next three pages.

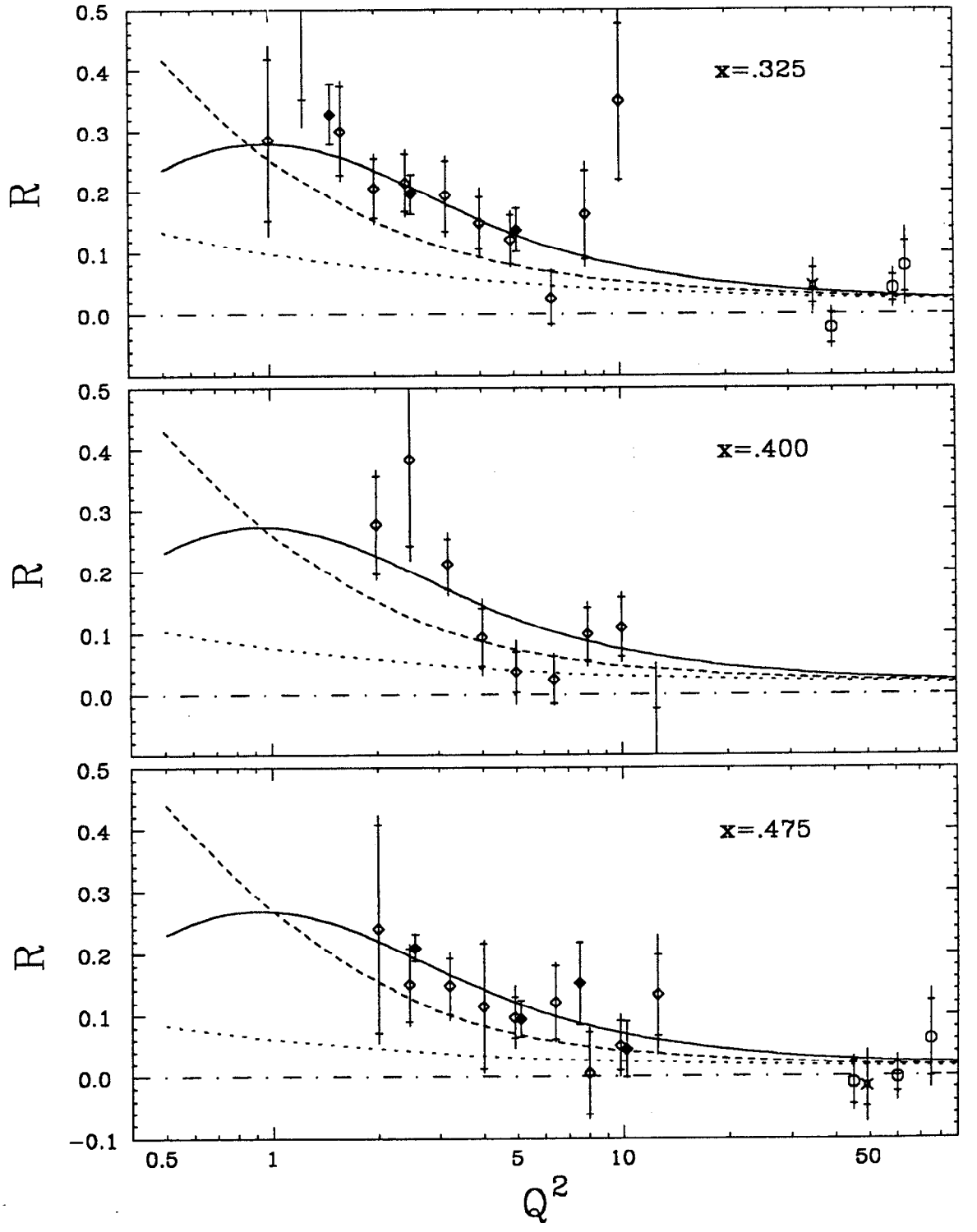

Figure 5.7/continued: Global extractions of $R(x, Q^2)$.

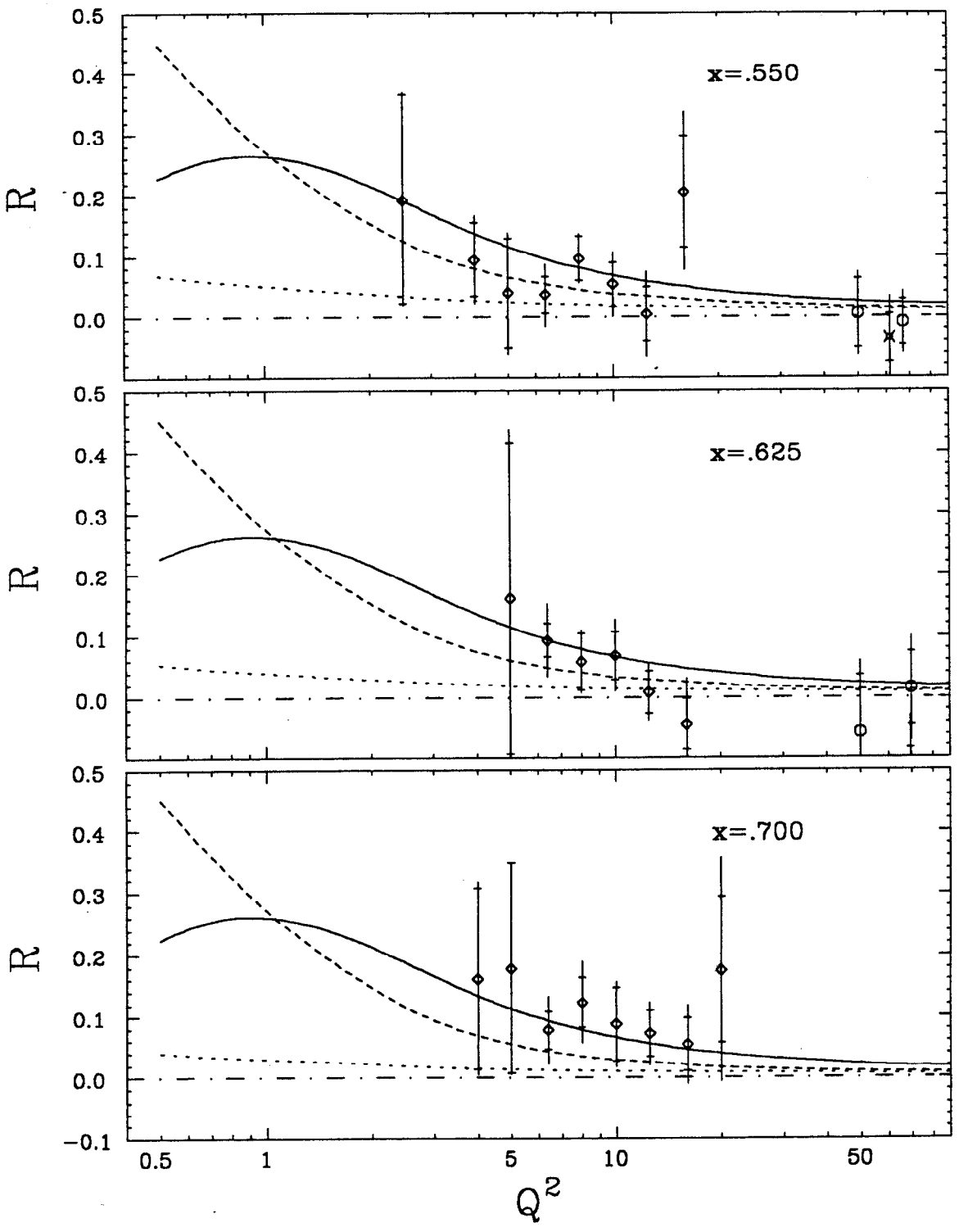

Figure 5.7/continued: Global extractions of $R(x, Q^2)$.

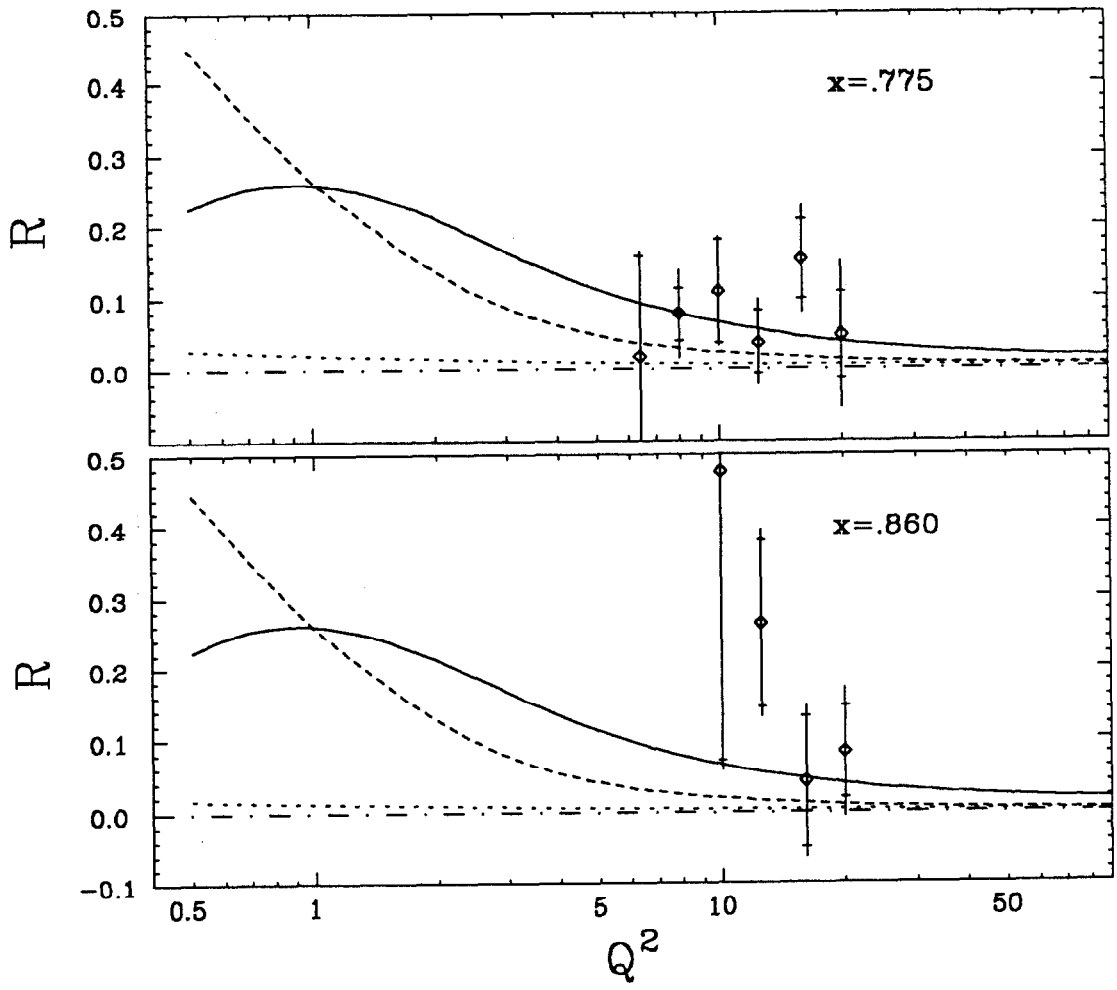

Figure 5.7/continued: Global extractions of $R(x, Q^2)$.

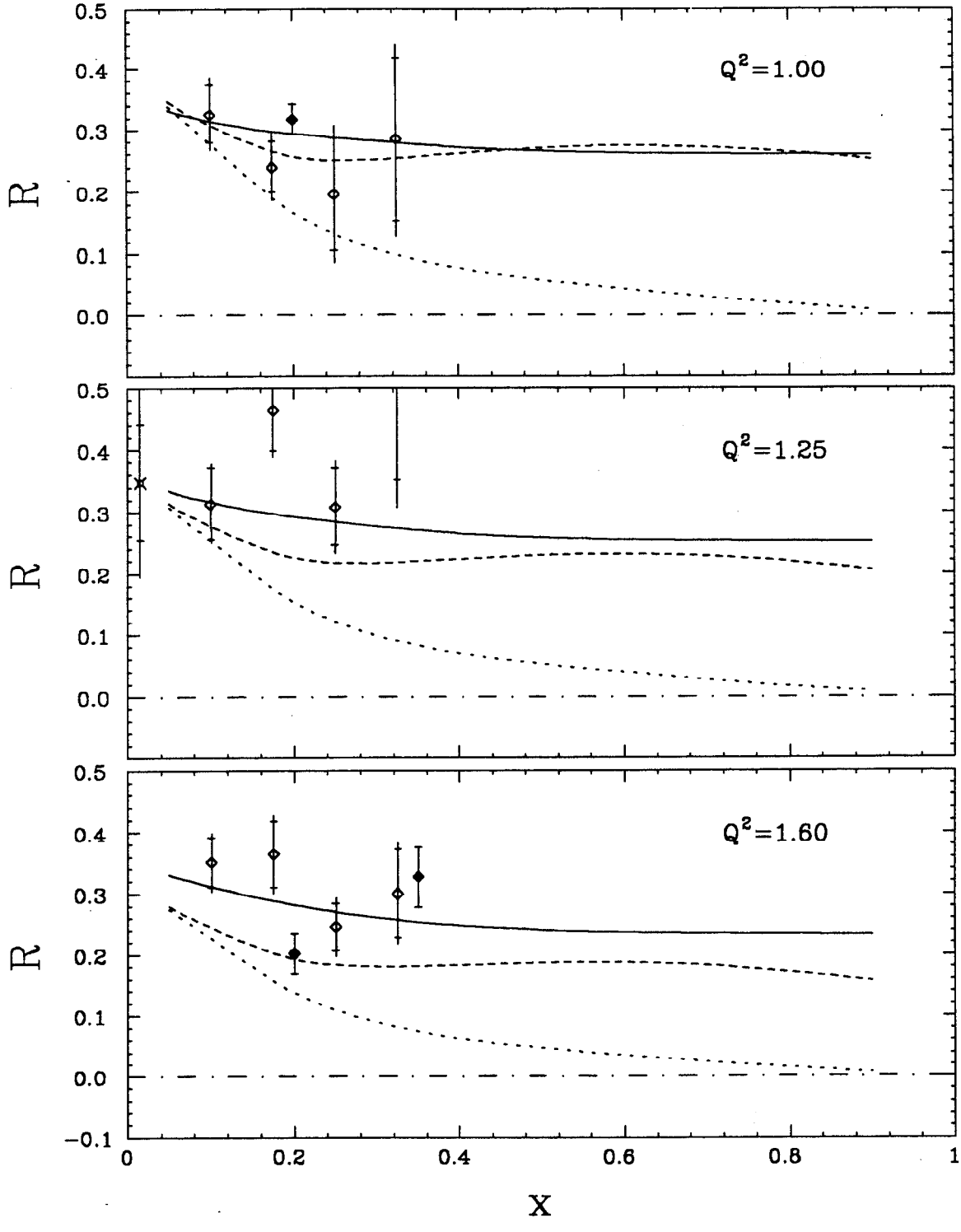

Figure 5.8. Shown are the global extractions of $R(x, Q^2)$ from Table 5.9. See Figure 5.7 and text for details. Figure continues on next four pages.

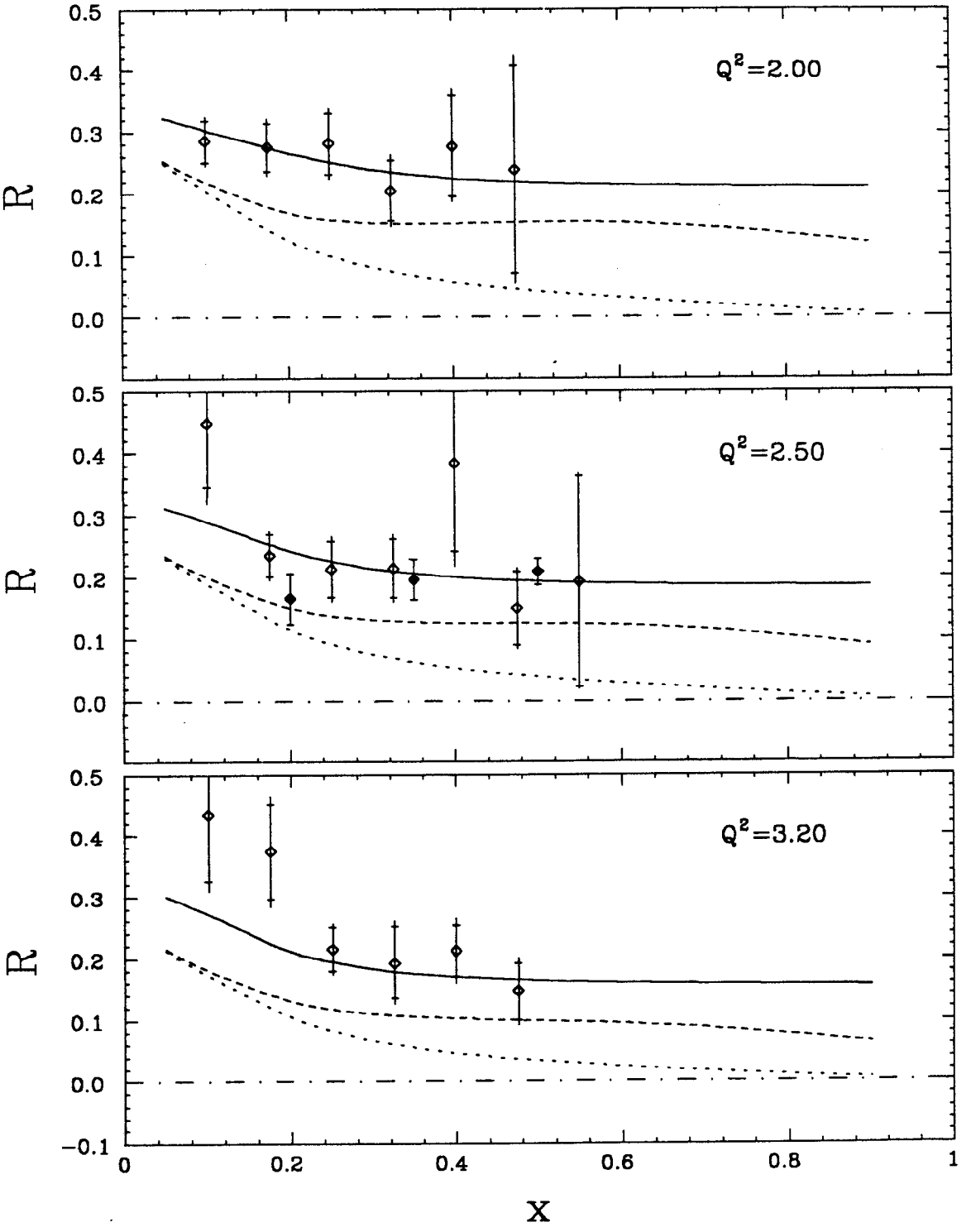

Figure 5.8/continued: Global extractioions of $R(x, Q^2)$.

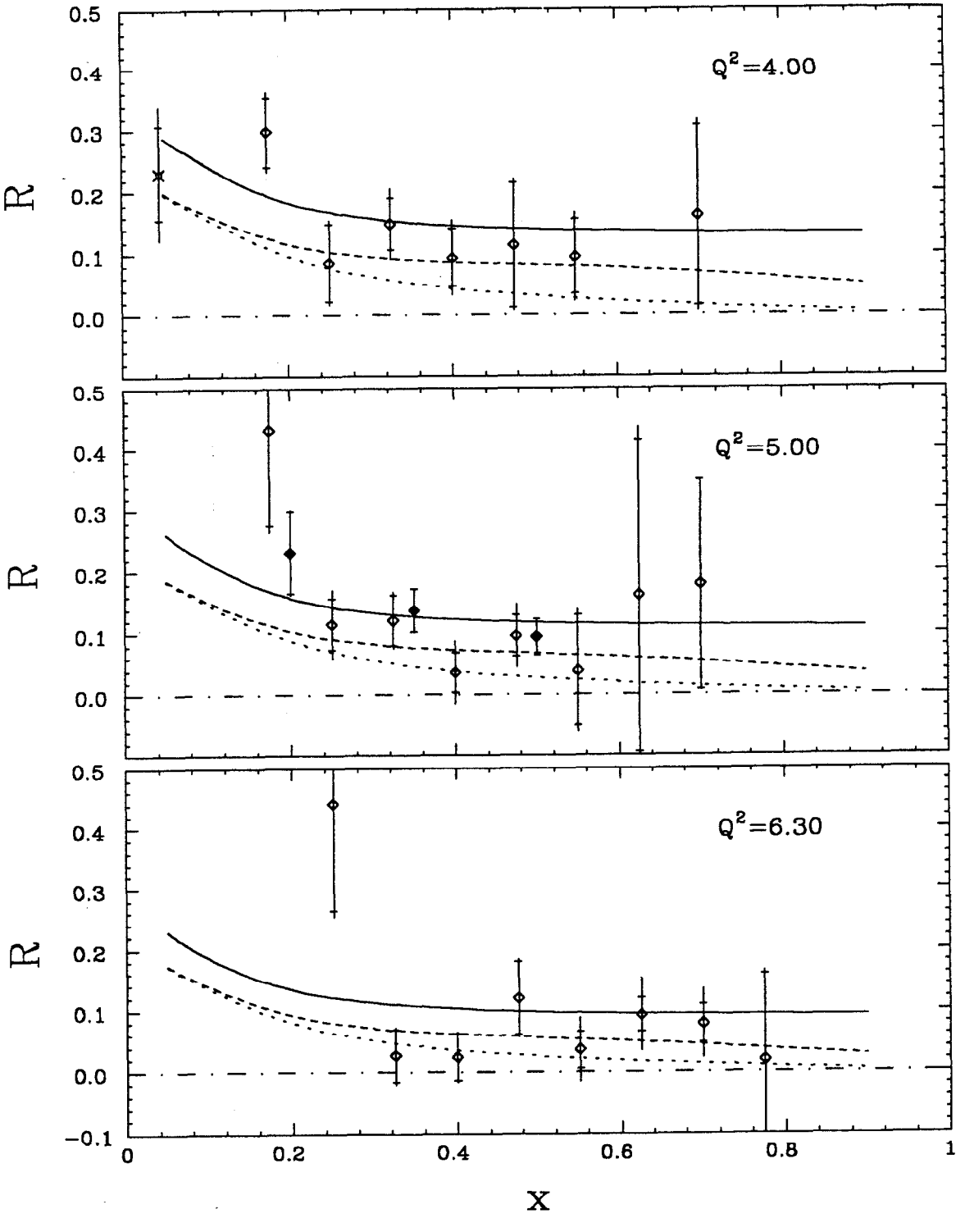

Figure 5.8/continued: Global extractions of $R(x, Q^2)$.

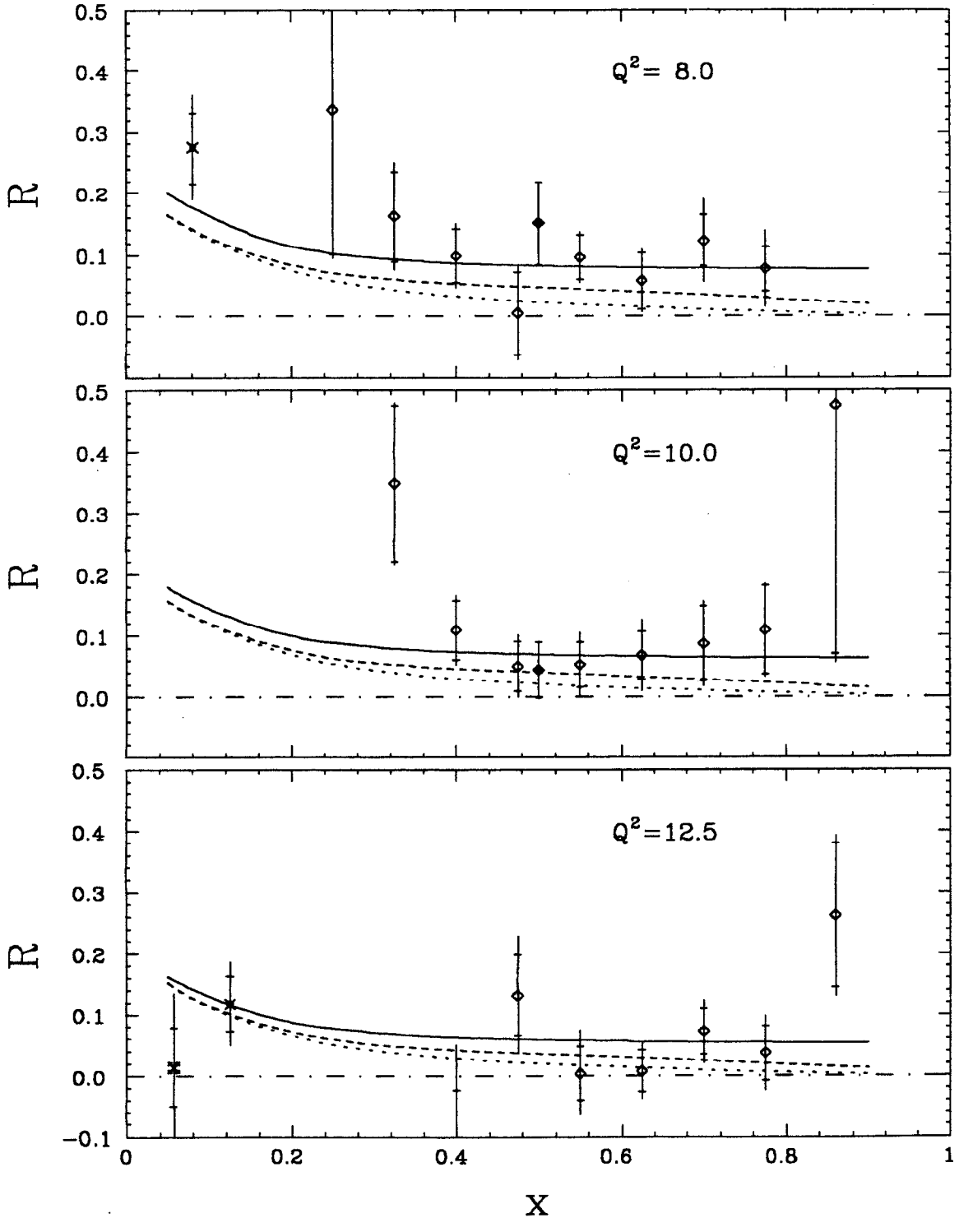

Figure 5.8/continued: Global extractions of $R(x, Q^2)$.

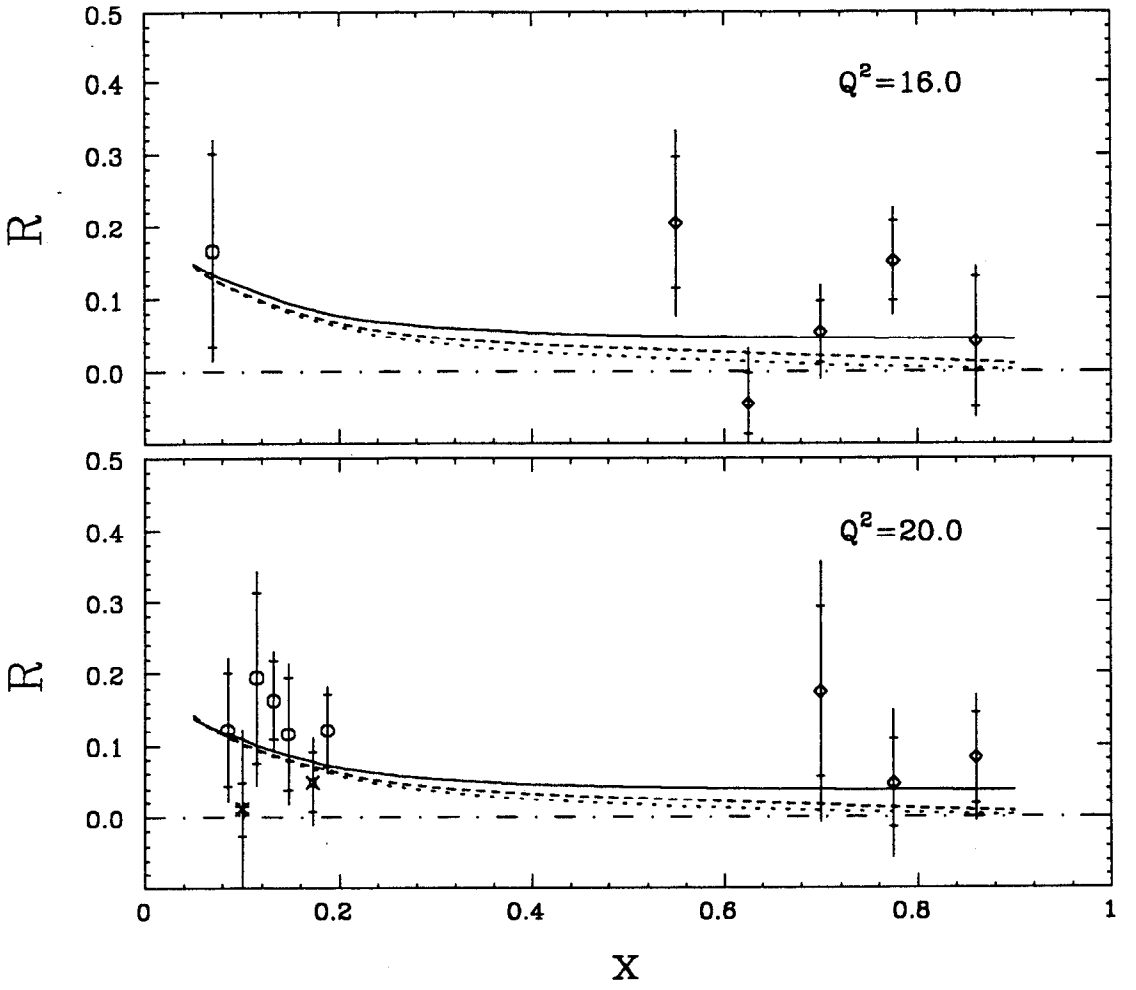

Figure 5.8/continued: Global extractions of $R(x, Q^2)$.

Table 5.9. Shown are goodness-of-fit tests of the E140 data to various models and calculations, including the naive parton model prediction, $R^{\rm npm} = 4M_p^2x^2/Q^2$, and the global mean value, $.143 \pm .005$.

Model	χ^2/df
$R = 0$	1412 / 139
$R = R^{\rm npm}$	720 / 139
$R = .143 \pm .005$	513 / 138
$R = R^{\rm QCD}$	479 / 139
$R = R^{\rm QCD+TM}$	221 / 139
$R = R^{\tau-4}$	61 / 72
$R = R^{1990}$	108 / 136

5.3.4 Phenomenological model of R: R^{1990}

As $R^{\rm QCD}$ and $R^{\rm QCD+TM}$ are not sufficient to describe the data, we are motivated to provide a phenomenological model of R for use in various technical applications, including the extraction of F_2 from the measured cross sections. We perform a fit to the set of world R measurements shown in Figures 5.7 and 5.8. This fit is performed with program FITPAR (see Section 5.22) in the logarithmic variable of Appendix B.2. Three functional forms were found to match the data quite well:

$$
\begin{aligned}
R_a &= \frac{a_1}{\ln(Q^2/.04)}\,\Theta(x,Q^2) + \frac{a_2}{\sqrt[4]{Q^8 + a_3^4}}\,, \\
R_b &= \frac{b_1}{\ln(Q^2/.04)}\,\Theta(x,Q^2) + \frac{b_2}{Q^2} + \frac{b_3}{Q^4 + .3^2}\,, \\
R_c &= \frac{c_1}{\ln(Q^2/.04)}\,\Theta(x,Q^2) + c_2\left[\left(Q^2 - Q^2_{thr}\right)^2 + c_3^2\right]^{-1/2},
\end{aligned}
\tag{5.31}
$$

where

$$
\Theta(x,Q^2) = 1 + 12\left(\frac{Q^2}{Q^2+1}\right)\left(\frac{.125^2}{.125^2+x^2}\right) \tag{5.32}
$$

gives the logarithmic term an x dependence which matches $R^{\rm QCD}$ at very high Q^2, and where

$$Q^2_{thr} = 5\,(1-x)^5 \ . \tag{5.33}$$

Though the data at low x and high Q^2 are insufficient to determine the best form of Θ, the one chosen appears to fit the data well.

The weights for the fitting procedure are determined by the total experimental error in R, given by the quadrature sum of δR^{ST} and δR^{SS}. This is approximately correct as the δR^{SS} are only partially correlated between neighboring measurements. Each of the three models fits the data well, with observed χ^2's of 110, 110, and 114, respectively, for 136 degrees of freedom.

Each model has strengths and weaknesses. We believe that the average of the three models is the best parameterization of the data over the full kinematic range. This best parameterization of R is given by

$$R^{1990} = \{R_a + R_b + R_c\}/3 \ , \tag{5.34}$$

where

$$\begin{aligned} a_1 &= .0672 \ , \quad & a_2 &= .4671 \ , \quad & a_3 &= \ 1.8979 \ , \\ b_1 &= .0635 \ , \quad & b_2 &= .5747 \ , \quad & b_3 &= -.3534 \ , \\ c_1 &= .0599 \ , \quad & c_2 &= .5088 \ , \quad & c_3 &= \ 2.1081 \ . \end{aligned} \tag{5.35}$$

The observed χ^2/df of R^{1990} is 108/136, with the specific χ^2 breakdown indicated in Table 5.10. This model is designed to extrapolate to reasonable values outside the measured kinematic range: inside the resonance region, as $x \to 1$, and as $Q^2 \to \infty$. This model should not be used, however, for values of Q^2 smaller than .3 GeV^2.

A study of the propagation of errors into R^{1990} reveals a convenient parameterization for the uncertainty in R^{1990} due to the experimental errors, δR^{ST} and δR^{SS},

$$\delta R^{1990} \ = \left[\left(\delta R^{1990}_{x\ low}\right)^2 + \left(\delta R^{1990}_{x\ high}\right)^2 + \left(\delta R^{1990}_{model}\right)^2 \right]^{1/2} , \tag{5.36}$$

Table 5.10. Shown is a χ^2 breakdown of the best fit model R^{1990}. The χ^2/df is based on the total uncertainties, given by the quadrature sum of δR^{ST} and δR^{SS}. Also shown, for comparison, is the χ^2/df we would obtain if only the δR^{ST} uncertainties had been used.

Dataset	Total Error	df	Statistical Only
SLAC	69	89	105
E140	17	11	17
EMC	3	4	14
BCDMS	4	12	8
CDHSW	5	11	15
Total	99	124	158

where

$$\delta R^{1990}_{x\ low} = .020 + (.006 + .03\,x^2)\left|\ln\left(\frac{Q^2}{B(x)}\right)\right| ,$$

$$B(x) = \max(.05, 8.33\,x - .66) ,$$

$$\delta R^{1990}_{x\ high} = \frac{.1\,x^{20}}{(.86)^{20} + x^{20}} , \tag{5.37}$$

$$\delta R^{1990}_{model} = \left[\sum_{i=a,b,c} (R_i - R^{1990})^2/2\right]^{1/2} .$$

The last term estimates the possible error in R^{1990} due to the assumed functional form. This parameterization of δR^{1990} also takes on reasonable values outside the kinematic range of the measurements. Away from measured kinematics δR^{1990} grows logarithmically in Q^2, and stepwise in x for very high x. For very large Q^2, the value of δR^{1990} at 64 GeV^2 is more reasonable and should be used instead.

Not included in Equation 5.36 are the radiative corrections uncertainties, δR^{RC}, given by Equation 4.5 with $\Delta\epsilon = .50$ and highly correlated over the entire set of SLAC and E140 measurements. For $x < .1$ or $Q^2 < 1$ GeV^2, we increase δR^{RC} by a factor of 1.5 (see Section 5.1).

For convenience we supply a Fortran implementation of R^{1990} and δR^{1990} in Appendix E.

5.4 F_2 Extraction and Modeling

We calculate F_2 from each cross section measurement using Equation 1.1 with $R = R^{1990}$. These F_2 values are tabled in Appendix E, along with the final cross section measurements.

The uncertainty vector of each F_2 extraction is exactly equal to the uncertainty vector of the corresponding cross section ($\delta F^k = \delta^k$) with two exceptions. First, a new component of the error vector of F_2 is generated by the experimental uncertainty in R^{1990}. We denote this error by δF_2^{SZ}, and note that

$$\delta F_2^{SZ} = \delta R^{1990} \left(1 + R^{1990}\right)^{-2} \left(\frac{1-\epsilon}{\epsilon}\right) \Big/ \left(1 + \frac{1-\epsilon}{\epsilon} \frac{1}{1+R^{1990}}\right) . \qquad (5.38)$$

Second, the uncertainty in F_2 due to radiative corrections, δF_2^{RC}, is smaller than δ^{RC} (Equation 3.12). This ϵ-dependent uncertainty is lessened due to an anti-correlated contribution which enters through δR^{RC} in the calculation of F_2. The sum of these effects is

$$\delta F_2^{RC} = .023 \left\{ \epsilon - .85 + \frac{1 + .5R^{1990}}{\left(1 + R^{1990}\right)^2} \left(\frac{1-\epsilon}{\epsilon}\right) \Big/ \left(1 + \frac{1-\epsilon}{\epsilon} \frac{1}{1+R^{1990}}\right) \right\} , \qquad (5.39)$$

and is everywhere smaller than $\pm .5\%$. For $x < .1$ or $Q^2 < 1$ GeV^2, we increase Equation 5.39 by a factor of 1.5 (see Section 5.1).

5.4.1 The Ω_9 and Λ_{12} Models

We present two fits to the sets of extracted F_2. The first model is the Ω_9 model defined by Equation 5.4. The second model is the Λ_{12} model, defined by

$$F_2^{\Lambda_{12}} = \beta\, F_2^{thr}(x)\left\{1 + \lambda_1(x)\ln\left[\frac{Q^2}{A(x)}\right] + \lambda_2(x)\ln^2\left[\frac{Q^2}{A(x)}\right]\right\}\,, \tag{5.40}$$

where

$$F_2^{thr}(x) = \sum_{i=1}^{5} C_i\,(1-x)^{i+2}\,,$$

$$\lambda_1(x) = \sum_{i=0}^{3} C_{i+9}x^i\,, \tag{5.41}$$

$$\lambda_2(x) = \begin{cases} C_6 + C_7x + C_8x^2\,, & \text{if } Q^2 < A(x)\,, \\ 0\,, & \text{otherwise}\,, \end{cases}$$

and

$$A(x) = 1.22\,\mathrm{e}^{3.2x}\,, \tag{5.42}$$

and where the deuterium binding term, β, is common to both models. The Λ_{12} model is inspired by the failure of the Ω_9 model to adequately fit the data at large x and large Q^2. The Ω_9 model tends to scale quickly as Q^2 gets large, whereas the Λ_{12} model, is linear in $\left[\ln Q^2\right]$ for $Q^2 > A(x)$, and quadratic below. Linearity above some threshold is expected from deep inelastic muon scattering data,[9,21] while quadratic dependence in $\left[\ln Q^2\right]$ at smaller Q^2 is entirely ad hoc.

The sets of best fit parameters are determined with program FITPAR (see Section 5.2.2) using weights determined by the total experimental error in F_2, given by quadrature sum of all components of the error vector except δF_2^{RC},

$$\begin{aligned} wt_j = \Big[&(\delta F_2^{ST})^2 + (\delta F_2^{SR})^2 + (\delta F_2^{SY})^2 + (\delta F_2^{SE})^2 \\ &+ (\delta F_2^{NM_1})^2 + (\delta F_2^{NM_2})^2 + (\delta F_2^{SZ})^2\Big]^{-1}\,. \end{aligned} \tag{5.43}$$

Table 5.11. Shown are the best fit model parameters for the Ω_9 and Λ_{12} models of F_2 for hydrogen (p) and deuterium (d).

	Ω_9 model		Λ_{12} model	
	p	d	p	d
C_1	.734	.609	1.417	.948
C_2	11.025	8.428	−.108	−.115
C_3	2.619	1.864	1.486	1.861
C_4	4.096	3.130	−5.979	−4.733
C_5	.121	.195	3.524	2.348
C_6	1.971	.821	−.011	−.065
C_7	3.889	3.281	−.619	−.224
C_8	−14.051	−8.297	1.385	1.085
C_9	8.808	4.489	.270	.213
C_{10}			−2.179	−1.687
C_{11}			4.722	3.409
C_{12}			−4.363	−3.255
χ^2/df	506/652	438/682	457/649	423/679

The best fit parameters are presented in Table 5.11. The uncertainties and correlation matrices of the parameters are used to estimate the experimental uncertainties of the Ω_9 and Λ_{12} models. A Fortran implementation of both models (with estimates of statistical and systematic uncertainties), $F_2^{1990}(x, Q^2)$, is provided in Appendix E.

The uncertainty in these models due to radiative corrections has been studied extensively, and is everywhere $\pm.2\%$. In all applications, we use the difference between these models to estimate the systematic errors due to the functional form of either structure function model.

The experiment-by-experiment breakdown of χ^2 contributions is shown in Table 5.12. The very small χ^2 contributions of E49a and E61 which were noted in Section 5.2.4 are again observed. The right-hand columns of Table 5.12 give the χ^2 contributions one would obtain allowing weights to be determined by δF_2^{ST} instead

Table 5.12. Shown is a χ^2 breakdown of the best fit Ω_9 and Λ_{12} models of F_2. The χ^2/df is based on the total experimental uncertainties, as indicated in Equation 5.43. Also shown, for comparison, is the χ^2/df we would obtain if only the δF_2^{ST} uncertainties had been used.

	Total Error		df	Statistical Only	
	Ω_9	Λ_{12}		Ω_9	Λ_{12}
Hydrogen					
E49a	47	50	117	58	62
E49b	187	177	208	248	232
E61	7	5	32	11	8
E87	69	66	109	127	116
E89a	88	64	77	179	136
E89b	107	94	118	174	147
Total	506	457	661	797	702
Deuterium					
E49a	46	44	117	57	57
E49b	172	166	193	270	254
E61	6	3	31	9	5
E87	63	68	109	124	136
E89a	44	47	71	94	113
E89b	65	56	100	107	99
E139	13	11	22	26	20
E140	28	27	48	47	46
Total	438	423	691	735	729

of the total experimental uncertainty used in Equation 5.43. The χ^2 contributions of E49a and E61 in these columns support the earlier contention that the statistical uncertainties on the data from these experiments, as published,[42,44] are anomalously large. In contrast, the χ^2 contributions of the other experiments are just as expected: $\chi^2/df < 1$ for total experimental errors, and $\chi^2/df > 1$ for statistical errors only.

5.4.2 Hydrogen and Deuterium Results

In Figures 5.9 and 5.10 we present plots of our global F_2 extractions structured into artificial "x-spectra," in the fashion of the EMC[9,21] and BCDMS[16,17] publications. These x-spectra are constructed in three steps. First, we bin the data into x-bins, matching the binning of either EMC or BCDMS. Second, we apply a correction factor, based on the best fit Ω_9 and Λ_{12} models to F_2, to adjust the F_2 measurements to the central x value of each bin while holding Q^2 fixed. The dependency of this correction factor on the choice of models is treated as a new source of systematic error and propagated accordingly (typically negligible for $x < .7$). Third, we then condense the data with respect to $[\ln Q^2]$ (see Section 5.2.1) over a maximum span in Q^2 of 6%. Throughout this condensing process, we propagate each component of the error vector of each F_2 measurement, respecting correlations both within and between experiments.†

Data from all eight experiments (E140 included) are fused into the x-spectra shown in Figures 5.9 and 5.10. Each datum represents the weighted average of as many as twelve F_2 extractions from as many as five experiments. The x-spectra presented in these figures match the x-binning of BCDMS. Numerical values for these spectra are tabled in Appendix E, along with an identical table conforming to the x-binning chosen by EMC. For $x < .275$ we apply a "scaling factor" to the plotted data,

$$\kappa = 150^{[.275-x]} , \tag{5.44}$$

thereby permitting the simultaneous presentation of the low-x data. The errors shown

† We present in Appendix E the Fortran implementation of this procedure, program SPECTRA. This program should serve as a detailed example of the (very nearly) exact propagation of the F_2 error vector through a sensitive analysis (see also the analysis in Section 5.3.1 and the general formulas in Appendix B.1). We do not *a prior* recommend such a detailed error propagation for all applications of these data, because, in general, the non-random systematic components of the error vectors are smaller than the random components (δF_2^{ST} and δF_2^{SR}) and it is often possible to make simplifying assumptions about the propagation of the non-random components.

in Figures 5.9 and 5.10 include all components of the error vector but do not include the uncertainties in overall normalization, given by $\pm 2.1\%$ for hydrogen and $\pm 1.7\%$ for deuterium (see Section 5.2.4).

The curves plotted in Figures 5.9 and 5.10 are the best fit Ω_9 and Λ_{12} models of F_2. The Λ_{12} model fits the data better at $x > .5$ and high Q^2, while the Ω_9 model fits the data better at $x < .1$. We expect that the Λ_{12} model would be improved by raising the number of terms in the definitions of $\lambda_{1,2}$ in Equation 5.41. We do not recommend the use of these models beyond the range of the data shown in these figures.

Figure 5.11 shows the Q^2 evolution of $F_2(x)$, as indicated by the best fit Ω_9 and Λ_{12} models. The data show a clear shift of $F_2(x, Q^2)$ to smaller and smaller x as Q^2 increases. This behavior can be understood very generally in terms of the increasing resolution of the photon probe[86] (see also Appendix A.2), or more specifically in terms of the QCD evolution of the quark probability distribution functions.[87]

Figure 5.12 shows the linear and logarithmic derivatives of $F_2(x, Q^2)$ with respect to $[\ln Q^2]$. Avoiding artificial x-bins, we present the best fit values of these derivatives using the Λ_{12} model. Specifically, in (a), we plot $\lambda_1 = \mathrm{d}[F_2]/\mathrm{d}[\ln Q^2]$; and in (b), we plot $\lambda_1 F_2^{-1} = \mathrm{d}[\ln F_2]/\mathrm{d}[\ln Q^2]$. The error curves in (a) are determined by program F_2^{1990} (see Appendix E) from the covariance matrix of the fit to Λ_{12}, and the errors in (b) include an additional term reflecting the variation of F_2 across the range of $Q^2 > A(x)$ (see Equation 5.42). Perfect scaling is observed only at $x = .195$ (for $Q^2 > 2.3$ GeV^2) with dramatic scaling violations at both lower and higher x.

Figure 5.13 compares the best fit Ω_9 and Λ_{12} models with the values of F_2 extracted previously by Bodek *et al.*[3] (see Section 1.2.2). These early results are in complete agreement with the values of $F_2(x, Q^2)$ reported here. Importantly, however, our new results span a much larger kinematic range, especially in Q^2, and display greatly reduced statistical and systematic errors.

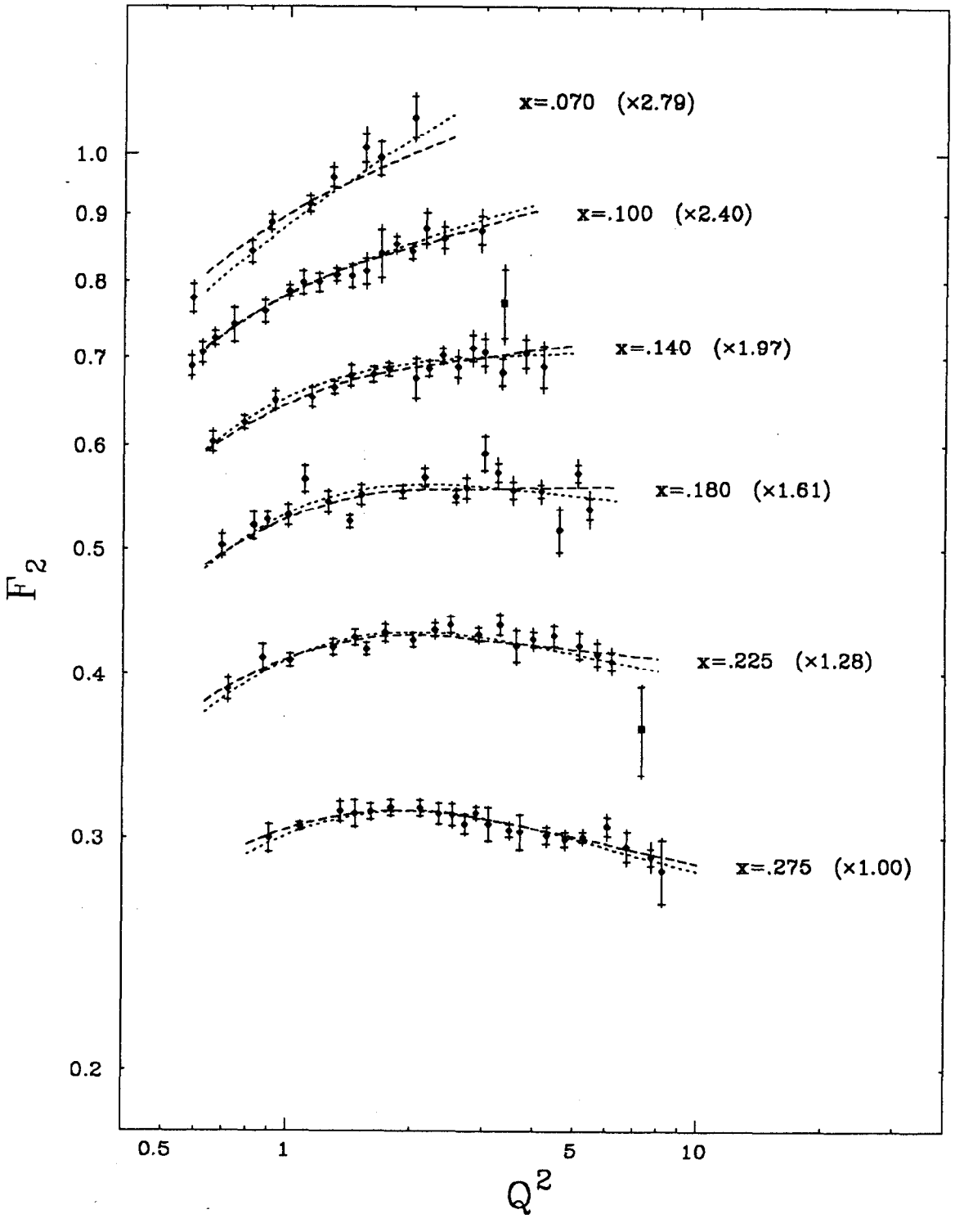

Figure 5.9. Shown are the combined SLAC hydrogen values of $F_2(x, Q^2)$ binned into BCDMS-like x-spectra. Also shown are the best fit Ω_9 and Λ_{12} models to the data (see next page). The data at $x < .275$ have been scaled by Equation 5.44. The two errant data points, marked by squares rather than diamonds, belong to the $x = .100$ and $x = .225$ spectra. Figure continues on next page.

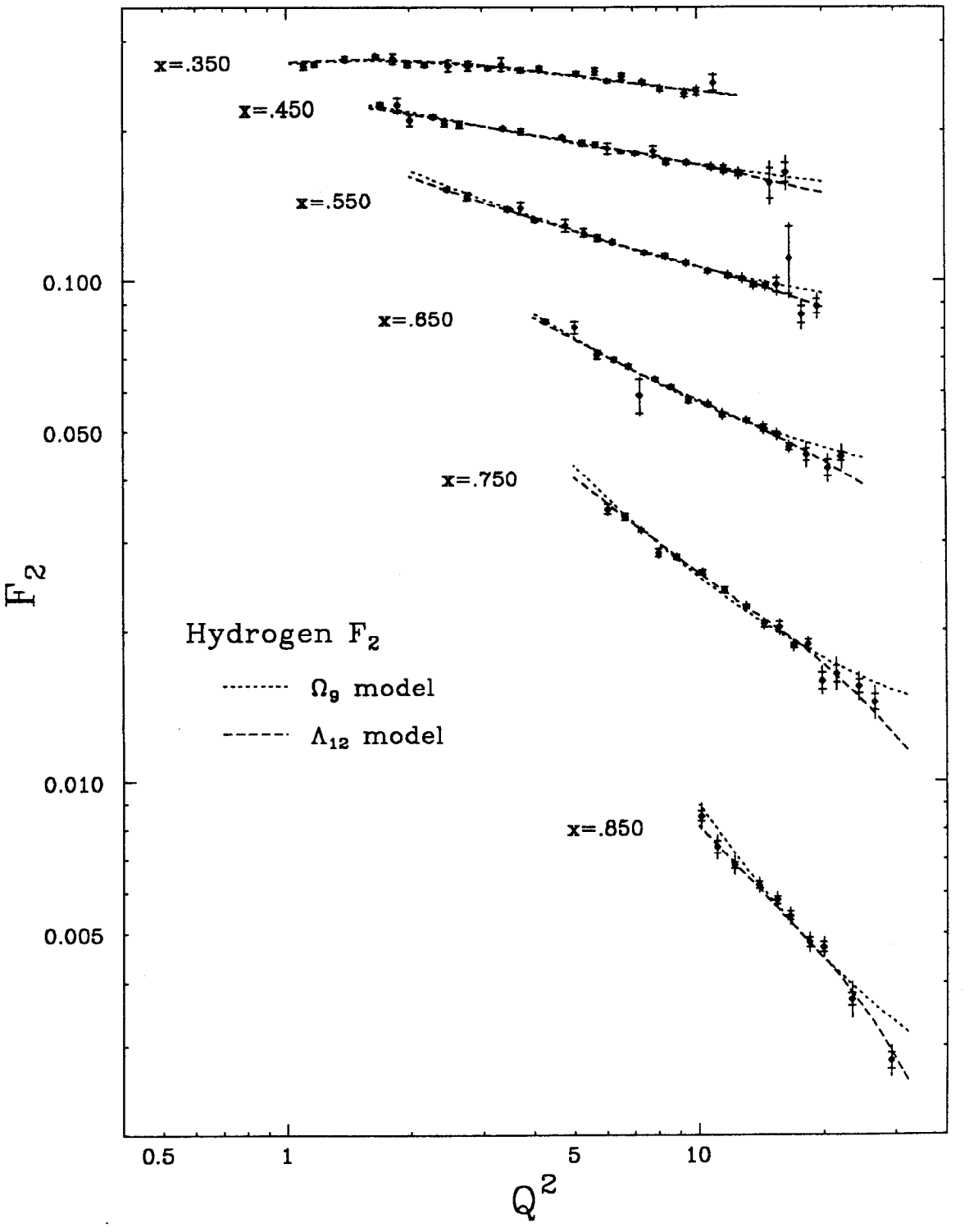

Figure 5.9/continued: Combined SLAC hydrogen $F_2(x, Q^2)$.

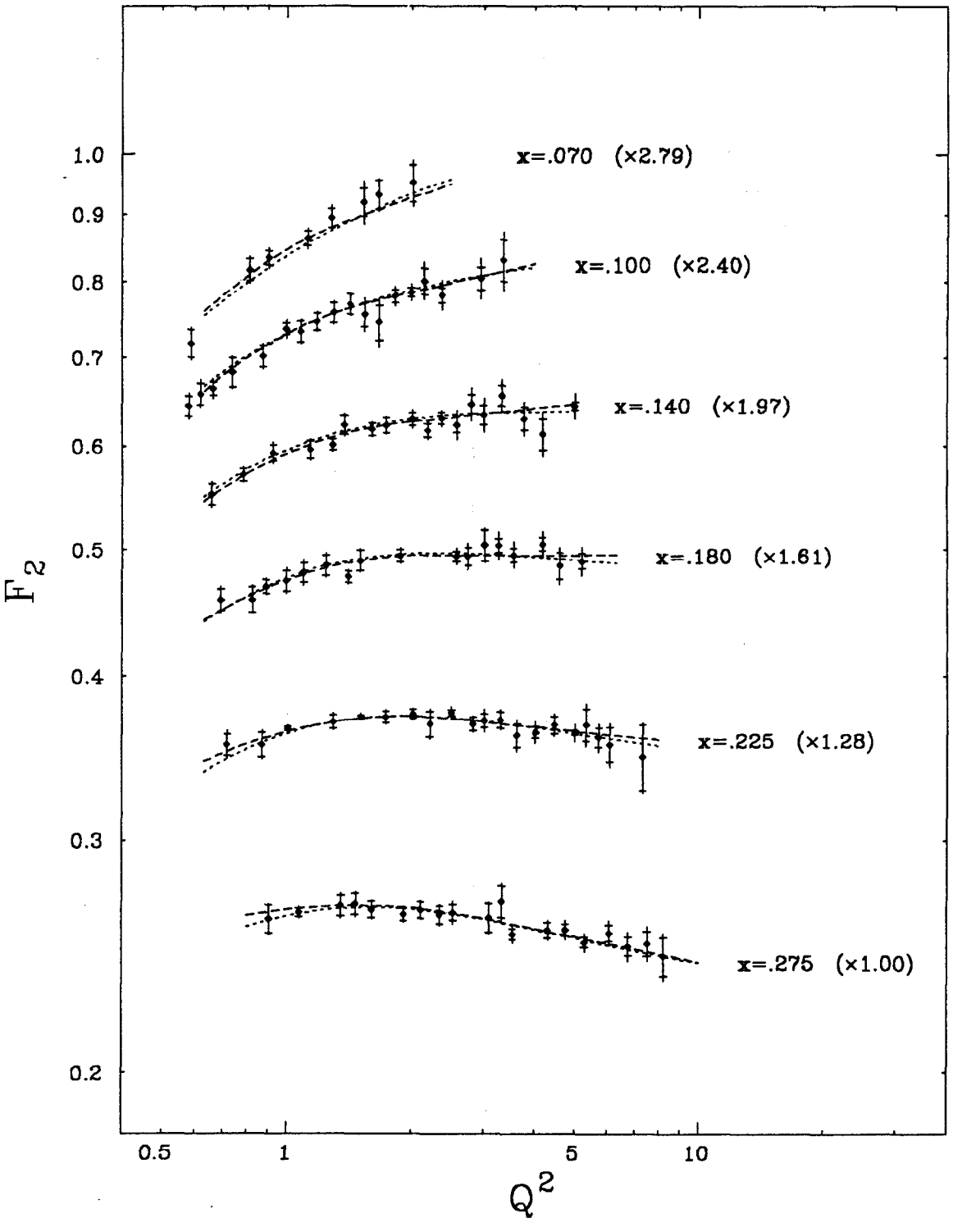

Figure 5.10. Shown are the combined SLAC deuterium values of $F_2(x, Q^2)$ binned into BCDMS-like x-spectra. Also shown are the best fit Ω_9 and Λ_{12} models to the data (see next page). The data at $x < .275$ have been scaled by Equation 5.44. Figure continues on next page.

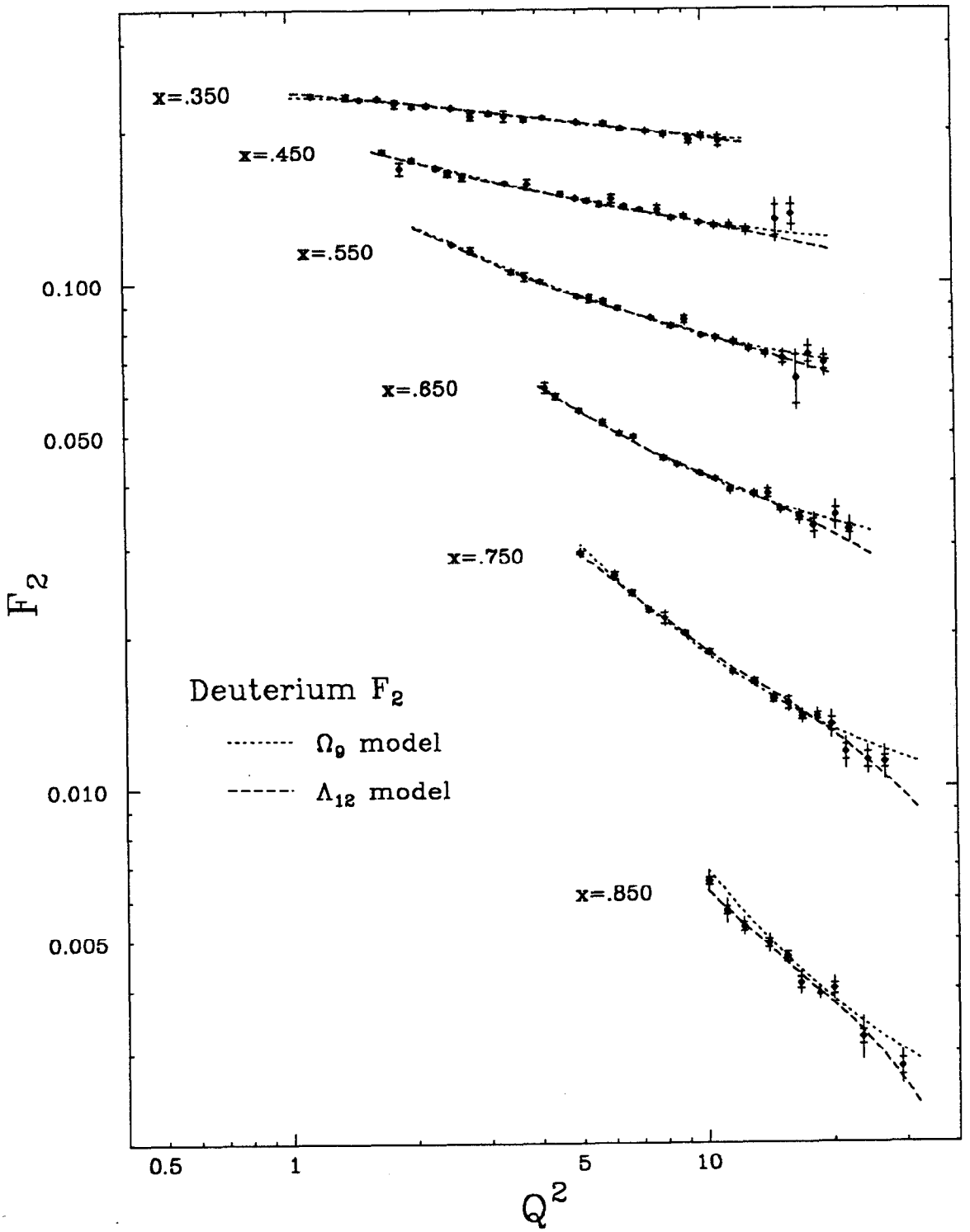

Figure 5.10/continued: Combined SLAC deuterium $F_2(x, Q^2)$.

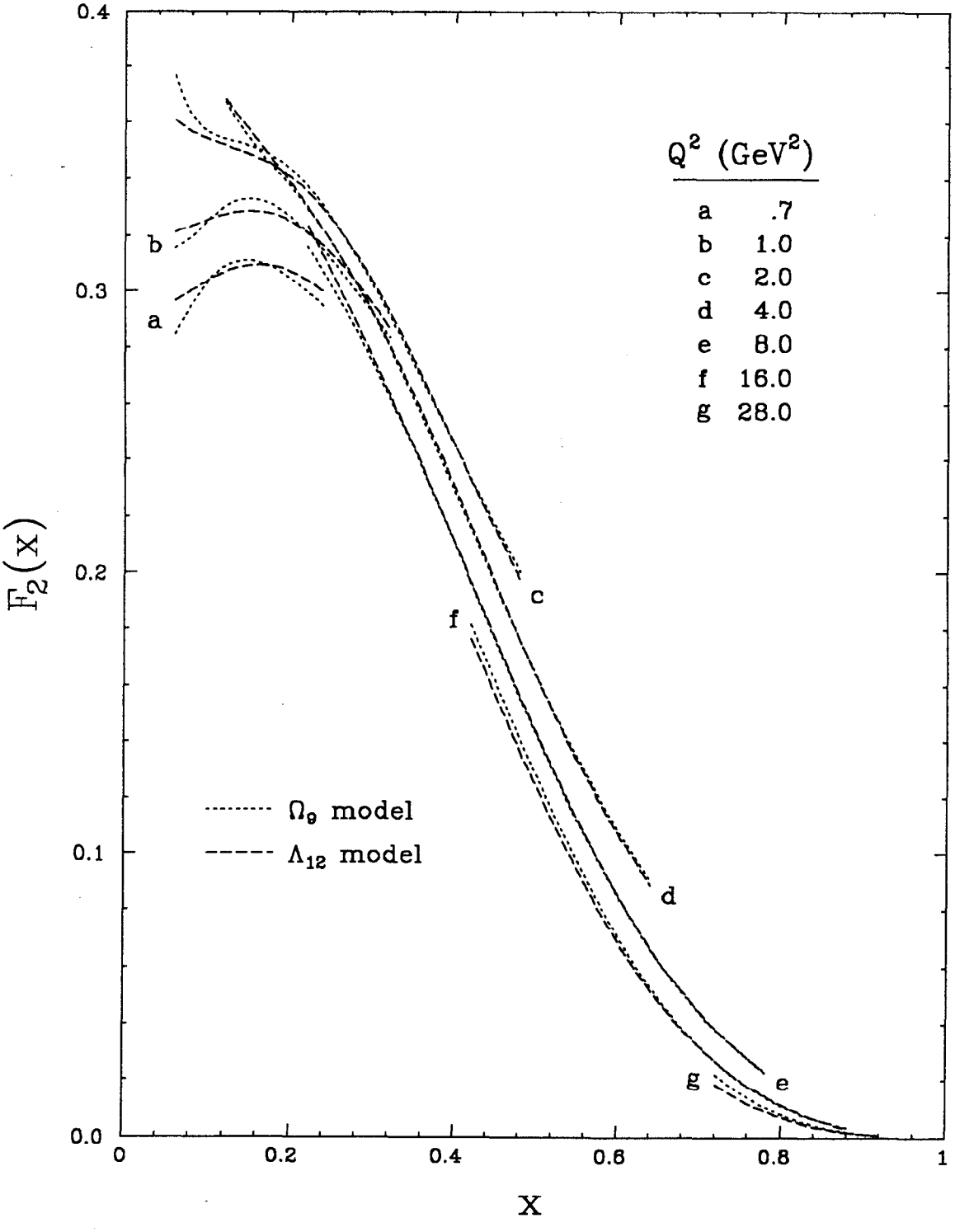

Figure 5.11. Shown is the Q^2 evolution of $F_2(x)$ in hydrogen. Shown are the Ω_9 and Λ_{12} models F_2 at fixed Q^2. Curves are shown over the range of the SLAC data only. Uncertainties in the data are generally larger than the difference between models and may be estimated from Figures 5.9 and 5.10 (also see Appendix E).

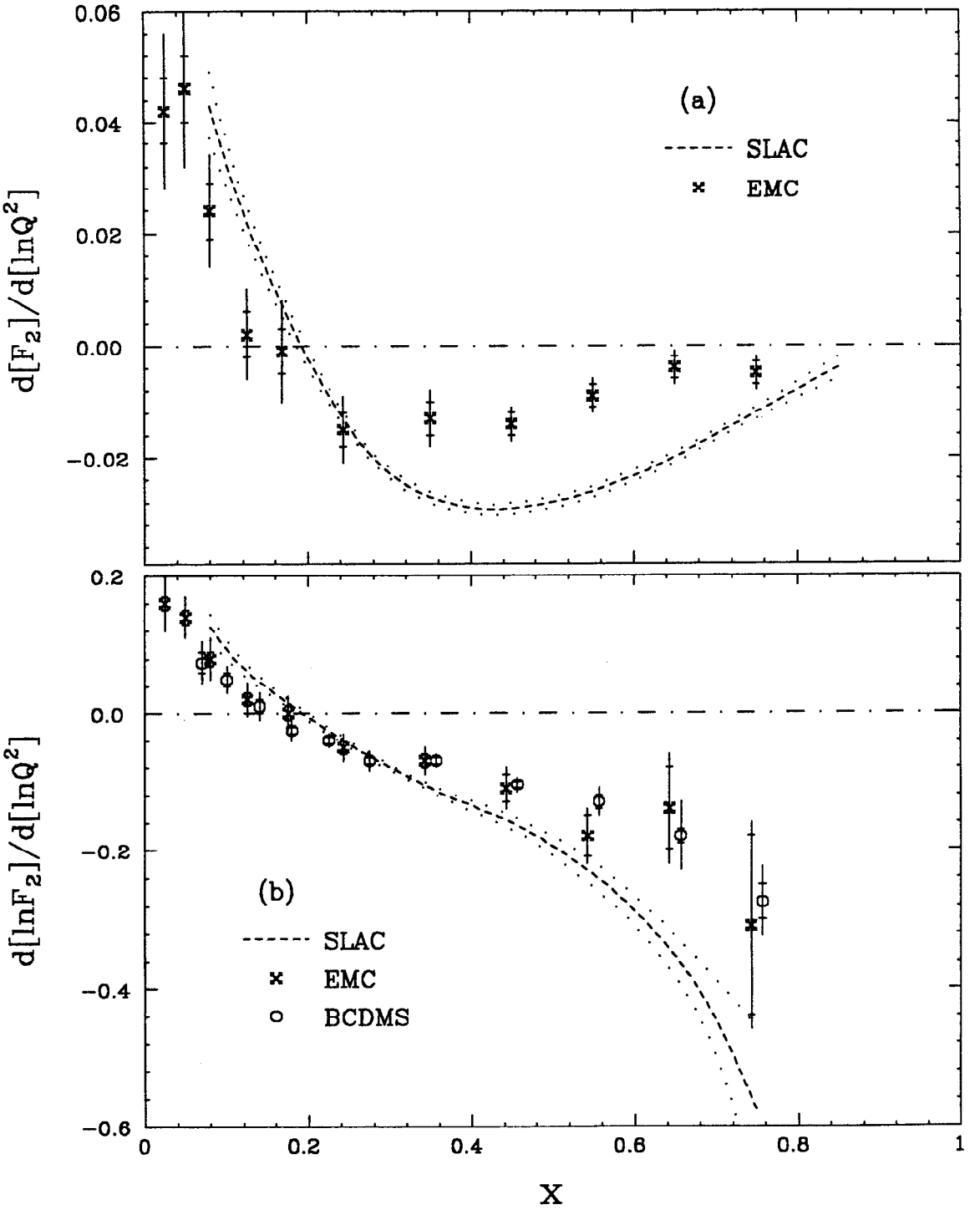

Figure 5.12. The slope of the Λ_{12} fit to our hydrogen data is compared to the slopes observed in the EMC and BCDMS data (from Reference 88). Errors in the SLAC data are represented by the dotted error curves. See Sections 5.4.2 and 5.4.3 for details.

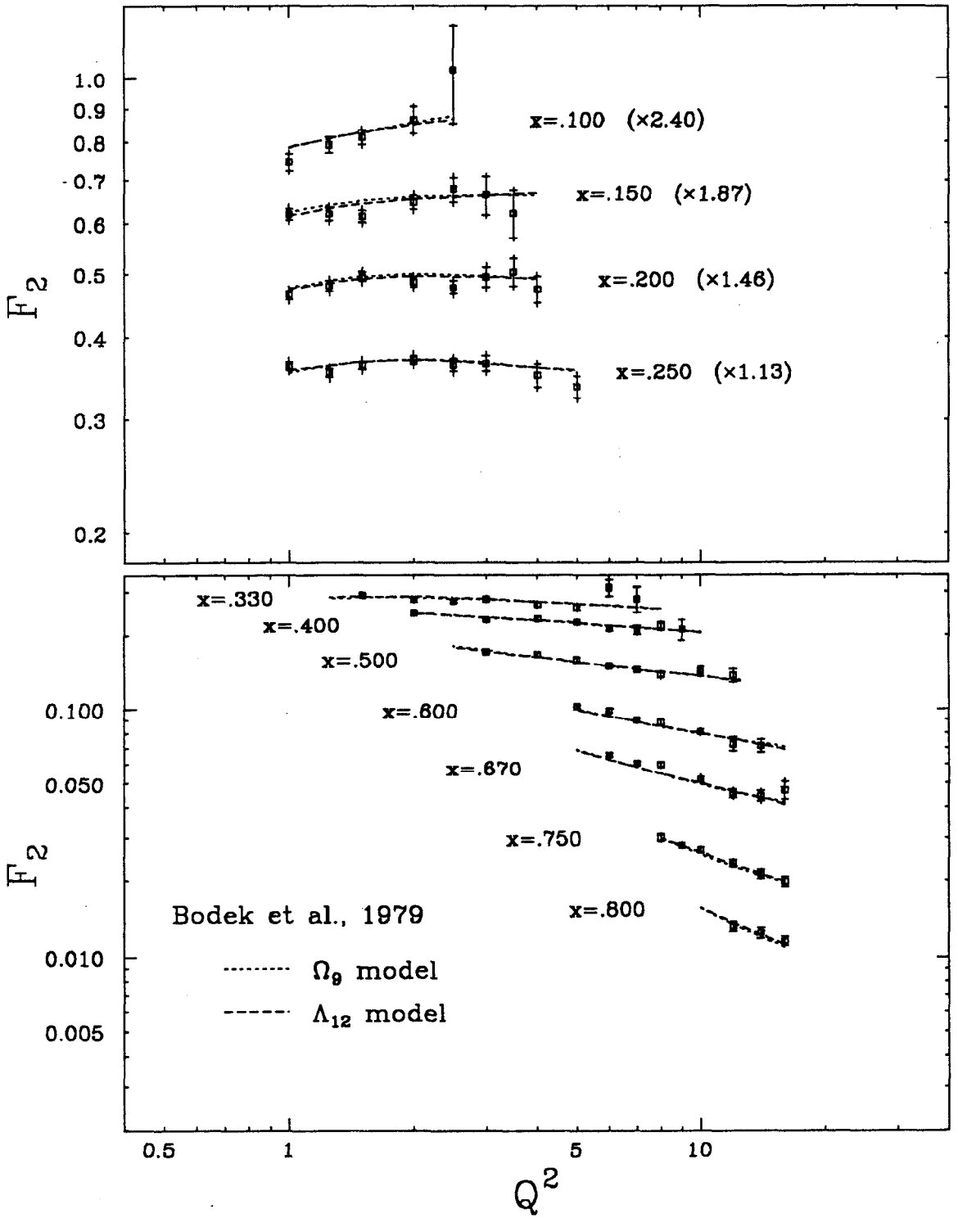

Figure 5.13. Shown is a comparison of the previous extractions of Bodek *et al.*[3] to the best fit models of our results (see Section 5.4.1). Note the effective scale change (÷2) as compared to Figures 5.9 and 5.10. See also Equation 5.44. Figure continues on next page.

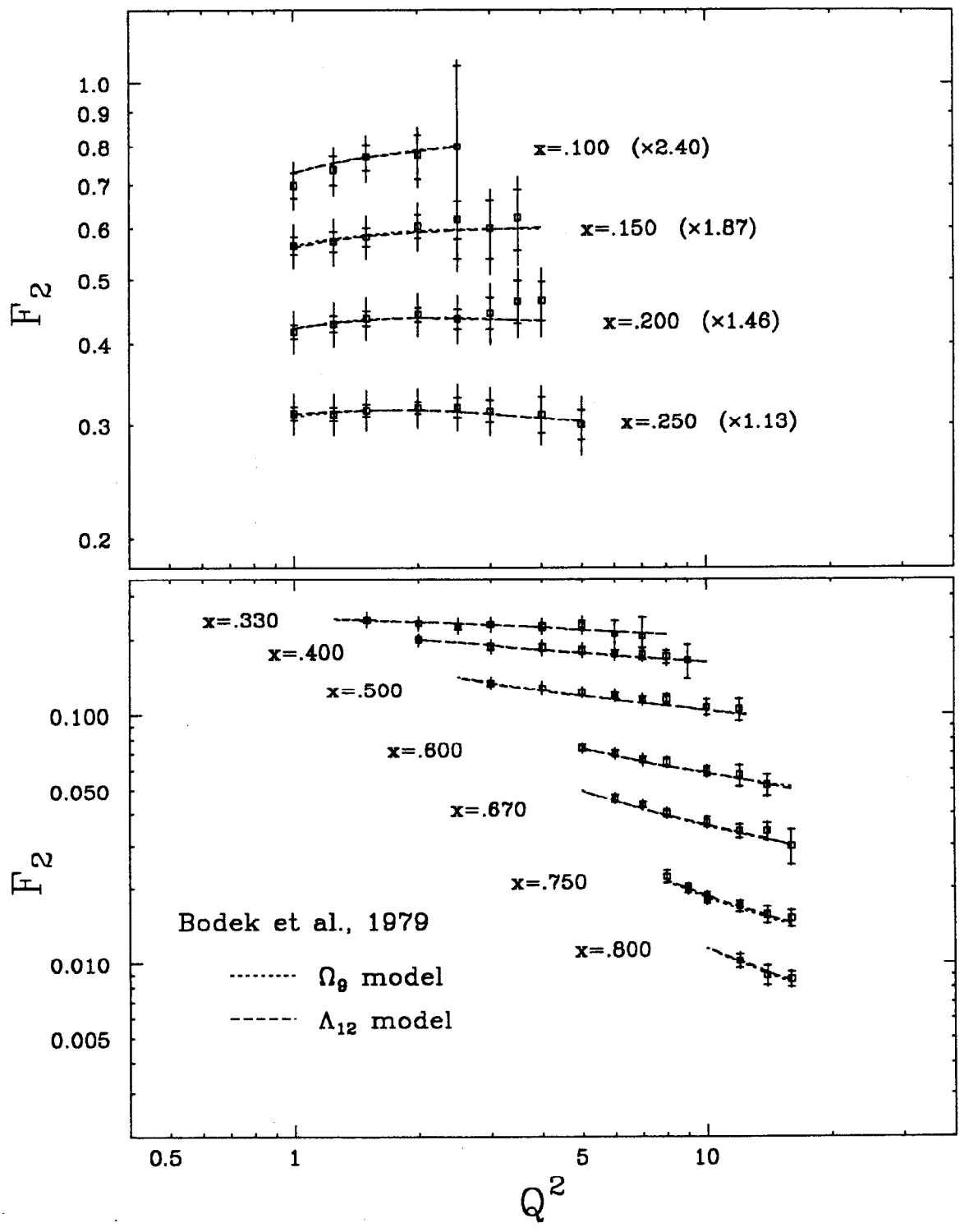

Figure 5.13/continued: Comparison with previous $F_2(x, Q^2)$.

5.4.3 *Comparison with* EMC *and* BCDMS

We now attempt to resolve the EMC/BCDMS F_2 disparity, shown in Figure 1.2, with comparisons to the precise SLAC data presented in the previous section. Though it is has been widely demonstrated[20,88,89] that the EMC data are 5% to 10% lower than other measurements, there remains a large systematic discrepancy with respect to x between the EMC and BCDMS extractions of F_2. The SLAC F_2 results extend well into the high-Q^2 domain of the μ-scattering data and offer an excellent basis for comparison.

Both EMC and BCDMS extract F_2 from the measured cross sections assuming that $R \equiv 0$. To correct the effects of this assumption, we apply a correction factor to their F_2 values which adjusts their data to reflect the new measurements of R, as parameterized by $R^{1990}(x, Q^2)$. This correction factor is

$$C^R = \frac{1 - y + \frac{1}{2}y^2 + z}{1 - y + \left[\frac{1}{2}y^2 + z\left(1 - R^{1990}\right)\right]\left(1 + R^{1990}\right)^{-1}} , \tag{5.45}$$

where $y = \nu/E_\circ$ and $z = Q^2/4E_\circ^2$.

For the BCDMS data, this correction factor is applied to each measurement at each beam energy, and then the corrected measurements are averaged over beam energies. For the EMC data, however, the process of averaging over energies is quite complicated,[9] so we adopt an approximate treatment. Instead we calculate the correction factor for each beam energy which contributes to a particular F_2 measurement in Table 10 of Reference 9; then average these correction factors with weights determined by the statistical errors of the individual F_2 measurements in Table 9 of Reference 9; and finally apply the averaged correction factor to the averaged F_2. For both BCDMS and EMC the total correction is typically less than 1% for $x > .2$ and rises to several percent for smaller x (especially at large Q^2). Errors in this correction factor, estimated from δR^{1990}, are typically below $\pm .2\%$ and are added in quadrature to the systematic errors of the EMC and BCDMS data.

Figures 5.14 and 5.15 compare the SLAC F_2 results with those of BCDMS,[16,17] corrected for the above effect. The uncertainties shown for BCDMS reflect our usual policy of using the full extent of the error bar to denote the quadrature sum of statistical and systematic uncertainties. In this case, however, it is important to note that the large BCDMS systematic errors at high x and low Q^2 are dominated by *perfectly correlated* uncertainties in spectrometer magnetic field calibration and in spectrometer resolution. The overall normalization uncertainty of the BCDMS data is $\pm 3\%$ and is not included in the error bars of the figures.

Figures 5.16 and 5.17 similarly compare the SLAC F_2 results with those of EMC,[9,21] normalized by [$\times 1.07$]. Also included are the recent EMC low-x deuterium results,[90] normalized by [$\times 1.00$]. The EMC data at $x = .75$ suffer from large uncertainties in the relative normalizations of data taken with different beam energies,[91] and so, must only be used with caution. The overall normalization uncertainty of the EMC data is $\pm 5\%$ and is not included in the error bars of the figures.

Visual inspection of Figures 5.14 and 5.15 indicates that there is generally good agreement between the SLAC and BCDMS results, with two noted exceptions. First, the three lowest Q^2 data of BCDMS at $x = .55$ and $x = .65$ are 10 to 15% lower than the SLAC data. Because these data are strongly correlated, the disagreement with SLAC might be explained, for example, in terms of a single ~ 2 standard deviation effect in spectrometer calibration and/or resolution. Second, between $x = .18$ and $x = .275$ there seems to be a basic 5% disagreement between the high-Q^2 "tendency" of the SLAC data and the low-Q^2 "tendency" of the BCDMS data. This is especially unfortunate because, as shown in Figure 5.12 (b), this x range is the only region in which SLAC and BCDMS display the same slope in F_2.

Visual inspection of Figures 5.16 and 5.17 indicates that there is excellent agreement between the SLAC and EMC results (modulo the 7% overall normalization factor). There does appear to be some disagreement at $x = .08$ between the "tendencies" of

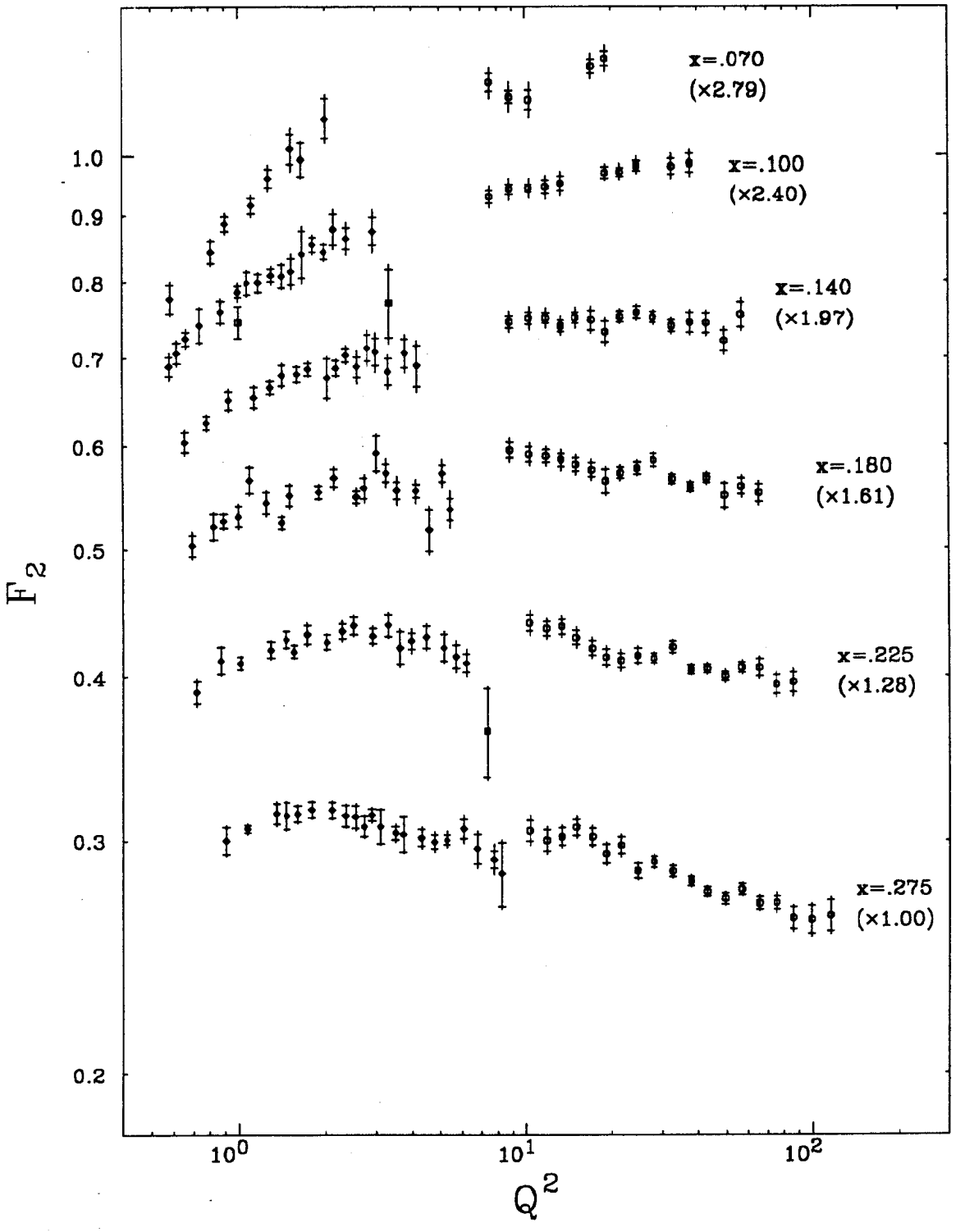

Figure 5.14. Shown is a comparison of the SLAC and BCDMS hydrogen F_2 results. A relative normalization of 1.000 is assumed. See also the caption to Figure 5.9. Figure continues on next page.

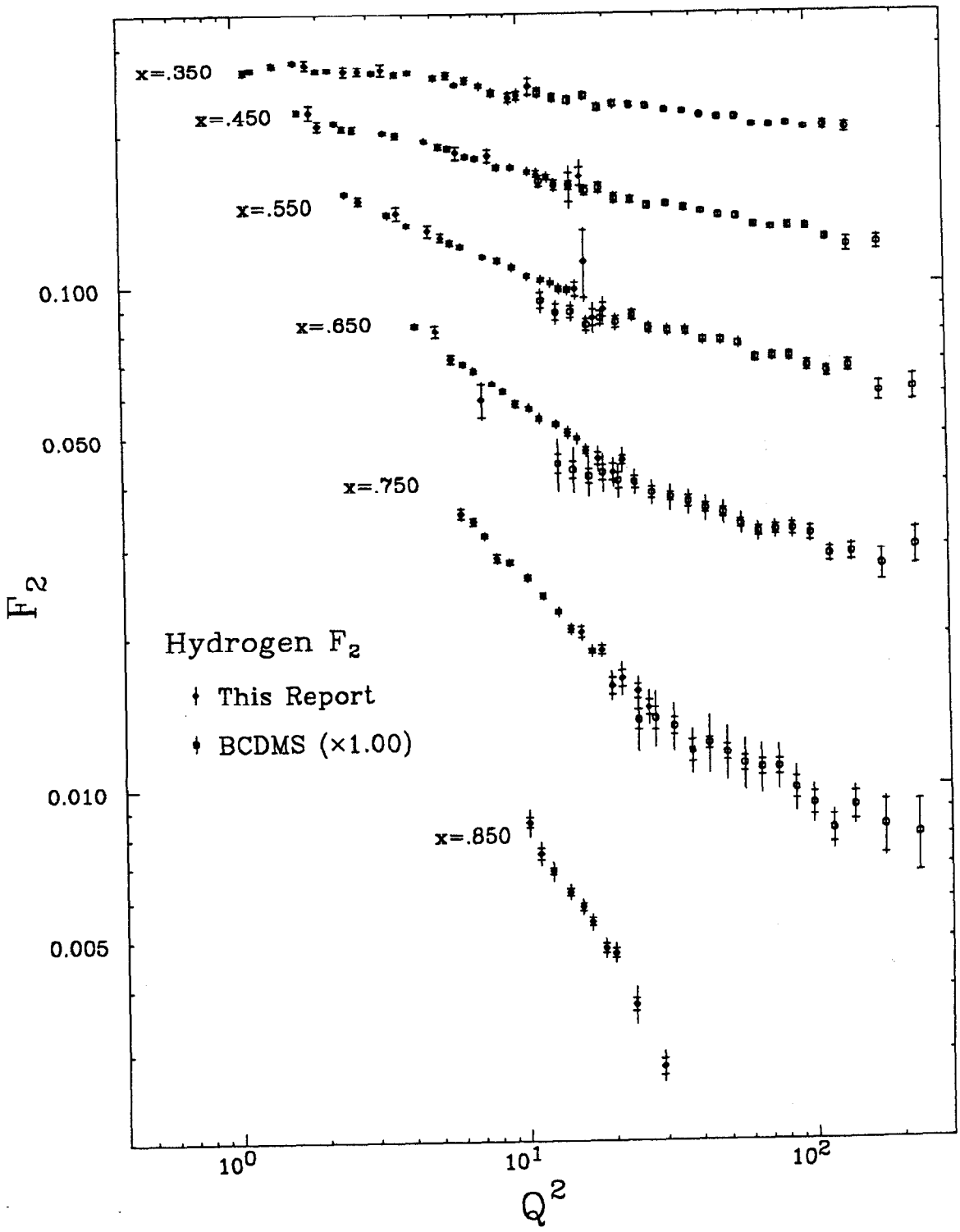

Figure 5.14/continued: Comparison of SLAC and BCDMS hydrogen F_2 results.

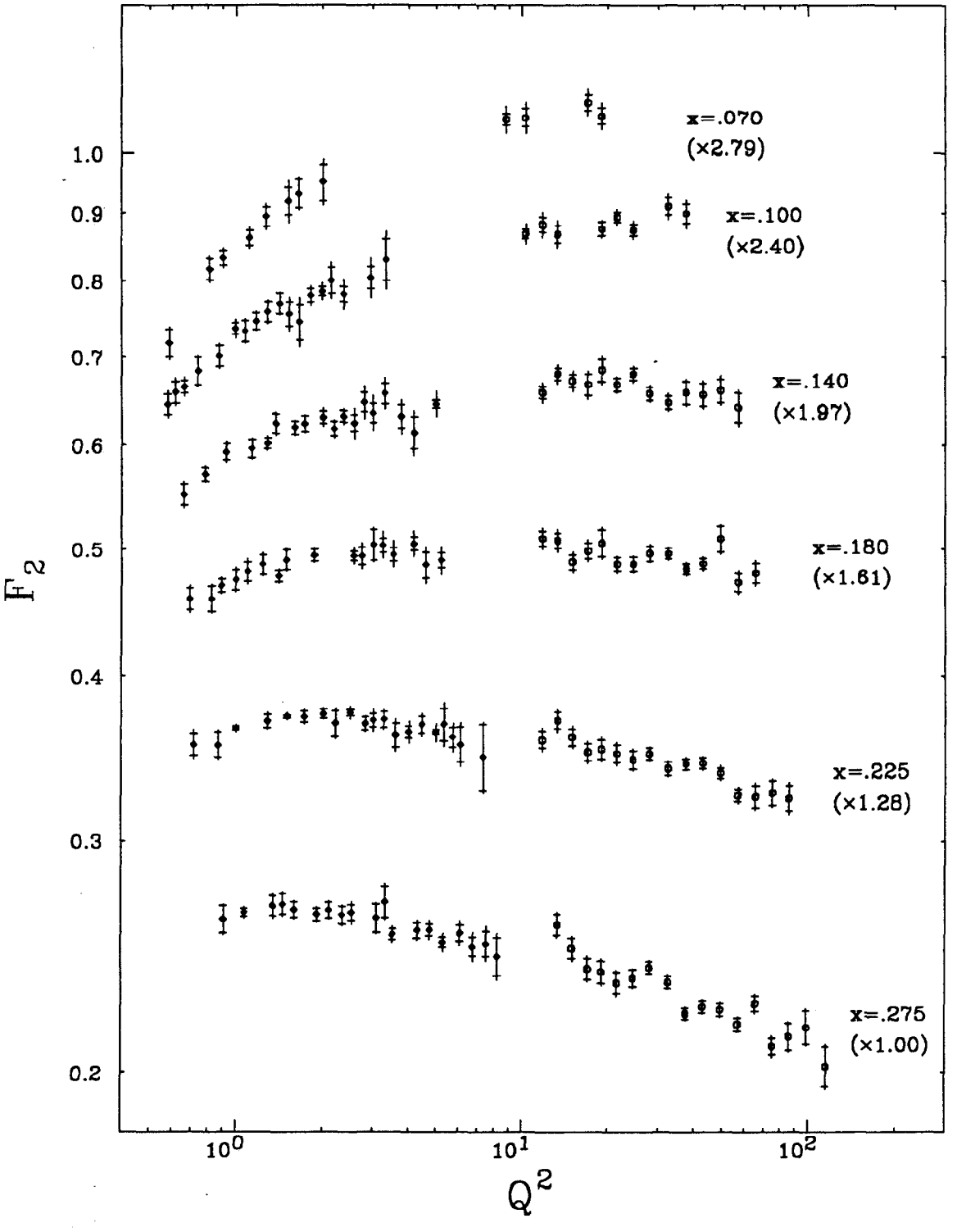

Figure 5.15. Shown is a comparison of the SLAC and BCDMS deuterium F_2 results. A relative normalization of 1.000 is assumed. See also Equation 5.44. Figure continues on next page.

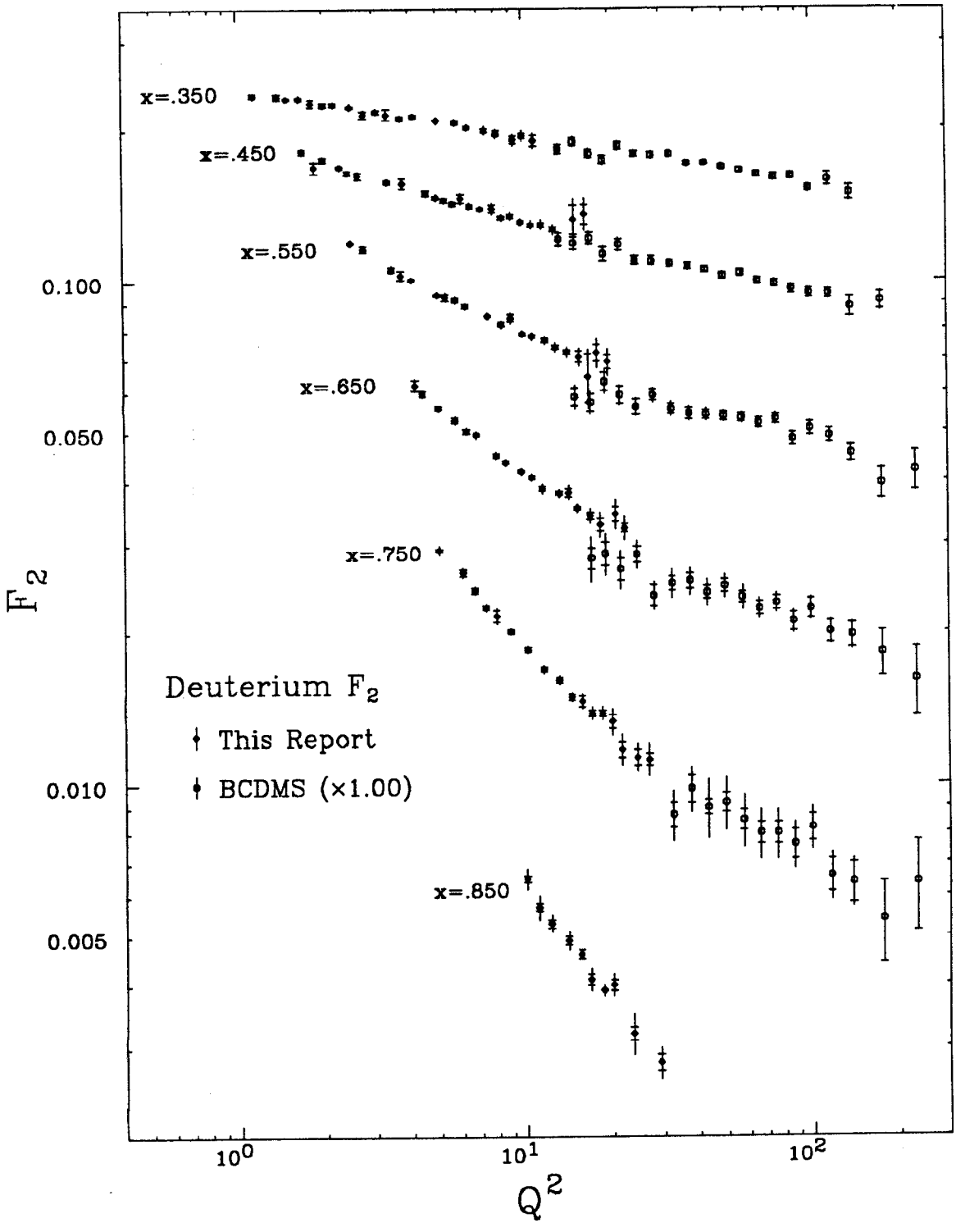

Figure 5.15/continued: Comparison of SLAC and BCDMS deuterium F_2 results.

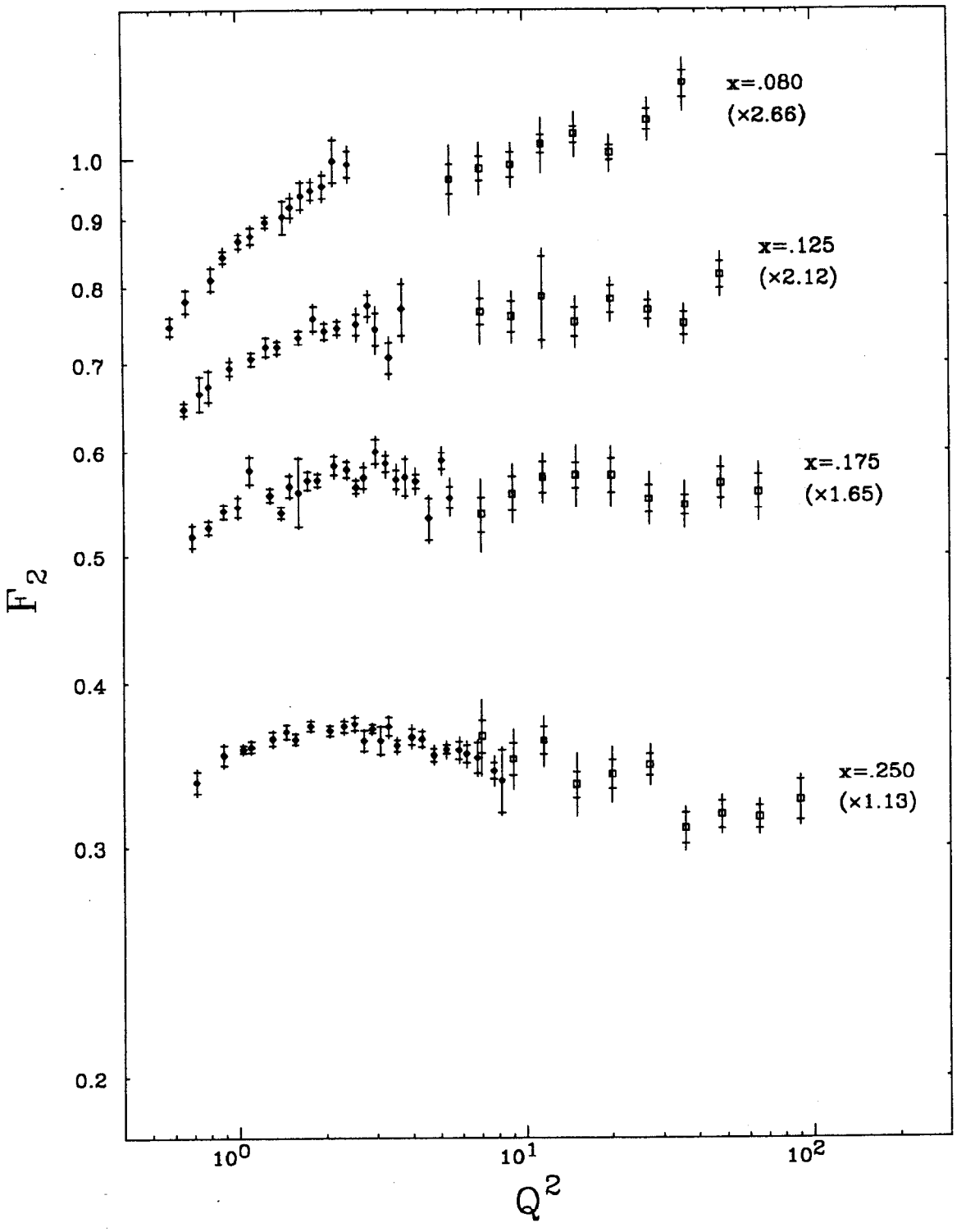

Figure 5.16. Shown is a comparison of the SLAC and EMC hydrogen F_2 results. A relative normalization of 1.070 is assumed. See also Equation 5.44. Figure continues on next page.

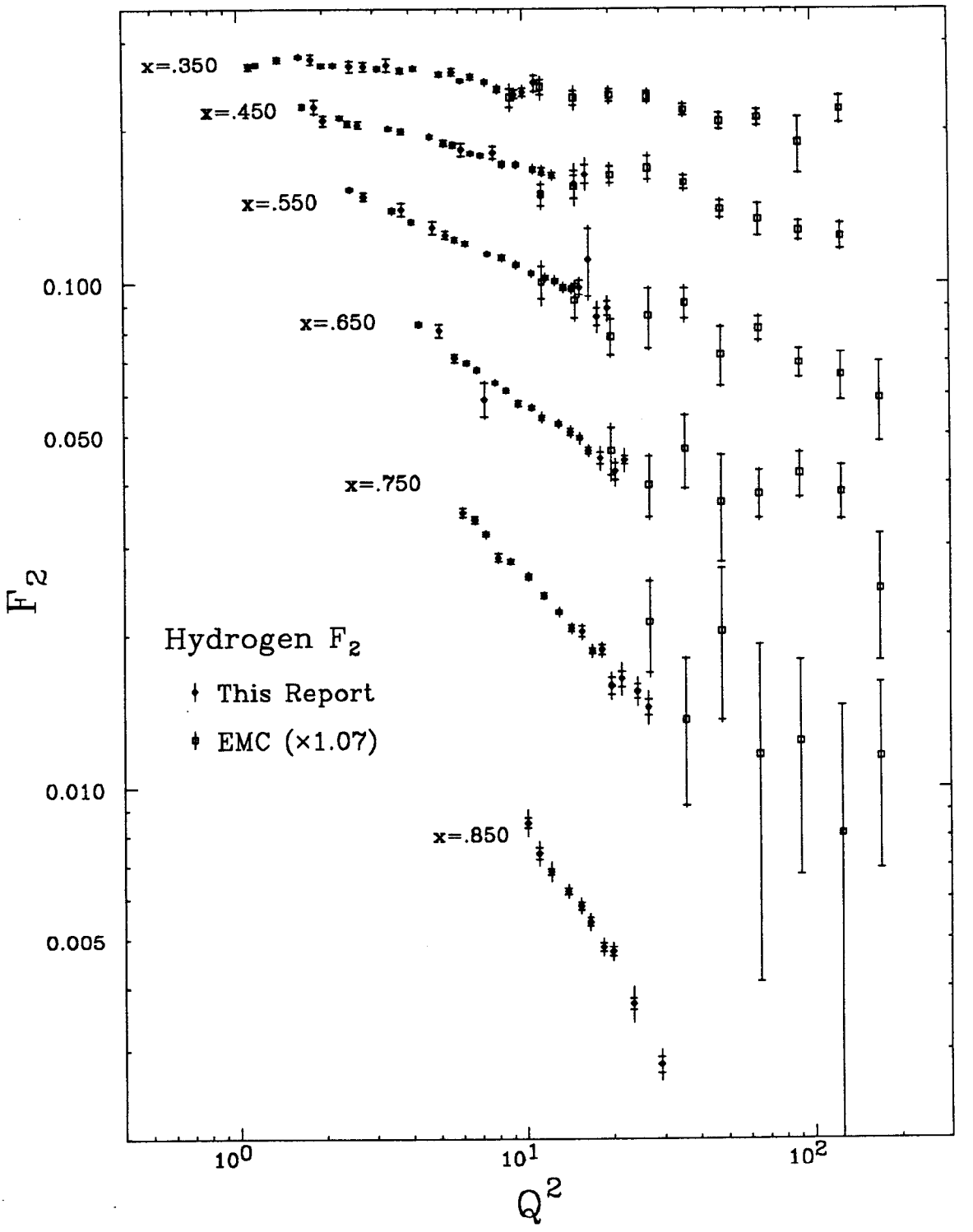

Figure 5.16/continued: Comparison of SLAC and EMC hydrogen F_2 results.

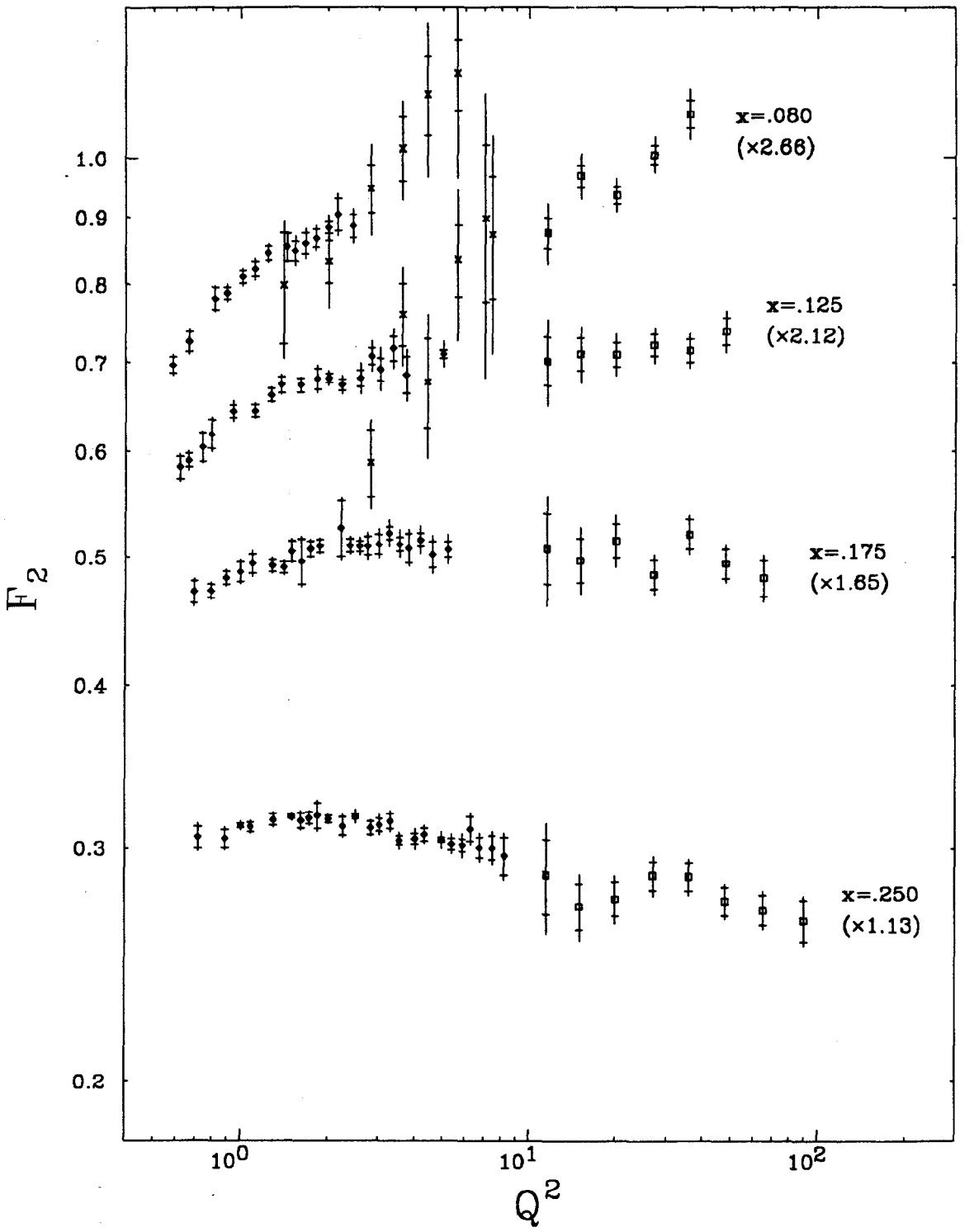

Figure 5.17. Shown is a comparison of the SLAC and EMC deuterium F_2 results. A relative normalization of 1.070 is assumed for the data of Reference 21 only. See also Equation 5.44. Figure continues on next page.

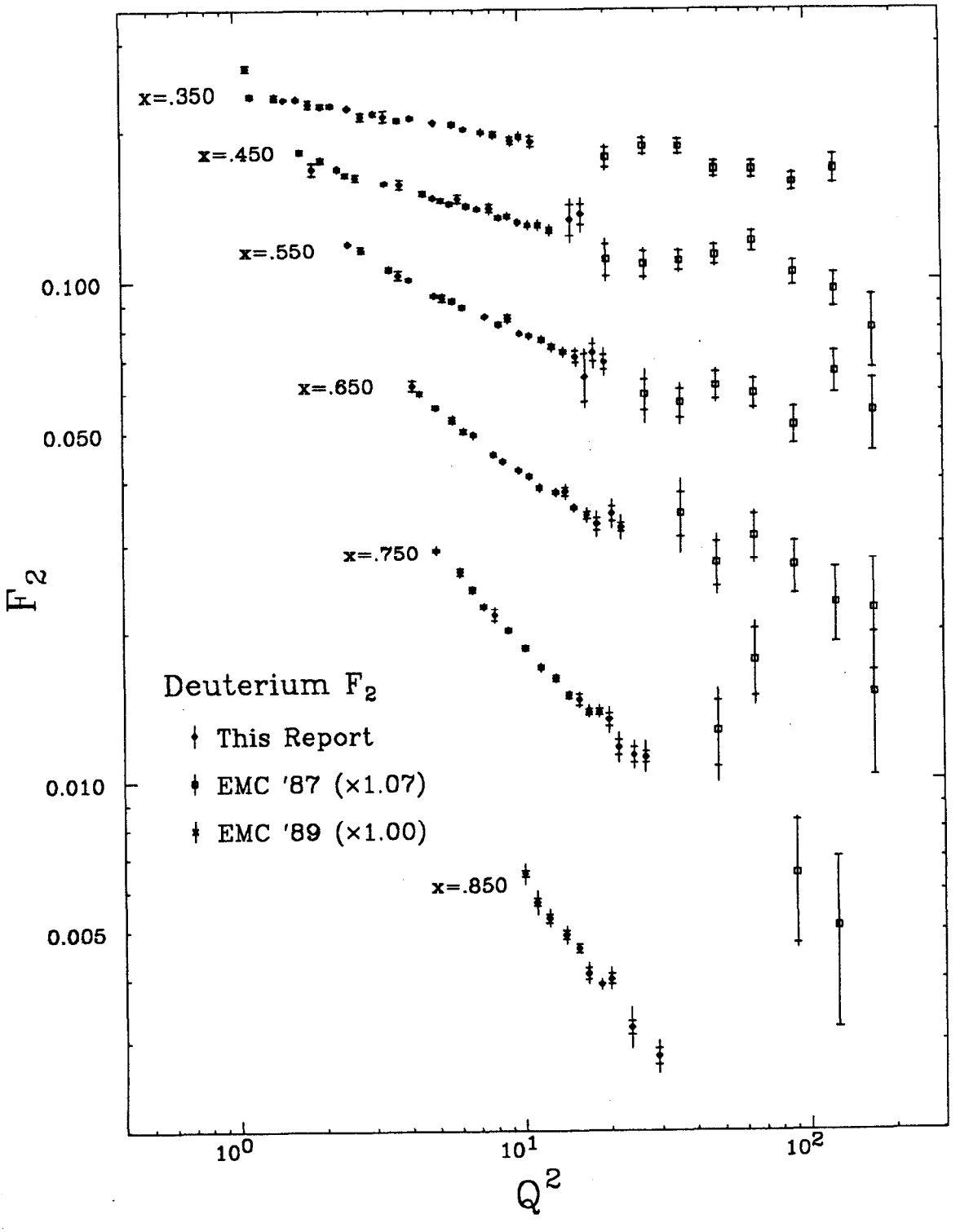

Figure 5.17/continued: Comparison of SLAC and EMC deuterium F_2 results.

the SLAC and EMC data,† though, the $\times 2$ gap Q^2 between the datasets lessens the value of this comparison.

Figure 5.12 compares the slopes observed in the SLAC data with those of EMC and BCDMS. The SLAC data tends to slope more steeply at both low and high x, as can also be seen in Figures 5.14 through 5.17. We interpret the sharp discontinuity in slope at $x = .65$ and $x = .75$ as strong evidence of $\sim 1/Q^2$ power corrections to QCD. To separate these power corrections from the QCD logarithmic scaling violations is difficult, especially in light of the discrepancies between the SLAC, EMC, and BCDMS datasets and the fact that the observed discontinuity in slope occurs precisely on the boundary between electron- and muon-scattering datasets.

In Table 5.13 we present the results of a naive normalization comparison of the SLAC hydrogen data and that of EMC and BCDMS. We compare measurements at identical or nearly identical kinematics; then average over Q^2, propagating all systematic errors as though they were perfectly correlated. This comparison, however, is very limited statistically and completely ignores the information available from the tendencies of the low x data. Note, for example, that the low-x data in Figures 5.14 and 5.15 clearly contradicts the global average for the BCDMS/SLAC normalization in Table 5.13.

A better method to study the relative normalizations of SLAC, EMC, and BCDMS is to use a smooth fit to guide the comparison over longer ranges in Q^2, and through the gap in Q^2 at low x. We perform a χ^2 minimization fit to the combined SLAC+EMC and SLAC+BCDMS datasets, allowing a simple normalization constant to be determined simultaneously with the parameters of either the Ω_9 or the Λ_{12} models. This is exactly the method of the normalization fits of Section 5.2, though, now with two added complications.

† In general, we shall not comment on the recent low-x low-Q^2 EMC deuterium data,[90] which, while in good agreement with the SLAC data, display $\pm 10\%$ total errors.

Table 5.13. Shown are the results of a naive normalization comparison of the EMC and BCDMS results to those of SLAC. This study is made by comparing measurements at identical or nearly identical kinematics and is misleading because that it ignores the low-x information (see text).

x	$\langle Q^2 \rangle$	EMC	BCDMS
.250	8.0	$1.029 \pm .023 \pm .055$	
.350	10.0	$1.094 \quad .035 \quad .050$	$1.018 \pm .044 \pm .032$
.450	12.9	$1.165 \quad .046 \quad .060$	$1.032 \quad .017 \quad .027$
.550	14.7	$1.126 \quad .051 \quad .069$	$1.090 \quad .018 \quad .033$
.650	20.0	$1.030 \quad .114 \quad .079$	$1.118 \quad .021 \quad .057$
.750	27.0	$.733 \quad .151 \quad .074$	$1.085 \quad .047 \quad .079$
Global Average			
.344	10.3	$1.068 \pm .016 \pm .057$	
.538	15.3		$1.072 \pm .010 \pm .039$

First, there is minimal kinematic overlap between SLAC and the other datasets which causes unavoidable model dependence in the best fit normalization parameters. We address this issue by using two models of F_2, one which scales quickly and one which does not, and by testing for sensitivity of the normalization parameters which might indicate a gross inadequacy in the models.

Second, there are strong correlations between the large BCDMS systematic errors at large x and low Q^2. We respect these correlations by altering the fitting routine (see Section 5.2.2) to include an additional parameter which permits the BCDMS F_2 values to vary *in unison* within the statistical bounds of these correlated systematic uncertainties.†

Extensive study reveals that within a percent or so, it is permissible to assume that the EMC hydrogen and deuterium datasets display the same normalization rela-

† See, for example, the seventh and eighth columns of Tables 3 through 6 of Reference 16.

Table 5.14. Shown are the results of normalization fits to the SLAC+EMC hydrogen (p) and deuterium (d) F_2 results. See text for details.

Model	Normalization Factor	EMC χ^2/df		SLAC χ^2/df	
		p	d	p	d
Ω_9	$1.075 \pm .009 \pm .010$	46/58	45/49	521/661	439/691
Λ_{12}	$1.060 \pm .009 \pm .015$	56/58	62/49	479/661	435/691

tive to their SLAC counterparts; and similarly for the BCDMS datasets. Thus, we fit both hydrogen and deuterium data simultaneously with a common normalization factor. For simplicity, we fit the data with weights determined by the quadrature sum of statistical and systematic errors, excluding the two above-mentioned correlated uncertainties of BCDMS.

The results of the SLAC+EMC normalization fits are shown in Table 5.14. The systematic uncertainties in the table reflect an extensive study of the dependence of the normalization parameters on a wide variety of kinematic cuts placed on the data (though, we do not use any data of $Q^2 > 50$ GeV^2). The χ^2/df quoted in Table 5.14 are for all data of $Q^2 < 50$ GeV^2, and are typical of all fits regardless of the kinematic cuts. The difference between models is an estimate of the systematic uncertainty in the normalization due to model dependence. We conclude that the relative normalization factor of the EMC data to the SLAC data is $1.07 \pm .02$. While this value is somewhat larger than the normalization uncertainty of the EMC data, it is in good agreement with comparisons[20,88] of the EMC iron F_2 values with F_2 measurements from ν-scattering on nuclear targets.[11,13,18]

We do not, however, quote the results of the SLAC+BCDMS normalization studies, as these fits produce uniformly unsatisfactory results. Though χ^2's of less than 1 per degree of freedom are easily obtained, they are characterized by small SLAC

contributions (as in Table 5.12) and much larger χ^2/df contributions from BCDMS. In particular, these best fit curves fit the data very poorly between $x = .18$ and $x = .275$: consistently greater than the high-Q^2 SLAC data and consistently less than the low-Q^2 BCDMS data.

We conclude from this study that SLAC and BCDMS agree in overall normalization to $\pm 3\%$, but we maintain the reservation that there remains a large x-dependent disagreement between the SLAC and BCDMS datasets. Although it is possible to understand the disparity at $x = .65$ and $x = .55$ in terms of a ~ 2 standard deviation effect in spectrometer calibration and/or resolution, it is not possible to match both the low-x data ($.18 \leq x \leq .275$) and the medium-x data ($x = .35$ and $.45$) with a single normalization constant.

We have considered the possibility that large x-dependent systematic problems pervade the SLAC dataset. This we consider extremely unlikely for several reasons. First and foremost, is the relative simplicity of the SLAC experimental apparatus and data reduction procedures compared to those of EMC and BCDMS. For example, the SLAC scattering kinematics are known very precisely, and the SLAC cross sections measurements do not rely on monte carlo studies of acceptances or efficiencies. Second, the SLAC results are extracted from many experiments, thereby reducing the impact of any single systematic error in any one experiment. Large systematic errors common to all experiments would have to lie in the incident electron beam monitoring and control systems. Such effects, however, are refuted by a series tests and recalibrations performed during the lifetime of those systems.[51,53,92] And third, large problems due to radiative corrections are unlikely because of the favorable propagation of the difference in Equation 3.11 through the F_2 extraction (Equation 5.39).

We conclude, therefore, that the source of the disagreement between EMC and BCDMS, as shown in Figure 1.2, lies in uncorrected systematic effects within both datasets. First, the EMC data is inconsistent with the carefully evaluated SLAC

normalization uncertainties. We conclude that EMC data is too low by a factor of $1.07 \pm .02 \pm .02$, where the second error is the overall SLAC normalization uncertainty. And second, we observe a significant x-dependent disparity between the SLAC and BCDMS datasets which is well outside the carefully evaluated and propagated SLAC systematic errors. This SLAC/BCDMS disparity is of the same size and direction as the x-dependent component of the EMC/BCDMS discrepancy shown in Figure 1.2, indicating that some uncorrected x-dependent effect may persist within the BCDMS dataset.

5.4.4 *Neutron/Proton Studies*

The new SLAC results for σ^d/σ^p are tabled in Appendix E. We obtain F_2^d/F_2^p from σ^d/σ^p under the assumption that $R^d = R^p$.† We note that the δ^{SY}, δ^{SE}, and δ^{RC} components of the error vector approximately cancel in the cross section ratio, and so are neglected in this analysis. The overall normalization uncertainty of the SLAC σ^d/σ^p ratios is conservatively estimated to be $\pm 1\%$ (see Section 5.2.4).

As the calculation of Fermi smearing corrections is outside the scope of this thesis, we work entirely with $(F_2^n/F_2^p)_S$, defined as the "smeared," or non-Fermi corrected, neutron/proton structure function ratio, given by

$$\begin{aligned} \left(\frac{F_2^n}{F_2^p}\right)_S &\equiv \left[\frac{2F_2^d}{F_2^p} - 1\right] , \\ &= S_n^{-1}\left(\frac{F_2^n}{F_2^p}\right) + (S_p^{-1} - 1) , \end{aligned} \tag{5.46}$$

where S_n and S_p are the ratios of unsmeared to smeared F_2^n and F_2^p, respectively. Our primary interest (see Section 1.1.3) is in the slope of F_2^n/F_2^p with respect to $[\ln Q^2]$, and so, we limit the main emphasis of our study to the $x < .7$ region, where smearing effects contribute negligibly to this slope.[93]

† The uncertainty in this assumption, given by Equation 5.29, generates a δ^{SZ} component in the error vector of σ^d/σ^p of roughly $\pm .2\%$. This, however, we choose to ignore, in the spirit of other F_2^n/F_2^p analyses.[21,26]

Phenomenologically, the SLAC $(F_2^n/F_2^p)_S$ are fit quite well by a simple parameterization,

$$\left(\frac{F_2^n}{F_2^p}\right)_S = P_1(x) + P_2(x)\left[\ln Q^2\right] \ , \tag{5.47}$$

where

$$\begin{aligned} P_1(x) = \ & .9004 - .0262x - 6.0915x^2 + 15.8103x^3 - 12.8660x^4 \ , \\ P_2(x) = & -.0035 - .2333x + 1.7832x^2 - \ 5.0908x^3 + \ 4.6070x^4 \ . \end{aligned} \tag{5.48}$$

These parameters are determined with the χ^2 minimization program FITPAR (see Section 5.2.2) working in the logarithmic variable of Appendix B.2, with weights determined by the quadrature sum of statistical and systematic errors. We avoid resonance effects by including in this fit only data for which $W^2 \geq 4$ GeV^2. The χ^2/df of this fit is 487/527, with an experiment-by-experiment breakdown closely resembling those of Table 5.3.

Figure 5.18 presents a contour map of the x dependence of $(F_2^n/F_2^p)_S$ for several values of Q^2, as represented by the above parameterization. The dramatic rise above $x = .7$ observed for large Q^2 is due to the uncorrected Fermi smearing of the deuterium structure function.

The slope of $(F_2^n/F_2^p)_S$ with respect to $\left[\ln Q^2\right]$ is shown in Figure 5.19. In this figure, the solid curve represents $P_2(x)$, and the sparse dotted curves represent one standard deviation uncertainties in $P_2(x)$. The points shown are the results of linear regression analyses to the SLAC $(F_2^n/F_2^p)_S$ data when binned into artificial x-spectra (see Figure 5.20 and Table 5.15 below). Also shown in Figure 5.19 are next to leading order calculations[93] of $\mathrm{d}\left[F_2^n/F_2^p\right]/\mathrm{d}\left[\ln Q^2\right]$ in the SLAC Q^2 range based on QCD and on QCD+TM.

We observe that $(F_2^n/F_2^p)_S$ falls as $\left[\ln Q^2\right]$ with a significant slope, in excellent agreement with QCD and QCD+TM. Motivated by the flatness of the data at low x, we determine the average slope over prediction, we determine the average slope over the $x \leq .5$ region by refitting the data to the model of Equation 5.47, constraining P_2

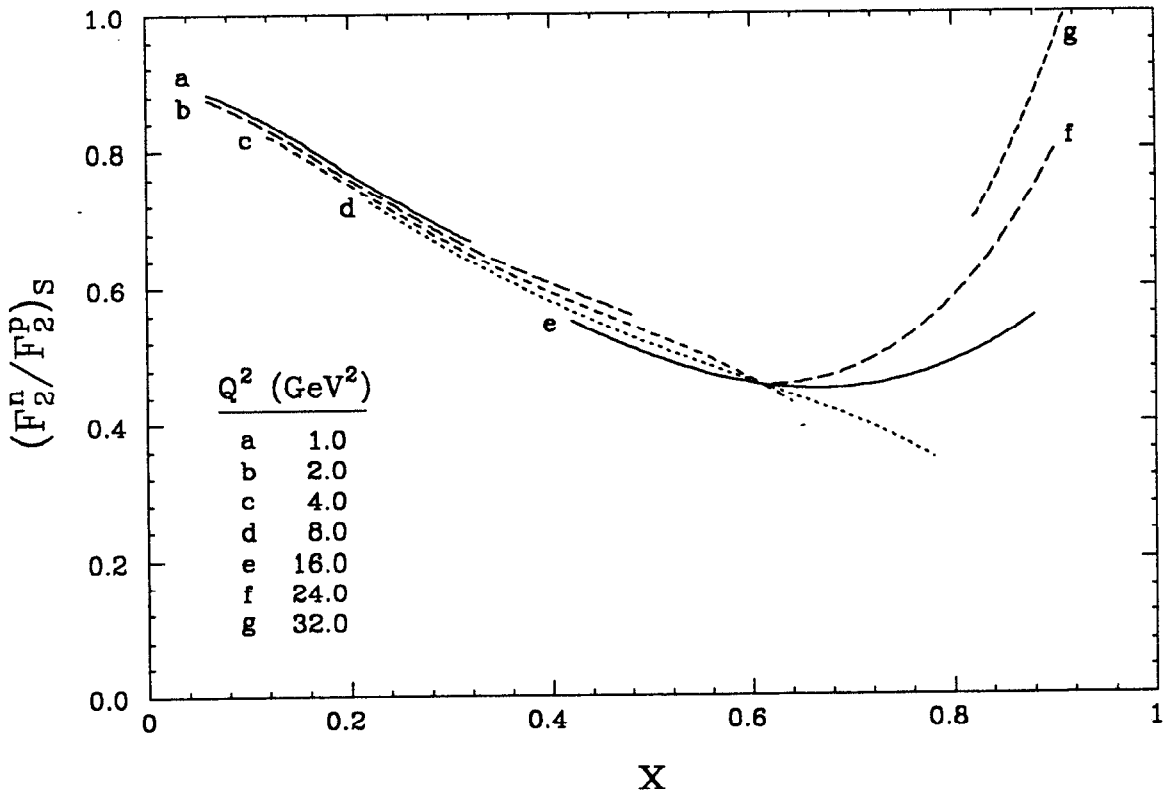

Figure 5.18. Shown is a contour map of the best fit to the SLAC $(F_2^n/F_2^p)_S$ data.

to a constant value. The best fit model, valid only for the range $x \leq .5$, is

$$\left(\frac{F_2^n}{F_2^p}\right)_S = .9498 - .9706x + .3102x^2 - .0146\left[\ln Q^2\right] , \tag{5.49}$$

with a χ^2/df of 312/331. The statistical uncertainty in this slope is $\pm.0040$, and we estimate an additional systematic uncertainty of $\pm.0030$ which accounts for the non-cancellation of some systematic effects in the cross section ratio, of roughly size $\pm 1\%$ over a $\times 10$ span in Q^2, averaged over all experiments. Thus, we conclude that for $x \leq .5$ and for SLAC values of Q^2

$$\frac{\mathrm{d}}{\mathrm{d}[\ln Q^2]}\left(\frac{F_2^n}{F_2^p}\right)_S = -.015 \pm .004 \pm .003 , \tag{5.50}$$

in good agreement with the mean QCD prediction over this range of $-.010$.

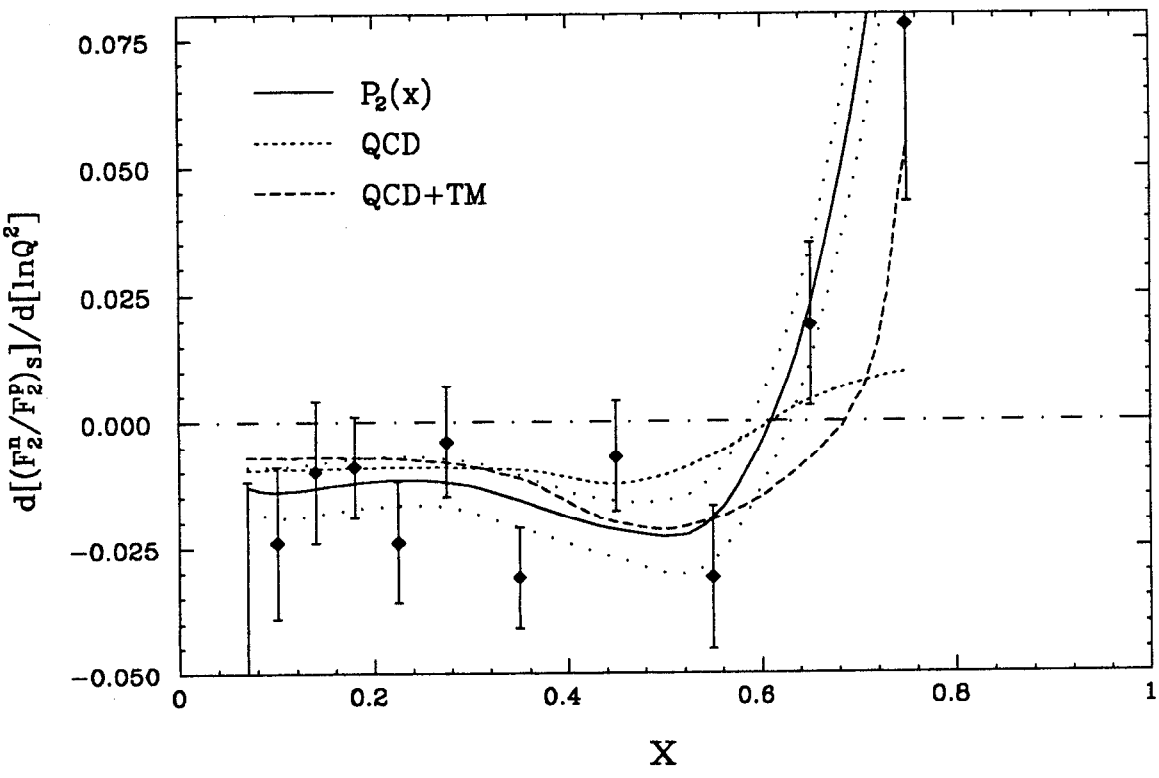

Figure 5.19. Shown is the derivative of $(F_2^n/F_2^p)_S$ with respect to Q^2 as determined by the best fit to Equation 5.47. Also shown are calculations of this slope based on QCD and on QCD+TM. See text for more details.

The slopes we observe in Figure 5.19 explain the systematic disparity in F_2^n/F_2^p between SLAC, EMC and BCDMS shown in Figure 1.4. To demonstrate this, we compare the best fit to the SLAC $(F_2^n/F_2^p)_S$ ratios, Equations 5.47 and 5.48, with $(F_2^n/F_2^p)_S$ from EMC and BCDMS, obtained via Equation 5.46. We similarly make the simplifying approximation that all systematic errors cancel in the ratio of F_2^d/F_2^p, with the exception of an overall normalization uncertainty of $\pm 3\%$ for EMC[21] and $\pm 2\%$ for BCDMS.[26]

Figures 5.20 and 5.21 compare the SLAC $(F_2^n/F_2^p)_S$ results with those of BCDMS and EMC. The SLAC data shown here are obtained by binning the data into x-spectra, then condensing the data with respect to $[\ln Q^2]$ (see Section 5.4.2). The solid lines

shown in these figures are the best fit of Equations 5.47 and 5.48, in excellent agreement with both the BCDMS and the EMC data, except at very large x where smearing effects become important.

Also shown in Figures 5.20 and 5.21 are straight line fits to the SLAC+BCDMS data and SLAC+EMC data in each x-bin, represented by the dashed lines. As before, we only fit the SLAC data above $W^2 = 4$ GeV^2. In general there is excellent agreement between the solid and dashed lines in these figures. At $x \geq .65$ the span in $[\ln Q^2]$ of the SLAC data is quite small, and so, the SLAC data is fit equally well by the dashed lines of Figure 5.20.

The slopes of these mutual best fit lines to the SLAC+BCDMS and SLAC+EMC data are presented in Table 5.15. Identical fits to the SLAC data alone are shown for comparison (see also Figure 5.19). Each value in this table actually represents the "mean" slope determined from two regression analyses, one in $(F_2^n/F_2^p)_S$ and one in $(F_2^p/F_2^n)_S$ (see, for elucidation, the text to Equation 4.11 and also Appendix B.2). These fits yield uniformly good χ^2's, indicating good agreement between datasets. We estimate the systematic errors in the slopes of Table 5.15 to be $\pm.003$ for the SLAC fits, $\pm.007$ for the SLAC+BCDMS fits, and $\pm.010$ for the SLAC+EMC fits. The dominant contributions to these systematic errors are the relative normalization uncertainties of the datasets.

In Figure 5.22 we compare the slopes of Table 5.15 to next to leading order calculations[93] of $\mathrm{d}[F_2^n/F_2^p]/\mathrm{d}[\ln Q^2]$ based on QCD and QCD+TM. We observe fair agreement between the SLAC+BCDMS slopes and QCD+TM, though the data seem consistently lower. This apparent disagreement with theory is less alarming in light of the x-dependent discrepancies between the SLAC and BCDMS hydrogen and deuterium datasets (see Section 5.4.3), some of which, might not perfectly cancel in the σ^d/σ^p ratio. A more careful propagation of systematic errors would likely result in larger uncertainties in the SLAC+BCDMS slopes. We observe excellent agreement, on the other hand, between the SLAC+EMC slopes and the QCD+TM calculations.

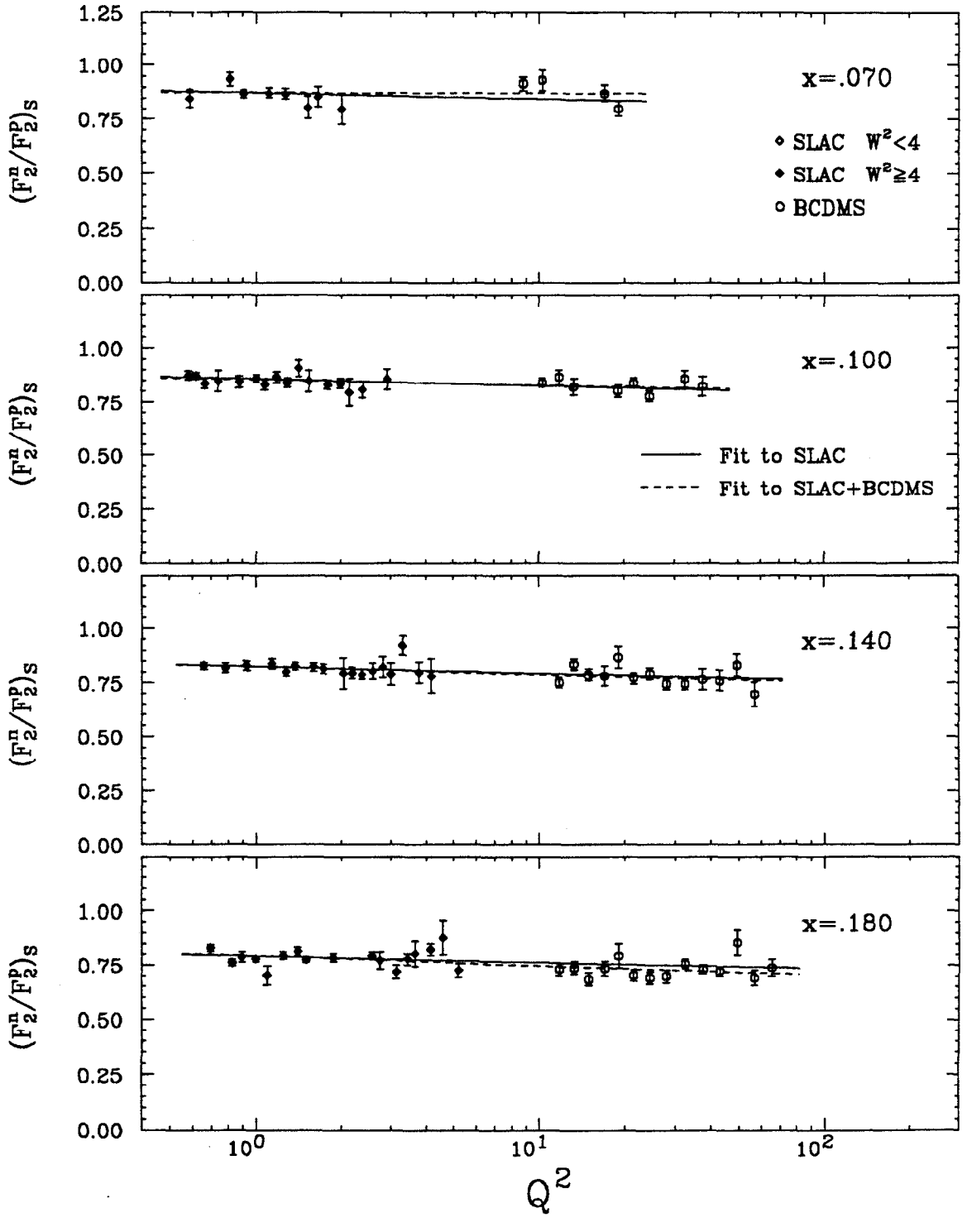

Figure 5.20. Shown is a comparison of the SLAC $(F_2^n/F_2^p)_S$ results with those of BCDMS. A relative normalization of 1.000 is assumed. The solid lines show the best fit of the SLAC data given by Equations 5.47 and 5.48. The dashed lines show the best linear fit to the combined data in each x-spectra. Figure continues on next two pages.

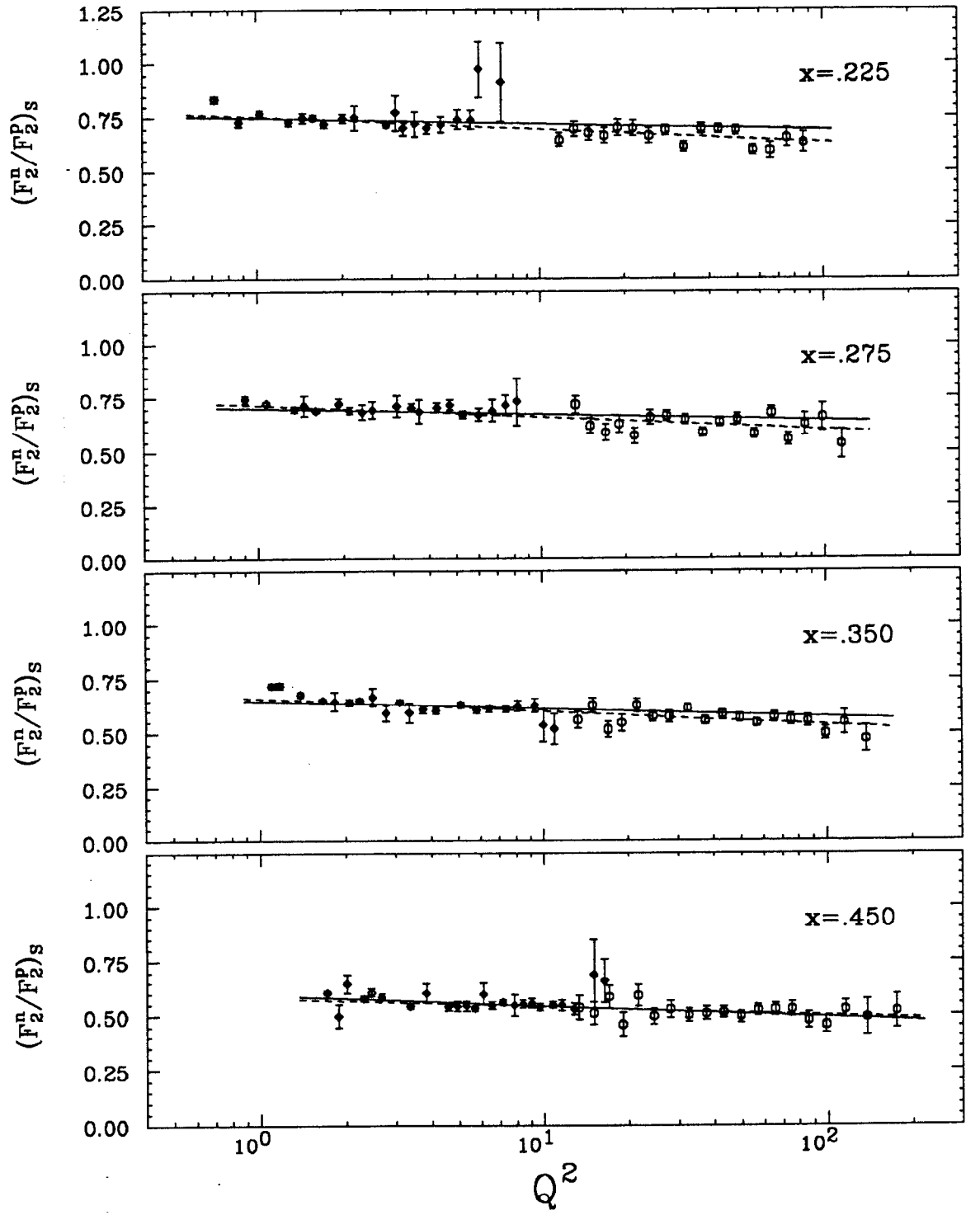

Figure 5.20/continued: Comparison of SLAC and BCDMS $(F_2^n/F_2^p)_S$ results.

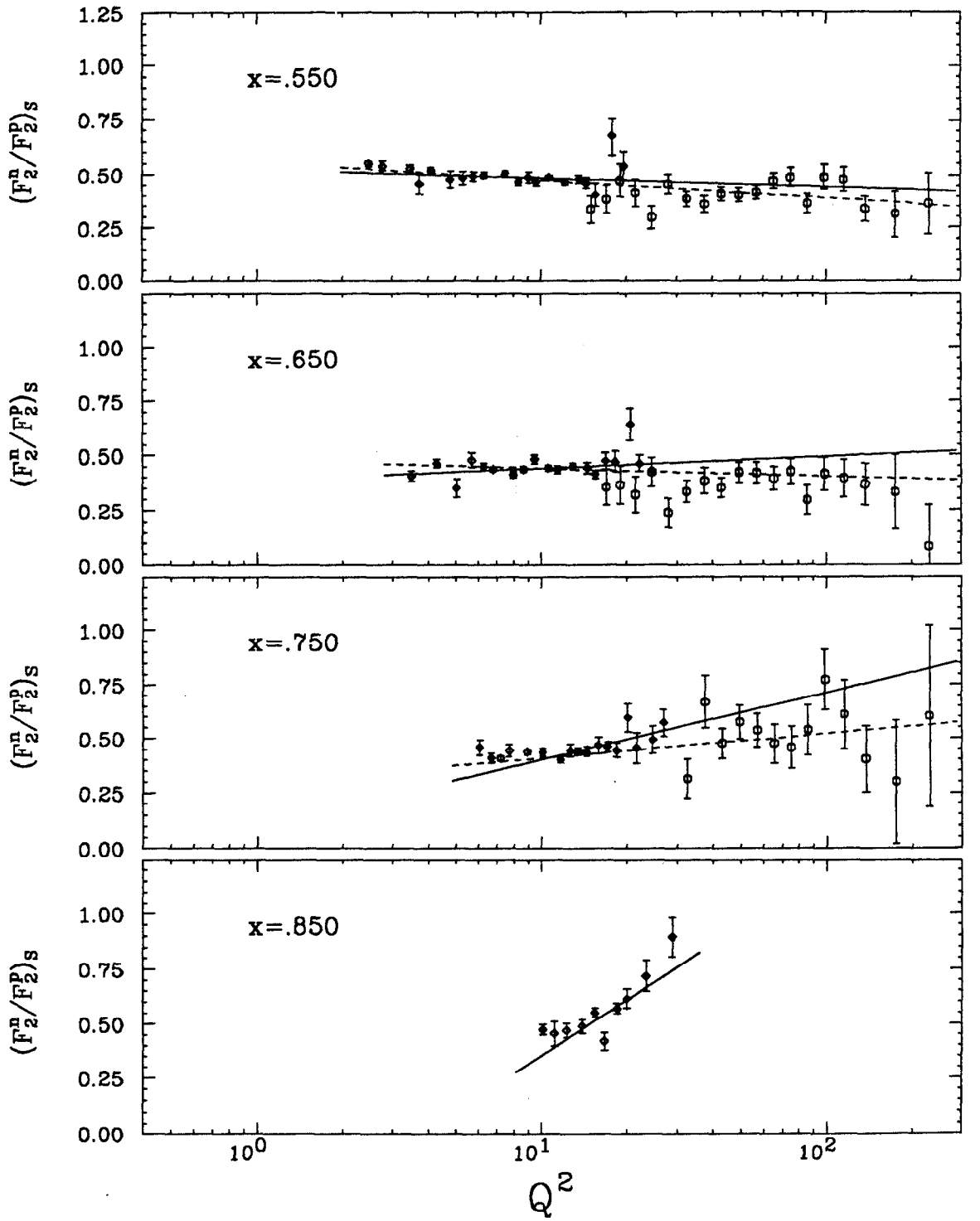

Figure 5.20/continued: Comparison of SLAC and BCDMS $(F_2^n/F_2^p)_S$ results.

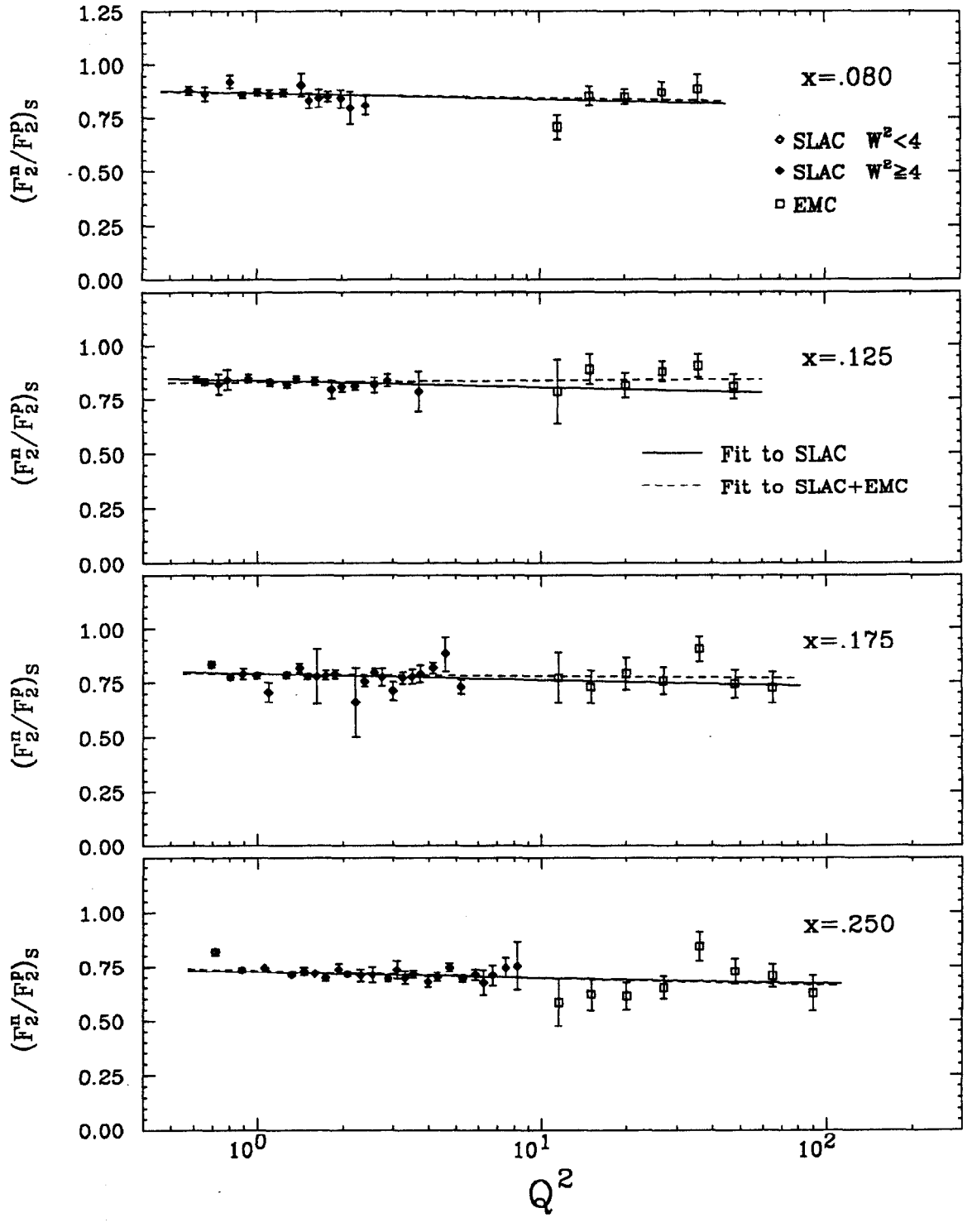

Figure 5.21. Shown is a comparison of the SLAC $(F_2^n/F_2^p)_S$ results with those of EMC. A relative normalization of 1.000 is assumed. The solid lines show the best fit of the SLAC data given by Equations 5.47 and 5.48. The dashed lines show the best linear fit to the combined data in each x-spectra. Figure continues on next page.

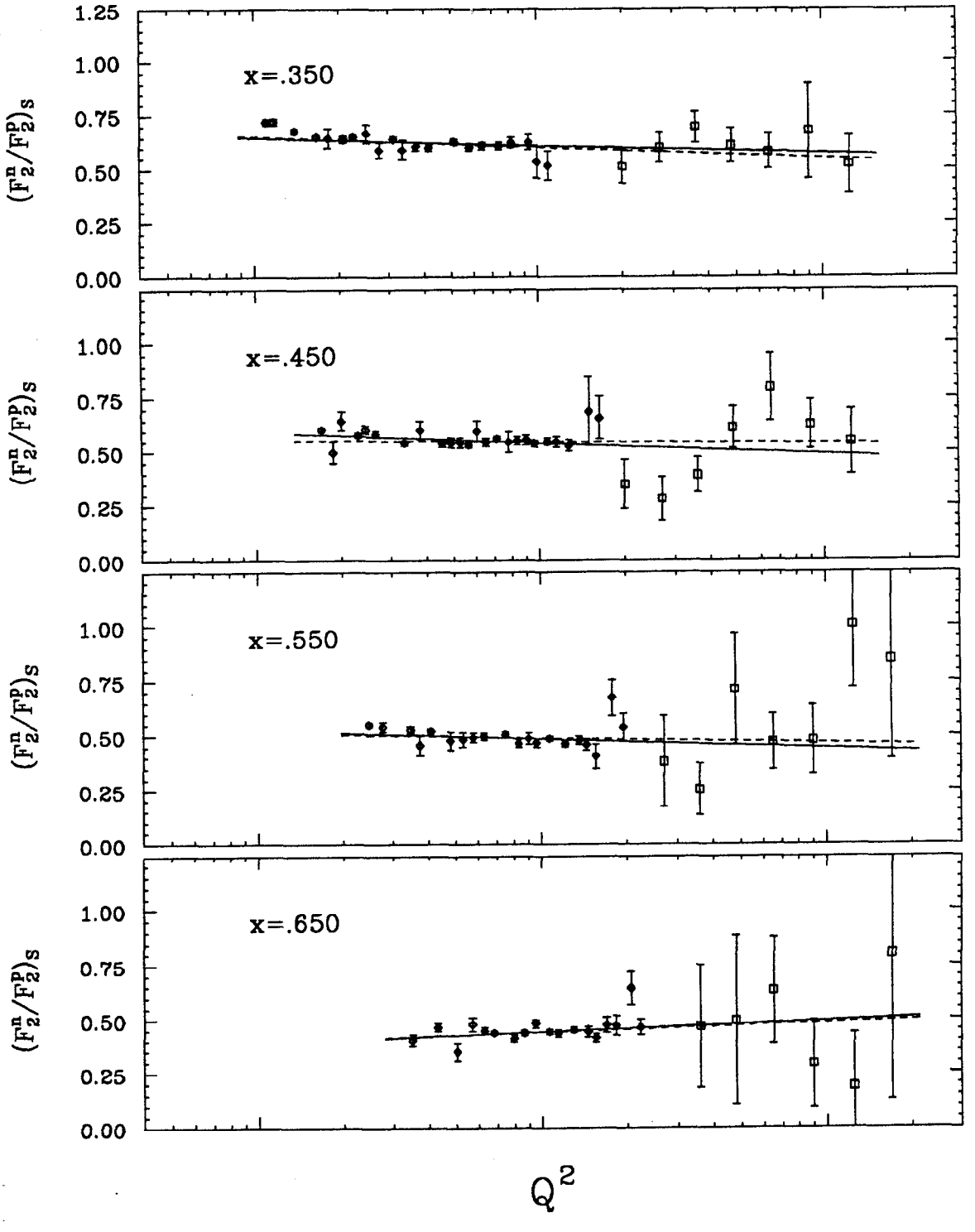

Figure 5.21/continued: Comparison of SLAC and EMC $(F_2^n/F_2^p)_S$ results.

Table 5.15. Shown are the best fit slopes, $d[(F_2^n/F_2^p)_S]/d[\ln Q^2]$, of the SLAC, SLAC+BCDMS and SLAC+EMC datasets, as shown in Figures 5.19, 5.20, and 5.21, respectively. Errors shown are statistical. See text for details and estimates of systematic errors.

	Slope	χ^2/df	Slope	χ^2/df	χ^2/df
x	SLAC	SLAC	SLAC+BCDMS	SLAC	BCDMS
.070	$-.052 \pm .042$	5 / 6	$-.001 \pm .008$	7 / 7	8 / 3
.100	$-.024 \quad .015$	7 / 14	$-.011 \quad .004$	7 / 15	7 / 7
.140	$-.010 \quad .014$	10 / 15	$-.015 \quad .004$	10 / 16	14 / 12
.180	$-.009 \quad .010$	24 / 15	$-.020 \quad .003$	25 / 16	18 / 13
.225	$-.024 \quad .012$	12 / 15	$-.025 \quad .003$	12 / 16	23 / 15
.227	$-.004 \quad .011$	6 / 15	$-.025 \quad .003$	9 / 16	29 / 16
.350	$-.031 \quad .010$	11 / 15	$-.027 \quad .003$	12 / 16	20 / 17
.450	$-.007 \quad .011$	11 / 17	$-.017 \quad .004$	12 / 18	10 / 18
.550	$-.031 \quad .014$	15 / 14	$-.037 \quad .006$	15 / 15	33 / 18
.650	$.019 \quad .016$	17 / 12	$-.016 \quad .008$	23 / 13	19 / 17
.750	$.078 \quad .035$	8 / 10	$.045 \quad .017$	10 / 11	13 / 12
.850	$.076 \quad .182$	0 / 2			
Total χ^2/df:		126 / 150		149 / 159	194 / 147

	Slope	χ^2/df	χ^2/df
x	SLAC+EMC	SLAC	EMC
.080	$-.009 \pm .007$	8 / 13	8 / 4
.125	$.004 \quad .007$	7 / 14	3 / 5
.175	$-.005 \quad .006$	14 / 21	6 / 6
.250	$-.015 \quad .005$	23 / 21	11 / 7
.350	$-.022 \quad .008$	20 / 16	4 / 6
.450	$-.003 \quad .009$	10 / 18	17 / 6
.550	$-.010 \quad .013$	33 / 15	9 / 6
.650	$.019 \quad .016$	19 / 13	3 / 5
Total χ^2/df:		134 / 139	61 / 45

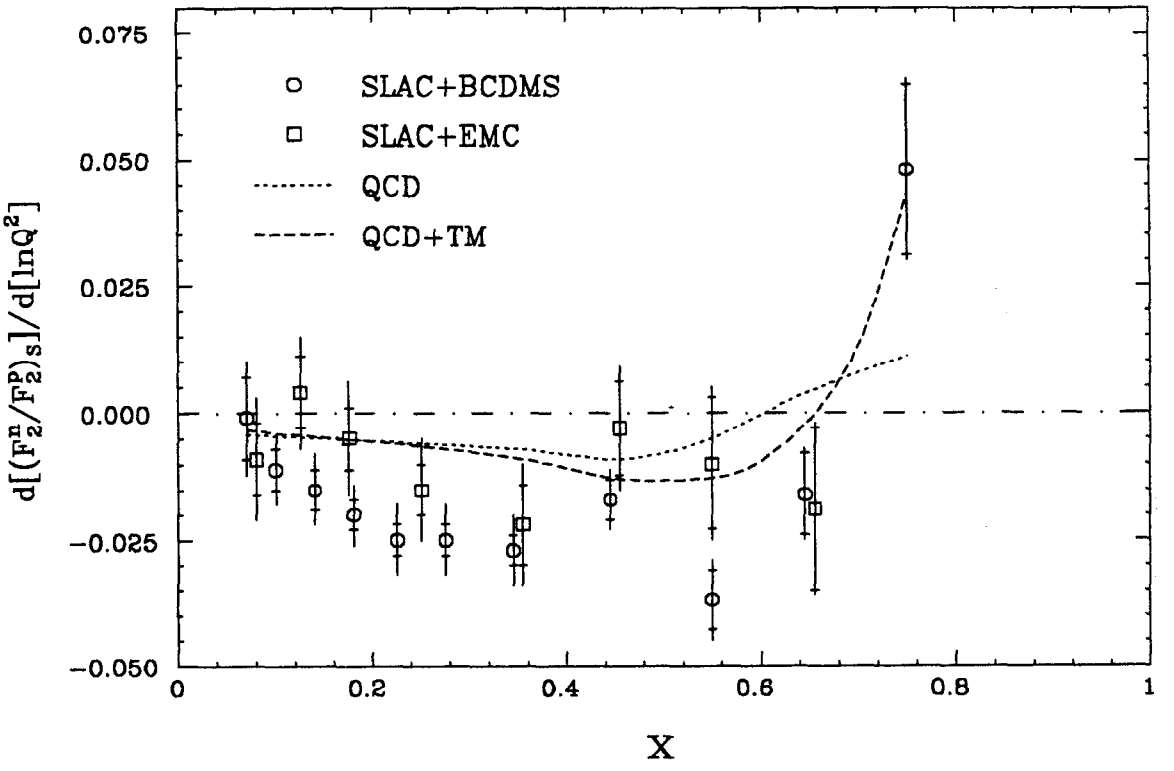

Figure 5.22. Shown are the values of $d[(F_2^n/F_2^p)_S]/d[\ln Q^2]$ extracted from linear regression analyses to the data of Figures 5.20 and 5.21 (dotted lines).

In conclusion, we resolve the SLAC, EMC, and BCDMS F_2^n/F_2^p disparity shown in Figure 1.4 in terms of a logarithmic Q^2 dependence of $(F_2^n/F_2^p)_S$. The SLAC $(F_2^n/F_2^p)_S$ data displays a significant non-zero slope in $[\ln Q^2]$, in good agreement with QCD calculations in the SLAC Q^2 range. Combined studies of the SLAC+EMC and SLAC+BCDMS confirm this falloff with $[\ln Q^2]$ out to very large values of Q^2, in excellent agreement with the results of the SLAC analysis, and in good agreement with QCD calculations at these higher Q^2.

Chapter 6

Concluding Remarks

The analysis presented here successfully unifies the pre-existing body of deep inelastic cross section measurements at SLAC with those of our recent experiment E140. The resulting global dataset displays a remarkable homogeneity and a statistical robustness when probed with a wide range of analytical tools. Within a framework of rigorous error analysis and propogation, we report new highly precise extractions of the structure functions R and F_2 over the entire SLAC kinematic range.

In this analysis we report several important fundamental observations. First, we measure no nucleon (or nuclear) dependence to R. This observation places sharp constraints on those nonperturbative contributions to parton dynamics which would generates large differences between R^d and R^p, for example, diquark formation.

Second, we observe that R is systematically and significantly much larger than $R^{\mathrm{QCD+TM}}$ over the entire SLAC kinematic range. This observation stands as a challenge for theorists and phenomenologists to develop the tools needed to understand the next to leading twist contributions to nucleon structure. Additionally, we report best fit phenomenological models of R and the uncertainty in R, $R^{1990}(x,Q^2) \pm \delta R^{1990}(x,Q^2)$, which can be used to extract F_1 and F_2 from any deep inelastic lepton scattering cross section measurement.

Third, we report new values of F_2 for hydrogen and deuterium throughout the SLAC kinematic range which set new standards for future structure function measurements. The $\pm 2\%$ overall normalization uncertainty of E140 combines with the

kinematic reach of seven other SLAC experiments to yield high precision structure functions measurements out to high Q^2 and over a wide range in x. Using these new structure functions we note excellent agreement with the higher-Q^2 EMC structure functions multiplied by a simple normalization factor of 1.07. We do not, however, find such agreement with the BCDMS data. Rather, we observe a significant x-dependent disparity between the SLAC and BCDMS structure functions consistent with previous comparisons of the EMC and BCDMS results.

And fourth, we resolve the historical disparity in F_2^n/F_2^p ratios between the high Q^2 data of EMC and BCDMS and the low Q^2 data of SLAC. We observe a statistically significant falloff of F_2^n/F_2^p with Q^2, in good agreement with calculations based on QCD. Extrapolations of this effect to high Q^2 are in excellent agreement with both EMC and BCDMS F_2^n/F_2^p ratios.

Possible future extensions of this work include phenomenological analyses of the higher twist contributions to R and F_2. The second of these can be done in context of a full QCD analysis over the two decades in Q^2 spanned by electron and muon scattering data. Within the SLAC kinematic range, it is still possible to improve on the work reported here, most importantly in understanding the x dependence of R, which is sensitive to competing higher twist effects. Lastly, a large amount of SLAC data exists for the resonance region which could be subjected to a similar, albeit more difficult, global reanalysis and structure function extraction.

Appendix A

Review of Deep Inelastic Scattering

This appendix is provided as a brief reference for deep inelastic electron scattering. The first section is a concise statement of the scattering kinematics used in this report. The second section is an intuitive introduction to the subject of deep inelastic electron scattering at an elementary level.

A.1 Kinematics

In deep inelastic electron scattering at SLAC, an incident electron of high energy, E_o, scatters from a nuclear target at rest in the laboratory frame. The scattered lepton is detected and is measured to scatter through an angle, θ, with secondary energy, E'.

In the first Born approximation, the electron scattering takes place through the exchange of a single virtual photon which carries energy ν and invariant momentum transfer Q^2, where

$$\begin{aligned} \nu &= E_o - E' \ , \\ Q^2 \equiv -q^2 &= 4\, E_o\, E' \sin^2(\frac{\theta}{2}) \ . \end{aligned} \tag{A.1}$$

Here, and elsewhere, we take $\hbar \equiv c \equiv 1$ and we neglect the rest mass of the electron. The square of the invariant mass of the undetected final hadronic state is

$$W^2 = M_p^2 + 2M_p\nu - Q^2 \ , \tag{A.2}$$

where M_p is the rest mass of the proton.

The differential cross section for deep inelastic scattering from a nuclear target is completely calculable in QED. This cross section is expressible in terms of two structure functions F_1 and F_2 which parameterize the virtual photon-nucleon coupling and contain all the interesting physics,

$$\sigma \equiv \frac{\partial^2\sigma}{\partial\Omega\partial E'} = \sigma^{mott}\left[\frac{1}{\nu}F_2(x,Q^2) + \frac{2}{M_p}F_1(x,Q^2)\tan^2(\frac{\theta}{2})\right] , \tag{A.3}$$

where

$$\sigma^{mott} = \frac{4\alpha^2 E'^2}{Q^4}\cos^2(\frac{\theta}{2}) \tag{A.4}$$

is the nonstructure Mott cross section, α is the fine structure constant, and x is the Bjorken scaling variable,

$$x = \frac{Q^2}{2M_p\nu} . \tag{A.5}$$

Alternatively, one can view the scattering process as the production and absorption of a single virtual photon. From this perspective, the cross section is expressible in terms of σ_T and σ_L, the cross sections for the absorption of transverse and longitudinal photons,

$$\sigma = \Gamma\left[\sigma_T(x,Q^2) + \epsilon\,\sigma_L(x,Q^2)\right] , \tag{A.6}$$

where Γ is the flux of transverse virtual photons,

$$\begin{aligned} \Gamma &= \frac{\alpha}{4\pi^2}\frac{kE'}{Q^2E_o}\left(\frac{2}{1-\epsilon}\right) , \\ k &= \frac{W^2 - M_p^2}{2M_p} , \end{aligned} \tag{A.7}$$

and $\epsilon \in [0,1]$ is the relative flux of longitudinal virtual photons,

$$\epsilon = \left[1 + 2(1+\frac{\nu^2}{Q^2})\tan^2(\frac{\theta}{2})\right]^{-1} . \tag{A.8}$$

One of the major goals of our effort is the extraction of the ratio $R = \sigma_L/\sigma_T$, which is expressed in terms of F_1 and F_2 as

$$R(x,Q^2) \equiv \frac{\sigma_L}{\sigma_T} = \frac{F_2}{2xF_1}(1+\frac{4M_p^2x^2}{Q^2}) - 1 \ . \tag{A.9}$$

The relationship of F_1 and F_2 to σ_T and σ_L is given by

$$\begin{aligned} F_1(x,Q^2) &= \frac{k}{4\pi^2\alpha} M_p \, \sigma_T(x,Q^2) \ , \\ F_2(x,Q^2) &= \frac{k}{4\pi^2\alpha} \nu (1+\frac{\nu^2}{Q^2})^{-1} \left[\sigma_T(x,Q^2) + \sigma_L(x,Q^2)\right] \ . \end{aligned} \tag{A.10}$$

Frequently, the literature makes reference to the longitudinal structure function, F_L, which is defined by

$$F_L \equiv F_2 - 2xF_1 + (\frac{4M_p^2x^2}{Q^2})F_2 \ , \tag{A.11}$$

and in terms of which we can write

$$R = \frac{F_L}{2xF_1} \ . \tag{A.12}$$

A.2 Structure Functions

In the first part of this section, we consider a simple non-relativistic description of electron scattering as an introduction to structure functions and form factors. In the second part we extend these ideas to the relativistic case, in particular, interpreting the deep inelastic structure functions described in this thesis in terms of the quark/parton model of the nucleon.

Consider the case of electron scattering from a target composed of N well-defined constituents and characterized by an initial state vector $|\Psi_i\rangle$. Assume that the final state, $|\Psi_f\rangle$, be unobserved and denote the incident and final electron 4-momenta by $P_\circ = (\vec{p}_\circ, E_\circ)$ and $P' = (\vec{p}', E')$, respectively.

A.2.1 Non-Relativistic Treatment

We use first-order perturbation theory for the transition rate from initial to final states (Fermi's Golden Rule), to calculate the cross section,

$$\frac{\partial^2\sigma}{\partial\Omega\partial E'} = \sum_f \left|\langle P'\Psi_f|H_I|P_\circ\Psi_i\rangle\right|^2 \delta\left(E_f - E_i - \nu\right) \frac{p'^2}{(2\pi)^3 v}\frac{dp'}{dE'} \ , \tag{A.13}$$

where v is the beam velocity, E_i and E_f are the initial and final energies of the target, and H_I is the interaction Hamiltonian. As H_I consists only of 2-body interactions between the electron and the target constituents, we write

$$H_I = \sum_{j=1}^{N} V_j(\vec{r}-\vec{r}_j) \ . \tag{A.14}$$

For electromagnetic interactions we make Born's first approximation, that the electron and target states are independent. Then, we note the following simplification within the matrix element of Equation A.13,

$$\begin{aligned} \langle P'|V_j(\vec{r}-\vec{r}_j)|P_\circ\rangle &= \int d^3r\, \mathrm{e}^{i(\vec{p}\,'-\vec{p}_\circ)\cdot\vec{r}}\, V_j(\vec{r}-\vec{r}_j) \ , \\ &= \mathrm{e}^{i\vec{q}\cdot\vec{r}_j}\, T_j(\vec{q}) \ , \end{aligned} \tag{A.15}$$

where

$$T_j(\vec{q}) = \int d^3r\, \mathrm{e}^{i\vec{q}\cdot\vec{r}}\, V_j(\vec{r}) \tag{A.16}$$

is recognizable as the elastic scattering amplitude for scattering off the jth constituent with momentum transfer $\vec{q}\equiv\vec{p}\,'-\vec{p}_\circ$.

Consider the special case where the $V_j(r_j)$ represent only the Coulomb interactions due to spherically symmetric charge distributions $\rho_j(r_j)$,

$$V_j(\vec{r}) = \int d^3r_j \, \frac{\rho_j(r_j)}{|\vec{r}-\vec{r}_j|} \ , \tag{A.17}$$

as in electron scattering from spin-0 nuclei. Then, $T_j(\vec{q})$ simplifies to

$$T_j(q^2) = \frac{4\pi}{q^2} F_j(q^2) \ , \tag{A.18}$$

where $F_j(q^2)$ is defined as the *elastic form factor* of the jth constituent, given by

$$F_j(q^2) \equiv \int d^3r \, \mathrm{e}^{i\vec{q}\cdot\vec{r}} \, \rho_j(r) \ , \tag{A.19}$$

and with the clear interpretation as the 3-dimensional Fourier transform of constituent charge distribution. Note that $F_j(0) = \mathcal{Q}_j$ normalizes the F_j to the static charges of the constituents. Note also that structureless constituents would yield $F_j = \mathcal{Q}_j$. The matrix element of Equation A.13 thereby reduces to

$$\mathcal{M}_{if}(q^2) = \langle \Psi_f | \sum_j F_j(q^2) \, \mathrm{e}^{i\vec{q}\cdot\vec{r}_j} | \Psi_i \rangle \ , \tag{A.20}$$

in terms of which, we define the target *structure function,*

$$W(\nu, q^2) \equiv \sum_f \left| \mathcal{M}_{if}(q^2) \right|^2 \delta(E_f - E_i - \nu) \ . \tag{A.21}$$

The cross section of Equation A.13 can thus be expressed in the simple form

$$\frac{\partial^2\sigma}{\partial\Omega \partial E'} = \left(\frac{d\sigma}{d\Omega} \right)_{Ruth} W(\nu, q^2) \ , \tag{A.22}$$

where

$$\left(\frac{d\sigma}{d\Omega} \right)_{Ruth} = \left[\frac{e^2}{2m_e v^2 \sin^2(\frac{\theta}{2})} \right]^2 \tag{A.23}$$

is the Rutherford cross section for electron scattering from a spin-0 structureless target.

Thus, all the interesting physics of the scattering process is dictated by the target structure function $W(\nu, q^2)$. Conversely, by comparing the measured cross section to

the Rutherford prediction one determines $W(\nu, q^2)$ and begins to decipher the internal structure of the target.

Consider the specific case of elastic scattering. The elastic cross section follows directly from Equation A.22,

$$\frac{d\sigma}{d\Omega} = \left(\frac{d\sigma}{d\Omega}\right)_{Ruth} |F(q^2)|^2 \ , \tag{A.24}$$

where $F(q^2)$ is defined to be the *elastic form factor* of the target and is given by

$$F(q^2) \equiv \mathcal{M}_{ii}(q^2) = \sum_j F_j(q^2) \langle \Psi_i | e^{i\vec{q}\cdot\vec{r}_j} | \Psi_i \rangle \tag{A.25}$$

(and where we have neglected the usual target recoil term $[1 + (2p_o/M)\sin^2(\frac{\theta}{2})]^{-1}$). Note that, as above, the target elastic form factor is normalized at $q^2 = 0$ to the total static charge of the target.

In the special case that all constituents are identical and the wavefunction is symmetric, then Equation A.25 simplifies to

$$F(q^2) = \sum_j F_j(q^2) \int d^3r_1 \ldots d^3r_N e^{i\vec{q}\cdot\vec{r}_j} \left| \langle \vec{r}_1, \ldots, \vec{r}_N | \Psi_i \rangle \right|^2 \ , \tag{A.26}$$

$$= N\, F_c(q^2) \int d^3r\, e^{i\vec{q}\cdot\vec{r}_j}\, \rho(\vec{r}) \ , \tag{A.27}$$

where $F_c(q^2)$ is the common constituent elastic form factor and where

$$\rho(\vec{r}) = \int d^3r_2 \ldots d^3r_N \left| \langle \vec{r}, \vec{r}_2, \ldots, \vec{r}_N | \Psi_i \rangle \right|^2 \tag{A.28}$$

is the single constituent density distribution. Here, $\rho(\vec{r})$ can be thought of as $|\Psi(\vec{r})|^2$ where $\Psi(\vec{r})$ is the wavefunction of an average pointlike constituent bound in the potential well formed by the other constituents. The integral in Equation A.27 is the

3-dimensional Fourier transform of this charge distribution and is termed the *body form factor*[94] of the target.

Thus, the measurable quantity, the elastic form factor of the target, is the product of constituent and body form factors,

$$F(q^2) = N\, F_c(q^2) \times F_b(q^2)\ . \tag{A.29}$$

In most applications the constituent size, R_c, is tremendously smaller than the target size, R_b. This implies $F(q^2) \sim F_b(q^2)$ in the range $qR_b \sim 1$. For example, the dramatic diffractive structure observed[95] in nuclear form factors at $q \ll 1$ fm^{-1} is due to scattering (transmission) resonances at $qR_b \sim n\pi/2$. Inverting the nuclear $F_b(q^2)$, one typically obtains[95] a flat charge distribution, $\rho(r)$, out to some well-defined R_b, beyond which $\rho(r)$ falls quickly to zero. The small r dependence of $\rho(r)$ dictates the asymptotic behavior of $F_b(q^2)$, and if $\rho(r)$ is normalizable at the origin, it follows[94] that $F_b(q^2)$ falls off at least as fast as $1/q^4$. Only at very large q^2, $qR_c \sim 1$, does the constituent form factor become important, though, in general, it can be quite difficult to separate constituent and body form factors.

In the case of electron-nucleon elastic scattering, one observes a smooth "dipole" elastic form factor, $F(q^2) = 1/(1 + q^2/.71\text{GeV}^2)^2$. The lack of resonant structure in $F(q^2)$ implies that R_b is not well defined, an idea consistent with the exponential charge distribution obtained by inverting $F(q^2)$. An estimate of the possible $F_c(q^2)$ contribution (quark substructure) to $F(q^2)$ would require that the large q^2 behavior of $F_b(q^2)$ be much more firmly understood in terms of QCD than at present.

The results presented here rely in part on several simplifying assumptions. Assumptions about $|\Psi_i\rangle$ are made only to simplify Equation A.25 to the more intuitive factorized form of Equation A.29. The assumption that H_I is purely Coulomb is likewise not critical – the inclusion of magnetic interactions generates a second form factor, magnetic in origin. The primary assumption of this presentation, however,

is the pertinence of a non-relativistic approach to a discussion of high energy electron scattering. For atomic or nuclear targets, this assumption is suitable, though, if we wish to address nucleon targets (composed of quarks and gluons), then we must extend our formalism into the relativistic domain.

A.2.2 Relativistic Treatment

A frame-independent treatment of electron scattering should be expressed in terms of Q^2, the invariant 4-momentum transfer, rather than q^2, as above. The invariant cross section can evaluated as above, though, the integration in Equation A.19 must be strictly an integral over space-time, with $[Q \cdot r]$ as a scalar product of 4-vectors. In general, therefore, $F(q^2)$ loses its interpretation as the Fourier transform of the spatial charge distribution, though, in the case of elastic scattering, $Q^2 \approx q^2$ (as the energy transfer is small) and we can still extract $\rho(r)$ by inverting $F(q^2)$. Thus, we see that for small energy transfers, the interaction time is large and the form factor accordingly reflects the time-average of the charge distribution. On the other hand, for large energy transfers we probe the "instantaneous" structure of the nucleon, which we interpret in terms of the invariant structure function, $W^{\mu\nu}$, the relativistic extension of Equation A.21.

The invariant cross section can be expressed in the form

$$\frac{\partial^2\sigma}{\partial\Omega\partial E'} = \frac{\alpha^2}{Q^4}\frac{E'}{E_\circ} L_{\mu\nu} W^{\mu\nu} \ , \tag{A.30}$$

where

$$L_{\mu\nu} = 2P_{\circ\mu}P'_\nu + 2P_{\circ\nu}P'_\mu - g_{\mu\nu}Q^2 \tag{A.31}$$

is the electron polarization tensor averaged over initial spin states,

$$W^{\mu\nu} = \sum_f \langle p|J^{\dagger\mu}|f\rangle\langle f|J^\nu|p\rangle\,\delta^4(p - p_f - Q) \tag{A.32}$$

is the unpolarized hadronic tensor (with an implied average over initial spins), and J^μ is the hadronic transition current. All the interesting target physics is contained

within $W^{\mu\nu}$. Without any *a prior* knowledge of nucleon structure it is possible to place strong constraints on the form of $W^{\mu\nu}$ and thus on the cross section. The most general form of $W^{\mu\nu}$ consistent with Lorentz and gauge invariances and parity is

$$\begin{aligned} W^{\mu\nu} &= W_1(\nu, Q^2)\left[\frac{Q^\mu Q^\nu}{Q^2} - g^{\mu\nu}\right] \\ &+ W_2(\nu, Q^2)\frac{1}{M_p^2}\left[p^\mu + \frac{M_p\nu}{Q^2}Q^\mu\right]\left[p^\nu + \frac{M_p\nu}{Q^2}Q^\nu\right] , \end{aligned} \tag{A.33}$$

where W_1 and W_2 are independent scalar functions of (ν, Q^2). Using this form in Equation A.30 yields

$$\frac{\partial^2\sigma}{\partial\Omega\partial E'} = \sigma^{mott}\left[W_2(\nu, Q^2) + 2W_1(\nu, Q^2)\tan^2(\frac{\theta}{2})\right] , \tag{A.34}$$

where σ^{mott} is given by Equation A.4. Here W_1 and W_2 are the two target structure functions reflecting the possibility of magnetic as well as electric scattering, or, alternatively, the possibility of photoabsorption of either transverse (helicity ± 1) or longitudinal (helicity 0) photons. Note that for structureless targets, W_1 and W_2 become constants and Equation A.34 reduces to the Dirac cross section for scattering from spin-$\frac{1}{2}$ targets.

It was suggested by Bjorken[96] that for large ν and Q^2, νW_2 and $M_p W_1$ should become functions solely of the ratio $x = Q^2/2M_p\nu$. This functional dependence was indeed observed[97] in the very early SLAC data, at least approximately, as shown in Figure A.1. Holding x fixed, as in this figure, is equivalent to imposing a delta function constraint on the structure function, $\delta(\nu - Q^2/2M_p x)$, and is similar to the delta function imposed by elastic scattering, namely, $\delta(\nu - Q^2/2M_p)$. If the nucleon constituents had internal structure (on this scale of $R_c \sim Q^{-1}$), denoted by $F_c(q^2)$, then, in analogy with the previous section, we would expect the data in Figure A.1 to be damped by an additional factor of $|F_c(q^2)|^2$. Thus, the lack of pronounced Q^2 dependence, known as scaling, suggests that the nucleon constituents are pointlike (see also Figure 5.14).

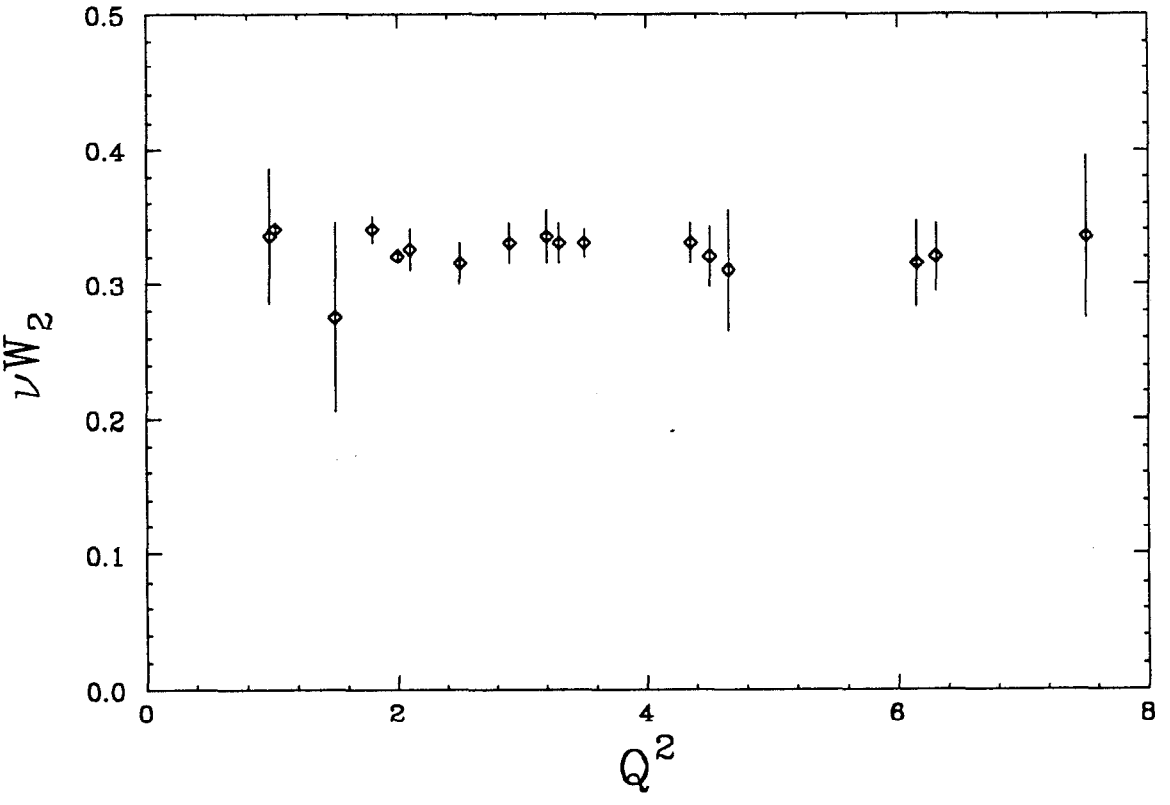

Figure A.1. Shown is an early observation[97] of scaling at $x = .25$. The abscissa is in units of GeV^2.

A simple approach to understanding this scaling phenomenon is offered by the naive parton model.[98,99] In this model, the nucleon is assumed to consist of a collection of pointlike constituent partons with well defined quantum numbers. Viewed from a frame in which the nucleon is highly relativistic, the so-called infinite momentum frame, deep inelastic scattering is seen to be simply incoherent scattering from the individual partons. In this highly boosted frame, the partons recombine to form the final hadronic state over a much longer time scale than that of the collision, and so, it is precise to consider these as quasi-free non-interacting particles. In this frame, the Bjorken scaling quantity, x, is identifiable as the momentum fraction of the elastically scattered parton. Spin-$\frac{1}{2}$ partons thus contributing incoherently to the Dirac cross

section yield the observable structure functions

$$\begin{aligned} F_1(x) \equiv M_p W_1 &= \sum_i f_i(x) Q_i^2 \ , \\ F_2(x) \equiv \ \nu W_2 &= x \sum_i f_i(x) Q_i^2 \ , \end{aligned} \tag{A.35}$$

where $f_i(x)$ is the probability density of finding the ith parton with fractional momentum x. The Callan-Gross relation, $F_2 = 2xF_1$, is a direct consequence of spin-$\frac{1}{2}$ partons and is strongly supported experimentally. To complete the identification of these partons with the quarks of Gell-Mann and Zweig[100] one compares electron and neutrino scattering results for F_1 and F_2 to infer the fractional charge assignments of the quark model (see, for example, Reference 86).

Experimentally, in Figures 5.9 and 5.10 we observe scaling as low as .6 GeV^2, though with distinct violations seemingly logarithmic in Q^2. As shown in Figures 5.11 and 5.12, as Q^2 increases, $F_2(x)$ shifts to smaller and smaller x. From the perspective of the earlier non-relativistic discussion, such behavior is understood in terms of the increasing resolution of the photon probe: for $Q^2 \ll 1$ GeV^2 we know elastic ($x = 1$) scattering is predominant; at $Q^2 \approx 1$ GeV^2, we see that $F_2(x)$ peaks around $1/N$ where $N \approx 5$ approximates the number of target constituents; and at larger Q^2, $F_2(x)$ peaks at smaller and smaller values of $1/N$. These large values of N reflect scattering from the populous low-x sea of quark and anti-quark pairs which become resolvable only at large Q^2 and small x. As N increases, an equilibrium is approached where the momentum of the proton, originally carried by the three "valence" quarks, is shared among all types of quarks and gluons. Thus, even at very high Q^2, we expect to observe some scaling violation as $F_2(x, Q^2)$ is driven to increasingly smaller values of x, tending ultimately to $\delta(x)$.

Theoretically, perturbative QCD predicts logarithmic scaling violations, with true scale invariance being approached only asymptotically in Q^2. The observed scaling violations are understood in terms of the Q^2 dependence of the quark and anti-

quark distribution functions (in Equation A.35) as dictated by the Alterelli-Parisi equations,[101] As Q^2 increases, the photon probe is more and more likely to resolve the struck quark into a quark and a radiated gluon. The resulting tendency is to drive the structure function momentum distributions to lower and lower x.

Perturbative QCD calculations of the structure functions, however, ignore all terms that fall off as fast as $\sim 1/Q^2$. It is possible, however, that these terms represent a significant, if not dominant, contribution to the observed scaling violations in the SLAC data.[102] Such an occurrence would invalidate any real test of QCD over the full decade in Q^2 spanned by the SLAC data.

These power corrections to QCD are of both a kinematic (or target mass) and dynamic (or higher twist) nature. The kinematic target mass corrections to perturbative QCD, aa calculated by Georgi and Politzer[8] within the framework of the operator product expansion, take the form of a power series in (M_p^2/Q^2). Kinematic occurrences of (M_p^2/Q^2) are linked in an intricate way to the x dependence of F_1 and F_2, leading to the identification of a new scaling quantity, the Nachtmann scaling variable,[103]

$$\xi = \frac{2x}{1+\sqrt{1+4M_p^2x^2/Q^2}} \; . \tag{A.36}$$

It has been shown by Ellis *et al.*[104] that the same power series in (M_p^2/Q^2) is obtained as a kinematic consequence of the naive parton model with the inclusion of a Lorentz-invariant intrinsic transverse momentum, though without off-shellness. In a QCD analysis which includes both off-shellness and interactions, Ellis *et al.* calculate the twist-4 corrections, which are in general expressed as a power series in $(\Lambda_{\rm QCD}^2/Q^2)^{\tau-2}$, where $\Lambda_{\rm QCD}$ is the usual QCD scale parameter and τ is the twist counting index,[105] given by $\tau \in \{2,4,6,\ldots\}$. These higher twist corrections are the dynamical complement of the target mass corrections: both are seen to be manifestations of the transverse degrees of freedom of the partons and gluon field. Higher twist corrections, however, are generally incalculable, as they depend on the unknown parton correlation functions which dictate the non-perturbative dynamics.

Within the framework of the naive parton model with spin-$\frac{1}{2}$ partons, R is given by $4M_p^2x^2/Q^2$. By allowing the partons in this model to have an intrinsic transverse momentum, p_T, and a nonzero mass, the value of R is increased and given by[99]

$$R(x,Q^2) = \frac{4\left[M_p^2x^2 + \langle p_T\rangle^2 + \delta\right]}{Q^2 + \langle p_T\rangle^2}\ , \tag{A.37}$$

where δ parametrizes the parton mass effects.

First order QCD calculations do not contribute to R. However, in second order QCD the inclusion of hard gluon bremsstrahlung and photon-gluon interactions contribute to F_L,[104,7] through the advent of transverse momenta, p_T. The gluon contributions to p_T rise $\sim Q^2$, while the p_T contribution to R falls $\sim 1/Q^2$. Thus the leading order QCD contribution to R varies as α_s, namely, $R^{\rm QCD} \sim 1/\ln Q^2$. Because these QCD calculations of R are quite small,† target mass and higher twist power corrections are expected to be significant, especially in the SLAC Q^2 range. See, for example, Section 5.3.3.

† Calculations[106] to fourth order in QCD are only slightly smaller.

Appendix B

Statistical Techniques

This appendix provides concise statements of the statistical identities and techniques employed in this thesis.

B.1 The Propagation of Errors

Consider a set of measured quantities $\{A_j\}$, each element of which has associated with it a vector of uncertainties, δ_j^k. Assume that the correlations between δ_i^k and δ_j^k are known, and denoted by the correlation matrices $\mathcal{M}^k$. Let $\mathcal{F}$ be any operator which acts on the set $\{A_j\}$, such that

$$A = \mathcal{F}\{A_j\} \ . \tag{B.1}$$

Then, the uncertainty vector of A is given by[107]

$$\delta^k = \left[\sum_{i,j} \delta_i^k \frac{\partial \mathcal{F}}{\partial A_i} \mathcal{M}_{ij}^k \, \delta_j^k \frac{\partial \mathcal{F}}{\partial A_j} \right]^{1/2} . \tag{B.2}$$

For most applications of Equation B.2 in this thesis, $\mathcal{F}$ is the operator which takes the weighted average of the $\{A_j\}$,

$$A = \sum_j A_j \, wt_j \Big/ \sum_j wt_j \ , \tag{B.3}$$

and the uncertainty vector of A is

$$\delta^k = \left[\sum_{i,j} \delta_i^k wt_j \mathcal{M}_{ij}^k \delta_j^k wt_j \right]^{1/2} \Big/ \sum_j wt_j \ . \tag{B.4}$$

All the interesting physics is in the assignment of the correct weights in this procedure. It is critical that the weights be determined only by the random components of the error vector,

$$wt_j = 1 \Big/ \sum_{\substack{k \\ \text{random}}} \left(\delta_j^k\right)^2 \ . \tag{B.5}$$

Because some components of the error vector are nearly random, or only partially correlated, it is often difficult to determine the correct summation in Equation B.5. For each application of Equation B.4, we explicitly state which components of the error vector are included in the assignment of the weights.

The correlation matrix used throughout this report is related to the more usual covariance matrix, $\mathbf{M}$, by

$$\mathcal{M}_{ij} = \mathbf{M}_{ij} \Big/ \left[\mathbf{M}_{ii}\,\mathbf{M}_{jj}\right]^{\frac{1}{2}} \ . \tag{B.6}$$

Thus the elements of $\mathcal{M}$ are bounded by ± 1.

These formal expressions, Equations B.2 and B.4, reduce to more familiar[80] forms under specific ideal assumptions. First, if the errors δ_j^k are perfectly uncorrelated (or random), then $\mathcal{M}^k = \mathbf{1}$. In this case, Equation B.2 reduces to

$$\delta^k = \left[\sum_j \left(\delta_j^k \frac{\partial \mathcal{F}}{\partial A_j} \right)^2 \right]^{1/2} , \tag{B.7}$$

and Equation B.4 reduces to

$$\delta^k = \left[\sum_j \left(\delta_j^k wt_j\right)^2 \right]^{1/2} \Big/ \sum_j wt_j \ , \tag{B.8}$$

which, for weights given by $1/\left(\delta_j^k\right)^2$ further reduces to the usual "inverse-root-sum-of-inverse-squares" propagation formula for statistical errors.[80]

Second, if the errors δ_j^k are perfectly correlated, then $\mathcal{M}^k$ is the matrix with all elements equal to 1. In this case, by inverting the summations and multiplications of Equations B.2 and B.4 we note the following simplifications. Equation B.2 reduces to the simple sum of propagated errors,

$$\delta^k = \sum_j \delta_j^k \frac{\partial \mathcal{F}}{\partial A_j} \ , \tag{B.9}$$

and Equation B.4 reduces to the weighted average of the correlated errors,

$$\delta^k = \sum_j \delta_j^k wt_j \Big/ \sum_j wt_j \ . \tag{B.10}$$

B.2 Non-Gaussian Error Distributions

An extensive numerical study[108] of the error distribution of the quotient of two measured quantities with gaussian errors recommends a simple approximate treatment for statistical operations on the data. We quote here only a formal statement of the observations of this report.

> If the independent quantities x_1 and x_2 conform to a gaussian distribution with *fractional* standard deviations δ_1 and δ_2, respectively, and $\delta_1 \approx \delta_2$, then $\ln(x_1/x_2)$ approximately conforms to a gaussian distribution with *absolute* standard deviation $\sqrt{\delta_1^2 + \delta_2^2}$.

The askewity of the error distribution in R is related to that of cross section ratios,[109] and can be seen in Figure B.2. Similarly,

> If $R \pm \delta R$ is extracted via a regression analysis of measured cross sections over a span in ϵ of $\Delta\epsilon$, and if the measured cross sections conform to gaussian distribu-

tions with roughly equal widths, then $\ln(1+\Delta\epsilon R)$ approximately conforms to a gaussian distribution with standard deviation $\Delta\epsilon\,\delta R/(1+\Delta\epsilon R)$.

Throughout this report, all statistical operations performed on the cross section ratios or on the R measurements are carried out in these pseudo-gaussian logarithmic variables, including the error propagations of Equation B.2. For $\Delta\epsilon$ we use the average ϵ span of the data, $\Delta\epsilon = .39$ for E140 and $\Delta\epsilon = .49$ for SLAC. The only exception to this procedure is in the regression analyses for $R^d - R^p$ and $R^{Fe} - R^d$ when a simpler technique is employed instead (see Section 4.2).

Because the error distributions of $R^d - R^p$ and $R^{Fe} - R^d$ are symmetric, we do not use the logarithmic variable in the analyses of these quantities, but instead make the very minor approximation that they are perfectly gaussian distributed.

B.3 On the Interpretation of χ^2

The data shown in the regression analyses in Figure 5.4 display the statistically expected amount of scatter, each best fit yielding a $\chi^2/df \approx 1$. The correct procedure for the analysis of data which display more than the statistically expected amount of scatter is a subject of some controversy. There are two philosophically different ways to define the uncertainties in the best fit parameters from any χ^2 minimization procedure:

① The correct parameter uncertainties are determined exclusively by the uncertainties in the data, without regard to the quality of the fit, or the size of the residuals;

② The correct parameter uncertainties are determined exclusively by the residuals to the fit. The parameter values are determined using the weights assigned to each point, but the parameter uncertainties are solely based on the residuals to the fit.

And, there is a simple relationship between these prescriptions,

$$\text{Errors①} = \text{Errors②} \times \sqrt{\chi^2/df} \ . \tag{B.11}$$

This is the same factor by which one would have to inflate the errors in the data in order to achieve a fit with $\chi^2/df = 1.00$.

The first philosophy is the standard high energy physics approach, where accurate knowledge of the statistical and systematic uncertainties in the data is a priority. The second philosophy is the accepted approach in the biological and social sciences, where the uncertainties in the data are often only partially understood. Yet, even in physical science applications, the additional factor of $\sqrt{\chi^2/df}$ is often touted[74–76] as a necessary correction to the uncertainties whenever the χ^2/df is greater than one.

The relevance to our work is the clear. We report the results of 260 linear regression analyses, many of which display much more than the statistically expected amount of scatter. In Figure B.1 we present two such regression analyses. To answer the question of whether or not the additional factor of $\sqrt{\chi^2/df}$ is required in the definition of δR^{ST}, we perform a monte carlo simulation of the R extractions. We randomly generate five cross sections from a gaussian distribution centered at 1.000 with a $\pm.020$ width, and assign them to ϵ values of $\{.4, .5, .6, .7, .8\}$. A linear regression analysis is applied, and the observed values of R and χ^2/df are recorded. This process is iterated 10^6 times to study the width of the distribution of observed R values as a function of χ^2/df. The results of this study are shown in Figure B.2. For each χ^2/df bin, the width of the observed R distribution is $\pm.08$. Thus, we conclude that regression analyses obtained by fits with large χ^2/df, within the assumptions of this study, measure R as accurately as those with much smaller χ^2/df.

This conclusion, to have any merit, must be accompanied by the statement that systematic effects do not contribute to the χ^2. Large systematic effects in the data will generate large χ^2/df, and will clearly not measure R as accurately as data which display no such systematic effects. We show with Figures 4.2 and 5.5 that no large

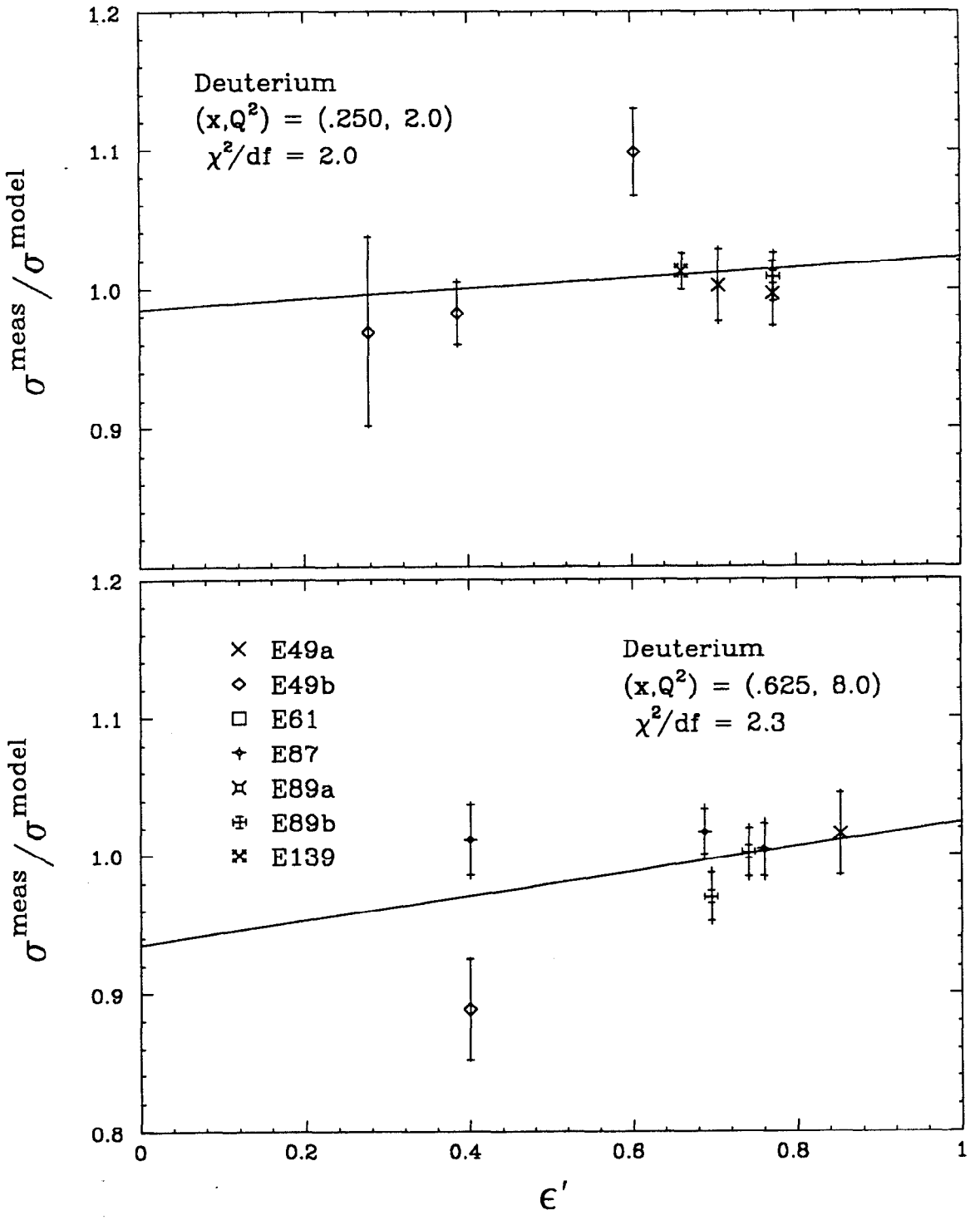

Figure B.1. Shown are two sample regression analyses which display more than the statistically expected amount of scatter. Compare with Figure 5.4. Poor fits such as these occur naturally and with the statistically expected frequency.

systematic effects remain within the E140 data or the SLAC data. For the six analyses outside the expected χ^2/df distribution in Figure 5.5, we hypothesize that some large systematic effect may exist in these data and we increase the δR^{ST} obtained from these regressions by the factor $\sqrt{\chi^2/df}$.

Further studies demonstrate that our conclusion is robust with respect to the main parameters of the monte carlo simulation. We hypothesize the generalization of our conclusion to include the treatment of errors from any χ^2 minimization procedure, though, in this thesis we rely only on the conclusion as stated.

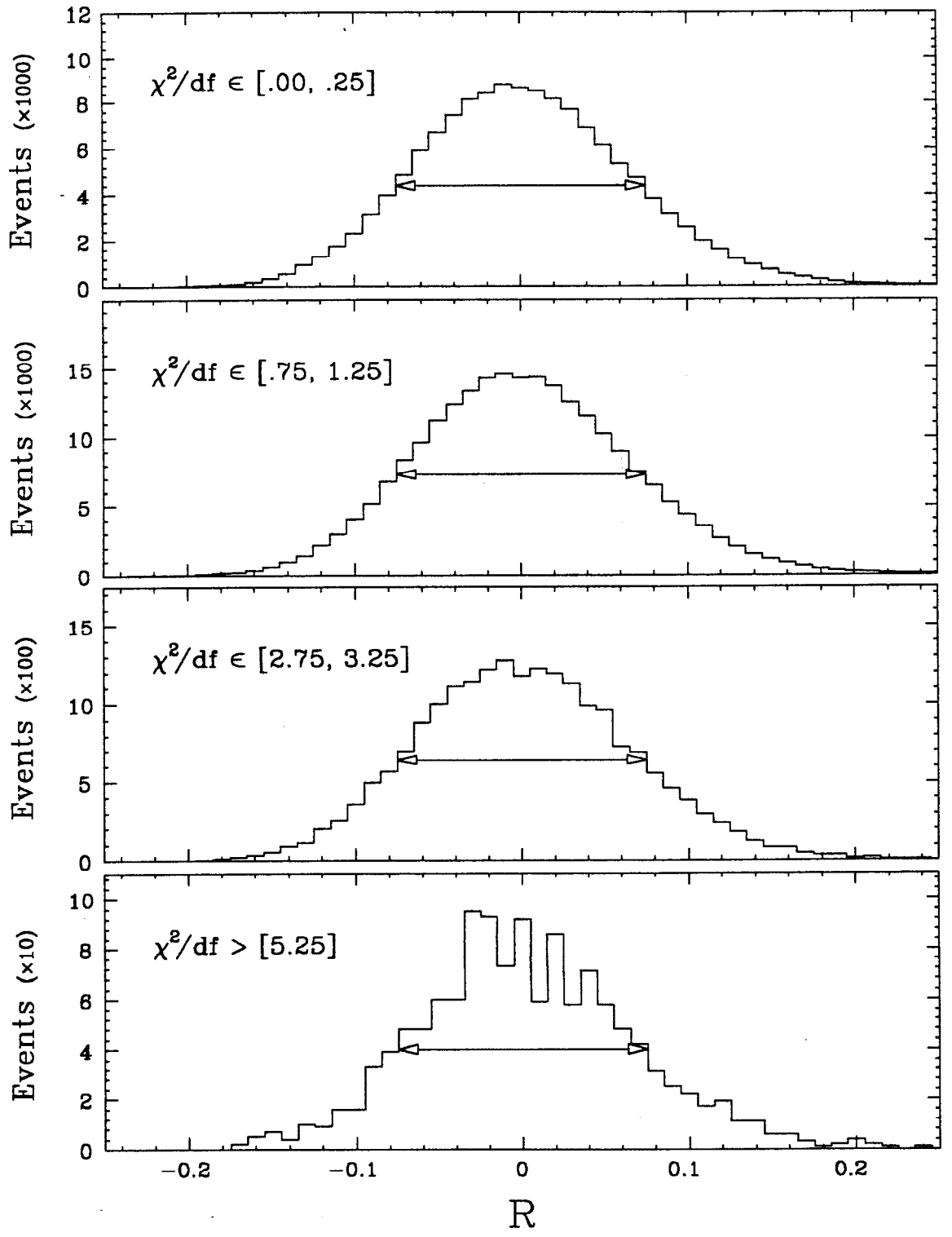

Figure B.2. Shown are the results from a monte carlo study of R extractions from cross sections with $\pm 2\%$ gaussian errors. The full width at half maximum of each distribution is indicated by the double arrows. The results indicate that regression analyses displaying large χ^2/df measure R as accurately as those with much smaller χ^2/df.

Appendix C

Systematic Errors

This appendix explicitly delineates all contributions to all components of the uncertainty vector assigned to each measured cross section and cross section ratio included in our global reanalysis.

Table C.1 presents the experimental uncertainty due to each contribution to the cross section calculation. Units are everywhere [%] in the cross section, with two exceptions. First, uncertainties in the scattering kinematics propagate complexly into the cross sections, as derivable from the cross section models $F_2^{\Lambda_{12}}$ and R^{1990}. Thus, energy uncertainties are expressed in units of [%] energy and angle uncertainties are in units of [mrd]. Second, uncertainties of type δ^{SE} are in units of [GeV^{-1}] and are propagated as in Equations 2.4 and 5.17, where $\langle E' \rangle$ for the eight experiments are $\{9.68, 3.04, 14.50, 6.26, 1.20, 7.68, 6.40, 3.99\}$ GeV, respectively. For E139 and E140 the δ^{SE} are taken from the wirefloat calibration studies,[63] (see Section 2.3.2) and for the other experiments these δ^{SE} represent limits imposed by the residuals studies of in Section 5.2.5.

Not shown in Table C.1 are the uncertainties due to radiative corrections procedure, which are taken to be perfectly correlated across all cross sections reported in this study. The δ^{RC} component of this uncertainty is given by Equation 3.12. Additionally, as noted in the text to Equation 3.12, there is a $\pm 1.0\%$ normalization-like uncertainty due to the radiative corrections this study.

The δ^{NM} portion of Table C.1 is presented for completeness only and is not used in the global reanalysis (with the exception of the E140 column which reproduces Table 3.3, modulo the above note). Rather, we use the measured relative normalization uncertainties, δ^{NM_1} and δ^{NM_2}, as discussed in Section 5.2. The measured normalization offsets of each experiment to E140, given in Table 5.2, compare favorably with the total of the δ^{NM} uncertainties given in Table C.1. After removing the common uncertainties in the world cryogenic data for hydrogen and deuterium densities, we observe an average χ^2/df of 7.4/6 for hydrogen and 9.9/7 for deuterium. Note that half of the χ^2 contribution in each of these is due to the large relative normalization difference observed between E89b and the other experiments.

For σ^d/σ^p ratios most components of the error vectors approximately cancel and become negligible. The δ^{SY}, δ^{SE}, and δ^{RC} components are thus assumed to cancel perfectly. Some elements of the δ^{SR} component are similarly assumed to cancel in the cross section ratio (the fluctuations in beam charge and detector efficiencies), while the other elements are independent and propagated exactly.

Using the δ^{NM} portion of Table C.1, it is possible to make a χ^2-based consistency check of the relative normalizations of Table 5.2. Making the worst case assumption that the first and last rows of the δ^{NM} section of Table C.1 are very strongly correlated, and after removing the common uncertainties due to the world cryogenic data, we observe a χ^2 of 4.5 for the deuterium data (with E140 "floating" and E89a excluded).

Table C.1. Presented is a concise summary of all contributions to the uncertainty vector of each cross section measurement. Tabled values are for both deuterium and hydrogen except where noted. See text for units and for further discussion. Table continues on next page.

	E49a	E49b	E61	E87	E89a	E89b	E139	E140
δ^{SR}								
Beam energy	.25	.25	.10	.25	.20	.20	.15	.10
Beam angle	.08	.08	.08	.08	.07	.07	.08[a]	.05
Beam charge	.70	.30	.60	.30	.50	.50	.30	.30
Target density	.30	.30[b]	.50[a]	.30	.30[a]	.30[a]	.50	.30
Scattering angle	.00[a]	.05[a]	.00[a]	.05[a]	.02[a]	.05[a]	.05[a]	.03
Secondary energy	.05[a]	.05[a]	.05[a]	.05[a]	.03[a]	.05[a]	.03[a]	.03
Detector								
Efficiencies	1.5	.70	1.4	.70	1.3	1.0[c]	.10[a]	.15
δ^{SY}								
Calibrations								
Beam energy	.10	.10	.10	.10	.10	.10	.10	.10
Scattering angle	.02	.05	.02	.05	.02	.05	.05	.03
Secondary energy	.10[a]	.10[a]	.10[a]	.10[a]	.10[a]	.10[a]	.05	.04
Background								
π^-	[d]	.30	[e]	.30	1.0[f]	[g]	.00	.00
$\pi^\circ \to e^+e^-$	[h]	.10	[h]	.30	[i]	[h,c]	.10	[j]
δ^{SE}								
Acceptance	.17	.43	.10	.02	1.00	.12	.04	.04
δ^{NM}								
Beam charge	.7	.5	.8[a]	.5	.5[a]	.5[a]	.5	.5
Target density[k]	1.0[a]	.9	.8	.7	.7	.7	.7	.7
Target length	.8[a]	.6	.4	.4	.5	.5	.4	.4
Target impurities	.2[a]	.2[a]	.1	.1	.2	.2	.1	.2
Target endcap								
subtraction[l]	.5[a]	.3	.5	.3	.4	.7[c]	.0	.0
Acceptance	2.0	1.5	2.0	1.5	1.0	2.0	1.1	1.1

[a] Assumed.

[b] For deuterium, if $E_\circ \in \{10.392, 13.320, 8.713, 11.900\}$ then $\delta = .5$.

[c] The value quoted in the E89b thesis is overly conservative. The value we use is more accurate, yet still conservative.

Table C.1/continued: Error vector summary.

[d] We use the parameterization: $\delta = .1$; if $4 < E' < 7$, $\delta = .6$.
[e] We use the parameterization: $\delta = .3$; if $6 < E' < 10$, $\delta = .7$.
[f] For hydrogen we use: $\delta = .5$.
[g] We use the parameterization: $\delta = .4$; if $5 < E' < 9$, $\delta = 1.0$;
if $5 < E' < 9$ and $\theta \leq 10°$ and $E_o > 15$, $\delta = 2.5$.
[h] We use a parameterization based on the E89b thesis:
$\delta = .2$; $W^2_{thr} = 2.15 + .14 E_o$; if $\theta \leq 6°$, $W^2_{thr} = W^2_{thr} + .35$;
if $W^2 > W^2_{thr}$, $\delta = .6$.
[i] We use a parameterization based on the E89a offline logbooks:[110]
$\delta = r/(1-r)$ where: if $E_o < 8$, $r = 31 \exp(-E'/.16)$;
else if $E_o < 11$, $r = 68 \exp(-E'/.16)$;
else if $E_o \leq 14$, $r = 23 \exp(-E'/.22)$;
else $r = 2.5 \exp(-E'/.54)$.
[j] We use the parameterization of Equation 3.4.
[k] For hydrogen, δ is smaller by .2 for E49a, E49b, and E61 and by .3 otherwise.
[l] For hydrogen we use: $\delta = 1.75\,\delta$.

Appendix D

Target Models

This appendix provides all the target and radiator information needed to reproduce the Bardin/Tsai radiative corrections calculations for the hydrogen and deuterium cross section measurements of all eight experiments.

A detailed reconstruction of each target from each experiment is attempted based on the theses of Table 1.1, information archived in the TASI Database,[78] and various logbooks and technical notes. As these sources frequently differed in their representation of the target information, the parameters presented here are our best estimates based on an overall average with greatest weight assigned to the earliest sources. Where possible, we calculate target thicknesses from the quoted density and target length (in cm) using modern values for the target radiation lengths[107]

$$\begin{aligned} \mathrm{RL_H} &= 61.28\ \mathrm{g/cm^2}, \\ \mathrm{RL_D} &= 122.6\ \mathrm{g/cm^2}. \end{aligned} \tag{D.1}$$

Otherwise, we have used the quoted target thicknesses (in RL) and applied a correction factor to account for changes in the known radiation lengths of hydrogen and deuterium.

Table D.1 presents the thicknesses in units of [RL] for targets, target cell wall thicknesses, and upstream and downstream radiators. The upstream radiator thicknesses include all material between the A-bend of the beam switchyard (see Section

Table D.1. Presented are the target thicknesses plus additional external radiators for the eight experiments. Units are everywhere [RL] and expressed in [%]. Except where noted, cell walls are aluminum. Other external radiators are predominantly aluminum. See text for further details.

	Target Type	Upstream Radiator	Hydrogen Target	Deuterium Target	Cell Wall	Downstream Radiator
E49a	VC	.027[a]	.824	.963	.086	.744[b]
E49b	VC	.031	.788	.976	.086	.582
E61	VC	.058	.794	.983	.086	.625
E87	VC	.036	1.594[c]	1.935[c]	.146[d]	.517
E89	VC[e]	.036	2.009	2.423	.248[d]	.018[f]
E139	HC[g]	.104		2.072	.132[h,i,j]	.913
E140	HC[g]	.103		2.769	.086[i,j]	.940

[a] For $\theta = 10.000°$ use $t = .032$.
[b] For $\theta = 10.000°$ use $t = .650$.
[c] Target cell is centered off beam axis, .040 towards the spectrometer.
[d] Target walls are steel.
[e] Target is a vertical oval tube rather than a vertical cylinder; see text.
[f] For E89b use $t = .560$.
[g] Target width perpendicular to the beam axis is .350 (2.54 cm).
[h] For target entrace window use $t = .078$ and for target exit window use $t = .115$.
[i] Exit window bows outward with radius of curvature .700 (5.08 cm).
[j] Additional material effectively increases the target cylindrical cell wall thickness:
Coaxial mylar flowguide (see Figure D.1): .024;
Epoxy and solder averaged over cell length: .043;
Aluminum superinsulation: .022.

2.1) and up to, but not including, the cell wall of the target. The downstream radiator thicknesses include all material between, but not including, the cell wall of the target (or, if used, target superinsulation) and the bending magnets of the spectrometer.

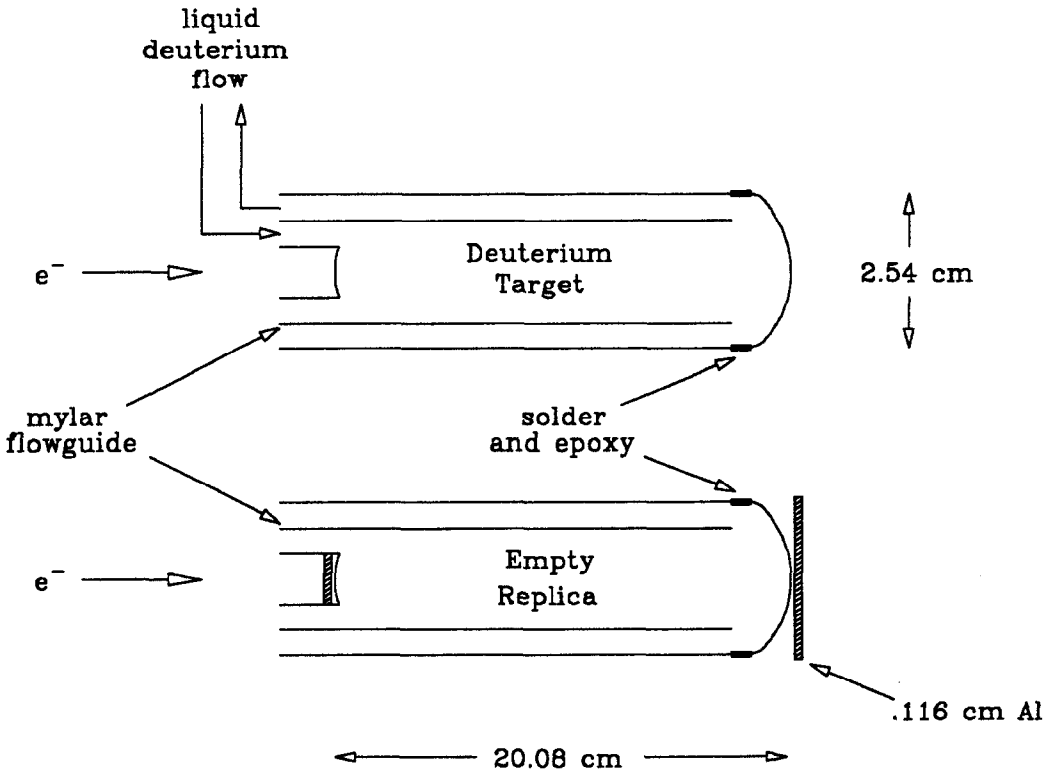

Figure D.1. Shown is a schematic of the E140 and E139 horizontal cylinder targets and empty target replicas. Additional radiators are added to the entrance and exit windows of the empty replica to improve counting rates and approximately match the external radiative corrections of the full targets.[57]

Also indicated in Table D.1 are the target shapes and orientations with respect to the incident beam. Targets of type VC are vertical cylinders centered on and perpendicular to the beam. Flow is perpendicular to the beam and fan driven. The general design of the VC targets is described in detail in Reference 3 and to varying degrees in the references of Table 1.1. Target type HC is a horizontal cylinder coaxial to the beam, shown schematically in Figure G.1. An internal coaxial flowguide separates flows parallel and antiparallel to the beam. Additional specifications for the HC target thicknesses are given in Table D.1. The general design of HC targets is discussed in References 58 and 111 and more specifically in the references of Table 1.1.

The large angle experiment E89a (performed simultaneously with E89b) required thick targets to improve the counting rates. To minimize the amount of target material viewed by the scattered particles the target cross section was not circular, but oval. For a horizontal (x, z) orthogonal coordinate system with origin at the target center and z parallel to the incident beam, the cell walls are located[35] at points

$$\begin{aligned} \left(\frac{x}{.132}\right)^2 + \left(\frac{z}{1.004}\right)^{7.3} &= 1 \ , \\ \left(\frac{x}{.160}\right)^2 + \left(\frac{z}{1.212}\right)^{7.3} &= 1 \ , \end{aligned} \tag{D.2}$$

for hydrogen and deuterium, respectively, in units of [RL].

To simplify the radiative corrections, the target walls, upstream and downstream radiators are assumed to be aluminum. We calculate the radiative correction at several points within the targets and average over the target lengths. The amount of target material viewed by the scattered targets is calculated for each angle, numerically for E89, and using a detailed target model for E139 and E140. Early studies support the assertion by Tsai[36] that for VC targets the external radiative correction does not depend strongly on the scattering location. Observed effects were at the $\pm.2\%$ level. The extended lengths of the E139 and E140 targets, on the other hand, required that the radiative corrections be calculated at and averaged over a minimum of nine points along the target central axis.

Appendix E

Data Tables and Software

The primary set of data tables for this thesis, including hydrogen and deuterium cross sections and structure functions, is stored on a floppy diskette, in the form of 19 ASCII files occupying a total of 460 kilobytes. Three storage media are available: high density $5\frac{1}{2}$ inch IBM PC/AT formatted diskettes, double density $3\frac{1}{2}$ inch IBM PS/2 formatted diskettes, and double density $3\frac{1}{2}$ inch Apple Macintosh formatted diskettes.

A copy of any of these diskettes may be obtained from: SLAC Publications, Mail Bin 68, P.O. Box 4349, Stanford, CA 94309-4349, phone (415) 926-2677. Request SLAC-REPORT-357/Appendix E Diskette, and specify computer format. Alternatively, these files can be obtained via bitnet from SER@SLACVM, EMR@SLACVM, or LWW@SLACVM during the foreseeable future.

Presented below is a brief summary of the 19 files found on each diskette.

File E.1. HELP.DOCUMENT. Provides detailed information about the other files found on the disk.

File E.2. SIGMA.HYDROGEN. Table of final normalized hydrogen cross sections with error vectors. Cross sections are condensed exactly as described in Section 5.2.1. This table also gives the Bardin/Tsai radiative correction factor applied to the raw cross sections.

File E.3. SIGMA.DEUTRIUM. Table of final normalized deuterium cross sections with error vectors. Cross sections are condensed exactly as described in Section 5.2.1. This table also gives the Bardin/Tsai radiative correction factor applied to the raw cross sections.

File E.4. F2.HYDROGEN. Table of final normalized hydrogen F_2 values with error vectors. Each element in the table is extracted from the corresponding element of File E.2 according to the prescription of Section 5.4.

File E.5. F2.DEUTRIUM. Table of final normalized deuterium F_2 values with error vectors. Each element in the table is extracted from the corresponding element of File E.2 according to the prescription of Section 5.4.

File E.6. F2.DPRATIO. Table of final normalized deuterium/hydrogen F_2^d/F_2^p ratios. Using our result that $R^d = R^p$ (see Section 3.5.2), we note that this table also gives the deuterium/hydrogen cross section ratios σ^d/σ^p. Ratios are condensed exactly as described in Section 5.2.1.

File E.7. SPECTRA.BCDMS. Table of SLAC hydrogen and deuterium structure functions as plotted in Figures 5.14 and 5.15.

File E.8. SPECTRA.BCDMSZ. Table of BCDMS hydrogen and deuterium structure functions, extracted assuming $R = R^{1990}$, as plotted in Figures 5.14 and 5.15.

File E.9. SPECTRA.EMC. Table of SLAC hydrogen and deuterium structure functions as plotted in Figures 5.16 and 5.17.

File E.10. SPECTRA.EMCZ. Table of EMC hydrogen and deuterium structure functions, extracted assuming $R = R^{1990}$, as plotted in Figures 5.16 and 5.17.

File E.11. SPECTRA.FORTRN. Fortran code used to generate Files E.7 and E.9 from files E.4 and E.5. The primary feature of this program is the (very nearly) exact propagation of all components of the error vector through the binning and averaging processes. This program is easily generalizable to produce other binnings in (x, Q^2) or to propagate the error vectors through any analysis. See footnote in Section 5.4.2.

File E.12. R1990.FORTRN. Fortran code for the phenomenological model of R defined in Section 5.3.4. The program encodes Equations 5.29 through 5.35 and returns the best fit value for R and the total uncertainty in R.

File E.13. F1990.FORTRN. Fortran code for both the $F_2^{\Omega_9}$ and $F_2^{\Lambda_{12}}$ models defined in Section 5.4.1. The program returns both F_2 and its statistical uncertainty. This program requires an external data file, supplied here as File E.14.

File E.14. F1990.MATRICES. Covariance matrices for the best fit solutions to the $F_2^{\Omega_9}$ and $F_2^{\Lambda_{12}}$ models. Accessed in this way, the models can be conveniently updated without altering the code of File E.13. Note that 10 digits of accuracy are required for the successful calculation of the statistical uncertainty in F_2.

File E.15. R.HYDROGEN. Table of extracted R values from the combined hydrogen data. Note that the R values presented in Table 5.8 are the average of these values and the deuterium values of File E.16.

File E.16. R.DEUTRIUM. Table of extracted R values from the combined deuterium data (E140 data excluded). Note that the R values presented in Table 5.8 are the average of these values and the hydrogen values of File E.15.

File E.17. R.WORLD. Table of world R values. Reproduces Tables 4.6 and 5.8, plus includes the R data from the EMC,[9,21] BCDMS,[16,17] and CDHSW[18] collaborations.

File E.18. SPECTRA.F2NF2P. Table of smeared neutron/proton F_2 ratios (as defined by Equation 5.41) for SLAC, as plotted in Figures 5.20 and 5.21, matching the binnings of BCDMS and EMC, respectively.

File E.19. SPECTRA.F2NF2PZ. Table of smeared neutron/proton F_2 ratios (as defined by Equation 5.41) for BCDMS and EMC as plotted in Figures 5.20 and 5.21, respectively.

References

1. S. Dasu *et al.*, Phys. Rev. Lett. **60,** 2591 (1988).
2. S. Dasu *et al.*, Phys. Rev. Lett. **61,** 1061 (1988).
3. A. Bodek *et al.*, Phys. Rev. **D20,** 1471 (1979).
4. M.D. Mestayer *et al.*, Phys. Rev. **D27,** 285 (1983).
5. NPAS Users Guide, SLAC-Report-269 (1984).
6. S. Dasu, private communication, 1988. These calculations supercede those presented in References 2 and 29.
7. G. Altarelli and G. Martinelli, Phys. Lett. **76B,** 89 (1978).
8. H. Georgi and H.D. Politzer, Phys. Rev. **D14,** 1829 (1976).
9. J.J. Aubert *et al.*, Nucl. Phys. **B259,** 189 (1985).
10. J.J. Aubert *et al.*, Nucl. Phys. **B272,** 158 (1986).
11. P.D. Meyers *et al.*, Phys. Rev. **D34,** 1265 (1986).
12. H.L. Anderson *et al.*, Phys. Rev. **D20,** 2645 (1979).
13. D. MacFarlane *et al.*, Z. Phys. **C26,** 1 (1984).
14. H. Abramowicz *et al.*, Z. Phys. **C17,** 283 (1983).
15. F. Bergsma *et al.*, Phys. Lett. **141B,** 129 (1984).
16. A.C. Benvenuti *et al.*, Phys. Lett. **223B,** 485 (1989).
17. A.C. Benvenuti *et al.*, preprint, CERN-EP/89-170 (1989), submitted to Phys. Lett. B.
18. P. Berge *et al.*, CERN-EP/89-103 (1989), submitted to Z. Phys. C.

19. S. Ekelin and S. Fredriksson, Phys. Lett. **162B,** 373 (1985).

20. T. Sloan, CERN-EP/87-188 (1987), presented at Int'l Europhysics Conference on High Energy Physics, Uppsala, 1987.

21. J.J. Aubert *et al.*, Nucl. Phys. **B293,** 740 (1987).

22. A.D. Martin, W.J. Stirling, and R.G. Roberts, Phys. Lett. **207B,** 205 (1988).

23. J.R. Cudell, DAMTP/88-12, (1988), presented at the Moriond Meeting on Current Issues in Hadronic Physics, Les Arcs, 1988.

24. E. Locci *et al.*, presented at Int'l Europhysics Conference on High Energy Physics, Uppsala, 1987.

25. R. Ansari *et al.*, Phys. Lett. **186B,** 440 (1987).

26. A.C. Benvenuti *et al.*, preprint, CERN-EP/89-171 (1989), submitted to Phys. Lett. B.

27. L.L. Frankfurt and M.I. Strikman, Nucl. Phys. **B184,** 107 (1979).

28. A.D. Martin, R.G. Roberts, and W.J. Stirling Phys. Lett. **189B,** 220 (1987).

29. S. Dasu, Ph.D. thesis, University of Rochester, UR-1059, unpublished (1988).

30. J.G. Gomez, Ph.D. thesis, American University, unpublished (1987).

31. J.G. Gomez *et al.*, to be published (1990); R.G. Arnold *et al.*, SLAC-PUB-3348 (1984); R.G. Arnold *et al.*, SLAC-PUB-3320 (1984); *R.*G. Arnold *et al.*, Phys. Rev. Lett. **52,** 727 (1984).

32. R. Arnold *et al.*, SLAC Proposal E140 (1984), addendum (1985).

33. F.E. Close *et al.*, Phys. Lett. **129B,** 346 (1983).

34. E.M. Riordan, Ph.D. thesis, Massachusetts Institute of Technology, MIT-LNS RX-648, unpublished (1973).

35. M.D. Mestayer, Ph.D. thesis, Stanford University, SLAC-Report-214 (1978).

36. Y.S. Tsai, Rev. Mod. Phys. **46,** 815 (1974); Y.S. Tsai, SLAC-PUB-848 (1971); L.W. Mo and Y.S. Tsai, Rev. Mod. Phys. **41,** 295 (1969); Y.S. Tsai, Phys. Rev. **122,** 1898 (1961).

37. R.L. Anderson *et al.*, Nucl. Instr. Meth. **66,** 328 (1968).

38. L.W. Mo, SLAC-TN-65-40 (1965).

39. E.D. Bloom *et al.*, SLAC-PUB-815 (1971), specifically, experiments numbered one through four.

40. G. Miller *et al.*, Phys. Rev. **D5,** 528 (1972).

41. J.S. Poucher, Ph.D. thesis, Massachusetts Institute of Technology, MIT-LNS, unpublished (1971).

42. J.S. Poucher *et al.*, Phys. Rev. Lett. **32,** 118 (1974).

43. A. Bodek, Ph.D. thesis, Massachusetts Institute of Technology, MIT-LNS COO-3069-116, unpublished (1972).

44. S. Stein *et al.*, Phys. Rev. **D12,** 1884 (1975).

45. W.B. Atwood, Ph.D. thesis, Stanford University, SLAC-Report-185 (1975).

46. W.B. Atwood *et al.*, Phys. Lett. **64B,** 479 (1976).

47. This thesis, superceding References 1 and 2.

48. K.L. Brown, SLAC-Report-75, Rev. 4 (1982).

49. R.F. Koontz *et al.*, SLAC-PUB-3615 (1985), presented at Part. Accel. Conf. IEEE, 1985.

50. R.B. Neal, *The Stanford Two-Mile Accelerator* (Benjamin, New York, 1968).

51. R.C. Walker, Ph.D. thesis, California Institute of Technology, UMI-89-15399, unpublished (1989).

52. R.S. Larsen and D. Horelick, SLAC-Report-100 (1969); R.S. Larsen and D. Horelick, SLAC-PUB-398 (1968).

53. R.C. Walker, "Calibration of the Toroid Charge Monitors for SLAC Experiment E140," E140 internal technical note, unpublished (1987).

54. D. Yount, Nucl. Instr. Meth. **52,** 1 (1967).

55. S. Rock, private communication, 1988; E133 Logbook II (1979).

56. J.W. Mark, SLAC-PUB-3169 Revised (1984), presented at Cryogenic Engineering and Int'l Cryogenic Materials Confs., Colorado Springs, 1983.

57. A. Bodek, Nucl. Instr. Meth. **109,** 603 (1973).

58. J.W. Mark, SLAC-PUB-3374 (1984), presented at Cryogenic Engineering and Int'l Cryogenic Materials Confs., Cambridge, 1985.

59. J.W. Mark, private communication, 1988.

60. L.W. Mo and C. Peck, SLAC-TN-65-29 (1965).

61. A.F. Sill, Ph.D. thesis, American University, unpublished (1986).

62. Z.F. Wang, S.J. Greene, and M.A. Plum, Nucl. Instr. Meth. **A243,** 413 (1986); L.G. Ratner and R.J. Lari, Argonne Nat'l Lab., ANL-RJL-???.

63. L.M. Clogher *et al.*, SLAC-PUB-???? (1990).

64. L.W. Whitlow, "Summary of the SP8 Angle," E140 internal technical note, unpublished (1986).

65. J.M. Lambert, "Survey Results for the 8 GeV Spectrometer," NPAS internal technical note, unpublished (1984).

66. L.M. Clogher, private communication, 1989.

67. L.W. Whitlow, "E' Calibration," E140 internal technical note, unpublished (1988).

68. P. Bosted and A. Rahbar, SLAC-NPAS-85-1 (1985).

69. S. Iwata, DPNU-3-79 (1979).

70. J.G. Gomez, SLAC-NPAS-TN-84-1 (1984).

71. L.S. Rochester *et al.*, Phys. Rev. Lett. **36,** 1284 (1976).

72. A.A. Akhundov, D.Yu. Bardin, and W. Lohman, JINR E2-86-204 (1986); A.A. Akhundov, D.Yu Bardin, and N.M. Shumeiko, Sov. J. Nucl. Phys. **44,** 1212 (1986); D.Yu Bardin and N.M. Shumeiko, Sov. J. Nucl. Phys. **29,** 499 (1979); A.A. Akhundov, D.Yu. Bardin, and N.M.Shumeiko, Sov. J. Nucl. Phys. **26,** 660 (1977).

73. A.A. Akhundov and D.Yu. Bardin, private communications, 1988.

74. B.R. Martin, BNL 12602, p104 (1968).

75. T. Chan, SLAC online numerical analysis programming document NAPL-LINLSQ, (1987).

76. S.C. Morton, private communication, 1988.

77. For example, C.E. Weatherburn, *Mathematical Statistics* (Cambridge Univ., Cambridge, 1962).

78. C. Logg, SLAC Group A, Programming Document Number XXVII, (1975).

79. E.D. Bloom and F.J. Gilman, Phys. Rev. **D4,** 2901 (1971).

80. P.R. Bevington, *Data Reduction and Error Analysis* (McGraw-Hill, New York, 1969).

81. R.C. Walker *et al.*, Phys. Lett. **224B,** 353 (1989.)

82. A.F. Sill, private communication, 1988.

83. M.D. Mestayer, private communication, 1990; see also Appendix A of Reference 35.

84. J.L. Miramontes, M.A. Miramontes, and J. Sanchez Guillen, Phys. Rev. **D40,** 2184 (1989).

85. L.W. Whitlow, presented at Div. Part. and Fields of the Am. Phys. Soc., Stoors (1988); A. Bodek, presented at High P_T Physics and Higher Twists, Paris (1988).

86. F.E. Close, *An Intro. to Quarks and Partons,* (Academic, London, 1979).

87. G. Altarelli, Phys. Reports **81C**, 89 (1982).

88. R.P. Mount, CALT-68-1519 (1988), presented at the XXIV Int'l Conf. on High Energy Physics, Munich, 1988.

89. D.W. Duke and J.F. Owens, Phys. Rev. **D30**, 49 (1984).

90. M. Arneodo *et al.*, preprint, CERN-EP/89-121 (1989), submitted to Nucl. Phys. B.

91. S.J. Wimpenney, private communication, 1989.

92. See Table 2.1.

93. M. Virchaux and A. Milsztajn, private communication, 1990.

94. G.B. West, Phys. Reports **18C**, 263 (1975).

95. R. Hofstadter, *Nuclear and Nucleon Structure* (Benjamin, New York, 1963).

96. J.D. Bjorken, Phys. Rev. **179**, 1547 (1969).

97. J. Friedman and H. Kendall, Ann. Rev. Nucl. Sci. **22**, 203 (1972).

98. R.P. Feynmann, Phys. Rev. Lett. **23**, 1415 (1969).

99. R.P. Feynman, *Photon-Hadron Interactions,* W.A. Benjamin Inc., Reading, MA (1976).

100. M. Gell-Mann, Phys. Lett. **11**, 255 (1964); G. Zweig, CERN-8409/Th.412 (1964).

101. G. Altarelli and G. Parisi, Nucl. Phys. **B126**, 298 (1977).

102. L.F. Abbott, W.B. Atwood, and R.M. BarnettPhys. Rev. **D22**, 582 (1980).

103. O. Nachtman, Nucl. Phys. **B63**, 237 (1973).

104. R.K. Ellis *et al.*, Nucl. Phys. **B207**, 1 (1982); R.K. Ellis *et al.*, Nucl. Phys. **B212**, 29 (1982).

105. D.J. Gross and S.B. Treiman, Phys. Rev. **D4**, 1059 (1971).

106. D.W. Duke *et al.*, Phys. Rev. **D25,** 71 (1977); A. Devoto *et al.*, Phys. Rev. **D30,** 541 (1984); A. Devoto *et al.*, Phys. Lett. **138B,** 418 (1984).

107. The Particle Data Group, Phys. Lett. **204B,** 1 (1988).

108. A. Bodek, Nucl. Instr. Meth. **117,** 613 (1974).

109. A. Bodek, SLAC-TN-74-2 (1974), a portion of which is available in Reference 108.

110. W.B. Atwood, private communication, 1988.

111. J.W. Mark, SLAC-PUB-3169 (1984), presented at Cryogenic Engineering and Int'l Cryogenic Materials Confs., Cambridge, 1983.